November 1, 1976

ANL/FPP/TM-74

CONF-760935--52

Argonne National Laboratory Papers

Presented at

Second ANS Topical Meeting on the Technology of Controlled Nuclear Fusion
September 21-23, 1976
Richland, Washington

by

Fusion Power Program
Argonne National Laboratory
Argonne, Illinois 60439

ANL/FPP Technical Memorandum Number 74

November 1, 1976

Work supported by the U. S. Energy Research and Development Administration.

DISCLAIMER

The facilities of Argonne National Laboratory are owned by the United States Government. Under the terms of a contract (W-31-109-Eng-38) between the U. S. Energy Research and Development Administration, Argonne Universities Association and The University of Chicago, the University employs the staff and operates the Laboratory in accordance with policies and programs formulated, approved and reviewed by the Association.

MEMBERS OF ARGONNE UNIVERSITIES ASSOCIATION

The University of Arizona
Carnegie-Mellon University
Case Western Reserve University
The University of Chicago
University of Cincinnati
Illinois Institute of Technology
University of Illinois
Indiana University
Iowa State University
The University of Iowa
Kansas State University
The University of Kansas
Loyola University
Marquette University
Michigan State University
The University of Michigan
University of Minnesota
University of Missouri
Northwestern University
University of Notre Dame
The Ohio State University
Ohio University
The Pennsylvania State University
Purdue University
Saint Louis University
Southern Illinois University
The University of Texas at Austin
Washington University
Wayne State University
The University of Wisconsin

November 1, 1976 ANL/FPP/TM-74

Argonne National Laboratory Papers

Presented at

Second ANS Topical Meeting on the Technology of Controlled Nuclear Fusion
September 21-23, 1976
Richland, Washington

by

Fusion Power Program
Argonne National Laboratory
Argonne, Illinois 60439

ANL/FPP Technical Memorandum Number 74

November 1, 1976

Work supported by the U. S. Energy Research and Development Administration.

FOREWORD

The following papers from Argonne National Laboratory were presented at the Second ANS Topical Meeting on the Technology of Controlled Nuclear Fusion, September 21-23, 1976, in Richland, Washington.

Table of Contents

Table of Contents (Continued)

TOKAMAK EXPERIMENTAL POWER REACTOR*

W. M. Stacey, Jr., M. A. Abdou, P. J. Bertoncini, C. C. Bolta, J. N. Brooks, K. Evans, Jr., J. A. Fasolo, J. C. Jung, R. L. Kustom, V. A. Maroni, R. F. Mattas, J. S. Moenich, A. Moretti, F. E. Mills, B. Misra, J. H. Norem, J. S. Patten, W. F. Praeg, P. Smelser, D. L. Smith, H. C. Stevens, L. Turner, S-T Wang and C. K. Youngdahl

ARGONNE NATIONAL LABORATORY, ARGONNE, ILLINOIS 60439

A conceptual design has been developed for a tokamak Experimental Power Reactor to operate at net electrical power conditions with a plant capacity factor of 50% for 10 yr. The EPR operates in a pulsed mode at a frequency of ∿1/min, with a ∿75% duty cycle, is capable of producing ∿72 MWe and requires 42 MWe. The EPR vacuum chamber is 6.25 m in major radius and 2.4 m in minor radius, is constructed of 2 cm thick stainless steel, and has 2 cm thick detachable, beryllium-coated coolant panels mounted on the interior. A 0.28 stainless steel blanket and a shield ranging from 0.6 to 1.0 m surround the vacuum vessel. Sixteen niobium-titanium superconducting toroidal field coils provide a field of 10 T at the coil and 4.47 T at the plasma. Superconducting ohmic heating and equilibrium field coils provide 135 V-s to drive the plasma current. Plasma heating is accomplished by 12 neutral beam injectors which provide 60 MW.

INTRODUCTION

An integrated conceptual design has been developed for a tokamak Experimental Power Reactor (EPR).[1] The design of the EPR was based upon technology that is consistent with a mid-to-late 1980s operation date. This paper summarizes the conceptual design, including the performance evaluation and cost estimate.

The design-basis performance objectives of the EPR are (1) to operate for 10 yr with a plant capacity factor of 50% [the plant capacity factor is defined as the product of the duty cycle (75%) and the plant availability (67%)]; and (2) to operate under conditions such that net electrical power production is feasible.

The principal geometric parameters of the EPR are given in Table 1. A vertical section view is shown in Fig. 1.

PLASMA PHYSICS AND PERFORMANCE ANALYSIS

Steady-state plasma performance parameters were obtained from a consistent solution of the MHD equilibrium equations and the plasma particle and power balance equations. MHD equilibria were obtained for different pressure profiles and degrees of diamagnetism/paramagnetism. These equilibria determine allowable values of plasma current, the safety factor, q, and the plasma-to-magnetic pressure ratios, β_p and β_t. Characteristics of MHD equilibria corresponding to a peak field at the TF coils of 10 T and that satisfy the constraint $q \geq 1$ are shown in Fig. 2

*Work supported by the U. S. Energy Research and Development Administration.

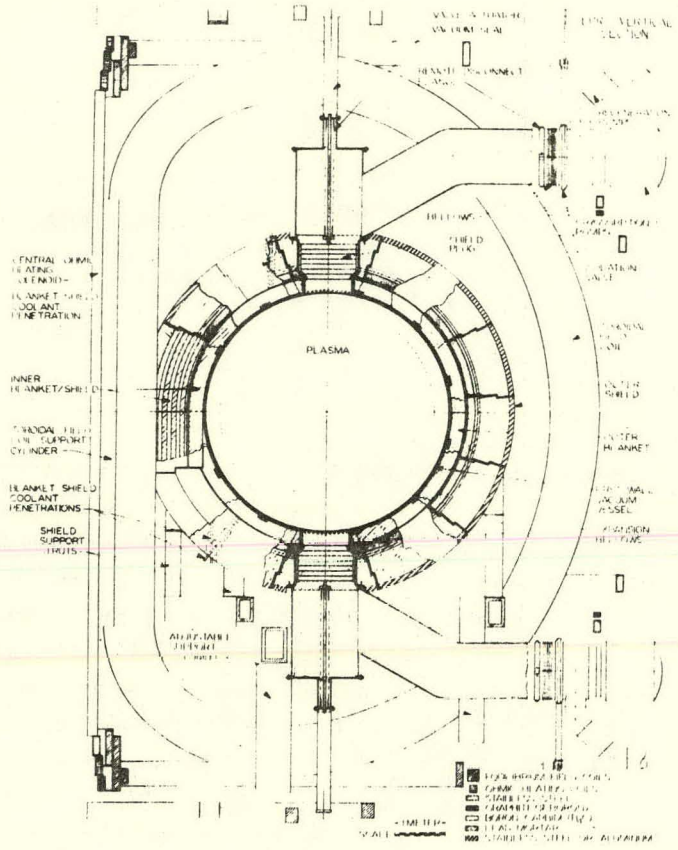

FIGURE 1. Detail of Vertical Section of EPR

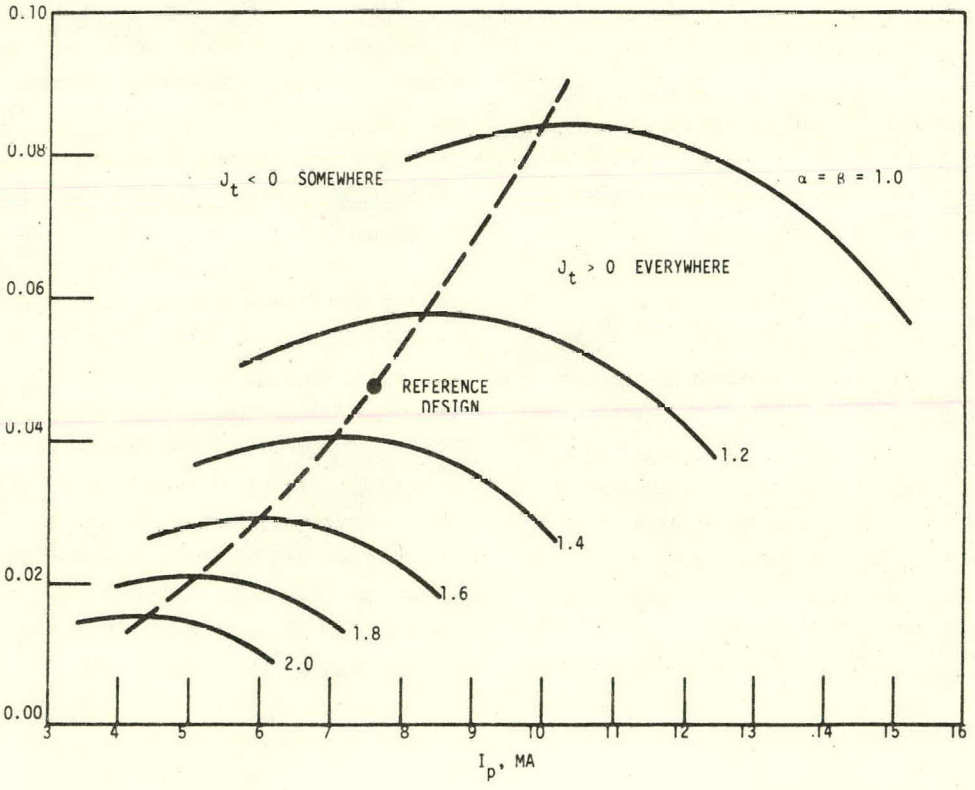

FIGURE 2. MHD Equilibria at B_{max}^{TFC} = 10 T — Total Beta

TABLE 1. EPR Geometrical Parameters

Radius (m)	
Major, R_0	6.25
Plasma, a	2.1
First wall, r_w	2.4
Aspect Ratio, A = R/a	2.98
Plasma Volume (m^3)	544
Toroidal Vacuum Chamber Volume (m^3)	711
First-Wall Area (m^2)	592
Blanket Thickness (m)	0.28
Shield Thickness (m)	0.58-0.97
Toroidal Field Coils	
No.	16
Horizontal bore, R_{bore} (m)	7.78
Vertical bore, Z_{eff} (m)	12.6

for different values of the pressure profile exponent, α.* The solid curves are loci of equilibria varying (from left to right) from highly diamagnetic to highly paramagnetic plasmas. Current reversal occurs for solutions to the left of the dashed line. The maximum value of β_t, hence the maximum power density, occurs for equilibria slightly less diamagnetic than those for which current reversal occurs. Thus, the dashed line represents a locus of "optimal" solutions — the value of β_p along this locus is confined to a rather narrow range of $1.8 \geq \beta_p \geq 1.6$. The safety factor evaluated at the plasma surface, q(a), increases with the degree of peaking in the pressure profile (i.e. with increasing α). The reference design point was chosen by selecting the pressure profile whose optimum solution has q(a) = 3.0, a value below which confinement has experimentally been found to deteriorate.

Steady-state plasma parameters corresponding to the reference design MHD solution of Fig. 2, and a similar solution for B_{max}^{TFC} = 8 T, are given in Table 2. A wide range of performance parameters is possible, corresponding to the range of MHD equilibria depicted in Fig. 2, and to the range of operating temperatures and values of energy confinement that may be obtained. Extensive analyses were performed to insure that the parameters shown in Table 2 are representative of the range of plasma conditions that may be obtained in EPR. With supplemental beam heating, the power output is not jeopardized by the possibility of subignition energy confinement.

*$p(r) \sim p_0[1 - (r/a)^2]^{\alpha}$.

TRANSIENT PERFORMANCE

Requirements on the plasma driving and heating systems and the power performance characteristics are determined from burn cycle dynamics simulations of the plasma, the ohmic-heating (OH) and equilibrium-field (EF) coil systems, and the neutral-beam injection system. The basic burn cycle is depicted schematically in Fig. 3, where the times correspond to the reference burn cycle. The plasma conditions of the reference case at B_{max}^{TFC} = 10 T (see Table 2) are approximated during the burn (flat-top) phase, and the dynamics calculations are constrained by the limit $\beta_p \leq \beta_p^{max} = 1.71$.

A variety of startup procedures were simulated in order to determine a compromise among several conflicting economical and technological limitations. The critical parameters which, to some extent, can be traded off against each other are (1) energy transfer from the homopolar OH supply (U_{OH}); (2) peak power required from the EF supply (P_{EF}); (3) total energy drawn from the energy storage unit for beam heating (U_{BE}); and (4) maximum rate of change of the field in the OH coil ($\dot{B}_{OH}$). Initiation of beam heating midway through the OH current reversal, thereby reducing resistive losses during startup, was found to be beneficial. The time of the OH current reversal, Δt_{OH}, is an important factor in determining the requirements of the plasma driving and heating systems, as indicated in Fig. 4. On the basis of these results, Δt_{OH} = 2 s was chosen for the reference case. As a result of

TABLE 2. Steady-State Plasma Parameters — Reference Design

Poloidal beta, β_p	1.7	
Total beta, β_t	0.048	
Safety factor		
Magnetic axis, q(0)	1.00	
Plasma surface, q(a)	3.05	
Plasma radius, a(m)	2.1	
Aspect ratio, A	2.98	
Average temperature, $\bar{T}$ (keV)	10	
Effective ion charge, Z_{eff}	1.3	
Confinement for ignition, $n\tau_E$ (s/m^3)	2.4×10^{20}	
Peak field at TF coils, B_{max}^{TFC} (T)	10.0	8.0
Field at centerline B_{t0} (T)	4.47	3.58
Plasma current, I_p (MA)	7.58	6.06
Average D-T ion density, $\bar{n}_{DT}$ (m^{-3})	9.4×10^{19}	6.0×10^{19}
Power output, P_T (MW)	638	261
Neutron wall load, P_w (MW/m^2)	0.86	0.35
Ratio of $n\tau_E$ required for ignition to TIM value of $n\tau_E$, α_{TIM}	1.0	4.0

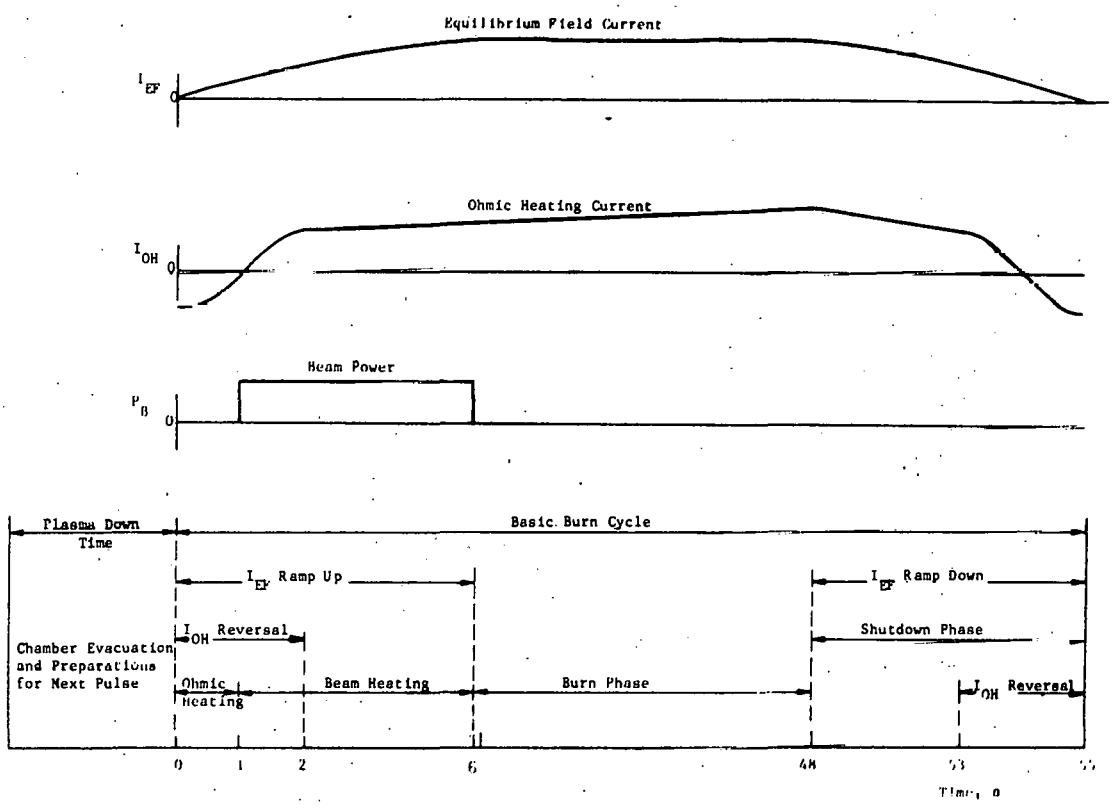

FIGURE 3. Burn Cycle Scenario

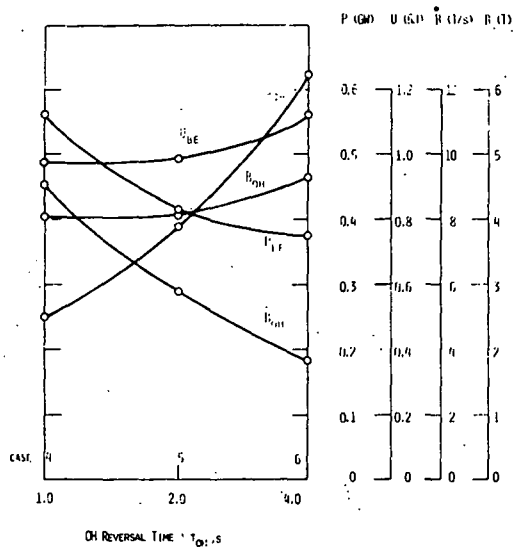

FIGURE 4. Effect of OH Current Reversal Time on Plasma Driving and Heating System Requirements

extensive studies of this type, which are presented in a separate paper,[2] the maximum requirements shown in Table 3 were identified.

The net energy flow for a burn cycle is shown schematically in Fig. 5. A total of 16.34 GJ of energy is incident on the first wall; of this, 15.96 GJ is produced by fusion and 0.38 GJ results from beam and ohmic heating of the plasma. An additional 0.45 GJ of thermal energy is recovered from the beam injector system, so that 16.79 GJ of thermal energy is available for conversion to electricity. With a conversion efficiency η_T = 30%, this would result in 5.04 GJ of electrical energy. Deducting the 2.95 GJ of electrical energy required to run the plant — 1.51 GJ to run the auxiliary systems and 1.44 GJ to make up deficits in the energy storage system caused by energy losses in the injection (0.98 GJ) and OH/EF (0.46 GJ) systems — results in 2.09 GJ net electrical energy. Averaging this over a 70 s operating cycle (a 55 s burn plus a 15 s replenishment period) results in a net electrical power of 29.9 MW. The EPR may well operate without a thermal conversion system, in which case 2.95 GJ per cycle, or a continuous power of 42.1 MW, is required from the electric power grid.

Burn cycles shorter than 55 s can be achieved either by injection of a high-Z gas to radiatively cool the plasma or by termination of refueling. Longer burn cycles can be achieved by using supplemental beam heating to maintain thermonuclear temperatures, the required beam power increasing with time to offset the accumulation of helium and wall-sputtered beryllium. It is assumed that the plasma density can be maintained by a combination of recyling from the wall and refueling, but limited operation without refueling appears feasible. The power performance with only recyling and refueling (reference case) and with supplemental beam heating, is shown in Fig. 6 as a function of the burn cycle length. The required supplemental beam power increases with time to a maximum of 35 MW for a 95 s burn pulse. An increase of as much as 30% in net electrical power, relative to the reference case, can be achieved by using supplemental beam heating to extend the burn.

PLASMA INITIATION

The time development of the plasma at the initiation of the discharge has been studied. A small plasma (a = 0.35 m) will be created at the center of the chamber (R = 6.25 m) by a toroidal electric field. Certain features of the initiation are illustrated in Fig. 7. The driving voltage, V_{LOOP}, produced by the changing flux in a special startup coil rises in about 2 ms to 500 V, and holds for ~6 ms. In the first 1.2 ms, the electron avalanche converts essentially all the neutral gas in the chamber to plasma. As soon as the electron density is sufficiently large, the plasma current starts to rise and Ohmic heating occurs. When the plasma

TABLE 3. Plasma Driving and Heating System Maximum Requirements

Ohmic Heating Coil System	
Volt-seconds to plasma	85
Peak field, B_{OH} (T)	5.0
Maximum field rise, $\dot{B}_{OH}$ (T/s)	6.7
Maximum voltage, V_{OH} (kV)	51
Maximum current, I_{OH} (kA)	80
Maximum power required, P_{OH} (MW)	1900
Maximum energy transferred, U_{OH} (MJ)	1200
Minimum current reversal time, Δt_{OH} (s)	2
Equilibrium Field Coil System	
Volt-seconds to plasma	50
Maximum voltage, V_{EF} (kV)	21
Maximum current, I_{EF} (kA)	80
Maximum power required, P_{EF} (MW)	420
Maximum energy transferred, U_{EF} (MJ)	1500
Neutral Beam Injection System	
Deuteron energy (keV)	180
Power to plasma, P_B (MW)	60
Energy to plasma, P_B (MJ)	300
Energy from energy storage, U_{BE} (MJ)	1000

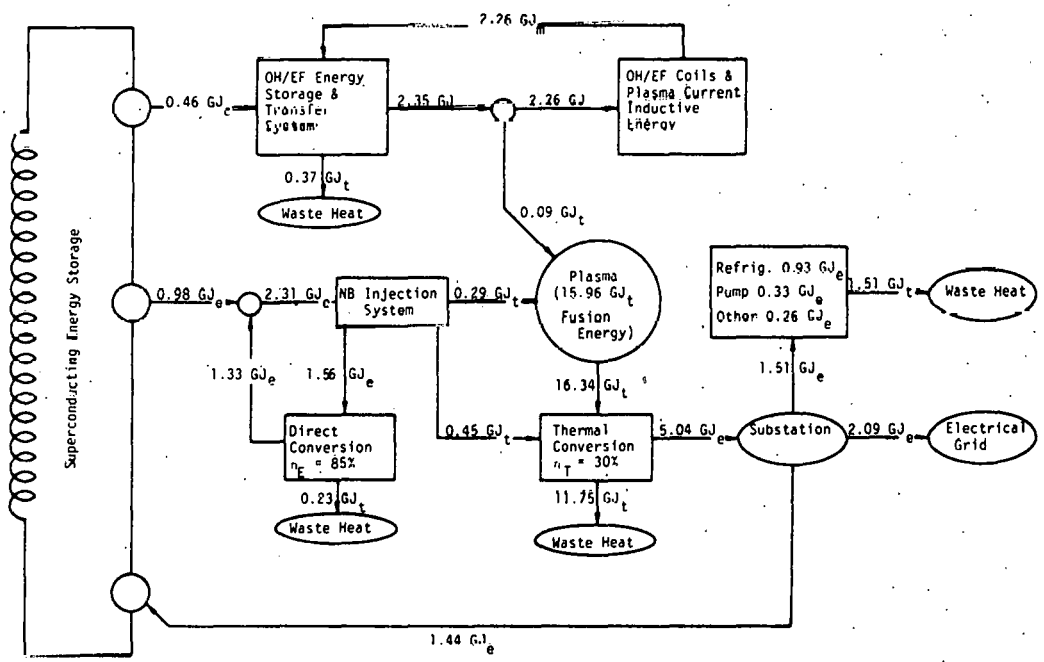

FIGURE 5. Net Energy Flow in Reference Burn Cycle (with Thermal Energy Conversion)

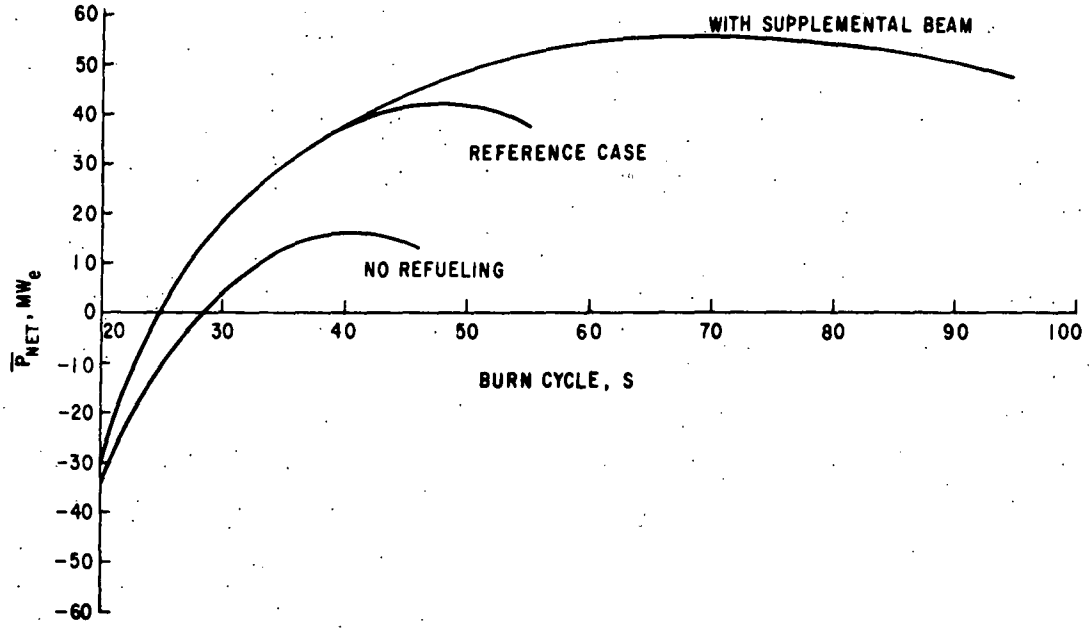

FIGURE 6. Power Performance as a Function of Operating Mode

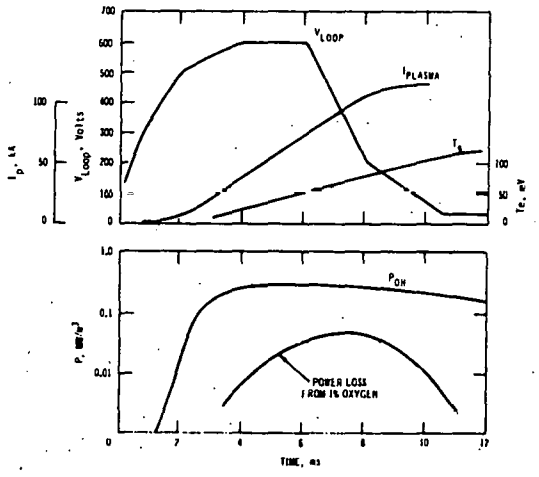

FIGURE 7. Plasma Breakdown — Normal Startup Cycle

heats up, the resistance drops and it becomes possible to maintain the plasma current with a reduced voltage. A discharge with a plasma current of 115 kA and an electron temperature of ∿130 eV can be maintained with a voltage of 28 V.

The voltage induced by the sinusoidal OH current reversal should reach 25 to 30V at about 0.3 s; thus, the special startup coil should be pulsed about 0.3 s after the initiation of the OH current reversal, forming the plasma at this time. Creating the plasma at 0.3 s will waste only about 4 V-s of the OH inductive flux. After the plasma is created and the OH and EF coils are providing the driving voltage, additional gas can be added to the chamber and the plasma radius and current can be increased simultaneously.

MAGNET SYSTEM

The EPR magnet system consists of the toroidal-field (TF) coil system and the poloidal-field coil system. These coils interact with one another during operation and also interact with the other systems of the EPR. The magnet system design was developed in sufficient detail to evaluate problems in the construction and operation of EPR magnets. Details of the magnet system design are presented in a separate paper.[3]

Toroidal Field Coils

The TF coils use niobium-titanium as the superconductor because of its good ductility and proven performance in large magnets. The toroidal field strength should be as high as practical in order to enhance the plasma confinement and boost the power performance. A peak field of 10 T can be achieved with a large amount of superconductor at 4.2°K or with much less superconductor at 3°K. It is more economical to operate the 10 T TF coil at 3°K because the difference in refrigeration cost is much smaller than the difference in the cost of the superconductor. The problem of refrigeration at temperatures lower than 4.2°K for large systems was evaluated. The TF coils will achieve 10 T peak field at 3°K and 8 T peak field at 4.2°K with about 0.5°K temperature allowance for each case; 8 T is the minimum goal and 10 T is the maximum goal in the TF coil design.

A TF coil system consisting of 16 pure-tension "D"-shape coils with a horizontal bore of 7.78 m provides adequate space for the vacuum chamber, blanket and shield, provides adequate access for assembly and repair, and has a satisfactorily small maximum field ripple of 1.3%. The TF coil system is summarized in Table 4.

The superimposing field on the TF coils from the poloidal coils was found to be the most troublesome factor in the TF coil design. The out-of-plane load is large and creates serious problems for the structural design as well as a threat to the coil stability from bending moments and shear stresses in the coil structure. Moreover, unacceptably large ac losses will occur in the TF coil unless either the conductor is made of cable or the coil is shielded against changing fields. Both of these possibilities were evaluated.

The sponginess of cable conductor threatens coil structure integrity. In addition, cabling the conductor does not overcome all ac losses; changing the parallel field still couples filaments in a single strand. These ac losses, proportional to the conductor length, are still unacceptably large and the conductor stability is very poor. One possible solution is periodic twist-pitch reversal, but this is as yet only a hypothesis.

For the EPR, the option of a field shield was chosen. It was found that an aluminum shield operating at a mean temperature of 18°K is a reliable means of overcoming the varying field superimposed by the poloidal field coils. Detailed analyses of ac loss in field shields, the out-of-plane load, and dc field soaking were completed. AC losses

TABLE 4. Toroidal Field Coil System

Superconductor/stabilizer insulator/support	Nb-Ti/Cu fiberglass epoxy/SS
No. of coils	16
Coil shape	pure tension R_{10} = 2.45 R_{20} = 11.1 m
Field ripple (%)	1.3
Maximum access (m)	~3
Peak field (T)	10 @ 3°K 8 @ 4.2°K
Bore (m)	
Vertical	12.6
Horizontal	7.78
Field in plasma, B_t (T)	
10 T peak field	4.32
8 T peak field	3.46
Stability	cryostatic
Temperature allowance (°K)	0.5
Conductor design	monolithic
Cooling	pool boiling
Operational current (kA/turn)	60
Stored energy (GJ)	
Total	30
Coil	1.875
Inductance (H)	
Total	16.7
Coil	1.04
Ampere-turns (MAT)	
Total	134
Coil	8.37
Turns/coil	70 × 2
Mean turn length (m)	36
Total conductor length/coil (A-m)	151.2 × 10^6
Coil weight/coil (Ton)	~208
Coil and bobbin cross section (m^2)	0.619
Bobbin	
Material	316 SS
Thickness (cm)	1.25
Winding cross section (m^2)	0.572
Average current density (A/cm^2)	
Over bobbin and coil	1352
Over coil winding	1463
Over copper	3660
Smallest radius of curvature at ~10 T field region (m)	1.98
Average hoop force-turn (lb)	133 × 10^3
Average turn cross section (cm^2)	40.6
Cross section ratio, SS/Cu	~1.5
Overall average stress (psi)	
Stainless steel	26,000
Copper	14,500
Length of straight segment (m)	8.56
Compressive pressure (psi)	7660
Circumferential stress (psi)	<74,000
Refrigeration power (MW)	14.3

in the shield are preferable to ac losses in the conductor. Superconducting shields were also considered, but were not adopted because their use would require considerable development work.

With the coils shielded, a more solid cable conductor can be used. A conductor 0.5 cm thick and 30 to 50 cm wide has been chosen as the reference conductor. It will carry a current of 60 kA. Each TF coil will consist of two jelly-rolled windings side by side with a central rib between them. The combination of the central rib and the flat conductor with one turn per layer makes a strong structure with good transfer for hoop stress and centering force, a good mechanical stability, good rigidity against out-of-plane loads, and assurance of cryostatic stability for the TF coils.

Coil protection is also facilitated by this conductor design with a high current and relatively few turns. During a rapid (8-1/2 min) discharge, the voltage between neighboring turns will be low; and even the maximum voltage with respect to ground can be limited to 2000 V.

The TF coils must be operated in series at all times; otherwise unequal currents in different coils could create large forces and torques between coils and large bending

moments in each TF coil, even if the TF coil is in pure-tension shape. These would produce catastrophic damage to the TF coil system.

The radiation shield is designed to protect the TF coils from nuclear heating and radiation damage. The nuclear heat load is 1.5 kW, which is negligible in comparison with other heat dissipation in the TF coils. The copper stabilizer is designed to tolerate a radiation-induced resistivity of 1.5×10^{-8} Ω-cm. The shield is designed so that this value occurs after 2.5 MW-yr/m^2 integrated first-wall neutron load, which corresponds to 10 yr of operation at the nominal wall load of 0.5 MW/m^2 and a 50% capacity factor. The dose of 3.5×10^8 rads to the epoxy insulator is well below the range 10^9-10^{10} rads at which its properties degrade.

Poloidal Field Coils

The poloidal field coils present problems different from those of the TF coils, but equally challenging. The poloidal field coils consist of the initiation-trimming (IT) coils, the ohmic heating (OH) coils, and the equilibrium field (EF) coils. The OH coils and the EF coils are superconducting and are located outside the TF coils, as shown in Fig. 1. The smaller IT coil system is made of water-cooled copper and is located near the first wall. The IT coils initiate plasma discharge by delivering 4 V-s in 10 ms. The field from the IT coils can also be used to trim the plasma position.

Although the OH coils serve as the transformer primary for producing the plasma current and the EF coils provide equilibrium for the plasma, both coil systems have nearly identical problems, e.g. large stored energy, high operational current, rapid charging and discharging, and ring coil configuration. For this reason, the conceptual design of the eight pairs of EF coils and six pairs of OH coils were carried out together.

The design requirements summarized in Table 3 for the OH and EF coil systems were specified as a result of a detailed trade-off study. Burn cycle dynamic simulations of the plasma, the coupled OH and EF systems and the plasma heating systems were performed. Free-boundary plasma MHD equilibrium calculations were utilized in the design of an equilibrium field that would produce the circular plasma.

Characteristics of the OH and EF coils are given in Table 5. The OH coils and EF coils both have a maximum operational current of 80 kA supplied by two parallel 40 kA cables with fully transposed strands. The OH coils have 837 turns in each parallel path; the EF coils have 464. The charging voltage for the OH coils is 48 kV and the turn-to-turn voltage is about 60 V. The charging voltage for the EF coils is 21 kV and the turn-to-turn voltage is about 50 V. In the helium gas environment, the minimum turn-to-turn separation must be about 0.3 mm.

Multilayer coils would require large gaps between layers and present an awkward problem for coil design, especially for the long OH solenoids. Therefore, each coil will be wound with a single-layer conductor 15 cm wide.

The EF coils and OH coils will be cooled by helium pool boiling at 4.2°K, 1 atm pressure. Pool boiling is simple, inexpensive, reliable, and easy to control. Above all, a rather small heat transfer flux is adequate to remove the conductor ac losses if the helium bubbles can be properly vented to avoid bubble accumulation within the winding. Under this circumstance, the heat transfer flux ceases to be an important factor in determining the coil stability; instead the coil stability depends on the conductor current density, the amount of liquid helium surrounding the conductor, and the

TABLE 5. OHC/EFC Magnet Characteristics

	OHC	EFC
Superconductor/stabilizer	Nb-Ti/Cu	
Coil design	Single layer	
Conductor design	Fully transposed cable	
Stability	Cryostatic	
Cooling	Pool boiling	
Operating temperature (°K)	4.2	
Average current density (A/cm^2)	2640	2946
Magnetic field (T)		
in flux core	~5	
at plasma center		~0.46
Ampere-turns (MAT)	67	±18.6
Total conductor length (MA meters)	847	996
Maximum dB/dt in conductor (T/s)	6.7	~1
Stored energy in OH/EF/plasma field (MJ)	2262	
Maximum operational current (kA)	80	80
No. of turns	837	464
Self-inductance (H)	0.48	0.52
Mutual coupling	$K_{OHEF} = 0.015$	
Power supply voltage (kV)	48	21
Volt-seconds to plasma (V-s)	85	50
Coupling coefficient to plasma ring	$K_{OHP} = -0.2422$	$K_{EFP} = -0.2566$

extent of coil disturbances.

The equilibrium field must penetrate the blanket and shield to act on the plasma, but the blanket and shield are about a meter thick and consist mostly of metal such as stainless steel. Eddy currents in this material would distort the equilibrium field and delay its penetration if the blanket and shield were not sufficiently segmented. For a blanket and shield design of 16 segments, each made of 43 blocks, field distortion or time delay will be reduced to an insignificant level.

Structural Support

Two structural support concepts, a torque shell and a torque frame, were developed.*

*This work was performed by McDonnell-Douglas Astronautics Company-East in collaboration with ANL and is presented in detail in a separate paper.[4]

The torque shell design uses shear webs located between the TF coil cryostats to provide continuous support for the coil and to cancel the induced torques. This design provides the lightest weight design but requires removal of the shear web panels to permit access to the blanket and shield. The torque frame concept uses a frame at the top and bottom of the reactor to transfer the TF coil loads to the reactor building wall and floor, respectively. Both concepts provide blanket and shield access through an ~3 × 8 m opening between TF coils. Very little access, if any, will be available from above and below the TF coil because of required structure. Openings for vacuum ducts and instrumentation, however, can be provided through this structure. The floor area around the reactor will not be

restricted by structural members with either concept, thereby providing for ease of locating components such as neutral beam injectors and for freedom of movement for maintenance equipment. The outer and upper poloidal coils can be removed using their supporting structure as a lifting fixture, and the combined weight is compatible with planned crane capacity. The lower poloidal coils are captivated by the various support columns and require an in-place repair/replacement facility, which was conceptually included in the design. Use of 7075-T6 aluminum alloy joined by bolting results in a substantially lighter and lower cost structural support design than can be achieved using welded stainless steel. The torque shell concept has been tentatively chosen as the reference option.

PLASMA HEATING

Supplemental heating, in addition to ohmic heating, is required to heat the EPR plasma to ignition temperatures. A power input to the plasma of 60 MW is needed for about 5 s during startup, and somewhat less power may be required for periods up to a minute to maintain the burn in the face of unfavorable plasma conditions. Current experience dictates that neutral beam heating be the reference option for this supplement. Radio-frequency heating is considered as the primary backup option.

Neutral Beam Injection

Three neutral beam injection systems have been designed. These are summarized in Table 6. The reference design is based on modest extrapolations beyond presently achieved results with D^+ sources. The second design is based upon improved D^+ sources. The third design, which would require considerable advances in source technology, is based upon direct-extraction D^- sources, with neutralization by a gas target (3a) or by a lithium plasma (3b). All designs employ energy recovery, and the first two designs inject only the $D^+ \rightarrow D^0$ component into the plasma.

In the reference design, 12 injectors, arranged to tangentially inject into the plasma in a symmetrical clockwise and counter-

TABLE 6. Neutral Beam Injection System Characteristics

	(Reference) Design 1	Design 2	Design 3a	Design 3b
Atomic ion	D^+	D^+	D^-	D^-
Target for $D^\pm \rightarrow D^0$	D_2 gas	D_2 gas	D_2 gas	Li plasma
Beam composition (D^+, D_2^+, D_3^+, D^-)	(0.75,0.18,0.07/-)	(0.95,0.03,0.02/-)	(-/0.95	(-/0.95)
Neutral beam power (MW)	60	60	60	60
Neutral beam energy (keV)	180	180	180	180
Neutral beam current (Equiv. A)	333	333	333	333
No. of injectors	12	12	6	6
No. of ion sources/injector	2	2	2	2
Type of grid	multiaperture	multiaperture	multiaperture	multiaperture
Ion beam current density (A/cm^2)	0.135	0.175	0.135	0.135
Ion beam power (MW)	441	338	113	81
Gas load/injector (Torr-ℓ)	110	57	41	11
Direct conversion efficiency	0.85	0.85	0.85	0.85
Thermal conversion efficiency	0.30	0.30	0.30	0.30
Electrical power efficiency	0.29	0.41	0.66	0.77
Overall power efficiency	0.34	0.45	0.66	0.77
Net power input (MW)	207	145	91	78

pattern, provide 60 MW of 180 keV deuteron beams to the plasma. Each injector has two ion sources. The beam line for each ion source includes an accelerator to increase the energy of the D^+ ions, a magnet separator and energy grid to remove molecular ions and directly convert their energy into electricity, a neutralizer to form the neutrals, and a thermal energy recovery system. The pair of beams in each injector travel ~4 m along a beam duct and pass through a 0.75 m diameter port in the toroidal vacuum chamber wall. An electrical power efficiency (neglecting thermal energy recovery) of 0.29 and an overall power efficiency (including thermal energy recovery) of 0.34 are achieved with the reference design. These power efficiencies decrease rapidly with beam energy, because of a decrease in the neutralization efficiency in D_2 gas.

Substantial improvements in power efficiency and corresponding reductions in power requirements and gas loads can be realized if D^+ ion sources are developed with a very high atomic ion component, as indicated by Design 2 in Table 6. Even more dramatic improvements could be realized if direct-extraction D^- sources are developed.

Radio-Frequency Heating

Radio-frequency (rf) wave heating is an attractive alternative to neutral beam heating, from the technological point of view, since efficient power sources exist for several heating modes and the neutron penetration problems intrinsic to the neutral beam injectors can be ameliorated. However, wave heating experiments have not encountered the same degree of success as neutral beam experiments in heating plasmas.

Two rf heating designs were developed, one based upon heating in the lower hybrid resonance (LHRH) and the other in the ion cyclotron resonance (ICRH). The EPR reference design has four rf heating stations supplying 20 MW to the plasma, for added heating capability and experimentation. If rf heating becomes the primary option, the EPR design can accommodate 16 rf stations by replacing the neutral beam injectors with rf systems. The characteristics

TABLE 7. RF Heating Parameters

	ICRH	LHRH
Pump frequency (MHz)		
8 T	54	1120
10 T	68.6	1190
Output power (MW)		
4 ports	25	25
10 ports	60	60
Transmission efficiency from source to port (%)	64	48
Pulse duration, heating (s)		
25 MW	12.9	12.9
60 MW	5.4	5.4
Duty Cycle (%)		
25 MW	17.2	17.2
60 MW	7.2	7.2
Launcher	1/4 turn loops	"Grill" waveguide 8 across × 2 high
Transmission scheme	Coaxial cables	Waveguides
High power source	Tetrode amplifier	Klystron

of ICRH and LHRH systems which could provide 25 and 60 MW of heating power to the plasma are shown in Table 7.

ENERGY STORAGE AND TRANSFER SYSTEM

The energy storage and transfer (EST) system for the EPR consists of a central energy storage inductor (ESI), rectifiers to transfer energy between the ESI and the OH, EF, and neutral beam systems and a rectifier to transfer energy from the substation into the ESI. A separate inertial energy storage unit, consisting of radially stacked homopolar generators, is incorporated in the OH system, so that the inductive energy in the OH system is essentially transferred between the OH coils and inertial storage inductor, with the central ESI providing makeup for losses. Inductive energy is transferred between the OH/EF coils and the plasma current, with some dissipative loss in the plasma. The neutral beam energy is deposited in the plasma or dissipated in the injection system. Electrical energy is recovered directly and recirculated in the neutral beam injection system. If rf plasma heating is used instead of neutral beam injection heating, the required energy is transferred from the ESI by a rectifier. The EST system is depicted schematically in Fig. 8 and summarized in Table 8.

The OH coil current is reversed at the start and end of the burn cycle. The OH coil energy storage unit is designed to transfer and store the bulk of the OH coil stored energy during the reversal periods by using radially stacked drum-type homopolar generators. Additional energy required to provide 5 V-s for resistive plasma losses is transferred into and out of the OH coil during the burn cycle using an SCR-type inductor-converter bridge as the major transfer mechanism between the OH coil and a central superconducting energy storage inductor. The central ESI makes up the 0.46 GJ of energy which is dissipated in the OH-plasma system each burn cycle.

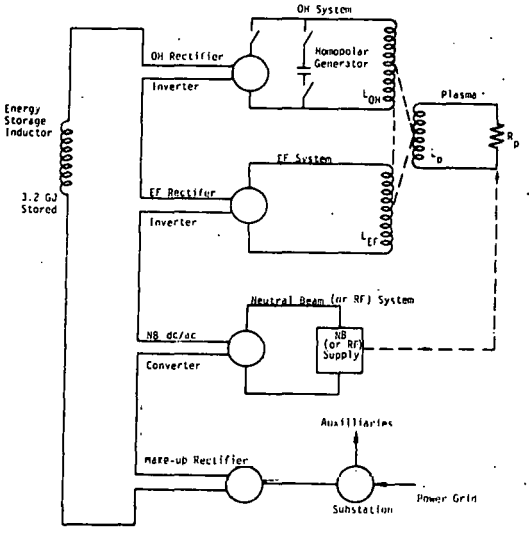

FIGURE 8. Circuit Diagram

The design of the homopolar generators is based on radially stacked epoxy fiberglass insulating cylinders and Type 17-4 stainless steel cylinders. The insulator cylinders are rigidly supported and aligned with respect to the central axis. The conducting cylinders rotate independently on a type of air bearing designed into the insulating cylinders. The innermost and outermost cylinders are made of insulating materials, so that high voltages can be achieved by electrically connecting many generators in series. A radially directed, azimuthally uniform magnetic field of about 5 T is produced by niobium-titanium superconducting coils. Brushes are located along the edges of the cylinders and connected so that current flows back and forth in the axial direction. Adjacent cylinders counter rotate. The arrangement is called the counter cyclonic generator (CCCG).

The energy transfer system for the EF coils must be actively controlled because the power demand varies with plasma current and temperature. The design of the power supply is based on storing and transferring

TABLE 8. Energy Transfer and Storage Systems — Maximum Ratings

Ohmic Heating Systems	
Drum homopolar generators	
No. of generators in series	16
No. of drums/generator	6
Total energy transfer (MJ)	1200
Peak power (MW)	1900
Peak voltage (kV)	51
Peak current (kA)	68
Equivalent capacitance (F)	0.897
Rectifier system	
Type	Inductor-converter bridge
Energy transfer (MJ)	600
Peak power (MW)	66
Peak current (kA)	80
Peak voltage (kV)	0.8
Equilibrium Field System	
Type	Inductor-converter bridge
Energy transfer (MJ)	1500
Peak power (MW)	416
Peak current (kA)	80
Peak voltage (kV)	21
Peak switching frequency (Hz)	1330
Neutral Beam System[a,b] (60 MW)	
Type	SCR, DC/AC/DC at 10 kHz
Energy transfer (GJ)	1
Voltage (kV)	180
Power (MW)	207
RF System (60 MW)[b]	
Type	5-phase inductor-converter bridge
Voltage (kV)	
ICR	18
LHR	64.5
Power (MW)	
ICR	94
LHR	125
Central Energy Storage Inductor	
Type	Superconductive ring dipole inductor
Energy stored (GJ)	3.2
Energy transfer (GJ)	2.4
Peak current (kA)	80
Peak power (MW)	620
Average power from 60 Hz line (MW)	21

(a) Assumes electrical energy recovery in power supply.

(b) Neutral beam and rf are alternative options.

the energy between the EF coils and the superconducting energy storage inductor using an inductor-converter (I-C) capacitor bridge. The design of the EF coil power supply uses typical SCR units currently available on the market. A three-phase bridge is used with 35 mF, 10 kV capacitors in each phase.

The design of the neutral beam injector energy transfer system is composed of two major components; a saturated time-delay transformer (STDT), which uses the saturation effects of magnetic cores to act as a current surge limiter, and a high-frequency polyphase-controlled rectifier using SCR switches to enable rapid de-energization of the beam in periods of less than 100 μs. The beam heating pulse is designed to last for 5 s. Energy is added to the central ESI throughout the fusion reactor cycle. The injector power supply extracts energy directly from the ESI during the beam heating phase, so that the power grid never sees a power bump. An I-C drives a high-frequency polyphase inverter. A 10 kHZ voltage is developed in a summing transformer, filtered and subsequently rectified. The output lead is connected to the injector through an STDT. A coil on the STDT is connected to a controlled time delay circuit that will trigger a crowbar and interrupting switches in the event the primary neutral beam injector protection systems fail.

The power supplies for the ion cyclotron region and the lower hybrid region rf heating systems are designed using the I-C concept used for the EF coil. Five-phase I-C bridge networks are designed to transfer energy from the ESI to the rf conversion units. Five-phase networks are used to avoid objectionably large voltage fluctuations on the frequency conversion tubes.

In order to operate the poloidal coil, neutral beam, and rf systems, it will be necessary to store energy on site so that large power pulses required to initiate and terminate the tokamak discharge do not perturb the electrical power network. A superconductive energy storage inductor was designed to handle these energy pulses. The energy storage ring uses 21.4 MW at a constant input rate and provides a peak net withdrawal of 2.4 GJ at the end of beam heating. The maximum current is 80 kA at a maximum short time-averaged voltage of 15 kV. The ring has a major radius of 5.7 m and a minor radius of 0.8 m. The coil will use 0.58 m^3 of niobium-titanium and is constructed of pancakes separated by micarta or fiberglass-epoxy boards. Alternate pancakes are wound clockwise and counterclockwise to facilitate layer-to-layer connections. Conductor transposition is achieved by winding top and bottom halves with 40 kA cable and operating coil halves in parallel. There are a total of 12 layers of coil.

VACUUM SYSTEMS

The EPR toroidal vacuum system must: (1) reduce the residual gas pressure in the toroidal chamber from $\sim 2 \times 10^{-3}$ to $\sim 1 \times 10^{-5}$ Torr in ~15 s after the burn pulse; and (2) achieve a base pressure of less than 10^{-8} Torr at the beginning of an operational period. These criteria can be satisfied by thirty-two 25,000 ℓ/s cryosorption pumps, each connected through a 1.1 m diameter duct to a 0.95 m diameter port in the vacuum chamber wall. To minimize the tritium inventory, the cryosorption pumps will be regenerated, using zirconium-aluminum getter pumps, every four hours to remove the tritium and deuterium that has accumulated on the liquid helium-cooled panels. An additional 32 cryosorption pumps are provided to allow for continued operation during the regeneration period.

Pumping requirements for the neutral beam injectors are very demanding. Twelve injectors will each have gas loads of 110 Torr-ℓ/s during operation. The required

pumping speed of ~5 × 10^6 ℓ/s will be provided by 100 m^2 of cryosorption panel in each injector. To avoid shutdown during regeneration, an additional 100 m^2 of the panel area must be provided and the design must allow for isolation of that portion of the cryosorption panel to be regenerated.

The principal parameters of the toroidal and neutral beam vacuum systems are shown in Table 9.

The high impedance characteristics of the waveguide used for lower hybrid rf heating will necessitate a separate pumping system to insure adequate vacuum along the length of the waveguide. Each waveguide must have either a mercury diffusion or turbomolecular pump with an effective pumping speed of 10,000 ℓ/s to maintain the required 1 × 10^{-6} Torr vacuum at the waveguide window.

FIRST WALL

The first-wall system consists of a vacuum wall and detachable coolant panels. The free-standing vacuum vessel is constructed from 16 cylindrical segments of 2 cm thick stainless steel plate and is reinforced with an external ring and spar framework. Two circumferential support rings and ten longitudinal spars are on each segment. The 16 segments are joined by formed rings that are welded to the ends of each segment. A chemically bonded Cr_2O_3 coating is applied to the joining surfaces in two of these rings to form a current breaker in the vacuum wall. Detachable 2 cm stainless steel coolant panels are roll-bonded to the inside of the vacuum wall. The surface of the coolant panel facing the plasma is coated with 100-200 microns of beryllium to control impurity contamination of the plasma by stainless steel. The substantial porosity (10-15%) and fine microstructure obtainable with the plasma-spray coating process facilitates gas re-emission, particularly helium, and minimizes blistering erosion. Pressurized water is supplied to the coolant panels by manifolds located in the connecting rings that join the first-wall segments. The toroidal vacuum wall is supported by a three-point per segment, roller/slide pad-type support from the blanket to the lower rings and spars. The three-point support minimizes the size of the reinforcing ring and the roller/slide support minimizes thermal stresses by allowing for expansion of the vessel.

Extensive thermal-hydraulic, mechanical, materials performance, and radiation damage

TABLE 9. Vacuum System Parameters

	Toroidal	Neutral Beam
Volume	754 m^3	250 m^3/injector
Surface area	771 m^2	254 m^2/injector
Gas load	2588 Torr-ℓ	110 Torr-ℓ/s per injector
Cryosorption pumping	32 - 25000 ℓ/s pumps	100 m^2 panel/injector
Effective pumping speed	4.25 x 10^5 ℓ/s	5 x 10^6 ℓ/s per injector
Secondary pumps		
Al/Zr getter pumps	32 - 10000 ℓ/s	12 - 25000 ℓ/s
No. 1300 CFM blower stations	16	Use same pumps
No. 1400 /s turbomolecular pumps	16	Use same pumps

TABLE 10. First-Wall Operating Parameters

Nominal Operating Conditions	
Capacity factor (%)	50
Operating cycle (s)	
Startup	5
Burn	35
Shutdown	5
Exhaust and replenishment	15
Average power loading during burn (MW/m^2)	
Neutron	0.5
Radiation, conduction, convection	0.13
Operating Parameters	
Stainless steel vacuum wall	
Maximum temperature (°C)	<500
Minimum yield stress at 500°C (ksi)	17
Maximum annual fluence (n/m^2)	6×10^{25}
Atomic displacement (dpa/yr)	2.8
Helium generation (appm/yr)	54
Hydrogen generation (appm/yr)	133
Stainless steel coolant panel	
Maximum temperature (°C)	380
Minimum yield stress at 500°C (ksi)	17
Maximum annual fluence (n/m^2)	6×10^{25}
Atomic displacement (dpa/yr)	2.8
Helium generation (appm/yr)	54
Hydrogen generation (appm/yr)	133
Maximum heat deposition (W/cm^3)	5.8
Maximum ΔT across panel surface (°C)	20
Maximum ΔT through panel face (°C)	
With Argon shutdown 100	
Without Argon shutdown	75
Maximum thermal strain range (%)	
Operating cycle	0.14
Burn cycle	0.09
Beryllium coating	
Maximum surface temperature (°C)	407
Helium generation (appm/y)	780
Hydrogen generation (appm/y)	13
Maximum erosion rate (μm/y)	30
Water coolant	
Maximum pressure (psi)	2000
Velocity (m/s)	1.6
Inlet temperature — first panel (°C)	40
Exit temperature — eighth panel (°C)	310
Pumping power (MW)	<1

analyses have been performed to evaluate the first-wall performance and to determine the design limits. Results are summarized in Tables 10 and 11.

The stainless steel vacuum wall should maintain its structural integrity for the 10-yr design life under the nominal operating conditions, viz., integrated wall loading of 2.5 MW-yr/m^2, maximum annual neutron fluence of 6×10^{25} n/m^2 (2.8 dpa/yr, 54 appm/yr helium, and 133 appm/yr hydrogen) and maximum wall temperature of $\leq$500°C. For these conditions the predicted radiation swelling of <4% is tolerable. The limiting criterion is loss of ductility caused by displacement damage and helium generation. For temperatures below 500°C, the residual uniform elongation, which is estimated to be

TABLE 11. First-Wall Design Limits[a]

Vacuum Wall	
Design life (yr)	10
Integrated neutron wall loading ($MW\text{-}yr/m^2$)	2.5
Yield strength — 10 yr (ksi)	75
Uniform elongation — 10 yr (%)	>1
Radiation swelling — 10 yr (%)	<4
Limiting criterion	Ductility
Coolant Panel	
Design life (yr)	5
Total burn cycles — 5 yr	10^6
Fatigue lifetime (yr)	5
Radiation lifetime (yr)	8
Limiting criterion	Thermal fatigue
Low-Z Coating	
Design life (yr)	3-5
Limiting criterion	D-T sputtering

(a) Based on a neutron wall load of 0.5 MW/m^2 and a plant capacity factor of 50%.

>1% at the end of the 10-yr life, is considered to be acceptable. The lifetime of the low-Z coating is limited by erosion caused primarily by D-T physical sputtering. A design life to 5 yr for a 100-200 μm thick beryllium coating appears feasible. Only limited data exists with which to estimate the lifetime of the ceramic current breaker; however, bulk radiation effects will likely be the limiting criteria.

In addition to the extensive radiation damage, the coolant panel will be subjected to severe thermal cycling produced by heat deposition on the surface during the plasma burn. The strain range for the burn cycle depends on the difference between the maximum and minimum values of ΔT during the cycle, and the strain range for the plant warmup/cooldown operating cycle is a function of the average ΔT during the burn cycle. Assuming that the duration of the operating cycle is long enough that stress relief occurs, the strain range for the coolant panels with sliding supports is 0.085% for the burn cycle and 0.14% for the warmup/cooldown operating cycle. These values correspond to fatigue design lifetimes for the coolant panels of 5×10^6 burn cycles and 1×10^5 operating cycles. Thus, thermal fatigue will limit the life of the coolant panel to 5 yr, which corresponds to $\sim 10^6$ burn cycles, for the current design parameters.

Although the current first-wall system design is based to a large extent on available materials and existing technology, it appears that adequate mechanical integrity of the system can be maintained for suitable reactor lifetimes under the postulated EPR conditions. Details of the first-wall and the blanket/shield design are presented in a separate paper.[5]

BLANKET/SHIELD

The blanket/shield system consists of the blanket, the inner bulk shield, the outer bulk shield, the neutral beam penetration shield, the vacuum duct penetration shield, and the biological shield. In order to insure penetration of the equilibrium field into the plasma region without intolerable distortion or phase delay, the blanket and bulk shield are constructed of 688 electri-

cally insulated blocks.

The blanket is made up of 0.28 m thick stainless steel blocks. Each of the 16 segments of the vacuum chamber is covered by 17 blanket blocks. The blocks are cooled with pressurized water flowing in a network of 1 cm diameter drilled channels, with each block having an independent cooling system.

The bulk shield surrounding each of the sixteen segments of the vacuum wall and blanket consists of 1 inner shield block and 25 outer shield blocks. The inner shield block is 0.58 m thick and consists of alternating layers of B_4C and stainless steel disposed so as to maximize the attenuation of neutrons and gamma rays. At the top, bottom, and outside of the torus, the bulk shield is 0.97 m thick and consists (going radially outward) of 0.03 m of stainless steel, 0.15 m of graphite with 1% natural boron, 0.05 m of stainless steel, 0.65 m of lead mortar, and 0.09 m of aluminum. The bulk shield is cooled with H_2O at atmospheric pressure.

Neutral beam lines, vacuum ducts, and other penetrations of the outer blanket and bulk shield represent large ($\sim$0.6-1.0 m^2 cross section) streaming paths for neutrons and require special shielding. A special, 0.75 m thick, annular shield surrounds the neutral beam tube after it exits from the bulk shield and extends beyond the TF coils, so that there is no unshielded line-of-sight path from the wall of the beam tube to the TF coils. The inner 0.65 m of this special shield is 50% SS/50% B_4C, followed by 0.05 m of lead and 0.05 m of aluminum.

A pneumatically operated shield plug is closed in the vacuum duct during plasma burn (see Fig. 1). This shield plug consists of two blocks. The inner block is 0.32 m thick, and is fabricated of stainless steel and cooled in the same manner as a blanket block. The outer block is 0.58 m thick, with a material disposition (SS/B_4C) similar to that of the inner shield.

The blanket, shield, and vacuum vessel assembly weighs over 2700 metric tons. This weight is supported from beneath the reactor on 16 individual frames. The frames can move vertically approximately 2 m to facilitate replacement of the blanket and shield blocks. The load is transferred through 32 columns from the reactor foundation to the 16 frames, which in turn support the reactor shielding blocks. The blanket block layer rests on the inner portions of the shield blocks on insulated roller pads to accommodate the high temperature of the blanket and the accompanying thermal expansion. The 360 metric ton vacuum vessel rests on the inner side of the blanket.

Extensive analyses have been performed to evaluate the performance of the blanket/shield system. These analyses are based on a nominal neutron wall load of 0.5 MW/m^2 and a plant capacity factor of 50%. The neutronics effects vary significantly around the wall in the poloidal direction, and a conservative analysis is used. Results are summarized in Table 12.

The 4 cm first wall and the 28 cm blanket region receive $\gtrsim$90% of the neutron and gamma energy. The nuclear heating varies from 3.5 W/cm^2 on the inside to 0.3 W/cm^2 on the outside of the blanket. The radiation damage level in the blanket adjacent to the first wall is $\sim$1.7 dpa/yr and drops by a factor of 2 every $\sim$7 cm going through the blanket. Operating temperatures in the load bearing portions of the blanket are, like the first-wall temperatures, restricted to $\leq$500°C, but may be allowed to rise above this level in nonstructural components. After 10 yr at a wall loading of 0.5 MW/m^2 and a 50% capacity factor, the swelling in the blanket adjacent to the first wall is expected to remain below 2%, the uniform elongation will drop to $\sim$3%, and the yield strength will increase to $\sim$75 ksi. As the neutron radiation is attenuated through the blanket, the swelling will

TABLE 12. Summary of Blanket Design Parameters

Design basis operating life (yr)	10
Nominal power during burn (MW)	400
Design basis neutron wall loading (MW/m^2)	0.5
Plant capacity factor (%)	50
Blanket structure	
Thickness (m)	0.28
Type metal/volume fraction	316-SS/0.9
Type coolant/volume fraction	$H_2O/\leq 0.05$
Penetration volume fraction	
Inner blanket	~ 0.02
Outer blanket	~ 0.05
Maximum temperatures (°C)	
In support structures	500
In bulk materials	550
Nuclear parameters	
Maximum heat deposition (W/cm^3)	3.5
Maximum fluence at 2.5 MW-yr/m^2 (n/m^2)	5×10^{25}
Maximum dpa at 2.5 MW-yr/m^2 (dpa)	17
Maximum helium production at 2.5 MW-hr/m^2 (appm)	230
Maximum hydrogen production at 2.5 MW-yr/m^2 (appm)	600
Mechanical parameters	
Design stress in support structure (ksi)	<10
Minimum material yield stress (ksi)	20
Ductility at 2.5 MW-yr/m^2 (% uniform elongation)	>3
Swelling at 2.5 MW-yr/m^2 (% of initial volume)	<2
Maximum torque from pulsed fields (ft-lb)	25,000
Coolant parameters	
Type	H_2O
Maximum pressure (psig)	2000
Pressure drop (psig)	<15
Maximum velocity (m/s)	2.4
Pumping power (MW)	<1
Coolant inlet temperature (°C)	40
Maximum coolant exit temperature (°C)	309
Residual activity from first-wall/blanket/shield after 2 yr operation in Ci/MWt	
Immediately after shutdown	3.5×10^6
1 yr after removal	8.0×10^5
10 yr after removal	7.0×10^4
100 yr after removal	60

be reduced to zero after a few cm, and the tensile properties will approach those of unirradiated material (~22% uniform elongation and ~20 ksi yield strength). The effect of creep and fatigue will be less than in the first wall since the blanket is not exposed to the surface radiation from the plasma and will not undergo the large thermal cycling of the first wall. Helium production rates will still be high in the first few cm, but the temperature limit of 500°C should insure against helium embittlement which is observed at temperatures above 550°C.

Regions in the outer bulk shield, 20 cm thick, surrounding the neutral beam penetrations will be constructed and cooled similar to the blanket. The remainder of the bulk shield will receive ~7% of the radiation energy. The major effect of radiation on boron carbide is the buildup of helium from (n,α) reactions which can induce swelling and cracking if it is present in high concentrations. Neutron irradiation can also substantially reduce the thermal and electrical conductivity. The degree to which radiation

affects the bulk properties depends to a large extent on the amount of porosity present in the unirradiated material. The first layer of boron carbide in the inner shield will be the most seriously affected by the neutron irradiation. The first few cm of boron carbide will produce ~3500 appm of helium during a 10 yr lifetime, but helium production will fall off rapidly past this point. This amount of helium is not expected to induce significant swelling or cracking if a sufficient porosity exists to accommodate the gas. Helium escaping from the boron carbide must be vented to prevent buildup of gas pressure within the shield. For the conditions expected in the EPR, the graphite in the outer bulk shield will densify rather than swell. It is expected that the volume change of graphite due to irradiation can be minimized by a suitable choice of material and should not present a problem. Helium production in the first few cm of the graphite/1% boron will reach ~770 appm after a 10 yr lifetime. As with boron carbide, porosity and venting considerations must be factored into the shield design to accommodate the helium. The materials lying past the first layer of boron carbide in the inner shield and the graphite in the outer shield receive a relatively small neutron fluence, and the bulk properties should not be adversely affected. The lead mortar and aluminum in the outer shield will operate at temperature below 100°C, which is well below the ~150°C at which the lead mortar will begin to break down.

ACCESS AND MAINTENANCE

During operation, the biological dose in regions external to the TF coils is about 10^6 mrem/hr, which is too high to permit access to the inside of the reactor building for any reasonable length of time. Outside the 1.5 m thick concrete building wall, the dose is about 1 mrem/hr. The biological dose in the vacuum chamber inside the first wall is 6×10^9 mrem/hr at shutdown and after 1 yr of cooldown the dose is 1×10^9 mrem/hr. After one day of cooling, the dose is 600 mrem/hr at a position above the reactor at the location of the TF coils and 2 mrem/hr outside the TF coils. The latter result does not include the effect of penetration streaming or activation of the neutral beam injector. These calculations indicate that the dose rate is too high to permit unshielded personnel access to the reactor during operation. At best, limited access would be allowed within a few days of shutdown. Personnel exposure can be reduced by two orders of magnitude by 10 cm of lead shielding.

The general approach to maintenance for the EPR is by use of remote handling apparatus. All large components will be repaired in place, where possible. This includes the vacuum vessel and the lower EF and OH coils. Smaller components like the blanket and shield blocks will be repaired in the hot cells. Special in-vessel remotely operated equipment will be designed to repair, replace, and inspect any portions of the vacuum vessel or first-wall panels that have been damaged. Support facilities for remote operations include a remotely-operated overhead crane/manipulator with a shielded personnel cab, floor-mounted snorkel-type units for servicing the vertical portions of the reactor and basement-positioned apparatus for maintaining the lower components of the reactor. A full-scale, quarter-section mockup of the reactor is vital to all remote operations.

TRITIUM

The EPR tritium handling system must separate tritium and deuterium from the spent fuel and must be capable of building atmosphere cleanup in the event of a large tritium release. The key tritium facility operating parameters are given in Table 13, and a detailed discussion of the design basis is presented in a separate paper.[6]

TABLE 13. Summary of Tritium-Handling Facility Parameters

	B_{max}^{TFC} 8 T	B_{max}^{TFC} 10 T
General		
Power during burn (MW)	200	500
Burn cycle duty cycle (%)	75	75
Plant availability factor (%)	67	67
Tritium burnup (g/day)	26	64
Throughput/burnup ratio	50	50
Tritium delivery rate (g/hr)	60	150
Fuel cycle turnaround time (hr)	4	4
Plant inventory (kg)	0.6	1.5
Annual tritium consumption at 50% capacity factor (kg)	6.4	16
Tritium Inventory Disposition		
Cryosorption pumps (g)	240[a]	600[a]
Getter beds (g)	240[a]	600[a]
Distillation columns (g)	10[a]	25[a]
Fuel cycle hardware (g)	10[a]	25[a]
Storage (g)	∿500[a]	∿1300[a]
Anticipated mean inventory (g)	600	1500
Fuel Cycle		
Nature of fuel processing and recycle systems	Nonmetallic element removal Debris removal Isotopic enrichment Fuel storage Fuel delivery	
Type of mainstream enrichment	Cryogenic distillation	
No. of columns	6	
No. of equilibrators	1	

(a) Maximum value at any single time.

The principal assumptions applied in determining these parameters are: (1) that the throughput/burnup ratio will be approximately 50; (2) that the fuel cycle turnaround time (fuel holdup) time will be 4 hr or less; and (3) that the initial tritium inventory of $\leq$1.5 kG will be supplemented as needed (from an outside production facility) to match the burnup encountered during operation. The fuel cycle turnaround time is determined mainly by the regeneration cycle on the cryosorption pumping system for the toroidal plasma chamber. The present plan is to carry out this regeneration cycle on a 4 hr basis.

Calculations have been made to estimate the rate of tritium permeation from the plasma chamber into the first-wall cooling water circuit. These calculations show that the tritium level in the first-wall cooling water ($\sim 10^5$ ℓ) increases to a maximum of $\sim$1 Ci/ℓ. The handling practices associated with this pressurized cooling water would essentially be the same as those currently applied in the pressurized D_2O primary circuits of heavy water reactors that commonly run up to 10 Ci/ℓ.

Potential off-site tritium exposure calculations have been made. Two events leading to off-site exposure due to the release of tritium have been considered. The first event considers 2% ($\sim 4 \times 10^5$ Ci) of a total inventory of 2 kg of tritium released at ground level as water vapor in an accident.

The dose commitment for an individual at the site boundary is 23.5 rem (whole body) at 500 m and 7.4 rem (whole body) at 100 m as compared to the 10 CFR 100 guideline for total body dose in an accident of 25 rem. The second event is the continuous daily release of 100 Ci of tritium for which the concentration at 500 m is $\sim 5 \times 10^{-9}$ Ci/m^3 and at 1000 m is $\sim 2 \times 10^{-9}$ Ci/m^3. ERDA Manual 0524 gives the uncontrolled concentrations guide as 2×10^{-7} Ci/m^3.

FACILITY DESCRIPTION

The reactor complex consists of 11 major facilities covering an area of 65,000 m^2. The focal point is the reactor containment building (Fig. 9), a structure 73.2 m in diameter × 50 m high made of reinforced concrete, 1.5 m thick, to meet both structural and biological requirements. A thin steel membrane, 1 cm thick, lines the inside walls of the building, forming a barrier in the event of a tritium release. The seal is carried through all penetrations and access ways. A reactor pedestal is provided slightly offset from the center of the building for convenience in positioning the 300 ton overhead polar crane used in assembly and maintenance of the reactor. The building is equipped for remote maintenance of the reactor.

COSTS AND SCHEDULES

The estimated total direct capital cost for the EPR is $579 M. Adding 25% for engineering and 25% for contingency brings the grand total to $868 M. A cost breakdown is given in Table 14.

A detailed design and construction schedule has been developed. Eight years are required from the initiation of preliminary design to initial operation, and six years

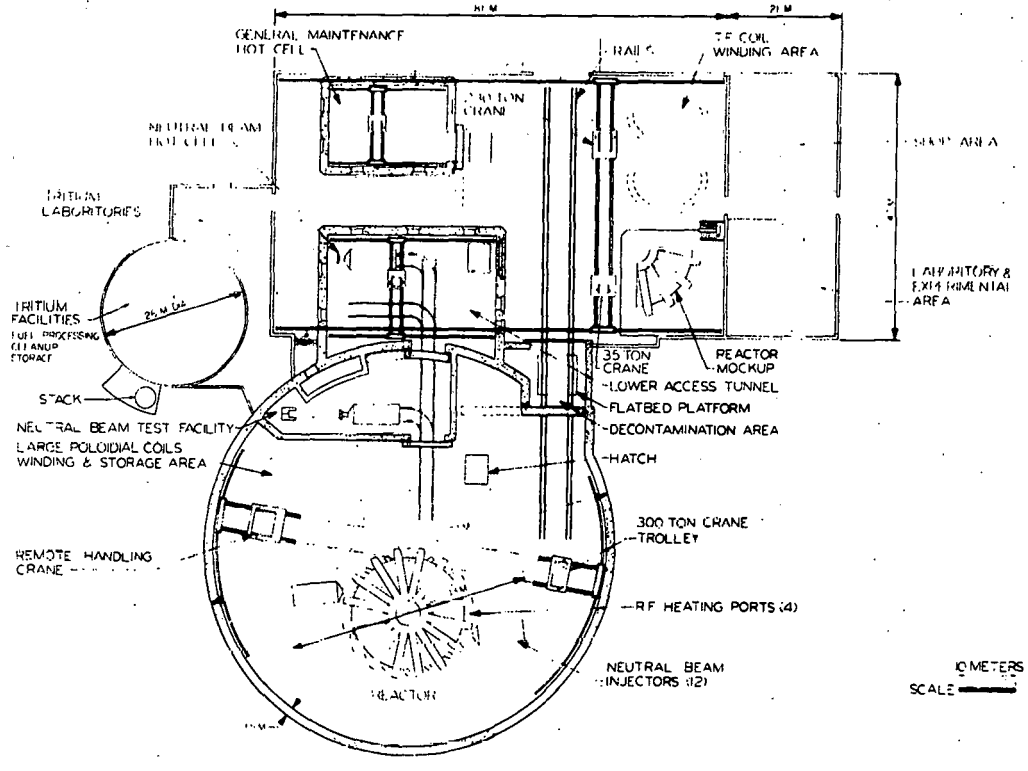

FIGURE 9. Reactor Containment Building

TABLE 14. Plant Capital Investment
Direct Cost Estimate

	$M(a)
Structures and site facilities	67.3
Reactor	248.6
Reactor plant facilities	245.0
Auxiliaries	18.0
TOTAL	578.9
Engineering (25%)	144.7
Contingency (25%)	144.7
GRAND TOTAL	868.3

(a) FY 1976 dollars.

are required from the initiation of detailed Title II engineering design to initial operation of EPR. This schedule is based on two-shift/five-days-a-week operation.

REFERENCES

1. W. M. Stacey, Jr., et al., "Tokamak Experimental Power Reactor Conceptual Design," Argonne National Laboratory Rep. ANL/CTR-76-3 (1976).
2. F. E. Mills, et a., "Plasma Driving Systems for a Tokamak Experimental Power Reactor," these proceedings.
3. S-T. Wang, et al., "Conceptual Design of Superconducting Magnet Systems for Argonne Tokamak Experimental Power Reactor," these proceedings.
4. C. Trachsel, et al., "Development of a Structural Support System for the Experimental Power Reactor," these proceedings.
5. H. Stevens, et al., "Tokamak Experimental Power Reactor Primary Energy Conversion System," these proceedings.
6. B. Misra, et al., "Computer Modeling of Hydrogen Isotope Enrichment for Fusion Power Reactors," these proceedings.

PLASMA DRIVING SYSTEMS FOR A TOKAMAK EXPERIMENTAL POWER REACTOR*

F. E. Mills, J. N. Brooks, K. Evans, Jr., R. L. Kustom
W. M. Stacey, Jr., and S. T. Wang

CTR Program
Argonne National Laboratory
Argonne, Illinois 60439

The Tokamak Experimental Power Reactor is a device designed to operate at or near ignition with the potential for production of net power. It utilizes technology which either exists or can be achieved with a modest extrapolation from the present. The plasma driving systems, and their implications for energy storage and transfer technology are analyzed utilizing dynamic simulation of the plasma startup, burn and shutdown.

INTRODUCTION

The plasma driving system for the Tokamak Experimental Power Reactor (TEPR) consists of an ohmic heating (OH) coil, an equilibrium field (EF) coil, and their respective power supplies. The ohmic heating coil induces the bulk of the plasma current during the reactor startup, and maintains the current during the burn. The equilibrium field coil is needed for stable positioning of the plasma within the vacuum chamber.

The driving system is one of the major subsystems for the TEPR and as such is critical to the success of TEPR and to eventual full scale tokamak reactors. The design and analysis of the coupled plasma-plasma driving system has been part of an ongoing effort at Argonne in connection with the overall ANL TEPR design.[1,2,3] A detailed sensitivity and tradeoff study has now been performed showing how the driving system power, energy, voltage, and magnetic field requirements depend on the way the TEPR is operated and on certain plasma physics parameters. This has led to the choice of a specific reference mode of operation, to power supply and magnet specifications and to initial design choices.

TEPR DEVICE DESCRIPTION

The device considered for the TEPR is one with a circular plasma of 6.25 m major radius, 2.1 m minor radius, a plasma current of 7.6 MA, a 1 m blanket and shield, and a toroidal magnetic field of 8-10 T produced by superconductive constant tension D magnets whose bore is $\sim 8 \times 12$ m. Considerations of shielding, assembly and maintenance in an experimental device of this size require the superconductive poloidal field coils to be exterior to the toroidal-field (TF) coils. The ohmic-heating flux is produced by a 4 m diameter solenoid through the central core plus outrigger coils which keep the OH flux away from the plasma. The equilibrium-field coils, which produce an 0.4 T field at the plasma, have some reverse turns at small radius to decouple from the

* Work supported by the U.S. Energy Research and Development Administration.

OH coil, while producing the proper field shape to maintain MHD equilibrium.

The first wall of the reactor is composed of stainless steel coated with a thin layer of beryllium (or other low-Z material). The Be serves as an impurity control measure in that it prevents erosion of iron into the plasma which would cause high levels of radiation. (However, even the erosion of beryllium serves to limit the maximum burn cycle obtainable.) As envisioned now, the EPR can support a range of plasma parameters, some controllable and some, if not most, dependent on the plasma physics obtained. For the purpose of this study, a specific plasma has been assumed, one that is relatively demanding from the standpoint of the driving system requirements. The minimum safety factor is 2.5, and the resistivity is given by the Spitzer formula but with an assumed anomaly factor of 3. The plasma is in MHD equilibrium at all times with specific density, temperature, current density and flux density profiles described in detail in Chapter 3 of Reference 1. The plasma is assumed to be at ignition at about 10 keV at least in the absence of substantial Be and He impurities but with an 0.5% oxygen background. The maximum toroidal and poloidal betas are respectively, $\beta_T^{max} = 0.048$ and $\beta_p^{max} = 1.72$.

COMPUTATIONAL MODEL

The driving system requirements have been analyzed primarily with three computer codes, a global dynamics plasma code, a MHD equilibrium code, and a driving system code. The dynamics code is based on a spatially averaged, time dependent model which solves particle and energy balance equations. The code includes an alpha slowing-down model, a neutral beam model, a radiation model, a plasma-wall interaction model, and a confinement time model. The model is described in detail in Appendix C of Reference 1. The plasma code is coupled to a driving system code based on the three mesh equivalent circuit shown in Fig. 1.

The codes are coupled in the following ways; the temperature, impurity content, etc. of the plasma determine R_p. Secondly, the EF current required at any time depends on both the plasma current and the poloidal beta. In turn, the magnitude of the plasma current determines the ohmic heating power in the plasma, as well as the confinement times.

The dependence of I_{EF} on I_p and β_p is determined by the MHD equilibrium code. This MHD code is also used to compute the basic MHD equilibrium solution during the flattop portion of the burn cycle.

During the startup and the rest of the burn cycle, it is assumed that the MHD equilibrium evolves with a fixed profile. The equilibrium at any time is then uniquely characterized by the values of I_p and β_t at that time. The burn cycle dynamics calculation at each time step involves: (1) determination of I_p and β_t from the coupled plasma power balance and plasma driving system circuit equations; (2) determination of the MHD equilibrium that is characterized by I_p and β_t; (3) determination of the equilibrium field, $\vec{B}_{EF}$, that is required for the equilibrium, and (4) determination of the current, I_{EF}, in the EF coils that is required to produce the equilibrium field. Thus, this procedure determines a self-consistent relationship $I_{EF} = I_{EF}(I_p, \beta_t \text{ or } \beta_p)$ that defines the current required in the equilibrium field coils.

ENERGY STORAGE AND TRANSFER

The TEPR poloidal coil power supplies must be able to store, transfer and recover gigajoules of energy efficiently at repetition rates of about once per minute. Conventional power supplies are not well suited to meeting the TEPR design goals because they tend to be too costly and inefficient in this mode of operation. Therefore, the designs of the poloidal field power supplies do not incorporate existent and proven technologies.

The power supply philosophy for the plasma driving system is as follows. The EF coil must be programmed and therefore has been chosen to be a phase controlled rectifier circuit operating out of magnetic energy storage. Since the magnetic energy is fixed by the required equilibrium field, the principal variable cost is associated with the power. Thus, the plasma heating cycle should be as slow as possible to minimize this EF power cost. The OH field need not be progammed but must cycle as rapidly as possible to build up the plasma current and heat the plasma rapidly in order to avoid wasting energy. Thus, high power is required in the OH circuit, and the power supply cost should depend primarily on stored energy, as opposed to power. High voltage multidrum homopolar generators are well suited to this task. They can operate efficiently, and have the property that their effective capacitance can be adjusted by changing the magnetic field, allowing control over the OH cycle time. They further can be connected in series or parallel to vary the voltage or capacitance. In this application the OH energy is in the coil, and the drums are nearly at rest except during OH field reversal, so that losses are minimized. The start and stop action is controlled by operation of a switch across the OH coil. An additional small phase controlled rectifier provides flux for maintaining the plasma current during the burn and for resetting the OH current prior to current reversal during shutdown. This rectifier can operate out of the same energy storage unit used with the EF coil.

The EF coil power supply is designed to have an actively-controlled rate of energy change using a three-phase inductor-converter (I-C) SCR bridge between the EF coil and a central superconducting energy storage inductor.

The central energy storage inductor is also used to smooth the power demand from the electrical grid for the neutral beam and rf heating systems. Energy is added to the central storage inductor at almost constant rate throughout the whole fusion reactor cycle. Energy is extracted from the central storage inductor at much higher rates than the average input rate during the heating periods. The power-grid can only see the relatively low, average power.

The power supplies for the neutral beam and rf heating systems also employ technology which is beyond the current state-of-the-art, in order to avoid excessive power bumps on the electrical grid and, in the case of the neutral beam injector supply, to also take advantage of the superior qualities of a new technology. The design of the energy transfer network for the neutral beam injector uses an I-C to drive a high frequency polyphase rectifier. The injector is protected against spark damage by using a saturated time-delay transformer (STDT) to limit surge currents at the outset by phasing back on the high frequency polyphase rectifiers within the

first 100 μs for longer surge periods. The design of the rf heating power supply uses a five-phase I-C so that voltage ripple on the power amplifier can be minimized.

SENSITIVITY ANALYSIS

The determination of the design requirements for the plasma driving and heating systems involves finding a compromise among several, often conflicting, technological and cost limitations. These design requirements are quite sensitive to the time sequence of the startup (and shutdown) procedure. A range of potential startup procedures were simulated dynamically, following the format described above. The main parameters of interest are: (1) energy transfer from the homopolar supply (U_{OH}) -- peak OH power (P_{OH}) requirements are less important; (2) peak power in the EF supply (P_{EF}) -- EF energy transfer (U_{EF}) does not vary appreciably since the plasma is very conductive during most of the EF ramp-up; (3) total beam energy to heat the plasma, (U_B) and the total energy (U_{BE}) drawn from the energy storage unit for the beam heating; (4) maximum rate of change of the field in the OH coil ($\dot{B}_{OH}$) -- the maximum coil voltage (V_{OH}) is proportional to $\dot{B}_{OH}$; and (5) maximum field (B_{OH}) in the OH coil -- the OH coil current is proportional to B_{OH}.

Parameters varied in the study are: (1) OH current reversal time, Δt_{OH} -- essentially determined by the equivalent capacitance of the homopolar system; (2) time of beam initiation, t_B; (3) beam power to the plasma, P_B; (4) plasma resistivity, η; and (5) oxygen concentration, as a measure of the effect of background impurities. The results of the study are summarized in Table 1, for a variety of possible startup procedures and conditions. Selected results are also plotted in Figures 3 to 7, to illustrate important features.

In Figure 3, U_{BE}, U_{OH}, P_{EF}, B_{OH} and $\dot{B}_{OH}$ are plotted as a function of the length, Δt_{OH}, of the OH current reversal. For times shorter than 2 s, a penalty is paid in the EF power requirement and in a very high $\dot{B}_{OH}$, with essentially no compensating reduction in U_{BE} or B_{OH}. On the other hand, the plasma current and temperature builds up rapidly, and U_{OH} and the resistive volt-seconds are considerably reduced by shorter Δt_{OH}. For times longer than 2 s, there are large increases in U_{OH} and U_{BE} because the OH voltage is quite ineffective at increasing the plasma current in the presence of the higher resistive losses associated with the cooler plasma. In fact the current rises slowly until U_{OH} reaches its maximum, wasting about one-half the OH flux, and more beam energy is required to heat the plasma. P_{EF} reaches its minimum for Δt_{OH} = 4 s, the maximum value occurring after ohmic heating, during beam heating. $\dot{B}_{OH}$, on the other hand, is reduced by the longer Δt_{OH}, but not to the level of present day technology. The two second reversal (Δt_{OH} = 2 s) is chosen as the reference case.

The ohmic heating requirements can be reduced by using supplemental beam heating during the OH current reversal period, Δt_{OH}, to reduce the resistive volt-seconds. In Figure 4, the beam initiation time, t_B, is varied during the ohmic heating current reversal, for Δt_{OH} = 2 s. At t = 0.5 s, the plasma current (~ 150 kA) has not really started, and injection heating too early may enhance the formation of plasma skin currents, leading to unfavorable confinement. (This phenomenon is not included in the global model simulation.) The compromise

position is to adopt t_B = 1 s for the reference case, but to design the coils and power supplies for the more demanding case in which the beam heating is not initiated until the end of the ohmic heating current reversal ($t_B = \Delta t_{OH}$ = 2 s).

Figure 5 shows the dependence upon beam power. At lower beam power, penalties are paid in all parameters except the EF coil power. The 20 MW case is singular in that ohmic heating (via the rectifier) is still effective after the homopolar swing (Δt_{OH}) because of the slow plasma heatup with P_B = 20 MW. The TEPR will start up satisfactorily with only 40 MW of power, and there is no reason to go beyond 60 MW. Thus, selection of P_B = 60 MW for the reference design provides some margin.

It is important to test the sensitivity of the design to parameters less easily controlled than those above. For this purpose the plasma resistivity and impurity concentrations are varied between $\eta = 10\ \eta_{sp}$ and $\eta = 6\eta_{sp}$, and from 0-1% oxygen impurity. The results are shown in Figures 6 and 7. The principal effects of increased plasma resitivity on impurity concentration are increased requirements on the ohmic heating energy (U_{OH}) and field (B_{OH}). The effect of high impurity concentration (1% oxygen) is to keep the plasma cool for a longer time (due to line and recombination radiation) and to increase the resistivity. The poloidal coil requirements for this case are similar to the $6\ \eta_{sp}$ case.

The considerations above led to a choice of case 5 in Table 1 as the reference case for performance calculations. Table 2 presents a more detailed list of the properties of the reference case.

A more demanding case (no. 3 in Table 1) was chosen as the design basis for the power supply, energy storage and coil systems. The EF coil system is designed to provide 50 V-s to the plasma, and the OH coil system is designed to provide 85 V-s, for a total of 135 V-s. About 4.5 V-s are required for a 1 minute burn, so 135 V-s provides an ample margin.

REFERENCE CASE BURN CYCLE - ENERGY TRANSFER

The general features of the burn cycle for the reference case are shown schematically in Figure 2. The basic burn cycle, begins just after plasma breakdown and continues for $\approx$ 55 s. The cycle begins when the homopolar generator is connected to the previously charged OH primary coil. The OH primary current than reverses in 2.0 s. inducing about 2/3 of the final plasma current and ohmically heating the plasma. At t = 2 s, the OH coil is connected to the OH power supply and is disconnected from the homopolar generator. Midway during the OH current reversal, at 1.0 s, injection of 60 MW of neutral beam power is initiated. The beam injection is initiated early (before the plasma current is fully ramped up) in order to reduce the resistive volt-seconds that would otherwise be expended. At about 5.8 seconds the plasma reaches ignition and the beam heating is terminated. During this period, from 0-5.8 s, the current in the equilibrium field coil is continuously adjusted to maintain the plasma in MHD equilibrium. At the time the beam is turned off, the EF current, the plasma current and the plasma β_p have reached their maximum values. The OH current continues to increase during the burn phase to offset resistive losses in the plasma.

After about 5 s, the plasma is in the burn phase, where substantial thermonuclear power is produced. Because of the buildup of impurities the plasma gradually cools off and at ∿ 48 s the plasma is no longer producing significant power and the shutdown period is initiated. (The cooling off of the plasma can be delayed by supplemental heating -- e.g. with beams.) For the next 5 seconds the OH, EF and plasma currents are all reduced somewhat in preparation for the final rampdown. During this period the OH current is reduced to the value it had at t = 2 s, so that the OH homopolar generator will handle the same current swing on shutdown and startup. The plasma cools rapidly during this time. Finally, for the last 2 seconds of the burn cycle, the OH homopolar generator is reconnected, all currents are ramped down, and the cycle terminates. These currents are shown in Figure 8. In the next ∿ 15 seconds the vacuum ports are opened, the toroidal chamber is evacuated, and preparations are made for the next burn cycle. The total OH coil power and energy transfer for this cycle can be seen in Figure 9.

Figure 10 shows the EF coil energy and power requirements. Essentially, the coil is ramped up in ∿ 7 s during startup and down in ∿ 7 s at the end of the burn, with the current chosen to provide equilibrium for the assumed profile. Some adjustment is necessary during the burn to accommodate variations in the plasma β_p. Since the EF coil current is ramped slowly, it does not provide much ohmic heating, but produces the final flux necessary to induce the final plasma current. As a result, there is little $I_p^2R_p$ loss in the EF circuit. The peak power is typically 400 MW and can come either three quarters of the way through the OH cycle or near the end of beam heating, depending on the cycle.

The homopolar generators communicate with the external power grid only through the OH rectifier and the energy storage system, so that the peak power produced by the homopolar generators does not appear in the storage system or the external electrid grid. The neutral beam system, the OH rectifier and the EF rectifier are the elements which operate out of the energy storage system. An instantaneous electrical efficiency of 0.29 is assumed for the beams, that is, pulsed electrical energy of 207 MW must be supplied to produce 60 MW of beam power. This is because the electrical energy recovery is simultaneous, while the thermal-electric energy recovery is averaged over the cycle. The net energy withdrawn at the end of the cycle is 1.44 GJ, of which 986 MJ is due to beams, and 85 MJ is $I_p^2R_p$ heating. Another 370 MJ must be added for power supply losses so that the average power to operate these systems is 20.6 MW, based upon a 70 s cycle with a 55 s burn and a 15 s replenishment. This power is provided uniformly. The maximum energy withdrawal occurs at the end of beam heating, which is also the time of maximum power. Then the energy storage unit must provide 2.44 GJ and a power of 620 MW at maximum depletion.

REFERENCE CASE BURN CYCLE-PLASMA

The initial D-T ion density in the plasma is 0.89×10^{20} m^{-3}, composed of equal parts of deuterium and tritium. During the cycle, the ions are lost by fusion and by transport to the first wall. The D-T ion loss can be replenished by a combination of recycling from the wall and an external refueling source. By varying the refueling rate from the external source, the ion density can be controlled.

During the cycle, Be is sputtered into the plasma by hot particles impinging on the first wall. This Be and the He produced by fusion contribute to the overall plasma kinetic pressure and hence to the β_p. Since the EPR is assumed to be pressure-limited, the D-T density is gradually reduced over the course of the burn cycle so that the β_p limit will not be violated.

Temperature variations during the burn cycle are shown in Figure 11. The ion and electron temperatures are 15 eV at the start of the cycle. Because of the short equilibration times between electrons and ions, $\bar{T}_e$ and $\bar{T}_i$ are almost equal at all times. During the first second ohmic takes the plasma to about 60 eV. When the beam is turned on, the plasma heats rapidly, at an average rate of 2.4 keV/s. When the beam is turned off, the plasma cools slightly, settling into an equilibrium by about 9 s. Were it not for the subsequent buildup of He and Be, the plasma would remain indefinitely at this ignited point.* Instead, the D-T density must be reduced to compensate for the He and Be buildup, less alpha heating of the plasma occurs, and the plasma gradually cools off.

The plasma poloidal beta, β_p, shown in Fig. 12 is the ratio of the plasma kinetic pressure to the poloidal magnetic pressure. During the first second of beam heating, both the plasma current and the temperature increase. They tend to offset each other and are responsible for the oscillatory behavior of β_p shown in Figure 12. At 2 s I_p = 5.32 MA, or about 70% of its final value. The magnetic pressure, which is proportional to I_p^2, doubles by the end of the beam heating period, but the kinetic pressure increases by almost a factor of 5. β_p rises accordingly. When β_p reaches the nominal maximum of 1.72 the beam is turned off. Subsequently, β_p oscillates slowly for a number of reasons. having to do with the accumulation of He and Be and the cooling of the plasma.

After about 40 s, β_p decreases rapidly as the temperature drops. However, during the rampdown period, I_p drops very rapidly, causing an abrupt spike in β_p. Because of the uncertainties in the representation of this phase of the burn pulse, it can be considered that the β_p limit could be exceeded at the time of the spike. As a consequence MHD equilibrium might be lost at this time. The plasma could then be assumed to deposit its remaining energy on the wall in a very short time. The shutdown period might present a problem in this regard. The plasma current should be ramped down at a time such that when (and if) MHD equilibrium is lost, the residual plasma energy is as low as possible. At the same time, the plasma must be hot enough (and ionized enough) to actually support a current; if the plasma is too cold, the current will decay resistively. In this analysis, this problem has been resolved by the judicious choice of rampdown rate. At the point where β_p peaks, only 4.5 MJ of thermal energy remains in the plasma, a trivial amount ($\lesssim$ 1.5% of the peak thermal energy). The plasma current at the time of the β_p peak is about 0.9 MA. This also represents less than 1.5% of the maximum inductive energy and is probably inconsequential if lost. A more serious concern is the potentially high voltage transient that could be induced across the OH and EF power supplies by the sudden loss of plasma current.

The constituents of the plasma power balance during the burn are shown in Figure 13 where P_B is the beam power, P_R is the radiation power, P_{TR} is the

* Assuming that recycling and refueling take place.

transport power to the first wall and P_N is the neutron power. The neutral beam power, is a square wave of 60 MW flattop. The neutron power increases rapidly at the beam heats the plasma and fusion starts. The peak in P_N just prior to the beam termination is due to the substantial suprathermal fusion between the fast beam deuterons and the background plasma tritons. During the burn, P_N oscillates a bit but basically decreases with time as both n_{DT} and T_{DT} decrease.

Figure 14 shows an expanded view of the various power terms during the startup period. Also shown is the alpha-heating ($P_\alpha \sim 0.2\ P_N$) and the ohmic heating ($P_\Omega = I_p^2 R_p$) power. The net power available to heat the plasma is given by the sum of the ohmic, beam and alpha components minus the radiation and transport components. The transport power ($\propto / \bar{T}/\tau_E$) varies directly with the plasma temperature and inversely with the (ion and electron) energy confinement times. As the plasma is heated the confinement times are determined by successively less collisional transport regimes, each of which scales differently with temperature. The energy transport mechanism which dominates the power loss is indicated on the P_{TR} curve: PS denotes Pfirsh-Schluter, PL = plateau, BAN = banana and TIM = trapped-ion-mode.

Ohmic heating increases at the start of the cycle as the plasma current is induced. When the beam is turned on, the electron temperature increases rapidly, R_p falls rapidly, and P_Ω decreases, in spite of the continued increase in I_p from 1-2 s. For the rest of the cycle P_Ω is insignificant ($\lesssim$ 0.5 MW) except for the shutdown period when the plasma temperature is again low. The contribution of ohmic heating to the total heating energy for the startup period is small; however, ohmic heating is very important in helping to overcome the large radiation peak at 1-1.3 s. This peak is due to line and recombination radiation arising from the 0.5% oxygen background of the plasma.

APPENDIX - ALTERNATIVE OH POWER SUPPLY ANALYSIS

A free running, homopolar generator, appears to be the best candidate for the OH power supply largely because the maximum power (> 1 GW) requirements seem prohibitive for a conventional supply. On the other hand, a controllable power supply allows substantial control over the plasma current waveform; the right choice of waveform could conceivably reduce the power requirements. An I_{OH} waveform that accomplishes this (together with an acceptable startup from the plasma standpoint) is shown in Figure 15. I_{OH} is specified by:

$$|P_{OH}| = \text{constant} = 850\ \text{MW} \qquad (1)$$

subject to

$$N_{OH} V_{OH} \leq 50\ \text{volts} \qquad (2)$$

where (1) and (2) define a differential equation for I_{OH}. The maximum voltage of 50 volts per turn is about the same as that needed for the reference case. (If V_{OH}^{max} was higher $|P_{OH}|^{max}$ could be somewhat lower.) As it happens the plasma current, EF current, and the resistive volt seconds for this method of startup are quite similar to the reference case. The power requirement of 850 MW is substantially less than the 1200 MW for the reference case but is probably still too high for a controllable supply to be cost effective compared to a homopolar, however, research on this topic is continuing.

REFERENCES

1. W. M. Stacey, Jr., et al., "Tokamak Experimental Power Reactor Conceptual Design," ANL/CTR/76-3, Argonne National Laboratory (1976).
2. J. N. Brooks and W. M. Stacey, Jr., "Driving Requirements for the Ohmic Heating and Equilibrium Coils of a Tokamak Experimental Reactor," Proceedings of the Sixth Symposium on Engineering Problems of Fusion Research, IEEE Press, (1975), p. 43.
3. W. M. Stacey, Jr., et al., "Tokamak Experimental Power Reactor Studies," ANL/CTR/75-2. Argonne National Laboratory (1975).

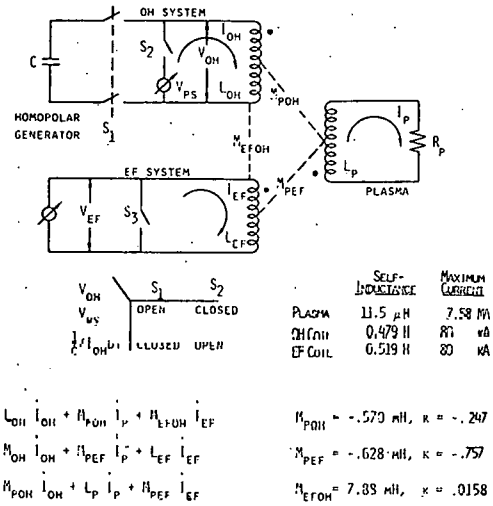

FIGURE 1. Plasma Driving System Circuit Diagram.

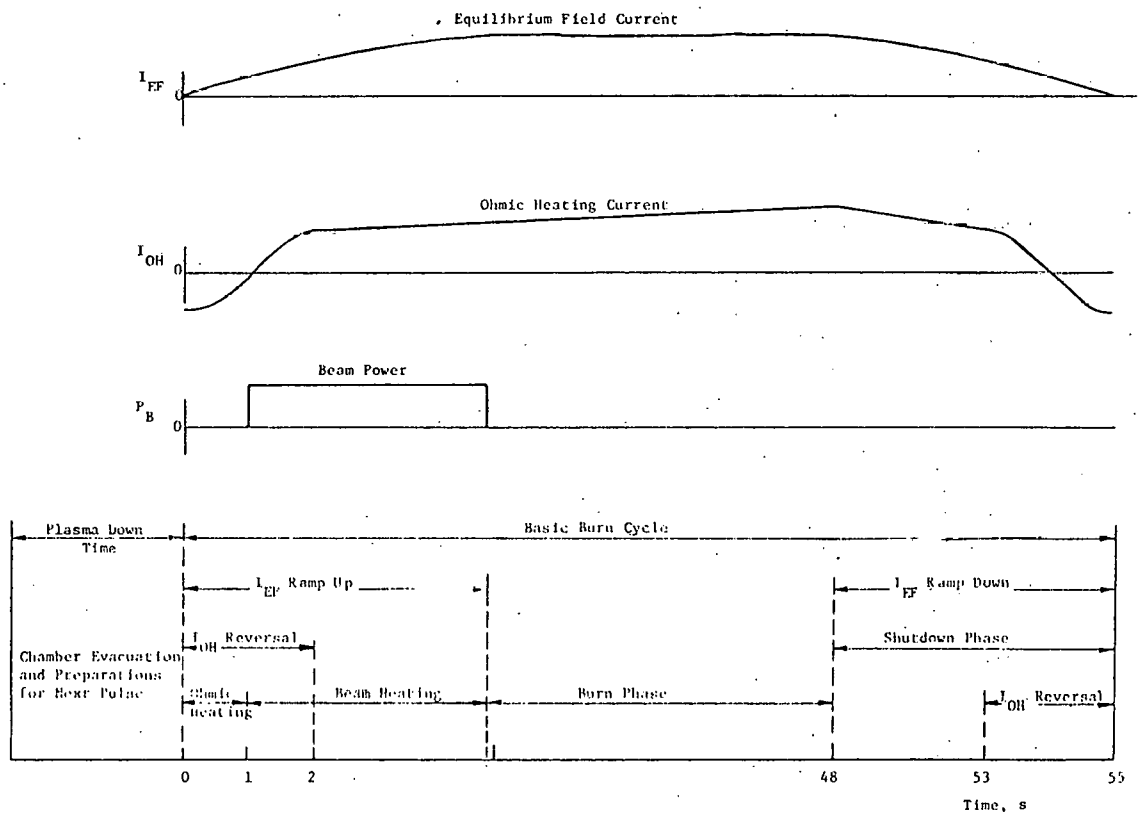

FIGURE 2. Burn Cycle Scenario

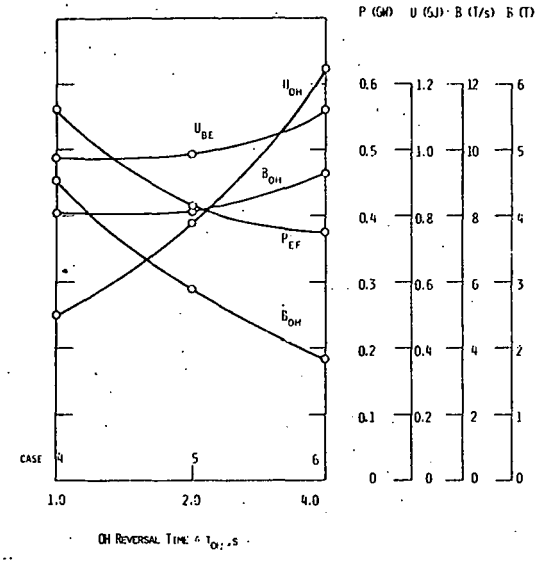

FIGURE 3. Effect of OH Current Reversal Time on Plasma Driving and Heating System Requirements.

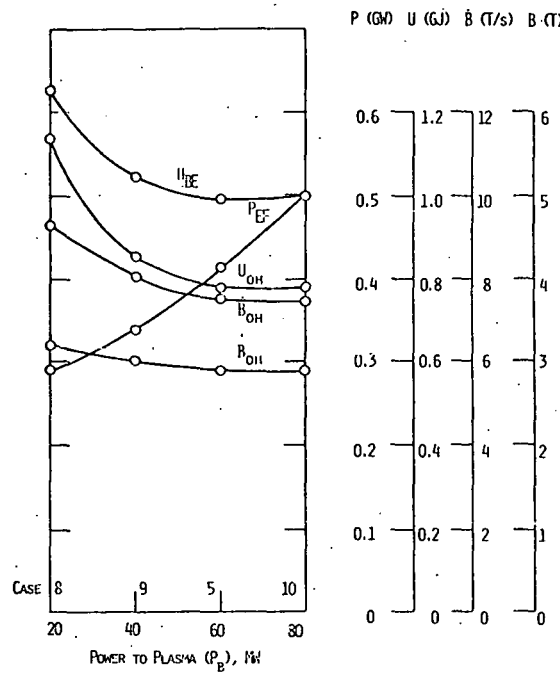

FIGURE 5. Effect of Beam Power on Plasma Driving and Heating System Requirements.

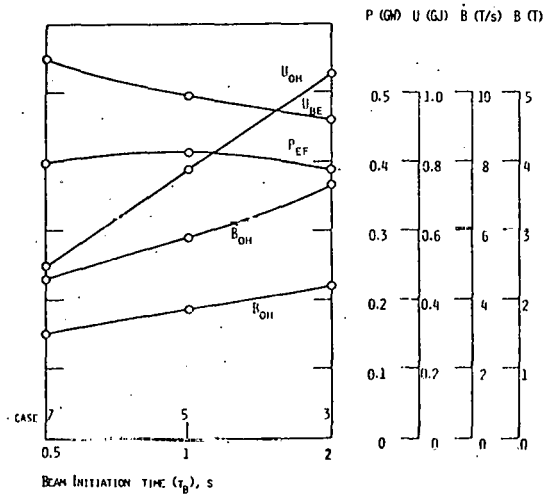

FIGURE 4. Effect of Beam Initiation Time on Plasma Driving and Heating Systems Requirements.

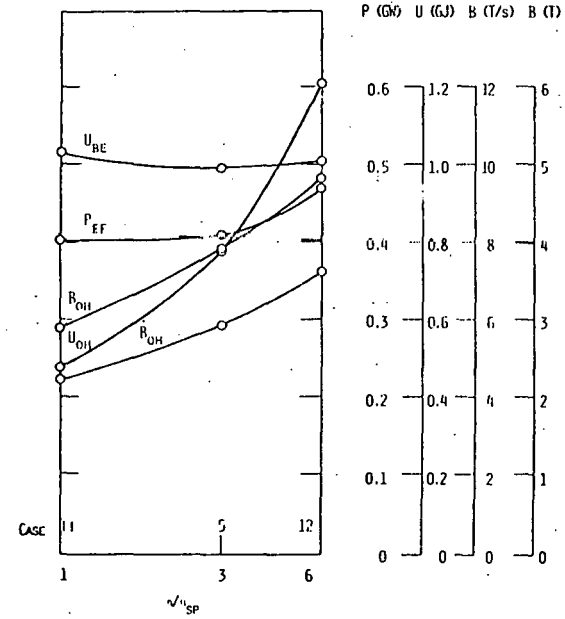

FIGURE 6. Effect of Plasma Resistivity on Plasma Driving and Heating System Requirements.

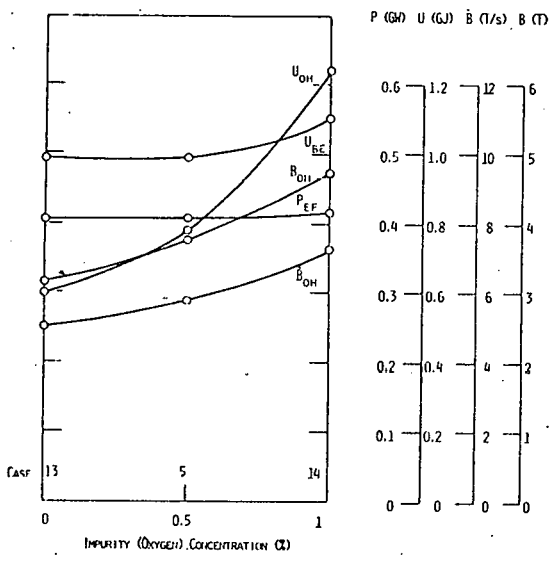

FIGURE 7. Effect of Oxygen Impurity on Plasma Driving and Heating System Requirements.

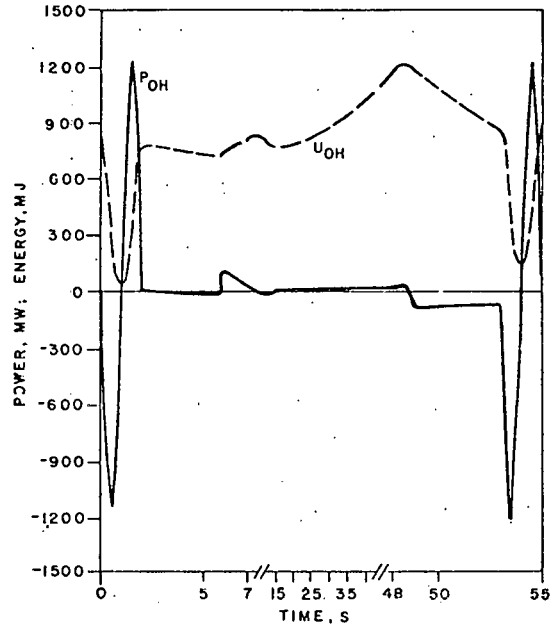

FIGURE 9. OH Coil System Power and Energy Transfer During Reference Burn Cycle.

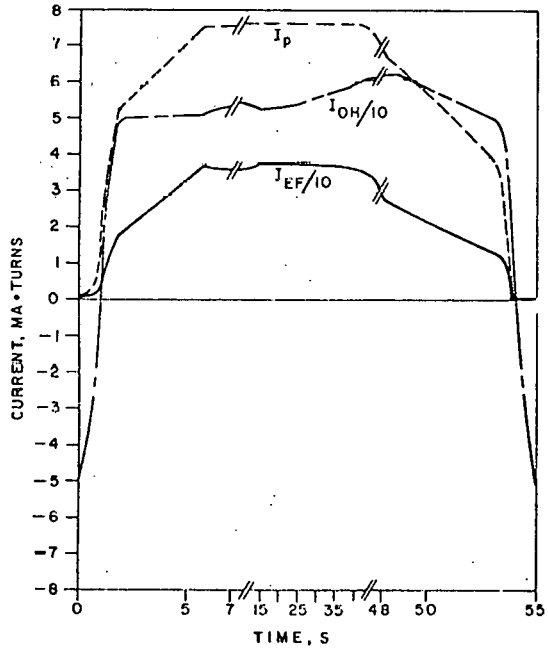

FIGURE 8. Plasma, OH and EF Currents During Reference Burn Cycle.

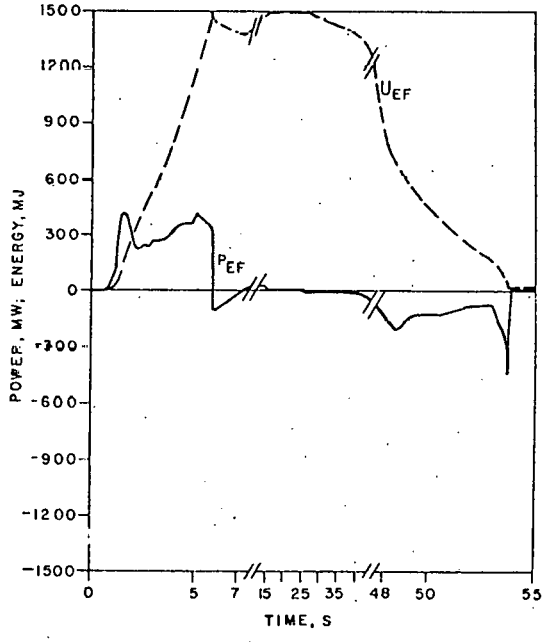

FIGURE 10. EF Coil System Power and Energy Transfer During Reference Burn Cycle.

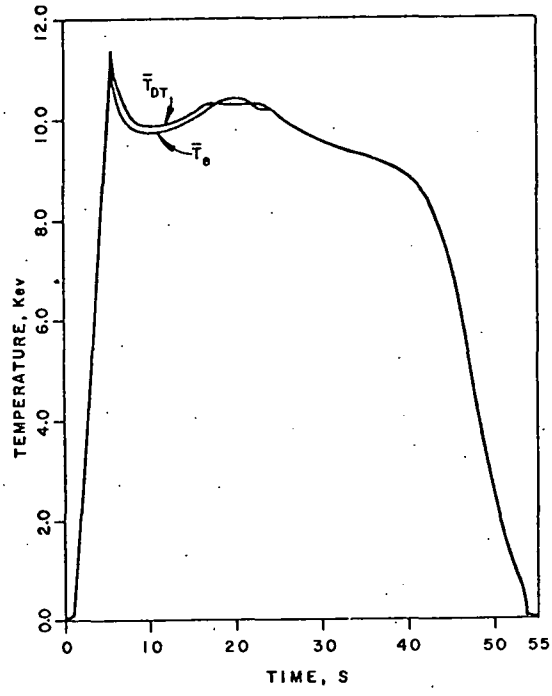

FIGURE 11. Ion and Electron Temperatures During Reference Burn Cycle.

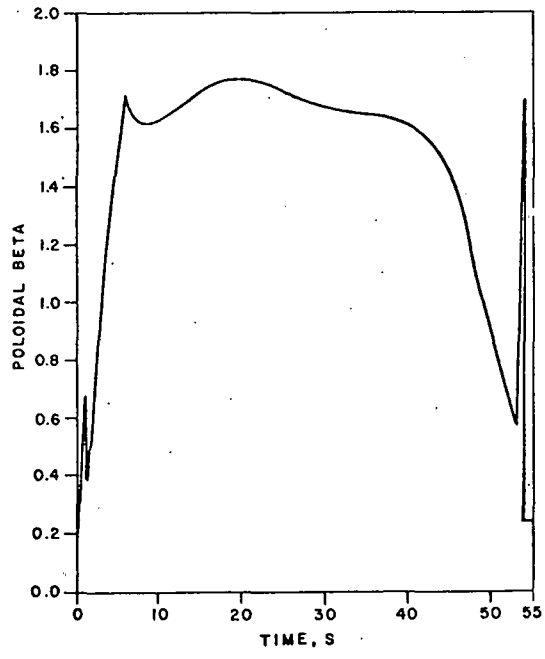

FIGURE 12. Poloidal Beta During Reference Burn Cycle.

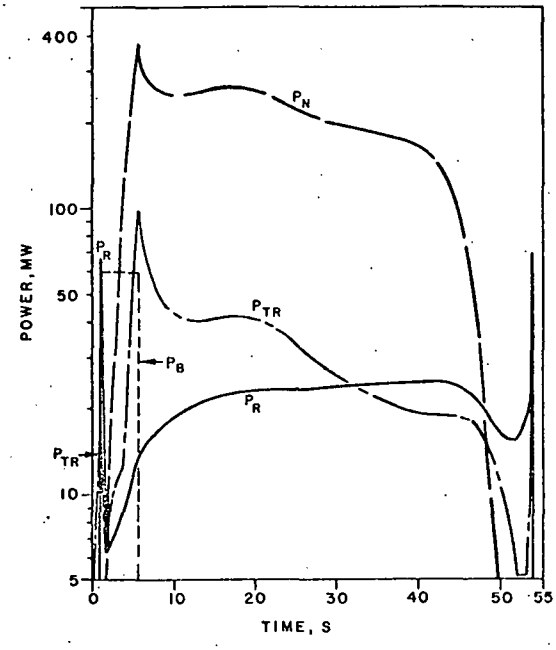

FIGURE 13. Power Components During Reference Burn Cycle.

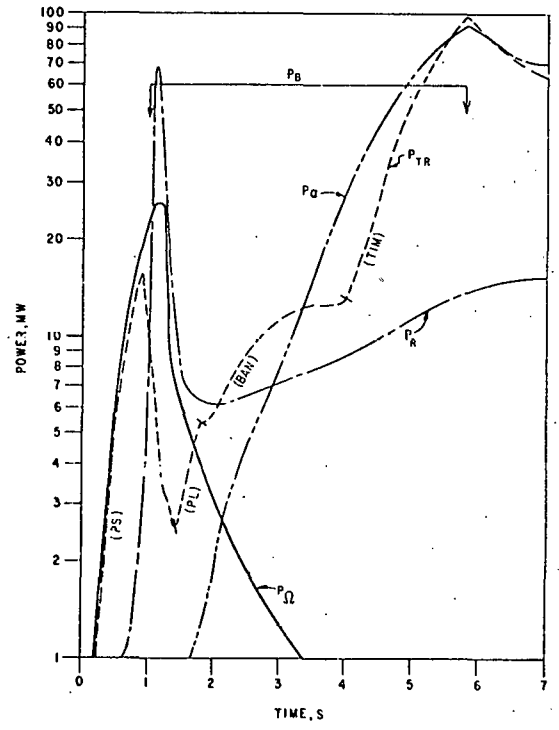

FIGURE 14. Power Components During Startup.

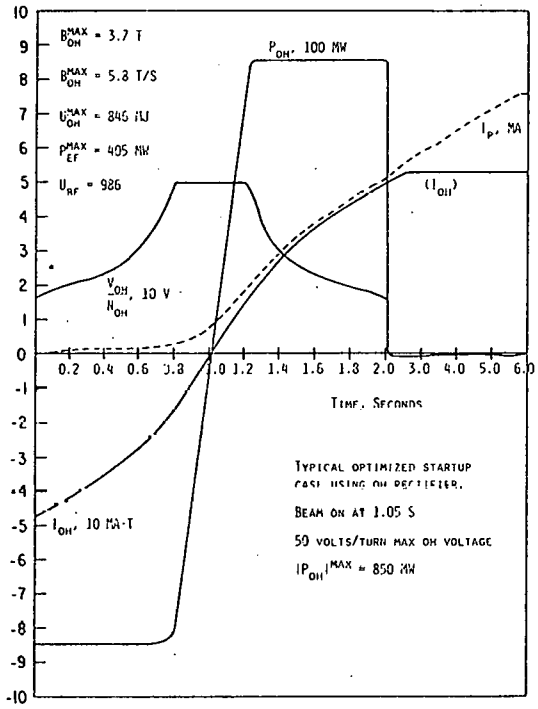

FIGURE 15. I_{OH}, V_{OH}, P_{OH} and I_p During Startup Using Controllable OH Power Supply.

TABLE 1. Plasma Driving and Heating System Requirements.

Case	Δt_{OH} (s)	t_B (s)	P_B (MW)	Other	OH								EF[a]		BEAMS		
					V-s Total	V-s Res[b]	$\dot{B}_{OH}$ Max (T/s)	B_{OH}[c] Max (T)	U_{OH} Max (MJ)	P_{OH} Max (MW)	I_{OH} Max (kA)	V_{OH} Max (kV)	P_{EF} Max (MW)	V_{EF} Max (kV)	U_B (MJ)	U_{BE} (MJ)	P_{Net}[d] (MW)
1	0.5	0.5	60	$\eta = 3\eta_{sp}$, 0.5% oxygen concentration	44.0	12.8	16.6	2.81	428	2390	45.1	118	650	42.5	263	907	43
2	1.0	1.0	60		53.3	21.9	9.9	3.43	603	1790	54.9	71	365	17.6	265	914	44
3	2.0	2.0	60		72.3	40.6	6.7	4.40	1060	1620	70.4	48	389	10.4	268	924	41
4	1.0	0.5	60		47.9	15.8	9.1	3.02	502	1520	48.4	65	561	27.4	283	975	45
5	2.0	1.0	60		61.2	29.9	5.8	3.78	776	1220	60.5	41	416	20.8	286	986	43
6	4.0	2.0	60		79.0	45.6	3.6	4.80	1240	989	76.8	26	373	30.7[e]	324	1117	39
7	2.0	0.5	60		47.8	14.8	4.6	3.02	503	770	48.4	33	398	18.9	319	1100	43
8	2.0	1.0	20		72.9	39.9	6.4	4.65	1140	1490	74.4	46	291	9.1	364	1255	35
9	2.0	1.0	40		65.1	33.3	6.0	4.03	857	1330	64.5	43	338	12.6	302	1041	40
10	2.0	1.0	80		60.9	27.8	5.8	3.76	776	1220	60.2	41	503	25.7	289	997	44
11	2.0	1.0	60	$1 \times \eta_{sp}$	45.9	13.6	4.5	2.90	474	722	46.3	32	403	16.9	301	1037	43
12	2.0	1.0	60	$6 \times \eta_{sp}$	78.4	45.8	7.2	4.79	1210	1910	76.7	51	471	23.3	291	1003	43
13	2.0	1.0	60	0% ^{16}O	52.6	20.4	5.0	3.29	595	927	52.7	36	413	27.4	285	983	56
14	2.0	1.0	60	1% ^{16}O	78.7	46.0	7.3	4.76	1240	1900	76.2	52	432	17.4	321	1107	28

a) I_{EF} = 80 kA, U_{EF} = 1500 MJ, EF Coil Provides 50 V-s to plasma

b) Resistive volt-sec

c) max during heating; further increase during burn

d) P_{Net} is for max cycle length

e) Shortly after transient during beam turn on.

TABLE 2. Plasma Heating and Driving System Reference Case Parameters

Plasma		
Maximum Current	7.58	MA
Maximum Thermal Energy	270	MJ
Resistive Energy Dissipation ($\eta = 3\eta_{sp}$)	90	MJ
Ohmic Heating System		
Current Reversal Time	2	s
Peak Current	60.5	kA
Peak Voltage	41	kV
Maximum Energy Transfer	776	MJ
Peak Power	1220	MW_e
Equivalent Capacitance of Homopolar Generator	0.896	F
Maximum Field in Coil	3.8	T
Maximum Field Rise in Coil	5.8	T/s
Volt-seconds to Plasma		
Inductive, startup	31.3	V·s
Resistive, startup	29.9	V·s
Resistive, burn	4.0	V·s
Equilibrium Field System		
Peak Current	80	kA
Peak Voltage	20.8	kV
Maximum Energy Transfer	1480	MJ
Peak Power	416	MW
Volt-seconds to Plasma	50	V·s
Neutral Beam Injection System		
Beam On	1.0	s
Beam Duration	4.77	s
Beam Energy	180	keV
Beam Power to Plasma	60	MW
Energy Deposited in Plasma	286	MJ
Power Required to Operate Injection System	485	MW
Directly Recovered Electrical Power	278	MW
Net Electrical Power to Operate System	207	MW
Net Electrical Energy to Operate System	986	MJ
Magnetic Energies		
$\frac{1}{2} L_p I_p^2$	332	MJ
$\frac{1}{2} L_{EF} I_{EF}^2$	1660	MJ
$\frac{1}{2} L_{OH} I_{OH}^2$	876	MJ
$M_{POH} I_P I_{OH}$	- 259	MJ
$M_{PEF} I_P I_{EF}$	- 386	MJ
$M_{EFOH} I_{EF} I_{OH}$	39	MJ
Total	2262	MJ

CONCEPTUAL DESIGN OF SUPERCONDUCTING MAGNET SYSTEMS FOR THE ARGONNE TOKAMAK EXPERIMENTAL POWER REACTOR *

S. T. Wang, L. R. Turner, F. E. Mills,
D. W. DeMichele, P. Smelser and S. H. Kim

CTR Program
Argonne National Laboratory
Argonne, Illinois 60439

As an integral effort in the Argonne Tokamak Experimental Power Reactor Conceptual Design,[1] the conceptual design of a 10-tesla, pure-tension superconducting toroidal-field (TF) coil system has been developed in sufficient detail to define a realistic design for the TF coil system that could be built based upon the current state of technology with minimum technological extrapolations. A conceptual design study on the superconducting ohmic-heating (OH) coils and the superconducting equilibrium-field (EF) coils were also completed. These conceptual designs are developed in sufficient detail with clear information on high current ac conductor design, cooling, venting provision, coil structural support and zero loss poloidal coil cryostat design. Also investigated is the EF penetration into the blanket and shield.

SUPERCONDUCTING TOROIDAL-FIELD COIL SYSTEM

Characteristics of Toroidal-Field Coil Design

The TF coil uses niobium-titanium as the superconductor because of its good ductility and proven performance in large magnets. The toroidal field strength should be as high as practical in order to enhance the plasma confinement and boost the power performance. A peak field of 10 T can be achieved with a large amount of superconductor at 4.2°K or with much less superconductor at 3°K. It is more economical to operate the 10 T TF coil at 3°K because the difference in refrigeration cost is much smaller than the difference in the cost of the superconductor. The problem of refrigeration at temperatures lower than 4.2°K for large systems was evaluated. The TF coils will achieve 10 T peak field at 3°K and 8 T peak field at 4.2°K with about 0.5°K temperature allowance for each case; 8 T is the minimum goal and 10 T is the maximum goal in the TF coil design.

A TF coil system consisting of 16 pure-tension "D"-shape coils with a horizontal bore of 7.78 m provides adequate space for the vacuum chamber, blanket and shield; provides adequate access for assembly and repair; and has a satisfactorily small maximum field ripple of 1.3%. The TF coil system is summarized in Table 1 and depicted schematically in Figure 1.

The hoop tension acting on a circular or oval toroidal coil system, either a continuous toroid or a bumpy toroid, is

* Work supported by the U. S. Energy Research & Development Administration.

TABLE 1. Toroidal Field Coil System

Number of coils	16
Coil shape	pure tension
Maximum access (m)	∿ 3
Peak field (T)	
10	3°K
8	4.2°K
Bore (m)	
Vertical	12.6
Horizontal	7.78
Field in plasma, B_t (T)	
10 T peak field	4.32
8 T peak field	3.46
Operational current (kA/turn)	60
Stored energy (GJ)	30 total
Inductance (H)	16.7 total
Ampere-turns (MAT)	134 total
Turns/coil	70 x 2
Mean turn length (m)	36
Coil weight/coil (Ton)	∿ 208
Coil and bobbin cross section (m^2)	0.619
Winding cross section (m^2)	0.572
Average current density (A/cm^2)	
Over bobbin and coil	1352
Over coil winding	1463
Over copper	3660
Average turn cross section (cm^2)	40.6
Cross section ratio, SS/Cu	∿ 1.5
Refrigeration power (MW)	14.3

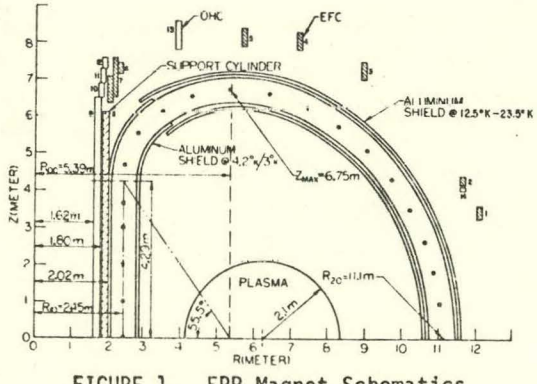

FIGURE 1. EPR Magnet Schematics

nonuniform. Large bending moments are exerted on the conductor. This produces high peak stresses; consequently, a larger amount of structural material will be needed than in the absence of bending moments. Although it is possible to contain the bending moment by an external mechanical structure, to do so may not avoid conductor slippage, and large shear stresses may exist from turn-to-turn and/or layer-to-layer. When the radius of curvature is such that the product of transverse force and radius of curvature is constant, the coil is in pure tension with no bending moments; then, a minimum amount of structural material will be needed and the in-plane hoop stress will be uniform with inner skin stress slightly higher than outer skin stress. The mean hoop stress will be the average value of the inner skin stress and the outer skin stress, as shown in Figure 2. Therefore, the toroidal coil system will behave exactly like a solenoid. The solenoid is known to the superconducting magnet engineer as the coil which is most stable and has the least mechanical disturbance. Consequently, it is expected that the coil stability of a pure-tension coil system will be better than that of circular or oval coil systems. For the 10-T TF coil design, the average hoop stress is about 21,000 psi.

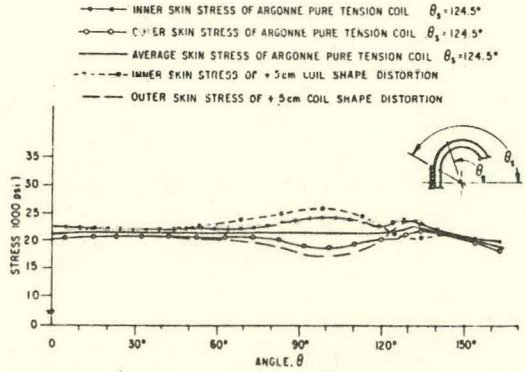

FIGURE 2. Hoop Stresses Distribution of Argonne Pure-Tension Coil.

Superimposing Fields and Out-of-Plane Loads

With a TF peak field of 10 T, the plasma current will be 7.6 MA. The ohmic-heating (OH) coil of ± 67 MA turns will swing a central field of ± 5 T. The equilibrium-field (EF) coil of 37.15 MA turns will generate 0.46 T at the plasma center for plasma equilibrium. Without a field shield, these poloidal coils and plasma currents would superimpose ac field onto the TF coil windings, exerting an out-of-plane load onto the TF coil, as well as producing large ac losses. The performance and design of the TF coil is severely affected by the superimposing fields. The OH coils produce little superimposing field, while the plasma current generates large amounts of parallel fields. The EF coil contributes large amounts of both parallel and perpendicular fields.

To compute the out-of-plane load exerted on the TF winding, the superimposing fields from the OH coils, the EF coils and the plasma were computed at various times in the cycle. The TF coils were divided into 70 angular segments with approximately equal angular spacings. On each angular segment cross section, superimposing fields were computed at nine locations. The out-of-plane load was obtained by Gaussian integration of the $\vec{J} \times \vec{B}$ body force over the superimposing fields at nine points. Computations at various times were necessary because the OH coils, the EF coils and the plasma contribute different amounts at different times. The distribution of out-of-plane loads at 5 representative times is shown in Figure 3(a), (b), (c), (d) and (e), respectively. It is important to note that there are many local bending moments exerted on the TF coil. (The out-of-plane load of the lower coil half is the mirror image

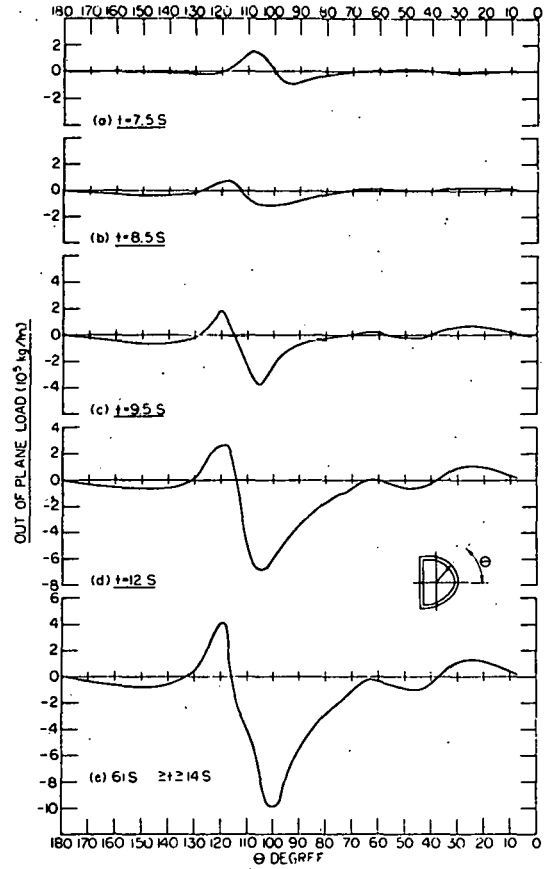

FIGURE 3. Time Evolution of Out-of-Plane Load.

of that for the upper coil half.) Surprisingly, the sign of the out-of-plane load reverses rapidly from segment to segment. For this EPR design, the most severe out-of-plane load acts on the coil segments within the angular position between 85° and 125°. The maximum out-of-plane load occurs during the burn phase with a maximum out-of-plane pressure of about 3000 psi at the 100° position. Since many bending moments exist along the TF coil, shear members will be effective for the out-of-plane load support.

Normal Metal Field Shielding Design

The TF coil reference design provides normal metal field shielding. With a field

shield, a monolithic conductor can be used without excessive ac losses. Without the shield, cable conductor must be used provided that all filaments in the cable are fully transposed. There is little experience of using cable conductor in a large magnet. It is fair to say that the sponginess of a cable conductor raises questions about its use in a large magnet system with large electromagnetic forces. As far as mechanical integrity is concerned, monolithic conductors are far better than cable conductors.

High-Purity Aluminum as Normal Metal Shield

High-purity aluminum or copper has a large residual resistivity ratio (RRR = $\rho_{273°K}/\rho_{4.2°K}$), on the order of 10^3 to 10^4. However, the large magnetoresistivity of copper severely reduces its conductivity gain at low temperatures. Aluminum, on the other hand, has a rather small magnetoresistivity that saturates at a rather low field ($\sim$ 0.5 T). The low magnetoresistivity of aluminum recommends it for use as the normal metal shield. To keep the strain-induced resistivity small, the aluminum must be reinforced. For example, if aluminum is explosively welded to stainless steel, then the stainless steel will be stressed to 60,000 psi while the aluminum suffers a strain of only 0.17%. The 0.17% strain cuases little increase in resistivity. For 5000 purity aluminum reinforced by stainless steel, recent data indicate that there is little increase in resistivity for up to 300 loading cycles.[2]

The 5000 purity aluminum with stainless steel backing is chosen for the field shield panels. These panels are formed into rectangular ducts around the TF coil as shown in Figure 1. For the present design, the shields around the inner leg of the TF coil are seriously restricted by the available space and are, therefore, wrapped directly on the TF coil form. The operating temperature is 3°K or 4.2°K depending upon the 10 T or 8 T operation. The remaining shields will be operated between 12.5°K and 23.5°K with a mean temperature of 18°K. Shield panels inside the TF coil will be subjected to a peak field ranging from 3 T to 10 T. The side panels will have an averaged magnetic field ranging from 1.5 T to 5 T. The outside panels will be subjected to only the ac superimposing field of 0.5 T. The overall averaged magnetic field in the shield is about 4 T. The resistivity[1] of 5000 purity aluminum at 3°K or 4.2°K and 4 T field is about 2 x 10^{-11} Ω-m.[1] These data are based on transverse magnetoresistivity measurements. The longitudinal magnetoresistivity, in general, is slightly smaller than the transverse values for the same purity of aluminum. At 18°K and 4 T field, the penetration depth for the 5000 purity aluminum is 3.1 cm for a period equal to 75 s. At 3 to 4.2°K and 4 T field, the penetration depth is about 1.95 cm. To provide nearly complete shielding, the 18°K shield should have a thickness of 5 cm. The 3 to 4.2°K shield should have a thickness of 4 cm.

AC Losses in Aluminum Shield

The reference cycles for the EF coil, the OH coil and the plasma current are shown in Figure 11. The ac losses in the field shield can be separated into those due to perpendicular fields and those due to parallel fields.

For a change of magnetic flux parallel to the TF coil, we can treat the shield as a long solenoid, with uniform induced flux within. The induced voltage, $\dot{\phi}_{App}$, from a

sinusoidal time variation of the applied flux can be written as

$$\dot{\phi}_{App} = j\omega B_o A \exp(j\omega t) = L\ell\, \dot{I}/\ell + R\ell\, I/\ell.$$

Here the length, ℓ, of the shield has resistance, R, and inductance, L, given approximately by

$$R\ell = \rho p/X,$$

$$L\ell = \gamma\mu_o A,$$

where p and A are, respectively, the cross sectional perimeter and enclosed area of the shield, ρ is the electrical resistivity, $\mu_o = 4\pi \times 10^{-7}$ H/m. The current depth, X, is determined by the smallest of three lengths: the shield thickness t, the skin depth δ, and the so-called mean hydraulic depth A/p. Then, the average power dissipated per unit length is

$$\frac{\bar{P}_{II}}{\ell} = \frac{X\,\omega^2 B_o^2 A^2}{2\,\rho p\,[1 + (\gamma\omega\mu_o\, AX/\rho p)^2]} .$$

In the limit of low conductivity ($R \gg \omega L$), the above equation becomes

$$\bar{P}_{II}/\ell = X\,\omega^2 B_o^2 A^2/2\rho p ,$$

and in the high conductivity limit ($R \ll \omega L$), it becomes

$$\bar{P}_{II}/\ell = \rho p B_o^2/2\, X\,\gamma^2\mu_o^2 . \qquad (1)$$

If the time-varying field is perpendicular to the axis of the shield, the general eddy-current problem does not have an analytic solution. For a circular cross section shield of radius a in the high conductivity limit with $\gamma = 1$, the power is given by

$$P_\perp/\ell = 4\pi a B_o^2 \rho/2\, X\mu_o = \rho p B_o^2/X\mu_o^2 = 2\,(\bar{P}_{II}/\ell) . \qquad (2)$$

From Equations 1 and 2 we can obtain the power loss in the shield of a TF coil in a sinusoidally-varying flux, if the high-conductivity limit applies

$$\bar{P} = (\rho p/X\mu_o^2) \oint (B_{o\perp}^2 + 1/2\, B_{o\parallel}^2)\, d\ell . \qquad (3)$$

If the time variation is not sinusoidal, but given by the Fourier series,

$$B(t) = B_o \sum_{n=0}^{\infty} a_n \cos 2\pi nt/\tau ,$$

with τ the period, and if $X = \delta_n = (2\rho/\mu_o\omega_n)^{1/2} = \sqrt{n}\,\delta_1$, then Equation 3 becomes

$$\bar{P} = (\rho p/\delta_1\mu_o^2) \oint (B_{o\perp}^2 + 1/2\, B_{o\parallel}^2)\, d\ell \sum_{n=1}^{\infty} \sqrt{n}\, a_n^2 . \qquad (4)$$

Since the three poloidal field wave forms are not alike, each individual wave form is expanded into a Fourier cosine series with coefficients evaluated separately. The Fourier series representing the resultant superimposing field is equal to the sum of the three individual Fourier series.

The ac loss distributions,[1] expressed as the power dissipation per meter, are shown in Figure 4. The total ac losses for the 3°K shield are 298.6 W per TF coil, with 147 W as the perpendicular field dissipation and 151.6 W from the parallel field loss. The remaining shields will be refrigerated between 12.5°K and 23.5°K with a mean temperature of 18°K. The shields will be bonded to a stainless steel backing of 1 cm in thickness. The total ac losses of the 18°K shield is 8.531 kW per coil with 3.295 kW from parallel field and 5.236 kW from perpendicular field losses.

DC Field Soaking

About 70% of the superimposing field is the dc field component. The dc field will soak through the aluminum shield in a time

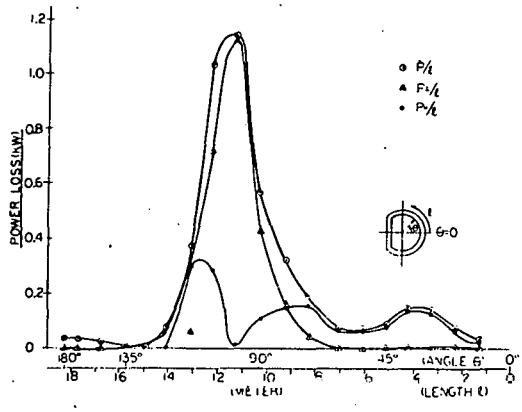

FIGURE 4. AC Losses Distribution Along the TF Coil.

constant of 6 minutes. The 6 minutes soaking time constant is considered rather long compared with the current ramping time of 2 s. Once soak through is complete, the dc field will remain as a static field interacting with the TF coil current producing 70% of the out-of-plane load previously calculated.

Out-of-Plane Load in Shield

The aluminum shield is now subject to the cyclic out-of-plane loads. If the superimposing fields had a time dependence that was a pure sine wave with no dc component, then the out-of-plane load on the shield would be the same as it would be on the TF coil in the absence of the shield. The loads on the shield are now due to the forces exerted by the toroidal field on the eddy currents in the shield. The distribution of the out-of-plane load on the shield is very similar to that in Figure 3(e) (load on TF coil with no shield) but at only 30% of the magnitude. There are, in addition, in-plane forces and twisting moments. Their magnitudes are such that their support appears manageable.

Conductor Design and Coil Structure

The full stability of the conductor will be assured if the conductor has good mechanical stability in a proposed coil structure. Careful investigation on all the forces exerted on the TF coil conductor reveals that there are at least four significant mechanical instabilities in a TF coil. These are as follows: (1) Out-of-Plane Load - Both the local moments and the over-turning moments are quite capable of generating shear stress between turns or between layers; (2) The Centering Force - Conductors, insulators and structural materials in the TF straight segment at the inner leg will experience a large radial inward compression of about 8000 psi. This will likely generate layer-to-layer shear unless each layer is flat and firm enough to support its neighboring layer; (3) Gravitational Load - The fact that the TF conductor in each coil weighs about 208 tons and is standing in a vertical plane could cause a problem in mechanical instability; (4) Other Bending Moments - Bending moments of a pure-tension TF coil may still exist if the coil shape is distorted because of imperfection in coil winding and the deflection of conductor and coil form due to g-load. Bending moments may also be developed if there is an in-plane coil displacement due to the imperfection of coil fabrication and assembly.

Based on the preceding design considerations, it is proposed that a wide sheet conductor, as shown in Figure 5, be used in the TF coils if a field shield is provided.

With two subdivisions in each TF coil and one turn per layer in each subdivision, the conductor stabilizer width will vary from $\sim$ 0.5 m for the innermost layer to 0.3 m for the outermost layer. Reasonable thickness per layer is needed to increase the out-of-plane rigidity and to avoid troubles in handling wide and thin metal sheet. A

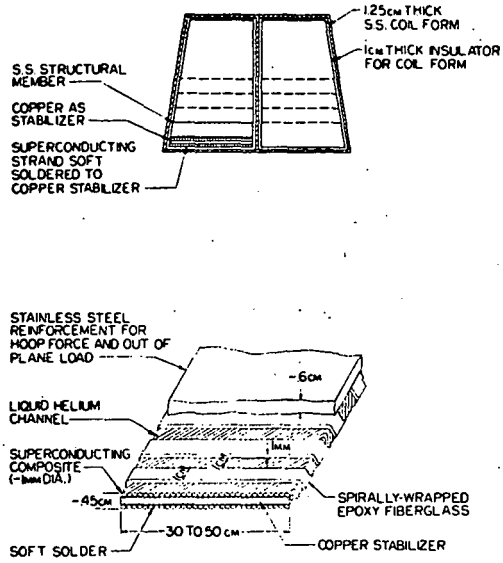

FIGURE 5. Reference Sheet Conductor (60 KA) for TF Coil and its Coil Cross Section (Jelly Roll Winding).

current of 60 kA per turn was tentatively determined; typical dimensions for copper sheet, stainless steel reinforced sheet and the proper superconductor cross section in each field region were chosen. The superconductor cross section was sized using a J-H curve with a temperature 0.5°K above the intended operating temperature. The conductor is graded into nine field grades between 3 T and 10 T. This is because the outermost layer conductor in the outer TF leg will see a field of 3 T rather than zero. Substantial cost saving can be made if conductor is graded in this manner.

The proposed sheet conductor is made of a copper sheet and many superconducting composite wires stranded around it. This stranding is necessary to eliminate the self-field instability that will be significant if the operational current is large. To assure good bonding, the strands are soft-soldered to the copper sheet.

The fiberglass epoxy is spiral wrapped around the sheet conductor covering 50% of the exposed surface. This will provide an exposed surface area of about 50 cm^2 per cm conductor length. The equivalent recovery heat flux per cm^2 is about 0.3 W. The coil form is stainless steel and insulated with a micarta or G-10 sheet of 1 cm thickness. These sheets are grooved to provide vertical liquid helium channels for venting.

A stainless steel sheet of variable thickness is wrapped along the conductor. As far as hoop stress is concerned, the multilayer stainless steel serves as a multishell stainless steel pressure vessel. For the out-of-plane load, the stainless steel sheet increases the rigidity of the coil form tremendously. Since the radius of curvature near a 10 T region is 1.98 m, the overall average hoop stress in stainless steel is 26,000 psi and that in copper stabilizer is 14,500 psi. These stress levels are fairly conservative at 4.2°K temperature.

Summation of Dissipation Loss and the Refrigeration Requirements

Heat dissipation in the TF coil system is summarized in Table 2. A neutron wall load of 0.5 MW/m^2 is used to compute the nuclear heating for both the 8 T and 10 T operation. As to the cryostat loss, the radiation loss between the 18°K field shield and the 3°K helium vessel is negligibly small. The radiation heat load from the 300°K vacuum wall to the 18°K shield is 64.5 W per TF coil or 1032 W for all 16 coils provided that multiple layer superinsulation is used. The heat conduction loss through the support system is small and there is no loss for the intercoil structure. The 60 kA leads will dissipate a total of 120 W.

Therefore, the total loss in the 3°K helium vessel is 6.40 kW for all 16 coils. The total loss in the 18°K normal metal shield is 137.5 kW for all 16 coils. If the TF coil is operated at 8 T, then the coils will be at 4.2°K. The ac loss in the 4.2°K helium vessel will be reduced by a factor of 0.64 relative to the 3°K use. The ac loss in the 18°K aluminum shield will also be reduced by a factor of 0.64. This is because the ac loss mainly is produced by the EF coil and the plasma current. Therefore, at 8 T operation, the total losses in the 18°K normal metal shield are 88 kW for all 16 coils. These losses, as well as the ac losses without field, are tabulated in Table 2.

The Effects of Fabrication Tolerances

The effects of TF coil fabrication tolerances include the imperfection of coil winding, the tolerances of coil forms, the static g-load deflection, the error in the assembly and the possible errors due to thermal contraction. Fabrication tolerance has been studied in five categories as follows (see Figure 6): (1) The TF coil shape may be distorted uniformly above or below the pure-tension shape by 5 cm; (2) The TF winding may be displaced radially or vertically by about 2 cm during assembly or cooldown; (3) The TF coil may be rotated by about 0.5° in the toroidal direction during the winding, cooldown or assembly; (4) The TF coil may be tilted about the

TABLE 2. TF Coil Heat Dissipation Summary

Heat Dissipation Items	With Aluminum Field Shield (Sheet Conductor)				Without Field Shield* (Cable Conductor with Twisting Reversal)			
	10 T (3°K)		8 T (4.2°K)		10 T (3°K)		8 T (4.2°K)	
	Per Coil (W)	16 Coils (kW)	Per Coil (W)	16 Coils (kW)	Per Coil (W)	16 Coils (kW)	Per Coil (W)	16 Coils (kW)
Nuclear Heating	91	1.5	91	1.5	91	1.5	91	1.5
3°K/4.2°K Al. Shield ac Losses	299	4.8	191	3.06	--	--	--	--
18°K Al. Shield ac Losses	8500	136	5500	88	--	--	--	--
Thermal Radiation Load on 18°K Shield	65	1.04	65	1.04	--	--	--	--
Thermal Radiation Load on Helium Vessel From 77°K shield	--	--	--	--	10	0.16	10	0.16
Cryostat Heat Conductor Loss on Helium Vessel	10	0.16	10	0.16	10	0.16	10	0.16
Current Leads Loss	--	0.12	--	0.12	--	--	--	--
Parallel Field Conductor Loss**	--	--	--	--	296	4.74	217	3.5
Perpendicular Field Conductor Loss**	--	--	--	--	130	2.08	84	1.34
AC Loss in Coil Form	--	--	--	--	631	10.1	404	6.46
Summation of Loss at 3°K/4°K	400	6.5	300	4.8	1168	18.7	816	13.3
Summation of Loss at 18°K	8565	137	5565	89	--	--	--	--
Refrigeration Power (Compressor input power)	14.3 MW		8.9 MW		9.3 MW*		4.7 MW*	

*AC Loss in Conductor reinforcing structural material is not included.

**Because of complex nature of $\dot{B}$ in the plasma ramping and EF Coil ramping, 2 s rise time is used in this calculation. The conductor is a hypothetical conductor used in the ac losses calculation.

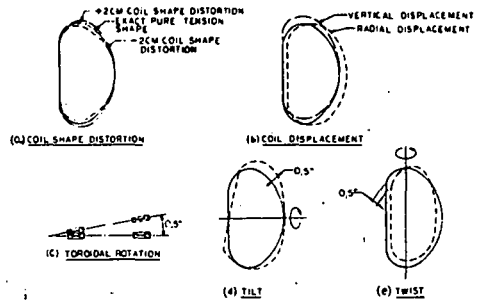

FIGURE 6. Five Possible Fabrication Tolerances.

horizontal axis by 0.5°; (5) The TF coil may be twisted about the vertical axis by 0.5°. It is clear that the effects of the first two fabrication errors will alter the transverse force pattern and induce bending moments in the otherwise pure-tension TF coil. To simulate the error in category (1), the pure-tension coil evolution was intentionally interrupted so that the coil shape is approximately 5 cm from the final pure-tension shape. The hoop stress analysis is shown in Figure 2. The coil displacement is done for one coil only. The result of these errors induce nonuniform hoop tension as shown in Figure 7.

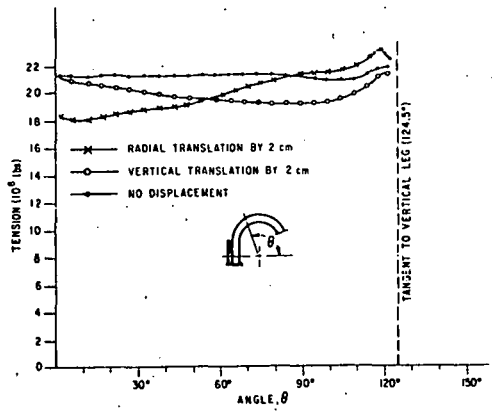

FIGURE 7. Tension Distortion of Coil Displacement and Coil Shape Deflection.

If the fabrication error falls into the third, fourth and fifth categories, the dominant effect is the unbalanced intercoil force in the toroidal direction as shown in Figure 8. It is seen that tilting and twisting by 0.5° will generate an additional attractive force on the order of 1 x 10^5 kg/m while a rotation of 0.5° produces an intercoil force of 4 x 10^5 kg/m.

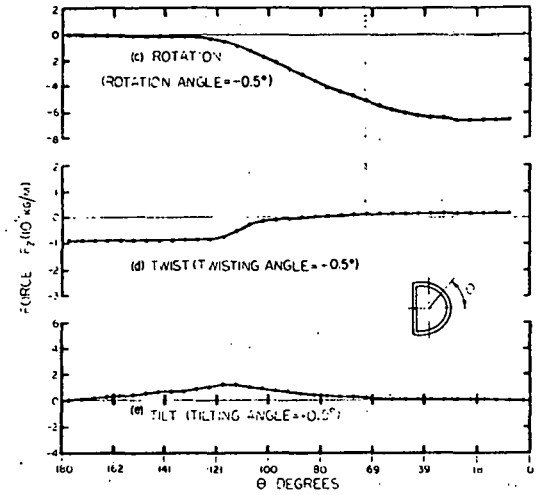

FIGURE 8. Out-of-Plane Load Due to Errors of Rotation, Twist and Tilt.

Coil Protection and Magnet Safety Analysis

Energy Release

The stored energy is 30 GJ in 16 coils at 10 T. The operational current is 60 kA and the total inductance is 16.7 H. This operational current is too large to allow one pair of leads out from each TF coil. Instead, only two leads, one from the number 1 TF coil and the other from the number 16 TF coil, are allowed to feed through the cryostat. All other connections between adjacent coils are done through intercoil tubing connecting the two adjacent cryostats. Therefore, for this design, the energy dumping circuit is shown in Figure 9. The dump resistor must always be connected to

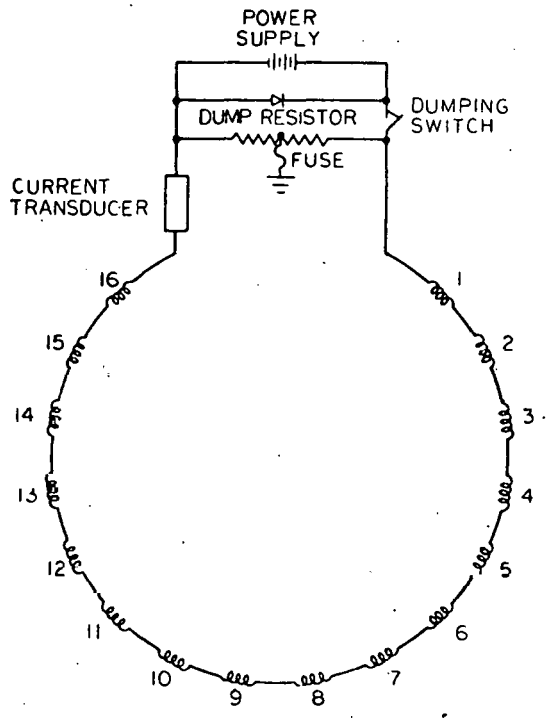

FIGURE 9. Dumping Circuit

the coil. The coil system energy will be discharged through the dump resistor. The terminal voltage of the magnet will be no greater than the voltage across the dump resistor. The discharge voltage will be 2000 V. The resistance of the dump resistor will be 0.033 Ω and the coil current will decay in a time constant of 506 s, or 8-1/2 minutes.

As shown in Figure 9, a fuse with a small current capacity is connected in the grounding loop to the discharge resistor to ensure that no large grounding current shall flow if any point in the coil winding should accidently be grounded. The discharge resistor must be tested at incrementally increasing current levels during initial system checkout. Multiple parallel paths should be provided in case interruption may occur in the discharge resistor.

Arcing

Arcing is always a serious threat to a large superconducting magnet, a large safety margin must be used in designing the coil insulation and the current leads insulation. For example, the 4000 V coil insulation must be provided in order to allow a 2000 V operating condition. In fact, the entire system should be tested with a high voltage and extreme low current output power supply to test the insulation strength of the coil with respect to ground under the liquid helium environment.

Coil Forces and Structure Stress

The most critical hazards are those in which the design forces in the conductor and forces in supporting structures are exceeded. Therefore, strain gauges are used to monitor these situations.

Cryostat Protection

Each TF coil cryostat shall be equipped with pressure rupture discs to guard against pressure buildup in the helium vessel.. The pressure rupture disc can also protect the magnet coil in the event that large resistive heating occurs with rapid pressure rise. Then, at a preset pressure, the rupture disc breaks and the bulk of the liquid helium will be rapidly transferred from the dewar to an emergency dump tank. This will remove liquid helium quickly and the whole coil will become normal and coil energy will be uniformly dissipated throughout the winding.

Short

Shorting from turn-to-turn, from layer-to-layer or from coil-to-ground is a very serious matter. The short will act as a discharge resistor. Should the coil energy be discharged, large amounts of energy deposition will occur at the short, and the conductor around the short will be melted into a copper block. Techniques for testing

the short must be developed. Potential taps for checking shorts after the coil is wound must be incorporated.

Current Leads Protection

If the discharge time constant is 8-1/2 minutes, then the current leads must be designed to allow adiabatic heating in that time period without raising the lead temperature dangerously high. The current leads are cooled by counter-flow helium gas. In-line gas flowmeters must be installed to monitor the amount of counter-flow helium gas. Alternatively, voltage taps across the leads are provided to monitor the current lead temperature. Temperature sensors may also be attached to the connector of the current leads.

Current leads are a weak link in magnet systems. The magnetic field and forces on the lead must be carefully evaluated. The leads must be firmly supported and must have sufficient insulation.

Connectors and Conductor Joints

Connectors and conductor joints are another weak link in the magnet system. The resistance of each joint and each connector must be carefully tested and voltage taps must be provided across the joints and connectors to monitor possible failures. All forces exerted on the connectors and joints must be carefully computed. The mechanical strength of joints and connectors must be thoroughly tested. In some instances, a redundant path should be provided.

Bending Moments

When two neighboring coils carry different currents, the unbalanced intercoil force is large. Furthermore, pure-tension TF coils will remain in pure tension only if all coils carry the same currents. If two coils carry different currents, large bending moments and peak stresses will occur in the coil and subsequent structure failure may occur. Therefore, it is exceedingly important to make sure the currents are the same. This probably can be guaranteed only through series operation under all circumstances.

Eddy Current Interaction

If the magnet is discharged in 8-1/2 minutes, large eddy currents will be developed in each vacuum vessel and the field shield. The interaction between the eddy currents and the decaying field may generate a large and complex force and ruin the field shield or radiation shields or structural members.

SUPERCONDUCTING POLOIDAL COIL SYSTEMS

Poloidal Field Coil Characteristics

The poloidal field coils consist of the OH coils and the EF coils. The OH coils and the EF coils are superconducting and are located outside the TF coils, as shown in Figure 10.

Although the OH coils serve as the transformer primary for producing the plasma current and the EF coils provide equilibrium for the plasma, both coil systems have nearly identical problems, e.g. large stored energy, high operational current, rapid charging and discharging, and ring coil configuration. For this reason, the conceptual design of the eight pairs of EF coils (coil numbers 1 to 8) and six pairs of OH coils (coil numbers 9 to 14) were carried out together.

The design requirements for the OH and EF coil systems were specified as a result of a detailed trade-off study. Burn cycle dynamic simulations of the plasma, the coupled OH and EF systems, and the plasma heating systems were performed. Free-boundary plasma MHD equilibrium calculations[2] were utilized in the design of an equilibrium field that would produce the

TABLE 3. OH Coil/EF Coil Magnet Characteristics

	OH Coil	EF Coil
Superconductor/Stabilizer	Nb-Ti/Cu	
Coil design	Single layer	
Conductor design	Fully-transposed cable	
Stability	Cryostatic	
Cooling	Pool boiling	
Operating temperature (°K)	4.2	
Average current density (A/cm^2)	2640	2946
Magnetic field (T)		
in flux core	~ 5	
at plasma center		~ 0.46
Ampere-turns (MAT)	67	± 18.6
Total conductor length (MA meters)	847	996
Maximum dB/dt in conductor (T/s)	6.7	~ 1
Stored energy in OH/EF/plasma field (MJ)	2262	
Maximum operational current (kA)	80	80
Number of turns	837	464
Self inductance (H)	0.48	0.52
Mutual couplings	$K_{OHEF} = 0.015$	
Power supply voltage (kV)	48	21
Volt-seconds to plasma (V-s)	85	50
Coupling coefficient to plasma ring	$K_{OHP} = -0.2422$	$K_{EFP} = -0.2566$

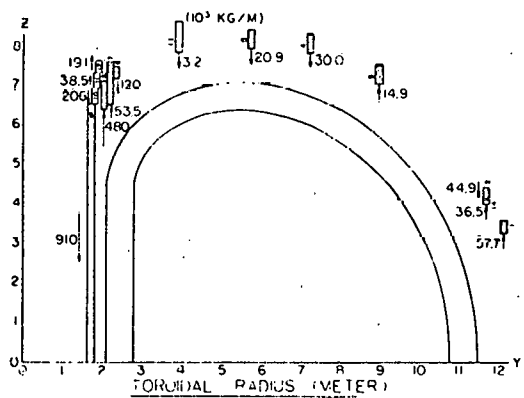

FIGURE 10. Vertical Force per Length During Burn Phase.

circular plasma. Characteristics of the OH and EF coils are given in Table 3.

The Superconducting OH/EF Coil Design

The poloidal coil design calculations were based on a design-basis burn cycle as shown in Figure 11.

The total volt-second requirement for the reference design is 135. The OH coils are capable of reversing from -5 T to +5 T, supply 85 V-s, with an OH flux core radius of 1.7 m. The EF coil will supply the remaining 50 V-s.

The OH coils are located outside the TF coil system so that the winding can be arranged to minimize the ac superimposing

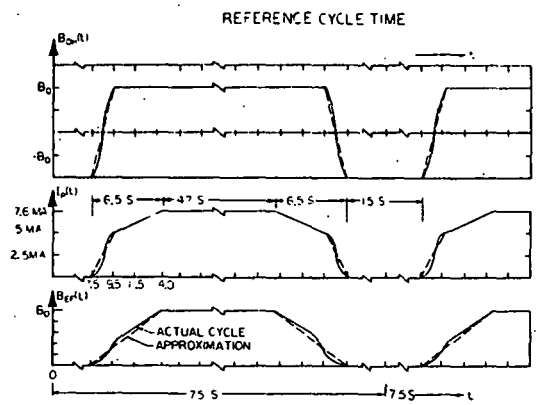

FIGURE 11. Reference Cycles for OH Coils, EF Coils and Plasma.

field on the TF coil. Since the OH coil is at full negative value before the onset of plasma startup, the OH coil windings must also be distributed so that the field produced by the OH coils at the plasma are less than 10 G or so. This requirement must be fulfilled in order to guarantee a stable startup. With these considerations in mind, the OH coils are arranged as shown in Figure 10. The winding dimensions are shown in Table 4, where R_1, R_2, Z_1 and Z_2 represent the inner radius, the outer radius, the initial axial coordinates and the final axial coordinates, respectively.

If the EF coils were placed inside the TF coils, there would be tremendous difficulties in coil assembly, disassembly, support, repair and maintenance, as well as in the assembly, disassembly and maintenance of the blanket and shield and the first wall. To avoid these problems, the EF coils are located outside the TF coils.

The OH coils would induce large voltages in the EF coils, if the EF coils were not decoupled from the OH coils. The decoupling ampere-turns should be positioned so that they produce small anti-vertical fields and small superimposing fields on the TF coils.

Axial Forces, Hopp Stress and Coil Interaction

In the EPR poloidal coil system, since all of the fourteen poloidal coils and the plasma ring contribute to the magnet field at any poloidal coil winding, the axial force and pressure of each coil depends on

TABLE 4. Poloidal Coil Winding Configurations

Coil Number	Z_1 (m)	Z_2 (m)	R_1 (m)	R_2 (m)	Coil Pair NI (MAT)	Coil Pair Cond. Lgth. (40 kA-r)
1	3.25	3.584	12.0	12.15	2.95	5599
2	4.15	4.417	11.55	11.70	2.36	4309
3	7.0	7.50	8.85	9.0	4.42	6195
4	7.8	8.30	7.10	7.25	4.42	4980
5	7.90	8.40	5.60	5.75	4.42	3939
6	7.16	7.44	2.25	2.40	- 2.48	904
7	6.48	7.571	2.10	2.25	- 9.642	3294
8	6.35	7.081	1.95	2.10	- 6.46	2055
9	0	6.5	1.62	1.77	51.48	13707
10	6.50	5.9	1.70	1.85	3.17	883
11	6.90	7.3	1.75	1.90	3.17	908
12	7.30	7.6	1.80	1.95	2.38	700
13	7.80	8.6	3.80	3.95	6.34	3857
14	4.03	4.1	11.55	11.70	0.55	1012

excitation of all coils. Therefore, it is difficult to predict either the magnitude or the direction of the vertical forces. It is entirely possible that during complete cycle the direction of vertical force at any coil reverses and that the magnitude of the vertical force changes rapidly in disproportion to self-excitation of that coil. Figure 10 shows the vertical force per meter coil length during the burn cycle with 7.58 MA plasma current, 5 T central field in OH coils and full excitation in EF coils. Note that some coils are subjected to repulsive forces while other coils are subjected to attractive forces. Note that some adjacent ring coils are subjected to vertical forces with opposite direction.

To obtain full information on vertical forces, the vertical forces on each coil were computed at different times during the entire reference cycle. The results are shown in Figure 12. Also investigated are the vertical forces on each coil when the plasma current suddenly quenches, a highly probable case for an EPR. It is interesting to note that, for all cases investigated, the vertical forces for coil numbers 2, 3, 4, 5, 6, 7, 11 and 13 will reverse their directions and coil supports for these coils must provide support in both directions.

The vertical force on the long solenoid is a body force and little structural support is needed. The vertical forces on coil numbers 6, 7, 8, 10, 11 and 12 will be transferred to the TF coil support cylinder with restraining rings for repulsive forces. Fortunately the remaining poloidal coils (namely, coil numbers 1, 2, 3, 4, 5, 13 and 14) have rather weak forces (no greater than 83 x 10^3 kg/m).

Although axial compressive stress for an ordinary solenoid is generally small in comparison with hoop stress, the axial pressure on the poloidal coils may be quite high because these axial forces result from many coil interactions. Computations of axial compressive pressure distributions for four typical poloidal coils are shown in Figure 13. It is seen that most poloidal coils have small compressive pressures (less than $\sim$ 100 kG/cm^2 or 1420 psi) with the exception of coil numbers 7, 8 and 9. The maximum compressive stress in coil numbers 7, 8 and 9 are 240 kg/cm^2, 301 kg/cm^2 and 592 kg/cm^2, respectively. These do not present mechanical problems.

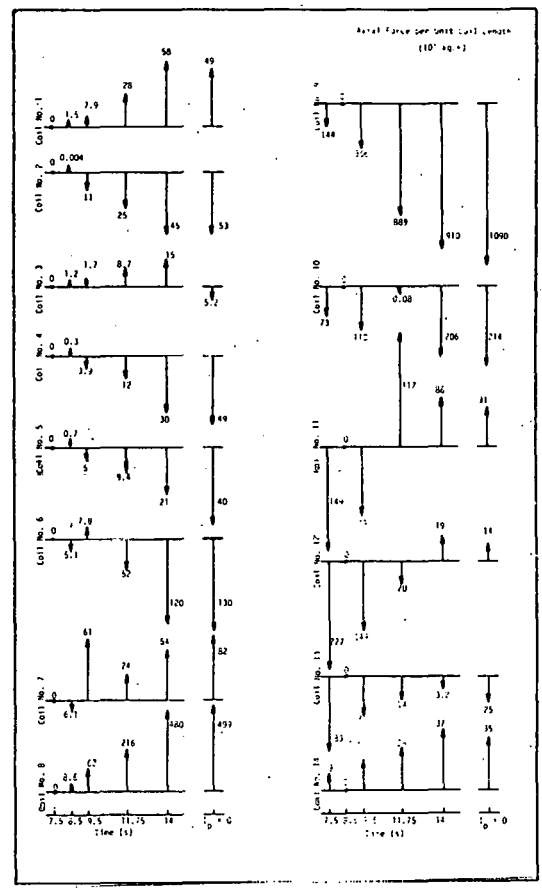

FIGURE 12. Axial Force per Unit Coil Length (10^3 kg/m).

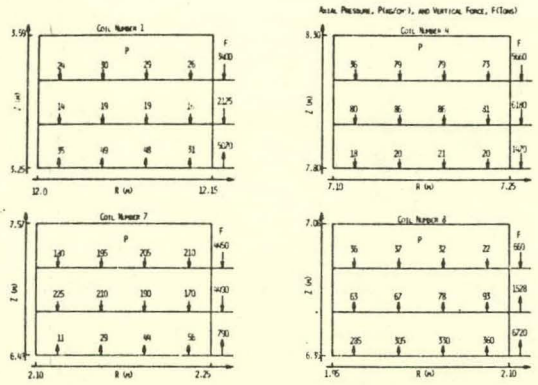

FIGURE 13. Axial Pressure, P (kg/cm^2), and Vertical Force, F (tons).

Computation of hoop stresses in a multilayer solenoid is a complicated problem because the hoop forces on any given turn will depend not only on the jRB_Z of that turn but also on the interaction body forces resulting from the other turns pushing on it. The exact solution is further complicated by the inhomogenous coil structure. Since the proposed poloidal coils in the EPR will have one layer to avoid the high voltage insulation problem, the hoop stress in any given turn is independent of all other turns. The average hoop stress is given by

$$\bar{\tau}_r = j_{avg} \overline{R}\, \overline{B}_Z,$$

where $\overline{R}$ is the mean radius of the turn and $\overline{B}_Z$ is the axial field component averaged over the turn cross section.

The averaged hoop pressure or magnetic pressure, assuming no body force interaction from neighboring turns among successive layers, can easily be shown to be

$$\bar{\tau} = j_{avg} t\, \overline{B}_Z,$$

where t is the radial thickness of the turn.

The computed $\bar{\tau}_t$ and $\bar{\tau}_r$ for the poloidal coils are tabulated in Table 5. It is interesting to see that coil numbers 6, 7, 10, 11 and 12 have hoop compression rather than hoop tension. Also note that coil numbers 5, 6, 8, 13 and 14 have high-averaged hoop stress and must have a substantial amount of reinforcement materials in the winding. The radial magnetic pressures for all coils are not high and they present no problems at all.

Conductor Design and Coil Structure

The operational current for both the OH coils and EF coils is 80 kA, supplied by two parallel 40 kA cables with fully transposed strands. The OH coils will have 837 turns in each parallel path. The OH coils will be cycled by a homopolar generator with peak voltage of 48 kV across the OH coil terminals if the OH coils are charged from -5 T to +5 T in 2 s. The EF coils will have 464 turns in each parallel path. The charging voltage will be around 21 kV across the EF coil terminals. Hence, turn-to-turn voltage will be about 60 V for the OH coil and about 50 V for the EF coil. The breakdown electric field in a helium gas environment is about 200 V/mm. Therefore, minimum separation between two adjacent turns in the same layer is about 0.3 mm for the OH coils and 0.25 mm for the EF coils.

It is clear that multilayer coils will require large gaps between layers. This presents an awkward problem for coil design. It is especially true for the long coils such as the long solenoid of the OH coils. Although good dielectric materials such as G-10 fiberglass may be used to fill the gaps between layers, the magnet designer will still face problems because it is very likely that pinholes or cracks may exist in these materials when the magnet is energized. Therefore, the proposed OH coils and EF coils will be wound with a single layer conductor. The width of the

TABLE 5. Hoop Stress and Radial Pressure of Poloidal Coils During Burn Phase

Coil Number	j (A/cm^2)	t (m)	$\bar{R}$ (m)	$\bar{B}_z$ (T)	$\bar{\sigma}_t$ (kpsi)	$\bar{\sigma}_r$ (kpsi)
1	2946	0.15	12.07	0.012	0.62	0.007
2	2946	0.15	11.63	0.29	14.3	0.19
3	2946	0.15	8.93	0.13	4.9	0.08
4	2946	0.15	7.18	0.39	12.0	0.25
5	2946	0.15	5.68	0.83	19.8	0.53
6	-2946	0.15	2.33	2.32	-22.8	-1.48
7	-2946	0.15	2.18	0.12	- 1.13	-0.08
8	-2946	0.15	2.03	-2.83	24.1	1.81
9	2640	0.15	1.70	1.41	9.1	0.8
10	2640	0.15	1.78	-2.11	-14.2	-1.2
11	2640	0.15	1.83	-1.20	- 8.2	-0.68
12	2640	0.15	1.88	-1.24	- 8.8	-0.71
13	2640	0.15	3.88	1.38	20.3	0.79
14	2640	0.15	11.63	0.37	16.7	0.21

conductor is 15 cm. Based on the information of axial compressive stress, this width will be adequate.

The EF coils and OH coils will be cooled by pool boiling at 4.2°K and 1 atm pressure. Pool boiling is simple, inexpensive, reliable and easy to control. Above all, since a rather small heat transfer flux is adequate to remove the conductor ac losses, the heat transfer flux ceases to be an important factor in determining the coil stability. The coil stability will depend on the conductor and the extent of coil disturbances. However, it is important to recognize that pool boiling will work for an ac magnet only if the helium bubbles, which are generated at a constant rate, can be properly vented to avoid bubble accumulation within the winding. This requirement further justifies the decision for a single-layer coil.

The 40 kA cable can be achieved by cabling a basic strand of 0.3 mm diameter as shown in Figure 14. In the basic strand

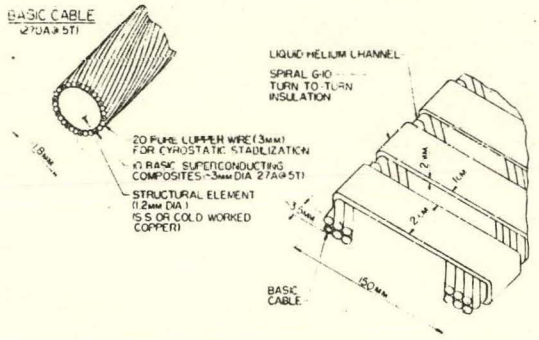

FIGURE 14. 40 kA Cable for Poloidal Coils

component, the copper to NbTi superconductor ratio is 2 to 1, with the NbTi cross-sectional area of 2.3×10^4 cm^2, or 1171 filaments with 5 m filament diameter. For a poloidal coil with a 5 T peak field, the conservative value of NbTi critical current density is about 117 kA/cm^2. Therefore, the basic strand shall carry 27 A. As shown in Figure 14, to assure current sharing with a higher Cu/NbTi ratio, 20

pure copper wires of 0.3 mm diameter were transposed along the 10 composite strands. High resistivity soft solder is used to solder these wires together around a central structural-reinforcing element. This raises the overall Cu/NbTi ratio of the basic cable to 11 to 1. This design offers good coil stability with low ac losses in mind. The composite with a single-component stabilizer rather than a cupronickel and Cu two-component stabilizer was chosen because of the rather poor conductor stability if cupronickel is incorporated. Therefore, as long as the ac loss is not too great, a conductor with a single-component stabilizer will be preferred. The basic cable shall carry 270 A at 5 T.

The 40 kA cable was finally achieved by transposing 150 basic cables into a height of 2 basic cables ($\sim$ 4 mm) by a width of 75 basic cables ($\sim$ 150 mm). The basic cable must be insulated with nomex paper before transposition. Otherwise, very large coupling eddy currents and ac losses will arise in the wide cable. Since the stability of the 40 kA cable is built into the stability of the basic cable, the fact that the basic cable is insulated probably will have no great effect on the stability of the 40 kA cable.

Finally, the 150 basic cables are banded together with spiral wrapping wetted fiberglass of 2 mm in thickness.

As shown in Figure 15, the poloidal coil is wound with a single layer wide cable of 40 kA.

The spiral wrapping fiberglass of 2 mm inch thickness will provide a turn-to-turn separation of at least 4 mm for adequate insulator. The width of the fiberglass is 2 cm and the wrapping pitch is 3 cm so that the liquid helium channel of 1 cm wide by

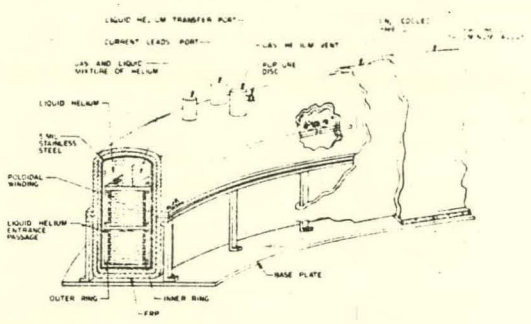

FIGURE 15. Poloidal Coil Structure and its Cryostat Configuration.

0.2 cm deep by 15 cm long will be provided on both faces of the cable. The bottom supporting plate is machined to have an inclined surface in the radial direction so that gas venting will move radially outward. An 0.1 mm nomex paper is used between turns to prevent the bubbles from rising through the turns. These measures should provide good bubble venting, separate the gas-liquid flow and allow each turn to see only the bubbles generated by itself.

The wrapped fiberglass is expected to be strong enough to transfer the hoop tension to the external rings, which are made to assist the hoop tension of the cable. The inner rings are made to overcome the hoop compression as well as to serve as the bobbin for winding. Many 2 mm wide slits are cut in these rings to allow gas venting and liquid circulation.

The axial compressive or repulsive forces of every 10 to 15 turns are supported by a 2-cm thick G-10 or micarta plate. This arrangement shall reduce the accumulation of axial compressive or repulsive pressures exerting onto the cable, which otherwise might short out the basic cables and deteriorate the coil stability.

Poloidal Coil Cryostat Design

Figure 15 illustrates a cryostat configuration for a poloidal coil. To reduce eddy current losses to a minimum, an essentially non-conductive inner shell is required. The illustrated design uses glass-reinforced epoxy, with an 0.013 cm layer of stainless steel for a helium permeation barrier. The construction technique consists of fabricating the shell by filament winding or braiding around the coil. The stainless steel barrier is installed after enough layers are built up to support it. Then fabrication continues until the required thickness is obtained.

The cryostat is insulated with high vacuum, plus a liquid-nitrogen-cooled radiation shield of laminated construction to minimize eddy current heating in the nitrogen shield. Multilayer insulation is used between the outer vacuum jacket and the nitrogen shield. The multilayer insulation is installed with the reflective coating in segments to avoid formation of eddy currents in the insulation layers.

The individual coils are supported internally as illustrated in Figure 15 with low thermal conductivity members. These supports are designed to take loads in both directions. The high loads per unit length of coil are distributed between supports by a stiff cryostat inner shell.

Equilibrium Field Flux Penetration on the Blanket and Shield

The magnetic field from the EF coils must penetrate the blanket and shield to act on the plasma. The blanket and shield contain much electrically conductive material, particularly stainelss steel. Eddy currents in this material would distort the EF and delay its penetration if the blanket and shield were not sufficiently segmented. The blanket and shield design of 16 segments, each made of 43 blocks, imposes very little field distortion and delay of penetration.

Table 6 summarizes the results for calculations of the field induced at the center of the plasma due to the eddy currents in the blanket and shield. Results are expressed as the ratio of the induced field to the applied field and as a phase and time delay.[1]

REFERENCES

1. W. M. Stacey, Jr., et al., "Tokamak Experimental Power Reactor Conceptual Design," ANL/CTR-76-3, Argonne National Laboratory (1976) Chapter IV.
2. R. W. Boom, Private Communication.
3. W. M. Stacey, Jr., et al., "Tokamak Experimental Power Reactor Conceptual Design," ANL/CTR-76-3, Argonne National Laboratory (1976) Chapter III.

TABLE 6. Induced Field in the Plasma Region Due to Eddy Currents in the Segmented or Subdivided Blanket and Shield

Toroidal Segments	Blocks per Segment	Maximum Induced Field B_{in}/B_o	Phase Delay ϕ	Time Delay ϕ
1	1	167%[a]	-	-
8	1	42%[a]	-	-
16	1	9.3%	10.5°	117 ms
32	1	2.3%	2.6°	29 ms
48	1	1.0%	1.1°	12 ms
64	1	0.6%	0.7°	8 ms
16[b]	36	1.5%	1.8°	20 ms

(a) Assumptions of model not valid for these cases.

(b) The 43 blocks per segment in the reference design are represented by 36 blocks per segment in the computational model.

TOKAMAK EXPERIMENTAL POWER REACTOR PRIMARY ENERGY CONVERSION SYSTEM *

H. C. Stevens, M. A. Abdou, R. F. Mattas, V. A. Maroni
J. S. Patten, D. L. Smith, and C. K. Youngdahl

CTR Program
Argonne National Laboratory
Argonne, Illinois 60439

A primary energy conversion system designed for the ANL Tokamak Experimental Power Reactor consisting of, the first wall assembly, the blanket region, the magnet shield and the penetrations for plasma access are herein described.

INTRODUCTION

A scoping study[1] and a conceptual design[2] of a tokamak experimental power reactor (TEPR) have been completed. The design objectives of the TEPR are to operate for 10 years at or near electrical power breakeven conditions with a duty factor $\geq$ 50% and to demonstrate the feasibility of tokamak fusion power reactor technologies. A primary energy conversion system (PECS), capable of meeting these objectives, is herein described. The PECS consists of: (Figure 1 and 2), the first wall assembly; the blanket region (a 28-cm zone immediately backing the first wall); the primary coolant; the magnet shield; and the penetrations which provide access for the vacuum system, neutral beam injection, diagnostics, and experimental facilities.

Major efforts have been undertaken at ANL[1,2] and elsewhere[3,4] to define the objectives of a Tokamak Experimental Power Reactor (TEPR). The ultimate goal of these studies has been to establish the scientific and engineering basis for a detailed reactor design. This paper will concentrate on the TEPR primary energy conversion system (PECS) as developed in the ANL study. The PECS is considered to include all components that lie between the plasma and the toroidal field coils, e.g., the first wall, blanket, magnet shield, coolant, penetrations for vacuum interfacing, neutral injection beam lines, diagnostics, and maintenance access. Previous reports[1,5] have described the underlying philosophy used in developing design criteria for a PECS that would meet the needs of a TEPR. Reference 2 contains a detailed description for the PECS design that has evolved in the ANL/TEPR studies. This paper contains a summary of the details relating to both the PECS first wall and blanket/shield designs. Figures 1 and 2 show, respectively, the vertical section and plan view of the ANL/TEPR and give some perspective as to the location and configuration of PECS components. Features of many of the systems interfacing with the PECS are described in other papers presented at this meeting.[6-10]

* Work supported by the U.S. Energy Research and Development Administration.

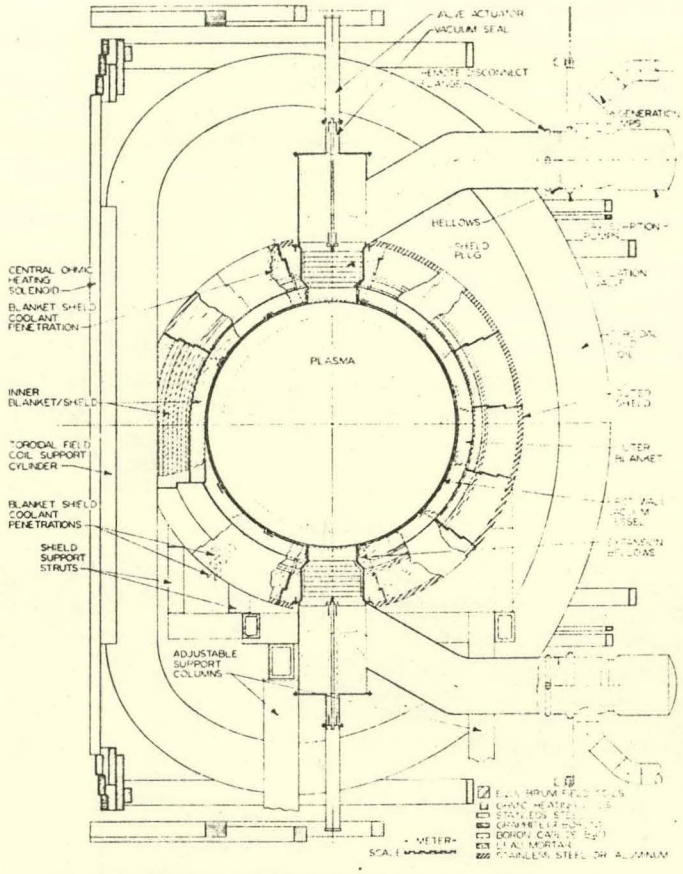

FIGURE 1. Vertical Section of EPR

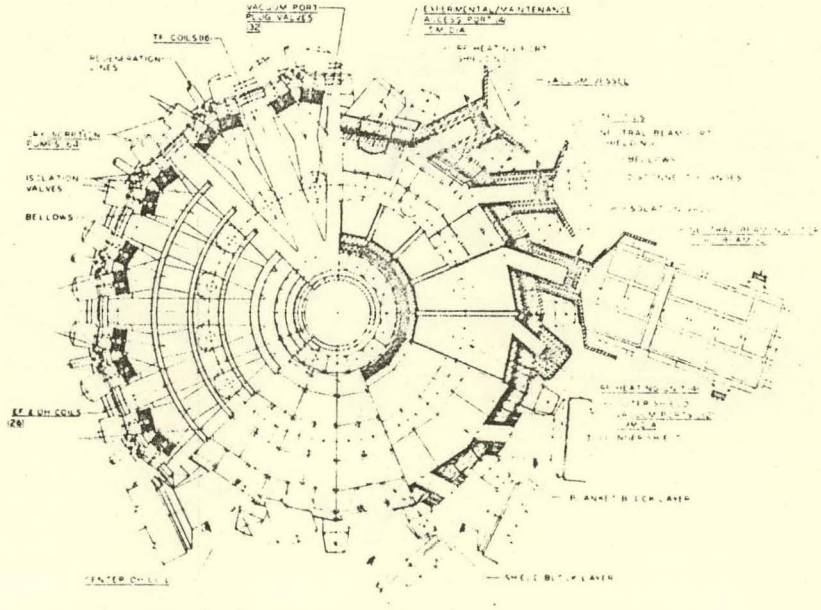

FIGURE 2. EPR Plan View

FIRST WALL

The first wall system (see Fig. 3) consists of a vacuum wall and detachable coolant panels. The free-standing vacuum vessel is constructed from 16 cylindrical segments of 2-cm thick stainless steel plate and is reinforced with an external ring and spar framework. Locations of the two circumferential support rings and ten longitudinal spars on each segment are shown in Fig. 3. The 16 segments are joined by formed rings that are welded to the ends of each segment. A chemically bonded Cr_2O_3 coating is applied to the joining surfaces in two of these rings to form a current breaker in the vacuum wall. The vacuum vessel wall is cooled by a separated pressurized water loop utilizing an integral nondetachable panel wall system as illustrated in Figure 3.

The surface of the detachable coolant panels facing the plasma is coated with 100-200 microns of beryllium to control impurity contamination of the plasma by stainless steel. The substantial porosity (10-15%) and fine microstructure obtainable with the plasma spray-coating process facilitates gas re-emission, particularly helium, and minimizes blistering erosion.

Water is supplied to these coolant panels by manifolds located in the connecting rings that join the first-wall segments. The toroidal vacuum wall is supported by a three-point per segment, roller/slide pad-type support from the blanket to the lower rings and spars. The three-point support minimizes the size of the reinforcing ring and the roller/slide support minimizes thermal stresses by allowing for

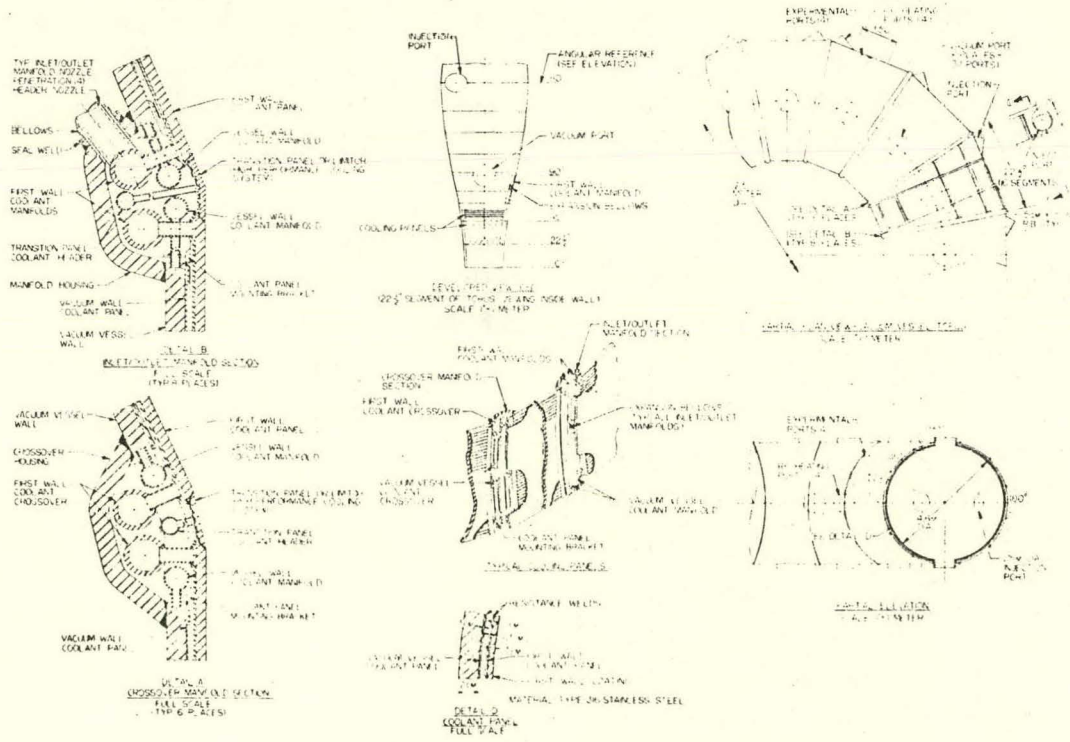

FIGURE 3. First Wall Vacuum Vessel Assembly

expansion of the vessel. The first wall design parameters are summarized in Table 1.

Extensive thermal-hydraulic, mechanical, materials response and radiation damage analyses have been performed to evaluate the first wall performance and to determine the design limits. Results are summarized in Table 2. The stainless steel vacuum wall should maintain its structural integrity for the 10 year design life under the nominal operating conditions, viz., integrated wall loading of 2.5 MW-yr/m^2, maximum annual neutron fluence of 6 x 10^{25} n/m^2 (2.8 dpa/year, 54 appm/year helium and 133 appm/year hydrogen) and maximum wall temperature of $\leq 500^{o}C$. For these conditions the predicted radiation swelling of < 4% is tolerable. The limiting criterion is loss of ductility caused by displacement damage and helium generation. For temperatures below $500^{o}C$, the residual uniform elongation, which is estimated to be $\geq$ 1% at the end of the 10 year life, is considered to be acceptable. The lifetime of the low-Z coating is limited by erosion caused primarily by D-T physical sputtering. A design life of 5 years for a 100 to 200-μm thick beryllium coating appears feasible. Only limited data exist with which to estimate the lifetime of the ceramic current breaker; however, bulk radiation effects will likely be the limiting criteria.

In addition to the extensive radiation damage, the coolant panel will be subjected to severe thermal cycling produced by heat deposition on the surface during the plasma burn. Temperature variations in the hottest coolant panel during operation are shown in Figure 4. The spike is caused by the radiation emitted when argon is injected to terminate the burn. The strain range for the burn cycle depends on the difference between the maximum and minimum values of ΔT during the cycle, and the strain range for the plant warm-up/cool-down operating cycle is a function of the average ΔT during the burn cycle. Assuming that the duration of the operating cycle is long enough that stress relief occurs, the strain range for the coolant panels with sliding supports is 0.085% for the burn cycle and 0.14% for the warm-up/cool-down operating cycle. These values correspond to fatigue design lifetimes for the coolant panels of 5 x 10^{6} burn cycles and 1 x 10^{5} operating cycles. Thus, thermal fatigue will limit the life of the coolant panel to 5 years, which corresponds to $\sim 10^{6}$ burn cycles, for the current design parameters.

Although the current first-wall system design is based to a large extent on available materials and existing technology, it appears that adequate mechanical integrity of the system can be maintained for suitable reactor lifetimes under the postulated EPR conditions.

BLANKET/SHIELD SYSTEM

The blanket/shield system consists of the blanket, the inner bulk shield, the outer bulk shield and the penetration shields. In order to insure penetration of the equilibrium field into the plasma region without intolerable distortion or phase delay, the blanket and bulk shield are constructed of 688 electrically insulated blocks, as illustrated in Fig. 5.

The blanket is made up of 0.20-m thick stainless steel blocks, as shown in Fig. 6. Each of the 16 segments of the vacuum chamber is covered by 17 blanket blocks. The blocks are cooled with pressurized water flowing in a network of 1-cm diameter drilled channels, with each block having an independent cooling system.

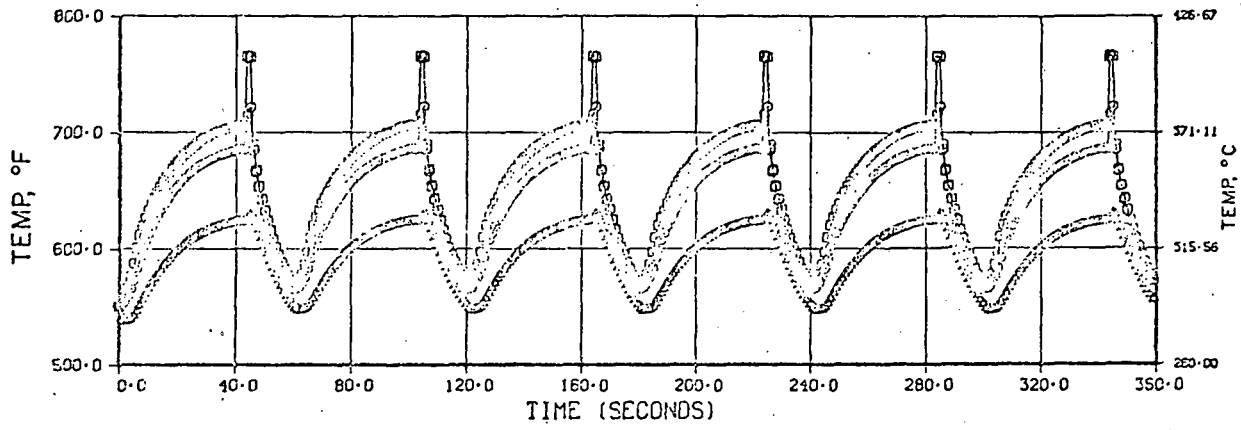

FIGURE 4. Transient Temperature Histories (0.5 MW/m^2) Locations on the Coolant Exit Plane at the Surface of the Beryllium Coating (upper curve), at the Surface of the Stainless Steel in Contact with the Coating (middle curve), and at the Stainless Steel Surface in Contact with the Coolant (lower curve).

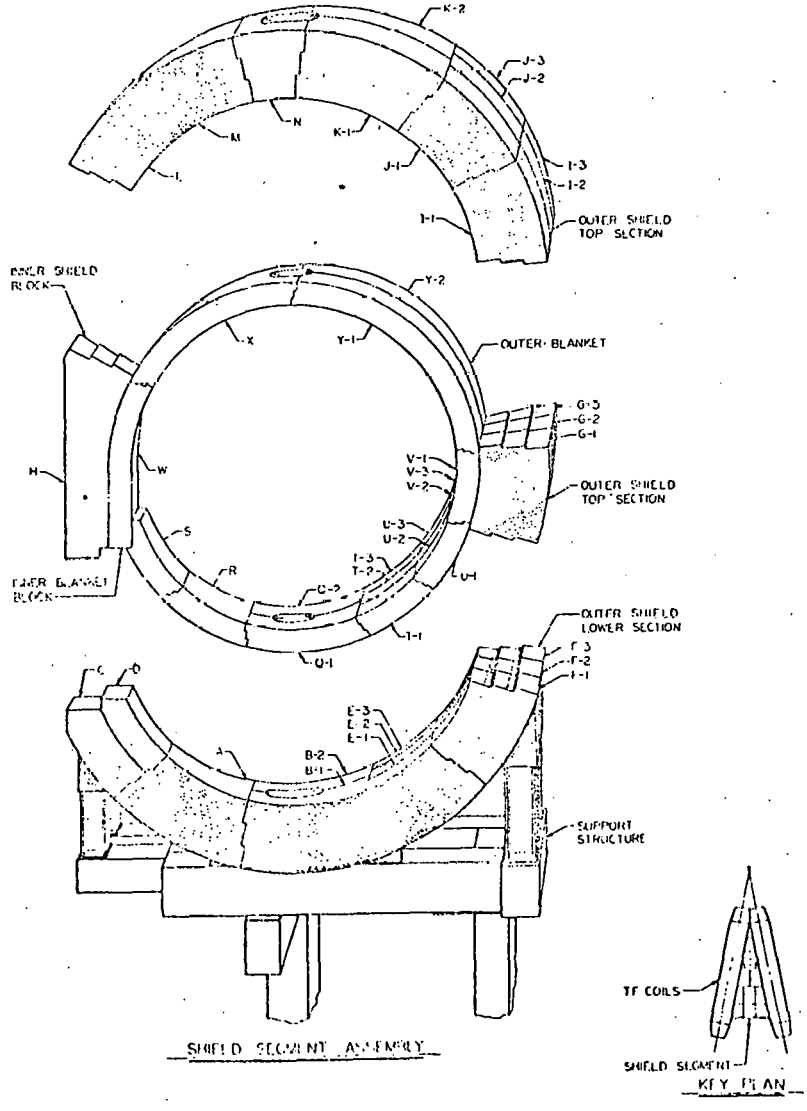

FIGURE 5. Blanket/Shield Arrangement Circular Option.

TABLE 1. First-Wall Design Parameters

Design Description

- Free-standing, stainless steel vacuum wall with rib and spar reinforcing.
- Detachable, water-cooled stainless steel panels to shield vacuum wall from plasma.
- Low-Z coating on plasma-exposed face of coolant panel for high-Z impurity control.

Design Parameters

Vacuum chamber	
Material	316 SS
Design stress (ksi)	10
Major radius (m)	6.25
Minor radius (m)	2.4
Volume (m^3)	711
Wall area (m^2)	592
Wall thickness (cm)	2
Ring and spar (cm)	
Width	5
Depth	11
Ports	
Vacuum (0.95 m diameter)	32
Heating (0.75 m diameter)	16
Experimental (1.5 m diameter)	4
Total port area (m^2)	31
Current breaker	
Material	Cr_2O_3
Form	Coating
Preparation	Chemical bond
Coolant panel	
Material	316 SS
Number	352
Area per panel (m^2)	1-2
Length (m)	1-2
Width (m)	$\sim$ 1
Total panel thickness (cm)	$\sim$ 1
Thickness front wall (cm)	0.5
Low-Z coating	
Material	Beryllium
Thickness (μm)	100-200
Preparation	Plasma spray
Coolant	H_2O

TABLE 2. First-Wall Operating Parameters and Design Limits*

Nominal Operating Conditions	
Capacity factor (%)	50
Operating cycle (s)	
Startup	5
Burn	35
Shutdown	5
Exhaust and replenishment	15
Average power loading during burn (MW/m^2)	
Neutron	0.5
Radiation, conduction, convection	0.13
Operating Parameters	
Stainless steel vacuum wall	
Maximum temperature (^oC)	< 500
Minimum yield stress at 500°C (ksi)	17
Maximum annual fluence (n/m^2)	6×10^{25}
Neutron damage (dpa/yr)	2.0
Helium generation (appm/yr)	54
Hydrogen generation (appm/yr)	133
Stainless steel coolant panel	
Maximum temperature (^oC)	380
Minimum yield stress at 500°C (ksi)	17
Maximum annual fluence (n/m^2)	6×10^{25}
Neutron damage (dpa/yr)	2.8
Helium generation (appm/yr)	54
Hydrogen generation (appm/yr)	133
Maximum heat deposition (W/cm^3)	5.5
Maximum ΔT across panel surface (^oC)	20
Maximum ΔT through panel face (^oC)	
With Argon shutdown	100
Without Argon shutdown	75
Maximum ΔT during burn cycle (^oC)	100
Maximum thermal strain range (%)	
Operating cycle	0.14
Burn cycle	0.09
Beryllium coating	
Maximum surface temperature (^oC)	407
Helium generation (appm/yr)	780
Hydrogen generation (appm/yr)	13
Maximum erosion rate (μm/yr)	30
Water coolant	
Maximum pressure (psi)	2000
Velocity (m/s)	1.6
Inlet temperature -- first panel (^oC)	40
Exit temperature -- eighth panel (^oC)	310
Pumping power (MW)	< 1
Vacuum wall	
Design life (yr)	10
Integrated neutron wall loading ($MW-yr/m^2$)	2.5
Yield strength -- 10 yr (ksi)	75
Uniform elongation -- 10 yr (%)	> 1
Radiation swelling -- 10 yr (%)	< 4
Limiting criterion	Ductility
Coolant panel	
Design life (yr)	5
Total burn cycles -- 5 yr	10^6
Fatigue lifetime (yr)	5
Radiation lifetime (yr)	8
Limiting criterion	Thermal fatigue
Low-Z coating	
Design life (yr)	3-5
Limiting criterion	D-T sputtering

* Based on a neutron wall load of 0.5 MW/m^2 and a plant capacity factor of 50%.

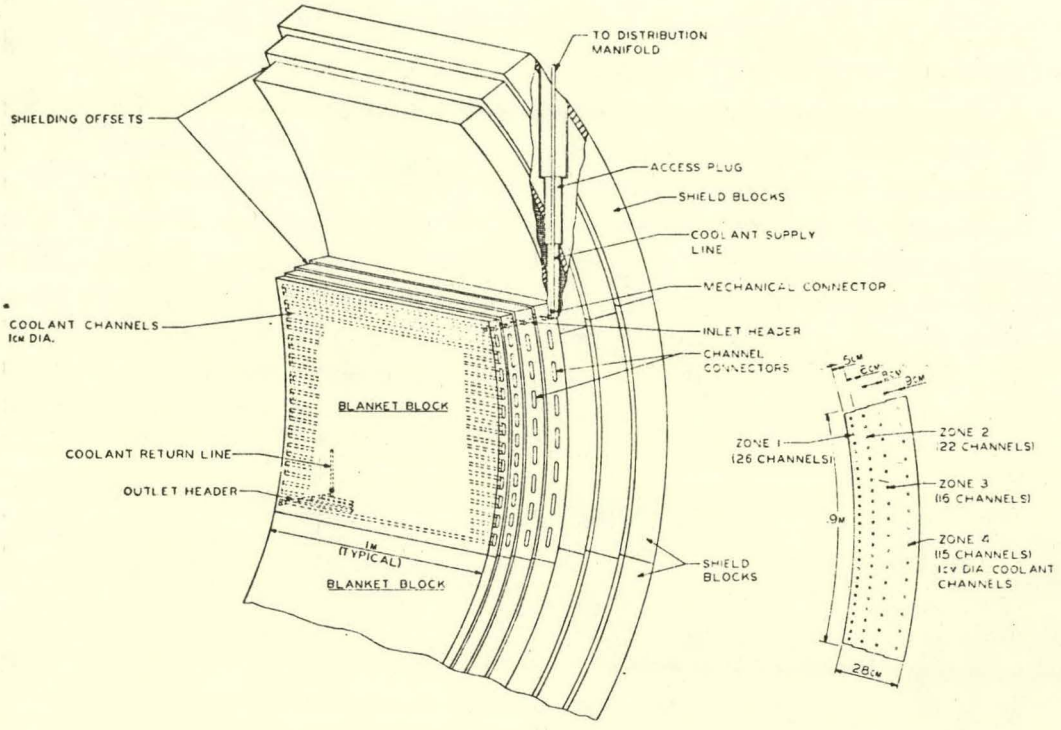

FIGURE 6. Blanket Block

The bulk shield surrounding each of the 16 segments of the vacuum wall and blanket consists of 1 inner shield block and 25 outer shield blocks, as shown in Fig. 5. The inner shield block is 0.58-m thick made up of alternating layers of B_4C and stainless steel disposed so as to maximize the attenuation of neutrons and gamma rays. At the top, bottom and outside of the torus, the bulk shield is 0.97-m thick and consists (going radially outward) of 0.03 m of stainless steel, 0.15 m of graphite with 1% natural boron, 0.05 m of stainless steel, 0.65 m of lead mortar and 0.09 m of aluminum. The bulk shield is cooled with H_2O at near atmospheric pressure.

Neutral beam lines, vacuum ducts and other penetrations of the outer blanket and bulk shield represent large ($\sim$ 0.6 to 1.0 m^2 cross section) streaming paths for neutrons and require special shielding. A special, 0.75-m thick annular shield surrounds the neutral beam tube after it exits from the bulk shield and extends beyond the TF coils, so that there is no unshielded line-of-sight path from the wall of the beam tube to the TF coils. The inner 0.65 m of this special shield is 50% SS/50% B_4C, followed by 0.05 m of lead and 0.05 m of aluminum.

A pneumatically operated shield plug is closed in the vacuum duct during plasma burn (see Fig. 1). This shield plug consists of two blocks. The inner block is 0.32-m thick and is fabricated of stainless steel and cooled in the same manner as a blanket block. The outer block is 0.58-m thick with a material disposition (SS/B_4C) similar to that of the inner shield.

The blanket, shield and vacuum vessel assembly weighs over 2700 metric tons. This weight is supported from beneath the

reactor on 16 individual frames. The frames can move vertically approximately two meters to facilitate replacement of the blanket and shield blocks. The load is transferred through 32 columns from the reactor foundation to the 16 frames, which in turn support the reactor shielding blocks. The blanket block layer rests on the inner portions of the shield blocks on insulation roller pads to accommodate the high temperature of the blanket and the accompanying thermal expansion. The 350 metric ton vacuum vessel rests on the inner side of the lower blanket blocks.

Extensive analyses have been performed to evaluate the performance of the blanket/shield system. These analyses are based on a nominal neutral wall load of 0.5 MW/m^2 and a plant capacity factor of 50%. Results are summarized in Tables 3 and 4. Radial distributions of the neutron heating rate and of the atomic displacement are shown in Figs. 7 and 8.

The 4-cm first wall and the 28-cm blanket region receive $\gtrsim$ 90% of the gamma energy. For the most part, the properties and requirements of the blanket material are the same as those of the first wall. The radiation damage level adjacent to the first wall is $\sim$ 1.7 dpa/year and drops by a factor of two every $\sim$ 7 cm going through the blanket. Operating temperatures in the load bearing portions of the blanket are, like the first wall temperatures, restricted to $\leq 500^{o}C$, but may be allowed to rise above this level in non-structural components. In general, the less severe radiation environment of the blanket will mean that property changes will be less than in the first wall. After 10 years at a wall loading of 0.5 MW/m^2 and a 50% capacity factor, the swelling in the blanket adjacent to the first wall is expected to remain below 2%, the uniform elongation will drop to $\sim$ 3%, and the yield strength will increase to $\sim$ 75 ksi. As the neutron radiation is attenuated through the blanket, the swelling will be reduced to zero after a few cm, and the tensile properties will approach those of unirradiated material ($\sim$ 22% uniform elongation and $\sim$ 17 ksi yield strength). The effect of creep and fatigue will be less than in the first wall since the blanket is not exposed to the surface radiation from the plasma and will not undergo the large thermal cycling of the first wall. Helium production rates will still be high in the first few cm, but the temperature limit of $500^{o}C$ should reduce the possibility of helium embrittlement, which is observed at temperatures above $550^{o}C$.

The bulk shield will receive < 5% of the total radiation energy produced in the EPR. No degradation of the bulk properties of stainless steel is expected. The boron carbide located in the inner shield is a brittle material with moderate tensile strength and high compressive strength. The major effect of radiation on boron carbide is the buildup of helium from (n,α) reactions that can induce swelling and cracking if it is present in high concentrations. Neutron irradiation can also substantially reduce the thermal and electrical conductivity. The degree to which radiation affects the bulk properties depends to a large extent on the amount of porosity present in the unirradiated material. The first layer of boron carbide in the inner shield will be the most seriously affected by the neutron irradiation. The first few cm of boron carbide will produce $\sim$ 3500 appm of helium

TABLE 3. Summary of Blanket Design Parameters

Design basis operating life (yr)	10
Nominal power during burn (MW)	400
Design basis neutron wall loading (MW/m^2)	0.5
Plant capacity factor (%)	50
Blanket structure	
Thickness (m)	0.28
Type metal/volume fraction	316-SS/0.9
Type coolant/volume fraction	$H_2O/\leq 0.05$
Penetration volume fraction	
Inner blanket	~ 0.02
Outer blanket	~ 0.05
Maximum temperatures (^oC)	
In support structures	500
In bulk materials	550
Nuclear parameters	
Maximum heat deposition (W/cm^3)	3.5
Maximum fluence at 2.5 MW-yr/m^2 (n/m^2)	5×10^{26}
Maximum dpa at 2.5 MW-yr/m^2 (dpa)	17
Maximum helium production at 2.5/MW-yr/m^2 (appm)	230
Maximum hydrogen production 2.5/MW-yr/m^2 (appm)	600
Mechanical parameters	
Design stress in support structure (ksi)	≤ 10
Minimum material yield stress (ksi)	20
Ductility at 2.5 MW-yr/m^2 (% uniform elongation)	≥ 3
Swelling at 2.5 MW-yr/m^2 (% of initial volume)	≤ 2
Maximum torque from pulsed fields (ft-lb)	125,000
Coolant parameters	
Type	H_2O
Maximum pressure (psig)	2000
Pressure drop (psig)	< 15
Maximum velocity (m/s)	2.4
Pumping power (MW)	< 1
Coolant inlet temperature (^oC)	40
Maximum coolant exit temperature (^oC)	309
Residual activity from blanket/shield radiation waste after 2 yr operation (Ci/MWt)	
Immediately after shutdown	3.5×10^6
1 yr after removal	8.0×10^5
10 yr after removal	7.0×10^4
100 yr after removal	60

TABLE 4. Summary of Shield Design Parameters

Design basis operating life (yr)	10
Shield structure	
Thickness (m)	
Inner bulk shield	0.58
Outer bulk shield	0.97
Beam duct shield	0.75
Evacuation duct shield (movable plug)	0.90
Biological shield	1.5
Materials	
Inner shield	304-SS/B_4C
Outer shield	304-SS/Pb mortar/C/Al
Beam duct shield	304-SS/B_4C/Pb/Al
Evacuation duct shield (movable plug)	304-SS/B_4C
Biological shield	Concrete
Temperature (^oC)	$\leq 100^oC$
Coolant	H_2O
Maximum torque from pulsed fields (ft-lb)	253,000
Maximum nuclear heating in bulk shield (W/cm^3)	0.3
Fraction of fusion power deposited in shield	< 0.05
Maximum energy current at outer surface of bulk shield (W/cm^2)	
Neutrons	$\sim 2 \times 10^{-4}$
Gammas	$\sim 5 \times 10^{-5}$

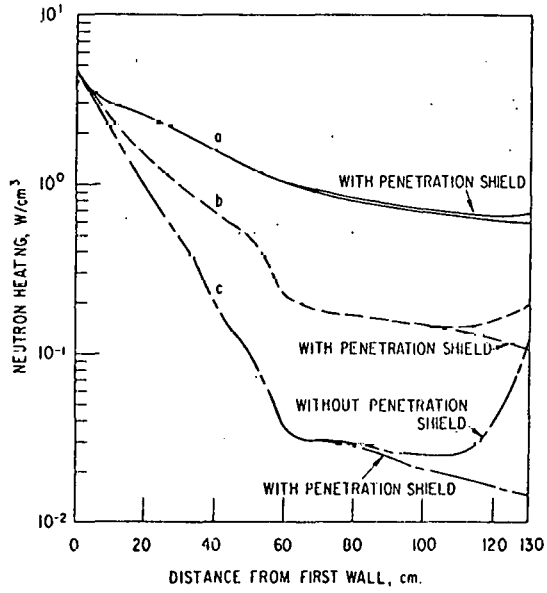

FIGURE 7. Neutron Heating in the Water Coolant as a Function of Depth in the Blanket/Shield for Three Locations with Respect to the Neutral Beam Duct: (a) at the wall of the beam duct, (b) at 10 cm from the wall of the beam duct and (c) at 30 cm from the wall of the beam duct.

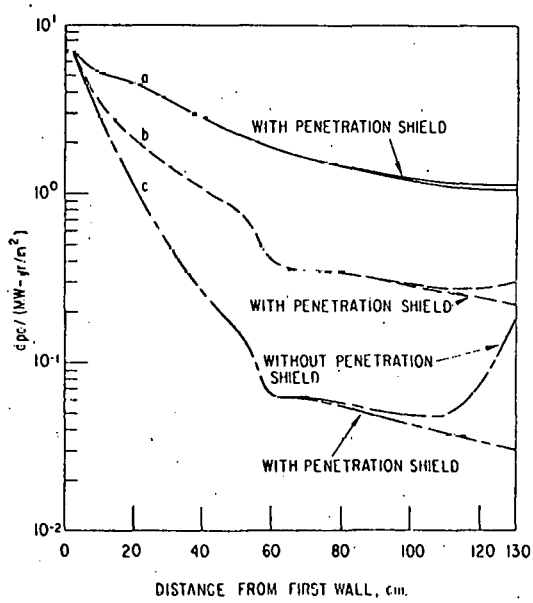

FIGURE 8. Atomic Displacement in Stainless Steel as a Function of Depth in the Blanket/Shield for Three Locations with Respect to the Neutral Beam Duct: (a) at the wall of the beam duct, (b) at 10 cm from the wall of the beam duct and (c) at 30 cm from the wall of the beam duct.

during a 10 year lifetime, but helium production will fall off rapidly past this point. This amount of helium is not expected to induce significant swelling or cracking if a sufficient porosity exists to accommodate the gas. Helium escaping from the boron carbide must be vented to prevent buildup of gas pressure within the shield. For the conditions expected in the EPR, the graphite in the outer bulk shield will densify rather than swell. It is expected that the volume change of graphite due to irradiation can be minimized by a suitable choice of material and should not present a problem. Helium production in the first few cm of the graphite with 1% boron will reach ~ 770 appm after a 10 year lifetime. As with boron carbide, porosity and venting considerations must be factored into the shield design to accommodate the helium. The materials lying past the first layer of boron carbide in the inner shield and the graphite in the outer shield receive a relatively small neutron fluence, and the bulk properties should not be adversely affected. The lead mortar and aluminum in the outer shield will operate at temperatures below 100°C, which is well below the ~ 150°C at which the lead mortar will begin to break down.

The radioactive inventory as a function of time for the EPR is shown in Figure 9. The level of neutron induced activation after two years operation is 3.5×10^6 Ci/MWt and decreases by a factor of 4 one year after shutdown and more rapidly for longer times. The curies per thermal megawatt are fairly independent of neutron wall loading for the range of 0.1 to 5 MW/m^2.

At shutdown, the decay heat is 2.5% of operating power and only drops about 20% during the first few minutes after shutdown,

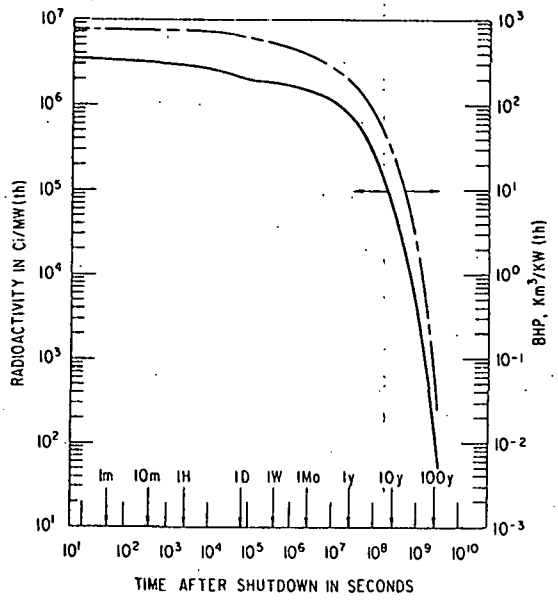

FIGURE 9. Radioactivity and Biological Hazard Potential as a Function of Time after Shutdown Following Two Years of Operation.

which is the period of time that is very crucial to emergency cooling.

During operation, the biological dose in regions external to the TF coils is about 10^6 mrem/hr, which is too high to permit access to the inside of the reactor building for any reasonable length of time. Outside the 1.5-m thick concrete building wall, the dose is about 1 mrem/hr. The biological dose in the vacuum chamber inside the first wall is 6×10^9 mrem/hr at shutdown and after one year of cooldown the dose is 1×10^3 mrem/hr. After one day of cooling, the dose is 600 mrem/hr at a position above the reactor at the location of the TF coils and 2 mrem/hr outside the TF coils. The latter result does not include the effect of penetration streaming or activation of the neutral beam injector. These calculations indicate that for a long period after shutdown the dose rate is too high to permit unshielded personnel access to the reactor building (in the region exterior to the TF coils) unless all pene-

trations and beam injectors are fully shielded.

The general approach to maintenance for the EPR is by use of remote handling apparatus. All large components will be repaired in place, where possible. This includes the vacuum vessel and the lower EF and OH coils. Smaller components like the blanket and shield blocks will be repaired in the hot cells. Special in-vessel remotely operated equipment will be designed to repair, replace and inspect any portions of the vacuum vessel or first-wall panels that have been damaged. Support facilities for remote operations include a remotely-operated overhead crane/manipulator with a shielded personnel cab, floor-mounted snorkel type units for servicing the vertical portions of the reactor and basement-positioned apparatus for maintaining the lower components of the reactor. A full-scale, quarter section mockup of the reactor is vital to all remote operations because it will be used to program the repair apparatus and perform practice runs.

REFERENCES

1. W. M. Stacey, Jr., et al., "Tokamak Experimental Power Reactor Studies," ANL/CTR-75-2, Argonne National Laboratory (June, 1975).
2. W. M. Stacey, Jr., et al., "Tokamak Experimental Power Reactor Conceptual Design," ANL/CTR-76-3, Argonne National Laboratory (August, 1976).
3. M. Roberts, et al., "Oak Ridge Tokamak Experimental Power Reactor Study - Reference Design," Oak Ridge National Laboratory (August, 1976).
4. C. C. Baker, et al., "Experimental Power Reactor Conceptual Design Study," GA-A-13534, General Atomic Co., (July, 1975).
5. J. S. Patten, et al., "A Primary Energy Conversion System for the Tokamak Experimental Power Reactor," Proceedings of the Sixth IEEE Symposium on Engineering Problems of Fusion Research, San Diego, California, November 16-21, 1975.
6. W. M. Stacey, Jr., et al., "Tokamak Experimental Power Reactor," Proceedings of the Second ANS Topical Meeting on the Technology of Controlled Nuclear Fusion, Richland, Washington, September 21-23, 1976.
7. M. A. Abdou, et al., "Multidimensional Neutronics Analysis of Major Penetrations in Tokamaks," ibid.
8. W. M. Stacey, Jr., et al., "Impurity Control in Near-Term Tokamak Reactors," ibid.
9. S. T. Wang, et al., "Conceptual Design of Superconducting Magnet Systems for the Argonne Tokamak Experimental Power Reactor," ibid.
10. F. E. Mills, et al., "Plasma Driving Systems for a Tokamak Experimental Power Reactor," ibid.

IMPURITY CONTROL IN NEAR-TERM TOKAMAK REACTORS*

Weston M. Stacey, Jr., Dale L. Smith, and Jeffrey N. Brooks
ARGONNE NATIONAL LABORATORY, ARGONNE, ILLINOIS 60439

Several methods for reducing impurity contamination in near-term tokamak reactors by modifying the first-wall surface with a low-Z or low-sputter material are examined. A review of the sputtering data and an assessment of the technological feasibility of various wall modification schemes are presented. The power performance of a near-term tokamak reactor is simulated for various first-wall surface materials, with and without a diverter, in order to evaluate the likely effect of plasma contamination associated with these surface materials.

The problem of plasma contamination by wall-sputtered impurities in near-term tokamak reactors is examined. A critical review of the relevant surface data is incorporated in a plasma-wall interaction model that is employed, together with a plasma power and particle balance model, to evaluate impurity contamination effects. Impurity control by charged-particle diversion and by modification of the first-wall surface are considered, and the adequacy of these methods is assessed.

A major purpose of this work is to determine if modification of the first-wall surface can provide adequate impurity control for near-term tokamak reactors, in general, and the experimental power reactor (EPR), in particular. A qualitative assessment of the technological feasibility and limitations of a low-Z coating, a low-Z separated liner, a carbon curtain, and a low-sputter coating is presented.

It is concluded from these studies that adequate control of sputtered impurities to sustain burn pulses on the order of a minute and to achieve net power conditions can be obtained in an EPR by suitable modification of the first-wall surface. Of the wall modifications considered, a low-Z material (e.g. beryllium) coated on a structural substrate appears the most technologically feasible.

COMPUTATIONAL MODEL

The basic computational model consists of a set of time-dependent, space-independent particle and power balance equations for the plasma, and a plasma-wall interaction model. Coupled balance equations for D-T ions, alpha particles, wall-sputtered impurities, electron temperature, and ion temperature are solved. Neutral beam and fusion-alpha heating and power loss by radiation and transport are treated. Transport processes within the plasma are modeled with particle and energy confinement parameters which are computed from a multiregime (pseudo-classical, neoclassical, trapped-particle-mode) model depending upon the value of the collision frequency.

The plasma-wall interaction model is depicted schematically in Fig. 1. Charged (D^+, T^+, He^{++}, impurity) and neutral (D^0, T^0, n) particle fluxes emerge from the plasma and strike the wall, with the charged particle fluxes being reduced by a factor n due

*Work supported by the U. S. Energy Research and Development Administration.

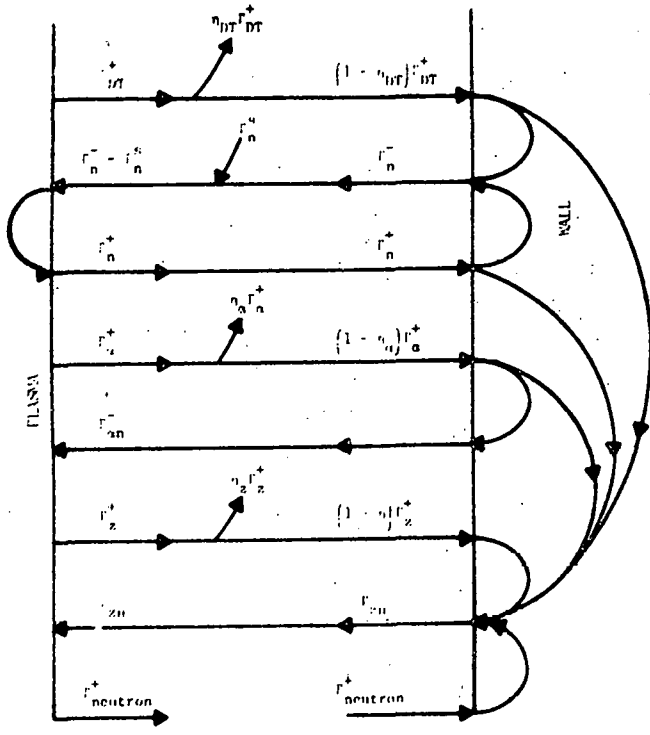

Balance Equations:

$$\Gamma_n^+ = \Gamma_n^- A_{cx} + \Gamma_n^a A_{cx}^a$$

$$\Gamma_n^- = \Gamma_n^+ \cdot R_n + (1 - \eta_{DT})\Gamma_{DT}^+ \cdot R_{DT}$$

$$\Gamma_{\alpha n}^- = (1 - \eta_\alpha)\Gamma_\alpha^+ \cdot R_\alpha$$

$$\Gamma_{zn}^- = (1 - \eta_{DT})\Gamma_{DT}^+ \cdot S_{DT} + \Gamma_n^+ \cdot S_n + (1 - \eta_\alpha)\Gamma_\alpha \cdot S_\alpha + (1 - \eta_z)\Gamma_z^+ \cdot (S_z + R_z)$$

$$\Gamma_{neutron} \cdot S_{neutron}$$

Subscripts:

n	neutral D-T atom
DT	D-T ions
α	alpha
αn	neutral helium atom
z	impurity ions
zn	neutral impurity atom

Definitions:

$\Gamma^{+/-}$ = outward/inward particle flux.

Γ^a = external neutral D-T source.

A_{cx} = charge-exchange re-emission probability.

R = wall reflection coefficient

S = wall sputtering coefficient.

η = charged particle removal efficiency.

FIGURE 1. Plasma-Wall Interaction Model

to particle removal (e.g. by a divertor). A fraction of these particles are reflected, predominantly as neutrals from the wall with reflection coefficient R.* The impinging particles produce wall erosion by sputtering with coefficient S. The returning particles are either ionized in the plasma or may initiate a series of charge-exchange interactions leading to the re-emergence of a D^0 or T^0 from the plasma with a probability A_{cx} which depends upon the relative charge-exchange and ionization cross sections and upon neutral transport.

Energy-dependent physical sputtering coefficients for the incident particles, viz., D^+, T^+, He^{++}, and impurity ions, on candidate first-wall materials are used for the calculation. Since insufficient experimental sputtering data are available for the range of parameters of interest (1-5 are general references that give a good indication of the state of technology), the sputtering coefficients used for the calculation have been developed from both theoretical and empirical considerations. The shapes of the energy-dependent sputtering curves are

*R includes backscattering and re-emission.

developed primarily from Sigmund's theory[6] and the magnitude of the coefficients have been adjusted in some cases to better conform with available experimental data.

Since the Sigmund theory does not adequately predict light ion sputtering at low energies, energy-dependent sputtering yield curves for light ions (deuterium, tritium, and helium) have been obtained by combining the theoretical curve at higher energies with an empirical relation for the lower ion energies.[7] The empirical curve assumes a direct energy dependence of the sputtering yield, which is in general agreement with reported helium sputtering data for a number of target materials.[8] The transition between the two segments forms a peak in the sputter curve at the ionization cut-off energy calculated from the Kinchin-Pease theory.[9] The threshold energies for sputtering have been determined by the method of Hotston.[10] Since the curves developed in this manner[7] give yields that are substantially higher than experimentally observed yields, these curves have been adjusted in magnitude to better conform to the available experimental data. Curves for the deuterium and tritium sputtering yields have been reduced by one order of magnitude and those for helium have been reduced by a factor of five. Figure 2 presents the resultant monoenergetic sputtering curves for deuterium on several wall materials of interest. Similar curves have been developed for tritium and helium. Experimental data in the low-energy range are shown in Fig. 3.

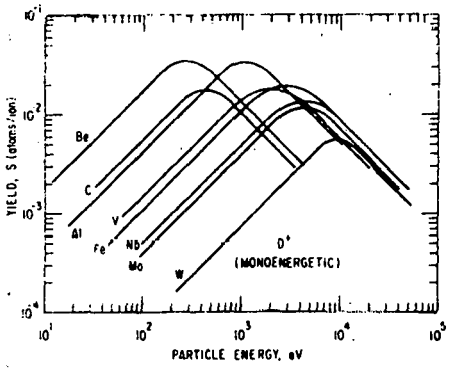

FIGURE 2. Energy-Dependent Physical Sputtering Yields of Potential First-Wall Materials Irradiated with Mono-Energetic D^+ ions.

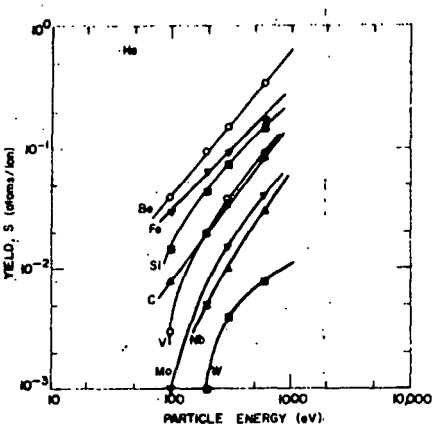

FIGURE 3. Plot of Selected Energy-Dependent He^{++} Sputtering Data

Figure 4 compares the selected energy-dependent light-ion sputtering curves with available experimental data on niobium. As indicated, the sputtering curves developed here

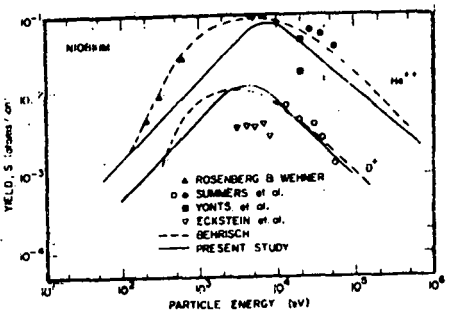

FIGURE 4. Plot of Light Ion Sputtering Curves for Niobium Showing Comparison with Available Experimental Data

for niobium are in fairly good agreement with similar curves proposed by Behrisch[11] for the same target material. In general, the present development gives sputter coefficients that are slightly higher than the corresponding experimental data for low-Z wall materials, and coefficients that are slightly lower than the corresponding experimental

data for the higher-Z wall materials. Sputtering by the neutral D^0 and T^0 particles are assumed to be identical to those for D^+ and T^+ ions, respectively.

In the present study three of the first-wall materials of interest are compounds, viz., BeO, B_4C, and SiC. Since sputtering data for these compounds are very limited, yields equivalent to those for beryllium, boron, and silicon, respectively, have been assumed for these compounds. This assumption appears plausible in view of the data of Kelly and Lam,[12] which indicate that sputter yields produced by 10-keV Krypton on a number of stable oxides are within a factor of 2-3 of the corresponding metals. The yields for these compounds are assumed to correspond to their stoichiometry, e.g., four boron atoms to one carbon atom for B_4C.

The Sigmund theory is a better representation of the yields observed for heavy (impurity) ion sputtering. Therefore, the self-sputter coefficients used for the calculations are derived from the Sigmund theory with slight modifications at low energies to compensate for electronic losses.[7] At the lower energies the curves are adjusted to approach a slope of unity on the log S versus log E plot. Figure 5 shows the energy-dependent self-ion sputter coefficients for beryllium, niobium, and tungsten.

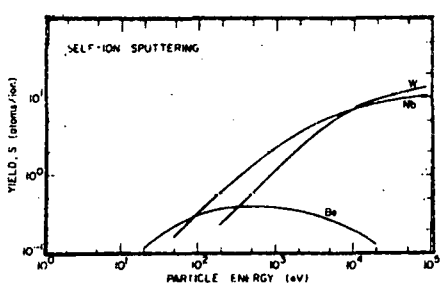

FIGURE 5. Energy-Dependent Self-Ion Sputter Coefficients for Beryllium, Niobium, and Tungsten

Large variations in the 14-MeV neutron sputter yields have been reported in the literature for various transition metals.[1-5,13-18] These differences are due primarily to chunk-type deposits that have been observed by some investigators.[13-14] Recent analyses indicate that yields for the chunk-type sputtering, which are dependent on both surface roughness and degree of cold-work, are typically less than 10^{-4} atoms/neutron.[13] Single-atom sputtering yields in the range 10^{-6} to 5×10^{-4} have been reported.[13-18] A total yield of 10^{-4} atoms/neutron is considered reasonable for the present analysis. Since the contribution of neutron sputtering to the total sputtering yield turns out to be very small for near-term reactors, the results are not very sensitive to variations or uncertainties in the neutron sputtering coefficient.

Chemical interaction between the incident particle and the target material can influence sputtering rates because of the effect of compound formation on lattice displacement energies, on sputtering mechanisms, and on the nature of the sputtered products.[19] Although this so-called chemical sputtering occurs in a number of systems, it is most commonly associated with the formation of hydrocarbons upon bombardment of carbon or graphite by the hydrogen isotopes.[19-27] In line with the chemical interaction energies, the chemical sputtering coefficients, in contrast to the physical sputtering coefficients, are sensitive to the target or wall temperature. For example, greatly enhanced (approximately 10X) chemical sputtering leading to CH_4 formation has been observed for H^+ ion bombardment of graphite at temperatures of 400-700°C.[20-25] Sputtering yields of nearly 0.1 atom/ion are reported by these investigators. For the present investigation, chemical sputtering coefficients for deuterium and tritium incident on carbon were assumed to be a factor

of 10 higher than the physical sputtering yield at temperatures of 300-750°C, and negligible at higher and lower temperatures. Similar enhancement of sputtering yields for silicon-carbide has not been observed,[20,21,28] and hydrides of the structural metals are not stable under anticipated wall conditions. Therefore, chemical sputtering has been considered in the present analysis only for the case of carbon or graphite.

The "reflection" coefficient, R, used in the plasma-wall interaction model includes both backscattering and re-emission. The backscattered particles are the incident particles that return from the wall via elastic and inelastic collisions (<<1 s) whereas the re-emitted particles are those which have penetrated the wall at an earlier time and are subsequently released by diffusion to the surface or by erosion of the wall material. Several models have been developed and experiments conducted to interpret the backscattering and re-emission of light ions (H^+ and He^{++}) from several materials.[29-38] The backscattering coefficients for the light ions typically increase with a decrease in incident ion energy below 1 keV, and the values may exceed 50% at energies below 100 eV.[29,36-38] The use of such coefficients is appropriate only for the initial startup, since the concentrations of light atoms (helium, deuterium, and tritium) in the surface regions build up in a matter of hours during operation. Therefore, re-emission of the hydrogen isotopes and helium from the surface of the first wall will occur during normal operation. Data of several investigators indicate that high percentages of light ions injected into a variety of target materials are re-emitted after fluences of the order of 10^{17} ion/cm^2.[30-38] This re-emission is further enhanced by the elevated wall temperatures. For purposes of the present calculation it is assumed that a steady-state is reached and that the combination of backscattering and re-emission results in the return of almost all of the incident light particles.

For the case of self-ions incident on the first wall, a high sticking probability is expected for a clean metal surface. In addition, the measured sputtering coefficients probably include any backscattered component. Therefore, a near-zero reflection coefficient can be assumed for self ions.

These surface data were incorporated into the calculational model as follows. The mono-energetic sputtering coefficients were averaged over Maxwellian distributions of incident particle energies, with the Maxwellian being characterized by the plasma-edge temperature. These results are given in Table 1. A neutron sputtering coefficient $S_n = 0.0005$ was used for all materials, and a chemical sputtering coefficient $S_{DT} = 0.07$ was used for carbon. Particle reflection coefficients $R_{DT} = R_\alpha = 0.98$ were used in the calculations to represent unity reflection probability and an allowance for a small loss during operation through ports in the vacuum wall, and $R_z = 0.05$ was used to represent the high retention probability for an ion of the surface material.

The charge-exchange re-emission probability was computed from

$$\bar{A}_{cx} = \frac{\overline{\sigma v}_{cx}}{\overline{\sigma v}_{cx} + \overline{\sigma v}_{ion}}, \qquad A_{cx} \equiv \bar{A}_{cx}\gamma ,$$

where $\overline{\sigma v}_{cx}$ and $\overline{\sigma v}_{ion}$ are averages of the charge exchange (D^+, $T^+ \leftrightarrow D^0, T^0$) and ionization cross sections of Refs. 39-43 over Maxwellian distributions corresponding to the plasma edge ion temperature. The results are $\bar{A}_{cx} = 0.50$ at $T_{DT}^{edge} = 100$ eV, $\bar{A}_{cx} = 0.56$ at $T_{DT}^{edge} = 200$ eV, and $\bar{A}_{cx} = 0.73$ at $T_{DT}^{edge} = 1$ keV. The factor γ represents the probability that a primary charge-exchange event for an incident neutral will result in the re-emergence of a neutral (either directly or as the result of subsequent secondary

TABLE 1. Maxwellian-Averaged Physical Sputtering Coefficients

Material	Plasma Edge Temperature (eV)	Sputtering Coefficient (atoms/part) S_{DT} (a)	S_α	S_z (b)
Be	60	0.016	0.017	0.26
	200	0.028	0.070	0.35
	1000	0.018	0.115	0.36
BeO	60	0.016	0.017	0.26
	200	0.028	0.070	0.35
	1000	0.018	0.115	0.36
C	60	0.007	0.018	0.26
	200	0.015	0.050	0.35
	1000	0.012	0.079	0.36
B_4C	60	0.011	0.017	0.26
	200	0.022	0.060	0.35
	1000	0.016	0.098	0.36
SiC	60	0.0055	0.015	0.26
	200	0.016	0.048	0.47
	1000	0.033	0.160	0.64
Fe	60	0.0015	0.0046	0.27
	200	0.005	0.015	0.59
	1000	0.016	0.067	1.49
Nb	60	0.006	0.0016	0.29
	200	0.002	0.005	0.83
	1000	0.009	0.023	2.62
W	60	0.0001	0.0004	0.11
	200	0.0003	0.0012	0.35
	1000	0.0016	0.0061	1.61

(a) $S_{DT} = \frac{1}{2} S_D + \frac{1}{2} S_T$.

(b) Self-sputtering.

charge-exchange events) from the plasma. $\gamma = 0.75$ is used in this work.

The wall-sputtered impurities entering the plasma affect the energy balance both through the transport loss, which goes as Z_{eff} for pseudoclassical and neoclassical scaling and as Z_{eff}^{-1} for trapped-ion-mode scaling, and through the radiative power loss. The radiation model is a modification of a model proposed by Hopkins,[45] which is based on the results of calculations using coronal equilibrium models.[46-49] The results of the coronal equilibrium calculations have been boon shown to be good approximations under reactor conditions by comparison with the results of a more general radiative-collisional model.[50,51]

The model may be summarized as follows: When $T_e \geq T_z$,

$$P_{rad}^z = n_c n_z \left(K_1 Z^2 T_e^{\frac{1}{2}} + K_2 Z^4 T_e^{-\frac{1}{2}} + K_3 Z^6 T_e^{-3/2} \right),$$

where P_{rad} is the radiated power per cubic meter in W/m^3, n_e is the electron density

and n_z is the ion density of the z-th ionic species, T_e is the electron temperature in keV, and T_z is the ionization potential, in keV, for the beryllium-like ion sequence. $K_1 = 4.8 \times 10^{-37}$, $K_2 = 1.82 \times 10^{-38}$, and $K_3 = 4.13 \times 10^{-40}$, when T is in keV and n in m^{-3}. When $T_e \leq T_z$, we insure $P_{rad} \to 0$ as $T_e \to 0$ by using,

$$P^z_{rad} = n_e n_z \left[K_1 Z^2 T_e^{\frac{1}{2}} + K_2 Z^4 T_z^{-\frac{1}{2}} + K_3 Z^6 T_z^{-3/2} \right] \left(T_e / T_z \right)^2 ,$$

T_z is given by[8]

$$T_z(\text{keV}) = [1.033 \times 10^{-7}(Z - 3)^3 + 3.4266 \times 10^{-3}(Z - 3)^2 + 5.5574 \times 10^{-3}(Z - 3) + 0.529 \times 10^{-3}] .$$

The total radiated power is thus given by

$$P_{rad} = \sum_z P^z_{rad} ,$$

where the sum includes all ionic species.

The above model was developed from radiation loss studies for nuclei with nuclear charge in the range $5 \leq Z \leq 18$. For impurities with $Z \geq 30$, the model was modified to account for radiation from high-Z materials which are not completely stripped at the 10-keV operating temperatures. In the formula for radiation loss, the nuclear charge, Z, was replaced by the actual ionic charge attained by the impurity at the plasma temperatures. Ionization potentials for various ions up to Z = 103 have been tabulated.[52] The radiation loss is reduced by a substantial factor for high-Z ions (e.g. 20 for tungsten), relative to a calculation using the atomic number. This reduced radiation power is consistent with results reported in Ref. 51.

ANALYSIS

The analysis was carried out for a specific tokamak reactor model with parameters that are characteristic of the ANL EPR design: R = 6.25 m, A = 2.98, I = 6.4 MA, q(a) = 2.5, B_t = 4.4 T. The confinement times were scaled up from the theoretical prediction by a factor $\omega_{TIM} = 1.79$ so that ignition would obtain at $\bar{T}$ = 10 keV, in the absence of wall-sputtered impurities and without helium recycling, in the trapped-ion-mode (TIM) transport regime. The thermonuclear power output of a reactor operating under these conditions at β_p = 2.25 is P_T = 410 MWt.

The analysis consisted of a dynamic simulation of the entire burn pulse. Ions escaping from the plasma were assumed to be recycled back as described in Fig. 1, so that essentially total (98%) recycling of deuterium, tritium, and helium occurred unless the particle removal (e.g. divertor) efficiency $\eta > 0$. Deuterium and tritium ion densities were maintained at their maximum allowable value by refueling, subject to the constraint that $\beta_p(t) \leq \beta_p^{max} = 2.25$. Wall-sputtered impurity ions were assumed to be able to penetrate immediately to the central region of the plasma, where they resided with a confinement time equal to that of the D-T ions. These impurity ions increase the radiative power loss as described in the previous section, modify the particle and energy confinement times ($\tau \propto Z_{eff}$ for TIM scaling) and reduce the allowable D-T ion density for a fixed β^{max}. Supplemental neutral beam heating, up to a maximum power of 80 MW, was used in some cases to offset excessive radiative power losses. The burn pulse simulation was carried out to the point at which the accumulation of helium and wall-sputtered impurities quenched the plasma.

A figure-of-merit for the burn cycle performance is the net electrical power averaged over the burn pulse,

$$P_{net} \equiv \left[U_T \eta_T - \frac{U_B}{\eta_T} - U_{REF} - U_{PUMP} - U_\Omega - U_{PS}\left(1 - \eta_{PS}\right) \right] \Big/ \Delta t_{burn} ,$$

where

U_T plasma thermal energy to wall during burn pulse

$U_B \equiv$ beam heating energy during burn pulse

$U_{REF} \equiv$ refrigeration energy during burn pulse

$U_{PUMP} \equiv$ coolant and vacuum pumping energy during burn pulse

U_Ω plasma ohmic heating energy dissipated during burn pulse

U_{PS} energy transferred by plasma driving system during burn pulse

$$\equiv \int_0^{\Delta t} |P|\, dt$$

$\eta_T \equiv$ thermal-to-electrical conversion efficiency = 30%

$\eta_B \equiv$ neutral beam power efficiency = 35%

$\eta_{PS} \equiv$ energy transfer efficiency = 95%

$\Delta t_{burn} \equiv$ length of the burn pulse.

The compressive refrigeration power for the superconducting toroidal field coils was U_{REF} = 660 MJ, the coolant and vacuum pumping energy was $U_{PUMP} = 0.02\ U_T$, and the energy transferred by the plasma driving system was $U_{PS} \simeq$ 2400 MJ.

The quantity P_{net} is plotted in Fig. 6 as

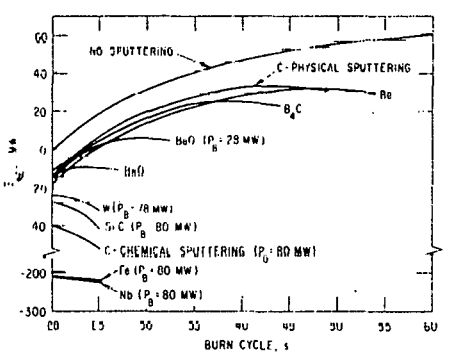

FIGURE 6. Effect of First-Wall Surface Material on Power Performance

a function of the length of the burn pulse for several first-wall surface materials. The assumed edge temperature is 200 eV for all cases. The burn cycle performance that would result in the absence of sputtering is also shown to provide a point of reference. In the absence of sputtering, the minimum burn pulse for which $P_{net} > 0$ is 20 s, including ~4 s for startup. In this case, the burn pulse is ultimately (~157 s) quenched by the accumulation of helium, and the maximum value of P_{net} is 66.5 MW.

Wall-sputtered impurities from a stainless steel (represented by iron) or refractory metal (niobium) first-wall surface have a devastating effect. A substantial supplemental beam heating is required to maintain the plasma at thermonuclear temperatures, resulting in a negative P_{net}, on the order of -200 MWe. The maximum length of the burn pulse could be extended beyond ~20 s by increasing the beam heating power $P_B > 80$ MW, but this would result in an even more negative P_{net}. Initially, the D-T sputtering is the main contributor to plasma contamination, but as the impurity concentration builds up to on the order of 1%, self-ion sputtering becomes a major contributor, as may be inferred from Table 1. The situation is somewhat improved if the plasma edge temperature is less than the 200 eV used in these calculations; however, even for T_{edge} = 60 eV, $P_{net} \simeq$ -100 MWe and the maximum burn pulse is ~20 s. Thus, it appears extremely unlikely that a reactor of this type will be able to operate with a stainless steel or refractory metal wall without some form of impurity control.

One form of impurity control is suggested by Fig. 6, namely to interpose between the plasma and the structural first wall a low-Z material, either as a coating or as a stand-off liner. Burn pulses of ~45-55 s can be achieved with very low-Z surfaces, viz., beryllium, carbon (without chemical sputtering), B_4C, which result in P_{net} about one-half of the value that obtains without wall sputtering. With a small supplemental beam

heating (P_B = 10 MW) to offset radiative losses, burn pulses in excess of 60 s with maximum P_{net} of ∿35 MWe can be achieved with a beryllium surface. If a carbon surface operates in the temperature range ∿400-700°C, then chemical sputtering precludes $P_{net} > 0$, which implies that carbon would be suitable as a standoff liner operating at temperatures in excess of 1000°C but would be unsuitable as a coating operating at 400-600°C. Surfaces with silicon or oxygen compounds are less satisfactory for impurity control in reactors of this type. In the case of beryllium oxide, $P_B \leq 28$ MW was adequate to offset radiative losses, but the accumulation of oxygen in the β_p-limited plasma forced a reduction in the D-T density which eventually quenched the plasma. For the beryllium surface, the self-sputtering rate is about half the D-T sputtering rate, the alpha-sputtering rate is about 5% of the D-T sputtering rate, and the neutron-sputtering rate is negligible.

Another possibility for reducing plasma contamination is to use a low-sputtering first-wall material such as tungsten. Although the plasma performance is better with tungsten than with stainless steel or niobium as the first-wall surface material, the performance with tungsten is considerably inferior to that with a low-Z material such as beryllium. Moreover, the plasma performance is much more sensitive to variations in the sputtering coefficients for a high-Z material than for a low-Z material. In the case of tungsten, the self-sputtering rate is ∿30% of the D-T sputtering rate and the neutron sputtering rate is ∿10% of the D-T sputtering rate.

The performance summarized in Fig. 6 is based upon a plasma-edge temperature of 200 eV, which corresponds to the maximum in the beryllium sputtering yield curves. Reduced sputtering, hence improved performance, occurs if the plasma-edge temperature is higher or lower for beryllium, as shown in Fig. 7. At an edge temperature of 60 eV, a burn pulse of 102 s with a maximum P_{net} = 57 MWe is obtained with a beryllium surface, which is close to the performance in the absence of wall sputtering. The effect of the plasma-edge temperature is even more dramatic for silicon-carbide, with $P_{net} > 0$ becoming possible for an edge temperature of 60 eV.

Another method of impurity control which has been proposed is to remove ions that escape from the plasma before they strike the wall — e.g., by means of a magnetic divertor. This process can be represented by the efficiency of charged particle removal, η. Results of a series of calculations for a stainless steel first-wall surface and various values of the charged-particle removal efficiency are shown in Fig. 8. For a very low plasma-edge temperature (60 eV) and a very efficient charged particle removal mechanism (η = 0.9), tolerable equilibrium iron (0.03%) and helium (1.5%) concentrations are maintained and the burn pulse is virtually unlimited. For a more realistic value of η = 0.5, the performance is marginal and $P_{net} > 0$ requires a low plasma-edge temperature (60 eV) in addition to substantial supplemental beam heating (P_B = 44 MW). If the plasma-edge temperature is 200 eV, a very high charged particle removal efficiency (η = 0.9) and some supplemental beam heating (P_B = 15 MW) are required to achieve $P_{net} > 0$. Thus, it appears that the success of a divertor or other impurity control mechanisms based upon charged particle removal depends critically upon the achievement of high particle removal efficiency and upon the operation of the plasma with a low edge temperature. These calculations have not accounted for the significant reduction in energy* of those charged particles which cross the divertor sweep-out region before

*Private communication from A. Mense, ORNL.

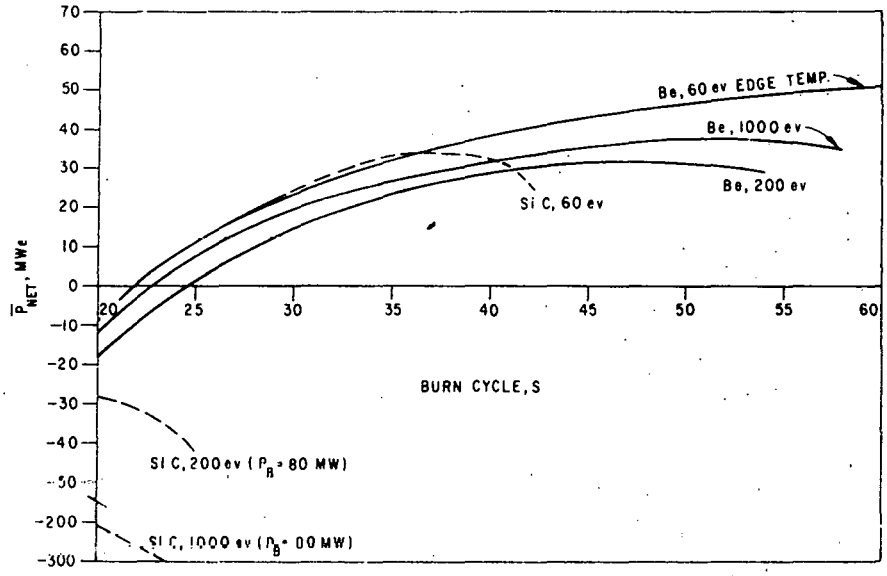

FIGURE 7. Effect of Plasma-Edge Temperature on Power Performance

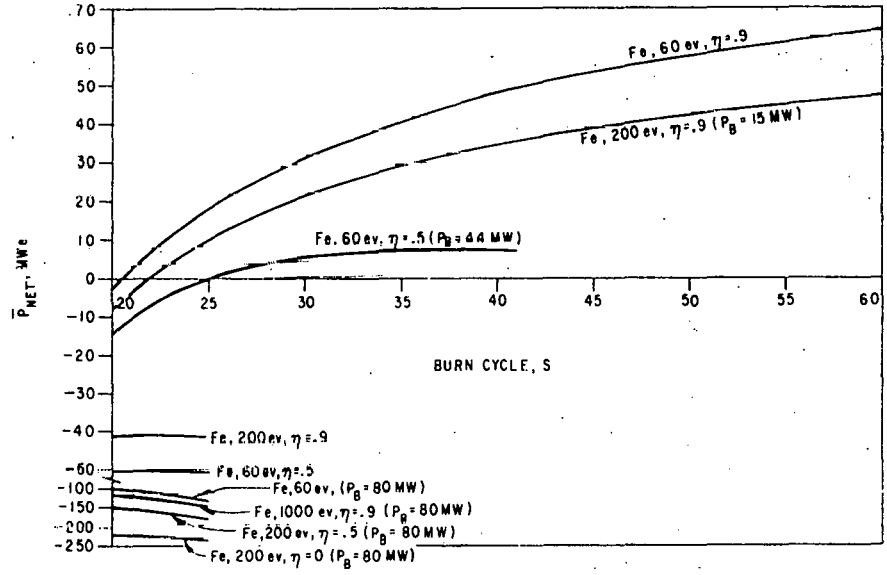

FIGURE 8. Effect of Divertors on Power Performance for Bare Stainless Steel Wall

striking the wall. This might improve the performance of divertors relative to the predictions of Fig. 8.

Combining a low-Z surface with a charged particle removal mechanism reduces the critical dependence upon high particle removal efficiency. Performance obtainable with beryllium and silicon-carbide surfaces are shown in Fig. 9, for a range of charged particle removal efficiencies. With a

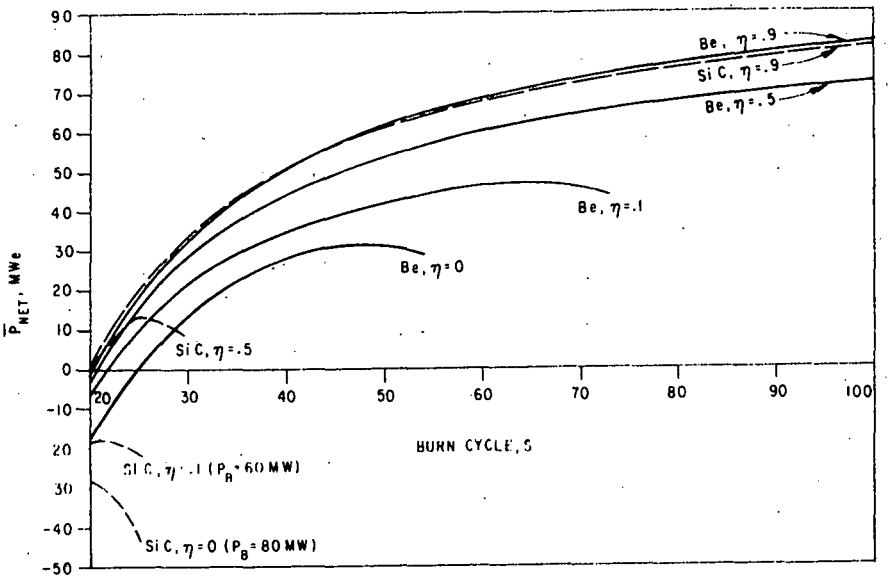

FIGURE 9. Effect of Divertors on Power Performance for Low-Z Coated Walls

beryllium surface, $\eta \geq 0.5$ suffices to achieve very long burns.

The quantitative results discussed above depend upon the particular reactor model and values for the sputtering coefficients used in the calculations, as well as upon the various assumptions in the calculational model, and are subject to change as understanding of the various processes improves. However, the general qualitative features should be relatively independent of the reactor model and the data.

TECHNOLOGICAL FEASIBILITY OF FIRST-WALL SURFACE MODIFICATIONS

On the basis of fabricability, vacuum properties, and economic impact, fusion reactor first walls constructed of transition metal alloys such as stainless steel are favored.[53] However, as indicated by the previous calculations, satisfactory plasma performance can only be attained with very low incident particle energies and an efficient divertor and/or supplemental heating. The unacceptable plasma performances were caused primarily by the high radiative losses produced by the high-Z transition metal impurities. An additional factor that will further degrade plasma performance will be the substantial erosion of the wall by the blistering phenomenon.[1-5,54-58] For anticipated conditions, erosion rates of structural materials such as niobium or stainless steel by blistering are greater than those by physical sputtering.[54-58] These erosion rates are temperature-dependent and peak at the temperature ranges of interest, viz., 400-500°C for stainless steel.[57-58] Although complete agreement on the contribution of the blistering phenomenon has not been reached because of uncertainties in incident particle energies and particle energy distribution, the data obtained by monoenergetic bombardments may be a reasonable representation of the 3.5-MeV contribution of the alpha-particle wall current. Effects produced by this component are probably independent of the other low-energy effects. An erosion rate greater than 10^{-1} atom/ion may be expected for stainless steel after a few days operation.[56,57] This contribution substantially

exceeds that produced by He^{++} sputtering at the low energies (<100 eV) and approaches the sputtering yields of D^+ and T^+ at low energies. Possible synergistic effects such as sputtering and vaporization of blister skins have not been investigated and, although likely to be detrimental, cannot be assessed at this time. Therefore, the conclusions presented in the previous section for the plasma performance with a stainless steel wall are probably quite optimistic.

Several concepts for modifying the first-wall surface are qualitatively assessed in this section: (a) a low-Z material coating on a structural substrate; (2) a separated monolithic low-Z material liner; (3) a carbon cloth liner; and (4) a low-sputter material coating on a structural substrate.

1. Low-Z Coating

The low-Z coating on a structural metal substrate has been proposed as a viable solution to the impurity control problem in EPR.[53] This concept utilizes the transition metal (stainless steel) substrate for structural support and the low-Z coating to protect the plasma from the high-Z transition metal atoms. Major considerations in this concept are the flexibility in first-wall design provided by the variety of low-Z coating materials that are considered feasible and the variety of coating procedures available. The coating selection and preparation can be optimized on the basis of its surface characteristics, and the substrate, which provides the structural support, can be selected primarily on the basis of desirable bulk properties.

Fabrication should not be much more difficult than for the simple metal wall discussed above. A substantial technology base exists for applying a variety of coatings to a number of substrate materials.[59] Much of this technology has been obtained recently under space and fission reactor programs. Although plasma spraying, chemical vapor deposition, chemical bonding, and sputtering can all be used to coat most of the materials considered,[59] the plasma spray process appears to be the most appropriate for the present application. Deposition rates necessary to obtain the desired coating thicknesses (~100 μm) can be achieved. The porosity and grain size can easily be varied in the plasma spray process to obtain optimum microstructures.[59-61] Graded coatings, which can also be prepared by the plasma spray process, may be desirable for better coating adherence. However, additional development work and modification of existing coating technology may be required to optimize selected properties for the present application. Since the coating material is not required to serve as a structural member, a wider variety of materials may be feasible. Materials requirements are minimized, since only thin coatings are being considered. As a result, materials cost and availability of more exotic materials are less restrictive for coatings than for low-Z monolithic structures.

The possibility of in situ coating may provide additional benefits for fabrication and repair of first-wall systems. Remote coating preparation by plasma spray, chemical vapor deposition, chemical bonding, and sputtering are all considered feasible, since the required environments can be attained in the vacuum chambers. However, further development work is required to develop an in situ coating technology.

The plasma performance calculations indicated that, on the basis of predicted physical sputtering and reflection coefficients, net power could be achieved in the EPR with several low-Z liner materials. However, other potential sources of wall impurities such as blistering and thermal evaporation were not considered in these calculations. Significant erosion rates from a blistering phenomenon can occur under certain conditions. In some cases the blistering yields

exceed those from physical sputtering.[54-58] However, the blistering phenomenon is strongly affected by the microstructure of the target material.[62,63] Erosion rates produced by helium bombardment are much less for sintered material, both beryllium and aluminum, than for cast or sheet material. Microstructures similar to those of sintered products can be obtained by selected coating procedures, e.g., plasma spray techniques, in which grain size and porosity can be adjusted over significant ranges. It appears that erosion by the blistering phenomenon can be maintained at acceptable levels by appropriate choice of coating parameters.

Depending on the proposed operating temperature and coating material, thermal vaporization may also contribute to impurity effects. Thin coatings on a convectively cooled substrate tend to minimize this contribution by maintaining the low-Z material at lower temperatures than are attained with separated liner concepts. Also, more refractory-type low-Z materials such as B_4C and beryllium oxide can be used if necessary to alleviate this problem.

Two types of impurity effects may be important with regard to the selection of the liner material. One relates to the presence of high-Z impurities in the coating that can reach the plasma by normal erosion phenomena and the second relates to absorbed gases on the wall that may be removed by photodesorption. Since a minimal amount of low-Z material is required for the coating concept, high quality base material can be effectively used to minimize high-Z concentrations. Predominant impurities typically picked up during coating preparation are oxygen and nitrogen. Since these elements are fairly low-Z, moderate amounts are not prohibitive. A major source of plasma impurities in present day physics machines is the desorption of gaseous impurities from the low temperature (room or cryogenic temperature) first walls. This problem will be considerably different for power reactors in which the first-wall is operated at elevated temperatures. For example, beryllium reacts chemically with oxygen at elevated temperatures to form a very stable compound. At elevated temperatures selected coating materials will chemically react with the impurities, e.g., beryllium with oxygen, to form stable compounds which will reduce the tendency for plasma contamination by gaseous impurity desorption. This effect, which is a major source of impurities in low-wall temperature devices, may not be of significant importance for power reactors.

Vacuum properties of coated walls should not differ substantially from those of a metal wall; in fact, sputter coating of walls in present day physics machines is used to produce clean walls.[64] High helium generation rates are typical of low-Z materials. Since steady-state release rates are reached in rather short times, this produces another impurity source. This effect is not significant for thin coatings, however, as discussed below, it may be significant for thick low-Z liners.

The mechanical integrity of the low-Z coating is an important consideration as it relates to the reliability, lifetime limitation, and failure mechanisms of the coating. An advantage of the coating concept is that the substrate provides the structural support. As a result, micro-cracking of the coating caused by swelling, gas production, or differential thermal expansion may not seriously degrade the effectiveness of the coating as long as it adhered to the substrate. By judicious selection of coating material and coating preparation, optimum properties can be obtained to accommodate these effects. For proposed coating thicknesses of a few hundred micrometers, lifetimes of three to five years are predicted on the basis of sputtering erosion rates in

the EPR. However, evidence exists that a significant fraction of sputtered first-wall material is redeposited on the wall.

The failure mechanism of most concern for the coatings is flaking or loss of adherency over significant areas. Excessive flaking or spalling of the coating is not tolerable, since exposure of more than a few percent of a high-Z substrate surface, e.g., stainless steel, would probably be unacceptable. This would expose the plasma to excessive high-Z impurity from the substrate. Enhancement of the plasma impurity source would result from vaporization of the loose coating due to loss of heat transfer capability. Any loose particulate material collected at the bottom of the vacuum vessel would likely revaporize during each cycle because of the lack of heat removal capability. This problem may be alleviated if the flakes are vaporized and subsequently vapor-deposited on the wall at the end of a burn cycle. In either case, a capability for recoating appears essential, and an in situ coating capability may have important consequences.

2. Low-Z Separated Monolithic Liner

With respect to effects on plasma performance, a low-Z separated liner has much in common with the low-Z coating discussed above. The major differences relate to the technological aspects of fabricability and mechanical integrity. Therefore only the significant advantages and disadvantages of the separated liner in comparison with the coating will be discussed.

Although fabrication, installation, and repair of separated liners appears to be more difficult than that for coatings, several possibilities have been proposed that appear technologically feasible.[65-67] A major difference from the coating relates to the much larger quantity of material required, which has a significant impact on cost and materials availability if the more exotic low-Z materials are used. Since a separated liner must provide a degree of its own structural support, the materials selection is probably more limited, and since most concepts operate with radiatively cooled separated liners, problems inherent to high temperature operation will be encountered.

In most cases the impurity control capability of a separated liner should be similar to that for a coating of the same material, since the physical sputtering and reflection coefficients should be the same in both cases. If chemical sputtering is important, as in the case of carbon or graphite, the wall temperature becomes critical. A separated liner will probably operate at temperatures above the chemical sputtering range for carbon, while the operating temperature of a coating is probably near the peak of the chemical sputtering range. It is assumed that monolithic separated structures of the sintered product type can be used to maintain "blistering" erosion rates at acceptable levels. However, this requirement may further limit the selection of materials.

Impurity contributions from thermal vaporization will be more critical for the stand-off liner than for the coating because of the inherently higher operating temperature of the radiatively cooled liner. Decreases in thermal conductivity of the liner material as a result of thermally induced or radiation-induced micro-cracking will lead to higher surface temperatures that may subsequently cause excessive thermal vaporization. Lower thermal conductivities characteristic of materials with substantial porosity, which is required to facilitate gas release and to minimize blistering, will also affect the operating temperature limitations.

Additional impurity effects produced by binders, which are commonly used in many sintered ceramic liner materials, must be considered. Helium generation in thick

low-Z liners may also produce significant effects if complete helium release occurs at high temperatures, as expected. For example, the helium generation rate in an ISSEC[68] could exceed the helium generation rate from the fusion reaction. However, this is not expected to be excessive for liners less than 1 cm thick.

The fusion reactor vacuum requirements will be greater for a separated, monolithic liner of either the bumper or shingle type, since the total surface area in the vacuum vessel will be substantially increased, i.e., probably a factor of three or four. The pumping problem may be further complicated by the geometric consideration, viz., the thin annulus behind the liner which is connected to the toroidal chamber.

Several problems relating to the reliability and mechanical integrity appear to be more severe for the separated liner than for the coating concept. Since the liner must provide its own structural support, microcracking and dimensional instabilities caused by thermal and neutronic effects may lead to premature failure. Accelerated deterioration of the liner caused by higher temperatures and more severe thermal cycling may also occur as a result of reduced thermal conductivity of the liner material during operation. Erosion of the liner by sputtering, blistering, etc., should not seriously affect the useful lifetime of the liner.

The failure mechanisms associated with the monolithic separated liners appear to be more critical than those of the coating concept with respect to the effect on reactor operation and subsequent repair and maintenance. Fracture of a liner section not only could expose the plasma to substantial areas of high-Z vacuum wall, but the fractured remnants could be a source of excessive plasma contamination caused by overheating and vaporization. Repair and maintenance of the separated liner plates would probably be more difficult than in situ recoating.

3. Carbon Curtain Liner

Since the carbon curtain liner has much in common with the separated monolithic liners, only those factors that are unique to the curtain will be discussed. The fabrication considerations with respect to technological feasibility, materials cost, and materials availability are all favorable for this concept. However, methods of attachment of the curtain have not been analyzed in detail. Since carbon is particularly susceptible to chemical sputtering, high-temperature operation, with its attendant problems, is mandatory. Gross differences in the behavior of carbon cloth after bombardment by helium and hydrogen have been observed.[20-25,69]

Thermal vaporization of graphite may be critical for this concept because of thermal conductivity effects related to the geometric considerations. Low thermal conductivity through the cloth related to strand-to-strand heat transfer coefficients for the large number of fibers (of the order of a thousand per thread bundle) may create excessive temperatures at the plasma surface, leading to vaporization.

Vacuum properties of the graphite cloth will require additional pumping capability relative to a metal or low-Z coated wall. Initial outgassing will be much more difficult than for some of the other concepts, because of the additional surface area and structure of the cloth.

Mechanical integrity limitations and unattractive failure modes may limit the usefulness of this concept. Although substantial variation in the degradation of graphite cloth from neutron and ion bombardment has been reported in the literature, severe degradation of the cloth has been reported for several conditions.[21,25,69] It is well known that neutron radiation effects in graphite are strongly dependent on the type

of structure. The structure of the graphite filaments is similar to structures in which radiation-induced swelling and damage is large. Light ion irradiation can also lead to severe degradation of the cloth fibers. A major concern with the graphite cloth concept is the mode of failure. Degradation and fraying or breaking of the filiments as a result of neutron and ion bombardment may cause accelerated deterioration of the cloth and enhanced contamination of the plasma. Frayed or broken filaments protruding toward the plasma region will have a reduced heat transfer capability and will probably overheat and vaporize, further increasing plasma contamination. This potential for enhanced degradation of the cloth liner resulting from accelerated damage of frayed or fragmented pieces hanging in the plasma region is a major concern relating to the viability of this concept.

4. Low-Sputter Coating

As indicated by the light ion sputtering curves in Fig. 2, some materials, particularly tungsten, have much lower sputtering coefficients at low incident particle energies than do the other materials. Tungsten also has a relatively high threshold energy, e.g., 217 eV for D^+,[10] for light ion sputtering. As a result, the feasibility of a low-sputtering first-wall surface has been assessed. Although the light-ion sputtering coefficients are very low at ion energies below 1 keV, the allowable plasma impurity levels of these high-Z ions are extremely low. Therefore, impurity contributions from other sources such as blistering and neutron sputtering, which were negligible for the low-Z surfaces, become more important for this concept.

Tungsten is considered to be the prime candidate for the low-sputtering surface. Because of fabrication difficulties with tungsten, viz., welding and machining, the most appropriate near-term approach for this concept is a thin tungsten coating on a stainless steel substrate. This approach minimizes the quantity of material required and alleviates many of the fabrication and joining difficulties. Several coating procedures such as plasma spray, chemical vapor deposition (CVD), and sputtering have been used for applying tungsten coatings.[59] As in the case of the low-Z coatings, the plasma spray or detonation gun processes[59,60] are preferred in order to obtain appropriate microstructures to minimize blistering.[62,63] Most of the other technical considerations and the failure mechanisms will be similar to those discussed above for the low-Z coatings. Since tungsten has favorable high-temperature properties, thermal vaporization should be minimal. The maximum temperature limitations will probably be established by the substrate. A low-sputtering tungsten coating appears as technologically feasible as a low-Z coating; however, the low-Z coating seems preferable from a plasma contamination point of view. A major consideration is the substantial increase in sputtering yield with an increase in incident ion energy. The plasma performance becomes extremely unfavorable for the tungsten liner if incident ion energies exceed a few hundred eV.

REFERENCES

1. H. Wiedersich, M. S. Kaminsky and K. M. Zwilsky, *Proc. Conf. on Surface Effects in Controlled Fusion* (1974); *J. Nucl. Mater.*, 53 (1974).
2. *Proc. First Topical Meeting on the Technology of Controlled Nuclear Fusion*, April 16-18, 1974, San Diego, Calif., USAEC Rep. CONF-740402 (1974).
3. *Proc. Symp. on Technology of Controlled Thermonuclear Experiments and Engineering Aspects of Fusion Reactors*, Nov. 20-22, 1972, Austin, Texas, USAEC Rep. CONF-721111 (1974).
4. *Proc. Sixth European Conf. on Controlled Fusion and Plasma Physics*, July 30-Aug. 4, 1973, Moscow (1973).
5. *Proc. Intern. Conf. on Surface Effects in Controlled Fusion Devices*, San Francisco, Calif. (1976); *J. Nucl. Mater.* (to be published).

6. P. Sigmund, "Theory of Sputtering. I. Sputtering Yield of Amorphous and Polycrystalline Targets," *Phys. Rev.*, 184, 383 (1969).
7. S. Danyluk and P. Bratt, "Studies of CTR First-Wall Erosion by Physical Sputtering," Argonne National Laboratory Rep. ANL/CTR/TM-60 (1976).
8. D. Rosenberg and G. K. Wehner, "Sputtering Yields for Low Energy He^+, Kr^+, and Xe^+ — Ion Bombardment," *J. Appl. Phys.*, 33, 1842 (1962).
9. G. S. Kinchin and R. S. Pease, "The Displacement of Atoms in Solids by Radiation," *Rep. Prog. Phys.*, 18,1 (1955).
10. E. Hotston, "Threshold Energies for Sputtering," *Nucl. Fusion*, 15, 544 (1975).
11. R. Behrisch, "First-Wall Erosion in Fusion Reactors," *Nucl. Fusion*, 12, 695 (1972).
12. R. Kelly and N. Q. Lam, "The Sputtering of Oxides, Part I: A Survey of Experimental Results," *Radiat. Eff.*, 19, 39 (1973).
13. M. Kaminsky and S. K. Das, "14.1 MeV Neutron Sputtering of Polycrystalline and Monocrystalline Niobium with Different Surface Microstructures," *J. Nucl. Mater.*, 60, 111 (1976).
14. M. Kaminsky and S. K. Das, "Particle Emission from Solids Under 14 MeV Neutron Impact," *J. Nucl. Mater.*, 53, 162 (1974).
15. O. K. Harling, et al., "Recent Neutron Sputtering Results and Status of Neutron Sputtering," *Proc. Intern. Conf. on Surface Effects in Controlled Fusion Devices*, San Francisco, Calif. (1976); *J. Nucl. Mater.* (to be published).
16. R. G. Meisenheimer, "Some 14 MeV Neutron Sputtering Characteristic of a Polycrystalline Nb Sample," *Ibid.*
17. L. H. Jenkins, et al., "Neutron Sputtering Yields from Ni, Nb, and Au," *Ibid.*
18. J. P. Biersack, E. Santner, R. Neubert and J. Ney, "Simulation Experiments for the Sputtering of Nb by 14 MeV Neutrons," *Ibid.*
19. D. M. Gruen, "Chemical Effects of Plasma Interactions with Thermonuclear Reactor Surfaces," in *The Chemistry of Fusion Technology*, D. M. Gruen, Ed. (Plenum Press, N.Y., 1972), p. 215.
20. J. Roth, et al., "Physical and Chemical Sputtering of Graphite and SiC by Hydrogen and Helium in the Energy Range of 300 to 6000 eV," *Proc. Intern. Conf. on Surface Effects in Controlled Fusion Devices*, San Francisco, Calif. (1976); *J. Nucl. Mater.* (to be published).
21. S. Veprek, M. R. Haque and H. R. Oswald, "On the Chemical Erosion of Some Low-Z Materials by Hydrogen Plasma and on the Possibility of Regeneration of the First Wall by Low Pressure Plasma CVD," *Ibid.*
22. R. Behrisch and B. B. Kadomstsev, "Plasma Physics and Controlled Nuclear Fusion Research," *Proc. Fifth Intern. Conf. on Plasma Physics and Controlled Nuclear Fusion Research*, Tokyo, Japan (1974).
23. I. P. Busharov, et al., "Chemical Atomization of Graphite by H^+ Ions," ERDA-TR-50 (Trans.) (1975).
24. M. Balooch and D. R. Olander, "Reactions of Modulated Molecular Beams with Pyrolytic Graphite-III Hydrogen," *J. Chem. Phys.*, 63, 4772 (1975).
25. B. Feinberg and R. S. Post, "Graphite Surface Erosion and Blistering," *J. Vac. Sci. Technol.*, 13, 443 (1976).
26. A. R. Krauss and D. M. Gruen, "Determination of Ion Fraction and Energy Deuterium Bombarded Surfaces," *Proc. Intern. Conf. on Surface Effects in Controlled Fusion Devices*, San Francisco (1976); *J. Nucl. Mater.* (to be published).
27. D. M. Gruen, P. A. Finn and D. L. Page, "Vaporization Thermodynamics and Molecular Sputtering of Binary Targets," *Nucl. Technol.*, 29, 309 (1976).
28. J. N. Smith, C. H. Meyer and J. K. Layton, "Sputtering Measurements on Controlled Thermonuclear Reactor Materials Using Auger Electron Spectroscopy," *Nucl. Technol.*, 29, 318 (1976).
29. R. Weissmann and P. Sigmund, "Sputtering and Backscattering of keV Light Ions Bombarding Random Targets," in *Ion Surface Interaction, Sputtering, and Related Phenomena*, R. Behrisch, Ed. (Gordon and Breach, N.Y., 1973), p. 47.
30. W. Bauer and G. J. Thomas, "Helium and Hydrogen Re-emission During Implantation of Molybdenum, Vanadium, and Stainless Steel," *J. Nucl. Mater.*, 53, 127 (1974).
31. K. L. Wilson, G. J. Thomas, and W. Bauer, "Low-Energy Proton Implantation of Stainless Steel," *Nucl. Technol.*, 29, 322 (1976).
32. G. Carter, "Ion Reflection, Penetration, and Entrapment in Solids," *J. Vac. Sci. Technol.*, 7, 31 (1970).
33. K. Erents and G. M. McCraken, "Trapping and Re-emission of Fast Deuterium Ions from Nickel," *Br. J. Appl. Phys.*, 2, 1397 (1969).
34. D. J. Reed, et al., "Thermal Evolution Spectrometry of Low Energy Helium Ions Injected into Stainless Steel and Nickel Targets," *Vacuum*, 24, 179 (1974).
35. L. Johnson, M. J. Dresser and E. E. Donaldson, "Adsorption and Absorption of Hydrogen by Niobium," *J. Vac. Sci. Technol.*, 9, 857 (1972).
36. W. Eckstein, H. Varbeek and P. Matschke, "Backscattering of Hydrogen," *Proc. Intern. Conf. on Surface Effects in Controlled Fusion Devices*, San Francisco (1976); *J. Nucl. Mater.* (to be published).
37. E. W. Thomas, et al., "Scattering of H^+ and He^+ Ions from Surfaces: Charge State and Excited State Composition," *Ibid.*

38. O. S. Oen and M. T. Robinson, "Computer Studies of the Scattering of Low-Energy Hydrogen Ions from Polycrystalline Solids," *Ibid.*
39. K. Takayanagi and H. Suzuki, "Collection of Cross-Section Data for Atomic Processes," Plasma Physics Institute, Nagoya Univ. Rep. IPPJ-DT-48 (1975).
40. R. A. C. Riviere, "Penetration of Fast Hydrogen Atoms into a Fusion Reactor Plasma," *Nucl. Fusion*, 11, 363 (1971).
41. W. Lotz, "Electron-Impact Ionization Cross Sections and Ionization Rate Coefficients for Atoms and Ions," *Astrophys. J. Suppl.*, 14, 207 (1966-67).
42. R. L. Freeman and E. M. Jones, "Analytic Expressions for Selected Cross Sections and Maxwellian Rate Coefficients," Culham Rep. CLM-R-137 (1974).
43. C. E. Moore, "Atomic Energy Levels," Nat. Bur. STandards Circular 467 (1949).
44. R. L. Kelly and D. E. Harrison, Jr., "Ionization Potentials, Experimental and Theoretical, of the Elements Hydrogen to Krypton," *Atomic Data*, 3, 177 (1971).
45. G. R. Hopkins, "Estimation of Impurity Radiation Losses from Fusion-Reactor Plasma," *Proc. Symp. on Technology of Controlled Thermonuclear Fusion Experiments and the Engineering Aspects of Fusion Reactors*, Nov. 20-22, 1972, Austin, Texas, USAEC Rep. CONF-721111 (1974), p. 795.
46. R. F. Post, "Impurity Radiation Losses from a High Temperature Plasma," *J. Nucl. Energy*, C3, 273 (1961).
47. A. P. Vasilev, G. G. Dologov-Savelyev and V. I. Kogan, "Radiation by Impurities in a Rarified Hot Plasma," *Nucl. Fusion Suppl., Part 2*, 655 (1962).
48. E. Hinnov, "Multiple Ionization in High-Temperature Plasmas," Princeton Plasma Physics Laboratory Rep. MATT-777 (1970).
49. Yu. I. Galuskin and V. I. Kogan, "Radiation Losses in a Dense High-Temperature Hydrogen Plasma Containing Impurities," *Nucl. Fusion*, 11, 597 (1971).
50. I. Galuskin, V. I. Gervids and V. I. Kogan, "Radiation Losses in Certain Thermonuclear Systems," *Nucl. Fusion Suppl.*, 193 (1972).
51. V. M. Gusev, et a., "Conditions of Vacuum Physics for Selection of the Material of First Wall and Diaphram of the Demonstration Thermonuclear Reactor-Tokamak (T-20)," IAEA-2545 (1975).
52. T. A. Carlson, et al., "Calculated Ionization Potentials for Multiple Charged Ions," *Atomic Data*, 2, 63 (1970).
53. W. M. Stacey, Jr., et al., "Tokamak Experimental Power Reactor Studies," Argonne National Laboratory Rep. ANL/CTR-75-2 (1975).
54. S. K. Das and M. Kaminsky, "Effect of He^+ and D^+ Ion Beam Flux on Blister Formation in Niobium and Vanadium" in *Applications of Ion Beams to Metals*, S. T. Picraux, et al., Eds. (Plenum Press, N.Y., 1974), p. 543.
55. J. Roth, R. Behrisch and B. M. Scherezer, "Blistering of Niobium Due to Low Energy Helium Ion Bombardment Investigated by Rutherford Backscattering," *Ibid.*, p. 573.
56. H. Verbeek and W. Eckstein, "Radiation Blistering After H^+, D^+, and He^+ Ion Implantation into Surfaces of Stainless Steel, Mo, and Be," *Ibid.*, p. 597.
57. S. K. Das and M. Kaminsky, "Radiation Blistering of Structural Materials for Fusion Devices and Reactors," *J. Nucl. Mater.*, 53, 115 (1974).
58. G. J. Thomas and W. Bauer, "Surface Deformation in He and H Implanted Metals," *J. Nucl. Mater.*, 53, 134 (1974).
59. A. A. Bauer and J. L. Bates, "An Evaluation of Electrical Insulators for Fusion Reactors," Battelle Columbus Laboratory Rep. BMI-1930 (1974).
60. J. F. Pesek and R. Tucker, Union Carbide Corp., Indianapolis Ind., Personal Communication.
61. W. Dodson, Oak Ridge National Laboratory, Personal Communication.
62. S. K. Das, M. Kaminsky and T. D. Rossing, "Reduction of Surface Erosion Caused by Helium Blistering: Microstructural Effects," *Appl. Phys. Lett.*, 27, 197 (1975).
63. S. K. Das and M. Kaminsky, "Reduction of Surface Erosion Caused by Helium Blistering in Sintered Beryllium and Sintered Aluminum Powder," *Proc. Intern. Conf. Surface Effects in Controlled Fusion Devices*, San Francisco (1976); *J. Nucl. Mater.* (to be published).
64. S. A. Cohen, "Plasma-Wall Interaction in the ATC Tokamak," *Ibid.*
65. C. C. Baker, et al., "Experimental Power Reactor Conceptual Design Study," General Atomic Company Rep. GA-A13534 (1975).
66. M. Roberts, et al., "Oak Ridge Tokamak Experimental Power Reactor Study — Reference Design," Oak Ridge National Laboratory Rep. ORNL/TM-5042 (1975).
67. L. H. Rovner and G. R. Hopkins, "Ceramic Materials for Fusion," *Nucl. Technol.*, 29, 274 (1976).
68. R. W. Conn, et al., "New Concepts for Controlled Fusion Reactor Blanket Design," Univ. Wisconsin Rep. UWFDM-115 (1974).
69. R. Ekern, S. K. Das and M. Kaminsky, "The Temperature Dependence of Surface Damage in Graphite Cloth Irradiated with Deuterons and Helium Ions," *Proc. Intern. Conf. on Surface Effects in Controlled Fusion Devices*, San Francisco (1976); *J. Nucl. Mater.* (to be published).

TOKAMAK ENGINEERING TECHNOLOGY FACILITY

W. M. Stacey, Jr., M. A. Abdou, C. C. Bolta, J. A. Fasolo
R. L. Kustom, V. A. Maroni, R. F. Mattas, F. E. Mills,
B. Misra, J. S. Moenich, J. S. Patten, D. L. Smith,
H. C. Stevens, S-T. Wang, C. K. Youngdahl

CTR Program
Argonne National Laboratory
Argonne, Illinois 60439

and

D. L. Jassby

Plasma Physics Laboratory
Princeton University

The Tokamak Engineering Technology Facility (TETF)[1] is a neutral beam driven D-T machine with a major radius (R) of 3 m and a plasma current (I_p) of 1.4 MA based on the counterstreaming-ion-torus mode of operation. It can be used to demonstrate fusion reactor technology required for the Experimental Power Reactor[2] and to serve as a radiation test facility.

PLASMA PHYSICS AND REACTOR PERFORMANCE

The TETF plasma will be fueled and heated by D and T neutral beams, injected parallel and antiparallel, respectively, to the toroidal magnetic field. These beams are used to stack large densities of oppositely traveling D and T ions, which together with neutralizing electrons, form a CIT (counterstreaming-ion torus) plasma.[3] This system of counterstreaming ions has a large fusion reactivity, even for rather modest injection energies, because of nearly head-on nuclear collisions between D and T ions. This mode of operation offers the most powerful means of generating a large fusion-neutron flux in a small-sized tokamak with modest confinement parameters.

Ideal CIT operation is attainable only if the inward diffusion of low-energy neutrals and ions to the reacting region is small compared with the rate of energetic particle injection by the neutral beams.[3] With an increasing population of low-energy ions, the reactor performance is degraded; in the limiting case, the plasma must operate in the TCT (two component torus) mode, fueled and heated by D and T injection. For injection energies $\sim$ 60 keV, the ideal CIT has a Q (fusion power/injection power) about six times that of the TCT. The key to achieving optimal reactor performance is adequate pumping of the neutral gas in the scrape-off channel outside the discharge, in order to minimize the influx of recycled plasma.

The present design specifies plasma operation in the transition regime between the ideal CIT and TCT modes. Injection of 15 MW of 60 keV D^0 beams and 15 MW of 90 keV T^0 beams maintains a plasma of $\langle n_e \rangle$ =

4×10^{13} cm^{-3} and T_e = 4.5 keV with energy confinement of $n\tau_E = 2.6 \times 10^{12}$ sec/cm^3. The Q value is 0.70, or 45% of the ideal CIT value. Other important plasma parameters are B_t = 4.0 T, vertical elongation $\leq$ 1.5 and I_p = 1.4 MA. The 14 MeV neutron production rate during the burn is 7.3×10^{18} sec^{-1}, which leads to a peak neutron current of 7.1×10^{12} n/cm^2/s. Plasma performance parameters are summarized in Table 1 for operation in the CIT mode.

TABLE 1. TETF Plasma Performance Parameters

Aspect ratio, $A = R_o/a$	5.45
Safety factor, $q(a)$	3.0
β_p (excluding alphas)	3.6
Magnetic field on axis, B_t	4.0 T
Plasma current, I_p	1.4 MA
Energy confinement, $\langle n_e \rangle \tau_E$	2.6×10^{12} sec/cm^3
Electron density, $\langle n_e \rangle$	4.0×10^{13} cm^3
Electron temperature, $\langle T_e \rangle$	4.5 keV
Q	0.7
Beam Power	
60 keV D^0	15 MW
90 keV T^0	15 MW
Thermal Power	51 MW
14 MeV neutron power flow to wall	0.130 MW/m^2
14 MeV peak neutron current	7.1×10^{12} n/cm^2/sec

All fueling is carried out by the injected beams, and the flux swing of the ohmic current transformer allows a burn time of $\sim$ 1 min, with a duty cycle of $\sim$ 75%. The nominal burn cycle is given in Table 2. Even longer burn times are possible when a significant portion of the plasma current is driven by the streaming ions.

REACTOR LAYOUT

The reactor, which weighs 2000 tons, is assembled inside the TETF facility. A cross section of the torus is shown in Figure 1 and principle geometrical parameters are given in Table 3. The elliptical/oval-shaped plasma has a minor radius of 0.55 m and an elongation ratio of $\leq$ 1.5. Surrounding the plasma is a type 316 stainless steel first-wall vacuum vessel consisting of twenty-four oval-shaped toroidal segments 2.2 m high by 1.7 m wide. These twenty-four segments are flanged and bolted together to form an irregular torus whose major diameter is 6 m. The inner surface of the vessel is coated with a low-Z material. An experimental volume, $\sim$ 0.20 m wide by 0.8 m high, has been provided within the vessel in the outer wall region. First wall vessel segments have been designed to be removed and replaced with relative ease to extend the flexibility of the reactor as

TABLE 2. Burn Cycle Sequence

Inject gas and form target plasma at $I_p \sim 500$ kA	0 - 0.5 s
Begin injection, raise I_p to 1400 kA, attain equilibrium plasma	0.5 - 2 s
Burn (continuous injection)	2 - 44 s
Shut-off beams and ramp-down plasma current	44 - 46 s
Exhaust torus to 10^{-6} torr and charge OH transformer primary	46 - 60 s

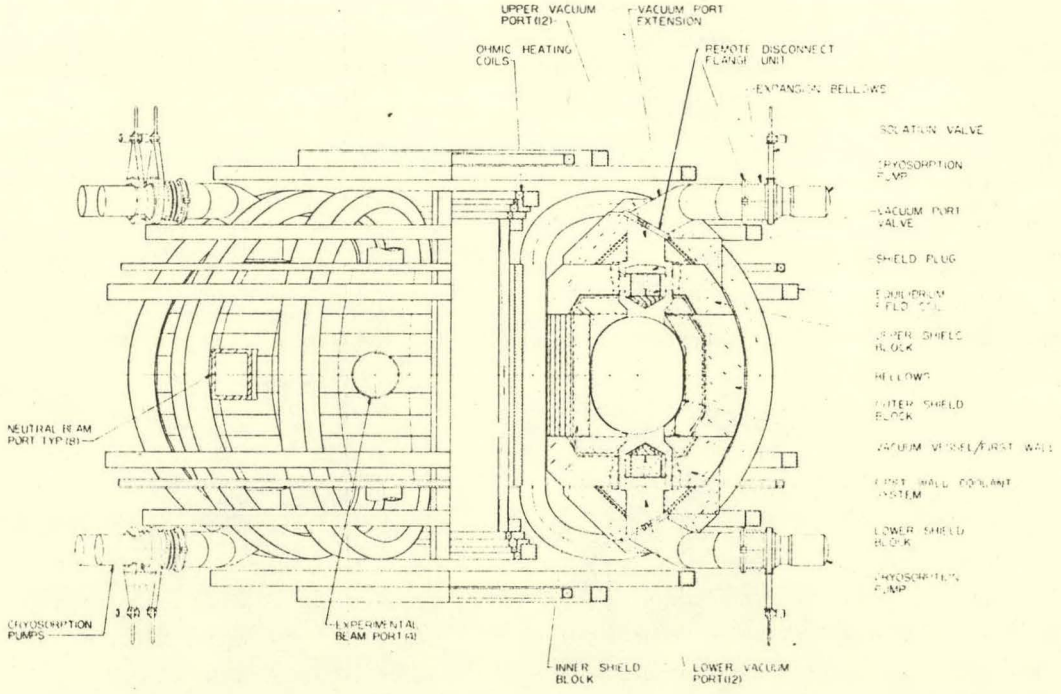

FIGURE 1. TETF Cross Section

TABLE 3. Geometrical Parameters

Major radius, R_o	3.0 m
Plasma	
radius, a	0.55 m
elongation	$\leq$ 1.5
scrape-off region	0.2 m
volume	30.7 m^3
Vacuum chamber	
nominal dimensions (oval)	1.5 m x 2.25 m
nominal wall area	131 m^2
test region on outside	$\sim$ 0.2 m x 0.8 m
nominal volume	58.5 m^3
Magnet shield thickness	
inside	0.9 m
outside	1.05 m
top and bottom	> 1 m
Toroidal-field coils (12)	
bore (pure-tension "D")	3.65 m x 6.0 m
thickness (including cryostat)	0.55 m
Support cylinder thickness	0.17 m
Central core radius, r_v	
air core	0.48 m
including Cu OH coils	0.63 m

a test facility. All surfaces of the vessel are water cooled.

Shield blocks, $\sim$ 1 m thick, surround the first wall vessel. The blocks are of a slab-type geometry. Ten pieces are used to shield two adjacent first wall segments for a total of 120 major blocks for the entire reactor. Inner and outer shield block arrangements are different. The inner blocks located between the first wall and the center core of the reactor are made of alternate layers of stainless steel and B_4C to give high radiation attenuation in the limited space. The outer shield blocks are dominantly lead mortar and are water cooled using a separate cooling system. Removal of the shield blocks has been simplified to accommodate experiments and first wall replacement. The outer shielding blocks can be modified to house many types of experiments with a minimum cost.

TOROIDAL FIELD COILS

Toroidal-field coils surround the reactor first wall and shield block assembly. Each coil is approximately 7 m high by 4.7 m wide and $\sim$ 0.6 m thick, weighing $\sim$ 35 tons. The TF coils are supported by an inner cryogenically-cooled cylindrical support spindle common to all TF coils and a lower support leg extending down and outward to the reactor building floor. The TF coil system includes load dump resistors, torque support frame, cryogenic and power supply systems. Superconducting toroidal field coil parameters are shown in Table 4.

POLOIDAL FIELD COILS

The ohmic heating (OH) coil system consists of twelve ring coils and a central

TABLE 4. TETF Superconducting Toroidal-Field Coil Parameters

Materials	
superconductor	NbTi
stabilizer	Cu
insulator	fiberglass epoxy
support	316 stainless steel
Coil dimension	
bore (pure-tension "D")	3.65 m x 6.0 m
thickness (including cryostat)	0.55 m
Number of coils	12
Field ripple, maximum	0.99%
Access between coils, maximum	2 m
Operating temperature	$3^{o}K/4.2^{o}K$
Peak field	10 T/8 T
Superimposed ac field	0.2 - 0.4 T
Operational current (10 T)	10,000 A
Average current density (10 T)	2650 A/cm^2
Ampere-turns	
total	59.5 MA-turns
per coil	4.96 MA-turns
Stored energy	
total	3100 MJ
per coil	258 MJ

solenoid. All coils are water-cooled copper. The 6 m high central coil, weighing ~ 45 tons, is positioned in the center of the TF coil inner support spindle. Four thin ring coils are located above and four coils below the central coil. Two sets of larger ring coils circumscribe the reactor TF coils from above and below the midplane, the largest being 11 m in diameter. The outer OH coils are supported and restrained in the magnet support/torque frame, which is attached to the reactor floor. The inner coils are supported through the central pedestal foundation.

Twelve equilibrium-field (EF) coils complete the magnet coil system. Eight coils are clustered adjacent to the inner OH coil sets; four above and four below the reactor, while four larger ring coils are distributed symmetrically around the outer extremities of the TF coils. The largest reactor coil is the outer EF coil whose diameter is 13 m and whose weight is 58 tons. The EF coils, like the OH coils, are of water-cooled copper design and are supported and restrained by the same magnet support/torque structure. Ancillary systems include the power supply, switch gear, power leads and water coolant system. Water-cooled copper poloidal field coil parameters are shown in Table 5.

VACUUM PUMPING

A large vacuum system is required to limit plasma recycling. Twenty-four 0.75 m diameter ports are located symmetrically around the first wall between TF coils both

TABLE 5. TETF Water-Cooled Copper Poloidal-Field Coil Parameters

Equilibrium-field Coils

Conductor	
material	Cu
volume	20.4 m^3
current density	1500 - 750 A/cm^2
Power dissipation	
instantaneous	21.5 MW
cycle-averaged	15 MW
Inductive stored energy	68 MJ
Operational current	30 kA
Operational voltage	5 kV
Ampere-meters	153 x 10^6
Volt-sec to plasma	7.8 volt-sec
Field at plasma	0.28 T
Number of coils	12

Ohmic-heating Coils

Conductor	
material	Cu
volume	6.3 m^3
current density	2534 A/cm^2
Maximum peak field	6.37 T
Power dissipation	
beginning of cycle	54 MW
end of cycle	77 MW
Inductive stored energy	116 MJ
Operational current	30 kA
Operational voltage	5 kV
Ampere-meters	321 x 10^6
Volt-sec to plasma	
startup	4.2 volt-sec
burn	5.0 volt-sec
Number of coils	12 plus solenoid

above and below the reactor centerline. Each of the ports extends outward into an annular shield plug volume containing a quick-closing valve in its outer extremity. Trapped gases will flow through the annulus provided around the centered shield plug and out into a removable Y-shaped extension duct to two 25,000 liter/sec or larger cryosorption pumps. The pumps are operated one at a time allowing for on-line regeneration of the off-cycle unit. Isolation valves are provided to allow for this regeneration purpose. In addition to the cryosorption pumps, a series of blowers and diffusion pumps are supplied for initiating the pumpdown in the first-wall

torus from atmospheric conditions. The design provides a method to accumulate fuel from all components including any leakage of fuel from the vacuum system during any of the operational procedures. Maintenance and repair of all vacuum components is accomplished through isolation, removal and replacement using special remote-operated flange connections, valves and lifting dollies.

All major vacuum equipment will be located within the reactor containment shell, with the exception of the helium compressors. This is a safety measure to minimize hazards.

NEUTRAL BEAMS

Eight neutral beam injector units, each containing two ion sources, ring the reactor. The beams are aimed tangentially into the plasma in a symmetrical pattern of clockwise and counterclockwise direction. Each beam enters on the centerline of the vacuum vessel at an angle of $\sim 45^{o}$ to the line of tangency through an 0.55 m wide by 0.8 m high rectangular opening, grazing the inside plasma toroidal centerline. The injector duct is shielded as it leaves the reactor. Each injector is attached to the reactor with an isolation valve. Each beam line consists of a source, accelerator, separator, neutralizer and ancillary vacuum and energy recovery equipment. Two lines are stacked in each injector and they aim into the torus from 6^{o} above and 6^{o} below the median plane. The beam length to the reactor first wall is $\sim$ 7 m. Table 6 shows neutral beam injection system parameters.

POWER SUPPLIES

Major power supply equipment is located in the adjacent building. However, hookup is made with special lead lines and step-up transformer units placed at the base of the injector units. A neutral-beam test facility is located on the reactor floor within the reactor containment shell. This area, enclosed by radiation shielding, contains remote maintenance and hookup equipment and a permanent power supply.

The power supplies for the OH coils and EF coils are based on normal conducting copper windings with an optional superconducting design. An important feature is that the level of powers for both coils are within the range of operation for pulsing directly off the power line.

The OH coil provides 4.2 V-s to heat the plasma and 5.0 V-s to maintain plasma current during the burn phase, and is charged to 30,000 A in one direction prior to heating and discharged to zero in two seconds for heating. After crossing zero field, the coil current is increased slowly to maintain the plasma current. A full 5.0 V-s requirement during burn requires a coil current of 35,700 A. Resistive power loss in the coil reaches 53.9 MW at 30,000 A. The coil time constant is 3.35 s.

The power supply envisioned to meet these requirements is a phase-controlled, polyphase SCR rectifier driven direc'ly off the power line. The main constituents of the power supply are the polyphase transformer, the SCR rectifier banks, the SCR reversing switches and an optional filter.

The EF coil is designed to operate at 30,000 A and store 68 MJ of energy. The peak resistive power loss in the coil is 21.5 MW, but because the magnet must be able to reach 30,000 A in 2 s, the possibility exists for drawing as much as 79.3 MW from the line. However, the time for which EF coil power is increasing roughly corresponds to the time that the

TABLE 6. TETF Neutral Beam Injection System

	D^0	T^0
Neutral beam power (MW)	15	15
Neutral beam energy (keV)	60	90
Number of injectors	4	4
Number of ion sources per injector	2	2
Ion beam current per source (A)	69	46
Beam composition ($X^+/X_2^+/X_3^+$)	0.75/0.18/0.07	0.75/0.18/0.07
Plasma emission current density (A/cm^2)	0.300	0.245
Type of grid	multi-aperture	multi-aperture
Tritium to torus (gm/hr)	-	∿ 15
Gas efficiency	0.45	0.45
Pulse length	dc	dc
Overall neutral injector efficiency	0.56 - 0.59	0.56 - 0.59

OH coil is feeding energy back into the line. The system is designed to take advantage of the energy balance to reduce the peak power demand during this 2 s period.

After the EF coil reaches full current, the coil voltage can be reduced to just satisfy resistive power requirements. Again, the power supply would be a phase-controlled, SCR rectifier type without the reversing circuits. The peak charging voltage required by the EF coil power supply is 2650 volts.

The TF coil power supply represents no major design difficulty. Its size is entirely dependent on how rapidly the coil is to be charged. A 70 KW supply will charge the coil in twenty-four hours and the 425 KW supply will charge the coil in four hours.

The neutral-beam power supply must provide approximately 22.5 MW at 60 kV for the D beams and 22.5 MW at 90 kV for the T beams. The power is taken off the electrical grid. Polyphase SCR rectifiers are the most likely choice for developing these voltages. Spark protection probably can be provided by vacuum switch tubes for these voltage ranges. A high frequency polyphase SCR rectifier with a saturated time delay transformer (STDT) could be considered as an alternative to the above system.

Characteristics of these power supplies are summarized in Table 7.

TRITIUM HANDLING

Essentially all of the tritium entering the torus during operation of the TETF is delivered by the T^0 neutral injectors. Maintaining a feed rate to the torus of ∿ 15 gram/hour requires that ∿ 120 gram/hour be supplied to the T^0 neutral injection system. Coupling these feed rates with other considerations related to injector pump turn-around times, processor hold-ups and reserve storage requirements has led to an estimated tritium inventory for the TETF of ∿ 650

TABLE 7. TETF Power Supply Parameters

Power pulsed directly off-line	
power	100 MW
voltage	132 kV
OH coil system (copper coils)	
type	polyphase SCR rectifier
peak voltage	2150 volt
EF coil system (copper coils)	
type	polyphase SCR rectifier
peak voltage	2650 volt
TF coil system	70 kW
Neutral beam injection system accelerators	
type	polyphase SCR rectifier
D injection (60 kV)	22.5 MW
T injection (90 kV)	22.5 MW

grams. TETF fuel recycle and processing is based on four T^0 neutral injectors, each equipped with two interchangeable gas pumping systems that are turned over for regeneration on an hourly basis. The tritium inventory within each injector is cleaned up twice a day by one of three parallel exhaust processing systems. Pumping and processing for the four D^0 neutral injectors is carried out in essentially the same manner as described above for the T^0 injection systems. The plasma exhaust is processed by a separate system and is turned around once a day. Each of the three processing systems (for the T^0 injectors, D^0 injectors and the plasma exhaust) contains: a purification train to remove non-hydrogeneous impurities and a cryogenic distillation cascade to carry out the required hydrogen isotope separations. Characteristics of the tritium systems are summarized in Table 8.

The TETF first wall consists of a type 316 stainless steel vacuum vessel made up of twenty-four oval cross section toroidal segments, 2.2 m high and 1.7 m wide. The twenty-four segments are flanged together to form an irregular torus with a major diameter of 6 m. The walls of the chamber are formed from two parallel layers of integrated cooling panel (overall thickness $\leq$ 2 cm/panel) that are welded to the mating end flanges of each segment and cross braced with lateral spars for additional support. The surface of the inner cooling panel facing the plasma is coated with a low-Z material to minimize degradation of plasma performance by sputtered high-Z materials. Both of the first-wall panel layers are cooled with water and the maximum temperature reached at any point in the vacuum vessel is < 400°C. Even in the regions of highest flux the strength properties of the 316 stainless steel structure will be satisfactory for a period in excess of five years.

The TETF shield consists of a series of slab-type blocks surrounding the vacuum vessel. The inner shield blocks (between

TABLE 8. TETF Tritium System Characteristics

Injection system requirements	
T^o injection rate to plasma	15 gm/hr
T^o input rate to injectors	120 gm/hr
Tritium inventory per injector	15 gm
Inventory disposition	
Injector systems (4)	120 gm
Processors for injector recycle (3)	45 gm
Plasma exhaust and processing system (2)	360 gm
Contingency reserve storage (1)	120 gm
Total	~ 650 gm
Tritium consumption rate	880 gm/yr
Tritium accumulation in first wall H_2O coolant after 1 year of operation	10^3 - 10^4 Ci

the vacuum vessel and interior straight section of the D-shaped TF coil) are composed of stratified layers of stainless steel and B_4C in a configuration designed to maximize the radiation attenuation in an 0.9 m thick zone. The upper, lower and outer shield blocks are composed of a 1.05 m thick zone of stainless steel, lead mortar and a limited amount of B_4C.

Characteristics of the first wall and magnet shield are summarized in Table 9. The nuclear performance is summarized in Table 10.

TABLE 9. TETF First wall and Magnet Shield Parameters

First Wall	
Material	low-Z coated 316 SS
Thickness	4 cm
Construction	2 layers of integrated coolant panel
Coolant	H_2O
temperature (inlet/exit)	38°C/< 100°C
pressure	< 2000 psi
Maximum temperature in SS	290°C
Maximum ΔT through coolant panel	150°C
Maximum ΔT during burn cycle	140°C
Maximum thermal strain variation	
fully restrained	0.35%
restrained against bending	0.15%
Magnet Shield	
Material	SS/B_4C/Pb-mortar
Thickness	
inside	0.9 m
outside	1.05 m
top and bottom	1.05 m
Coolant	H_2O
Maximum structural temperature	< 200°C

TABLE 10. Summary of the Nuclear Performance of the TETF First Wall and Shield

Average neutron wall loading	0.2 MW/m^2
Assumed duty factor	50%
First Wall	
Average fusion neutron current to wall	8.86×10^{12} $n/cm^2/s$
Maximum neutron fluence (0-15 MeV)	2.25×10^{21} $n/cm^2/yr$
Maximum gamma-ray fluence (0-15 MeV)	4.94×10^{20} $photon/cm^2/yr$
Surface heating (plasma and beam ions, neutrons and radiation)	25 W/cm^2
Maximum nuclear heating	2.1 W/cm^3
Atomic displacement	1.1 dpa/yr
Helium production	21 appm/yr
Hydrogen production	52 appm/yr
Specific radioactivity ($curies/cm^3$ after 5 years of operation)	20
Maximum Values in TF Coil	
Neutron fluence	2.1×10^{16} $n/cm^2/yr$
Gamma-ray fluence	2.9×10^{15} $photon/cm^2/yr$
Radiation-induced resistivity in Cu stabilizer (1 $MW-yr/m^2$)	6.6×10^{-9} Ω-cm
Dose to mylar (1 $MW-yr/m^2$)	1.0×10^8 rad
Nuclear energy deposition per coil	11 watt
Total nuclear energy deposition (12 coils)	132 watt

REFERENCES

1. W. M. Stacey, Jr., et al., Tokamak Engineering Technology Facility Scoping Study, ANL/CTR-76-1, Argonne National Laboratory, (March, 1976).
2. W. M. Stacey, Jr., et al., "Tokamak Experimental Power Reactor Conceptual Design, ANL/CTR-76-3, Argonne National Laboratory, (August, 1976).
3. D. L. Jassby, Nuclear Fusion, 16 (1976), p. 15.

REVIEW OF THE ANL PROGRAM ON LIQUID LITHIUM PROCESSING AND TRITIUM CONTROL TECHNOLOGY*

W. F. Calaway, E. H. Van Deventer, B. Misra, C. J. Wierdak** and V. A. Maroni

ARGONNE NATIONAL LABORATORY

Bench-scale experiments are currently in progress at ANL to remove tritium and other nonmetallic elements (H, D, C, N, and O) from molten salts. Results are reported for sparging experiments in which protium and deuterium at concentrations of 2 to 10 wppm have been recovered from LiCl-KCl and LiF-LiCl-LiBr solutions using HCl as the sparge gas. These results give firm evidence that a molten salt extraction process has the potential to maintain tritium levels in liquid lithium fusion reactor blankets at or below 1 wppm. Initial experimental tests on electrochemical evolution of protium and deuterium using specially prepared porous graphite electrodes are also presented. A lithium processing test loop (LPTL) is described which will be used to study the molten salt extraction concept on a larger scale. In a second project at ANL, experiments to measure hydrogen permeation through selected materials are continuing in an effort to develop barriers to tritium migration. Results are presented for experiments performed on metallurgically bonded aluminum bronze/304-SS multiplexes and on Haynes alloy 188 in the temperature range 200 to 700°C and with hydrogen (protium) driving pressures of from 0.3 to 200 Torr. A high resistance to permeation has been observed for aluminum bronze which is attributed to impurity coatings on the metal surface. The hydrogen permeability of Haynes alloy 188 was found to be in the same range as that of most conventional austenitic alloys. Experiments examining the thermal conductivity of multiplexes are also described.

INTRODUCTION

As demonstration of sustained D-T fusion approaches, it is becoming increasingly more imperative to develop the support technology required to transform proof-of-theory plasma experiments into practical power generating devices. An important aspect of this transformation will be demonstration of technology to contain and control tritium in fusion reactor systems. From an economic viewpoint, it is essential to minimize costly tritium inventories. This will require efficient recovery of tritium from the fusion reactor blanket where it is bred. In addition, for

*Work performed under the auspices of the U.S. Energy Research and Development Administration.

**Student Aide from Illinois Institute of Technology

D-T fusion power reactors to become the clean and safe energy source which has been envisioned, the tritium released to the environment will have to be maintained at very low levels. This too dictates minimizing tritium inventories as well as devising methods of inhibiting tritium migration.

An experimental research program is in progress at Argonne National Laboratory to evaluate and develop selected aspects of the required tritium technology. The projects currently being pursued are (1) permeation experiments to develop barriers to tritium migration through reactor structures and (2) developmental work on reactor blanket purification systems which can maintain low tritium inventories. To examine permeation barriers, studies are being conducted on proposed reactor structural materials, multilayer metal laminates, and impurity coatings on metals. Reactor blanket purification has focused on a molten salt extraction process for liquid lithium. Recent progress in these endeavors is presented below.

LIQUID LITHIUM PROCESSING

Because liquid lithium is a leading candidate for first generation fusion reactor blankets, initial studies have concentrated on schemes for removing tritium from liquid lithium. This has proven to be a formidable task since lithium has great tenacity for hydrogen isotopes[1] and since it will probably be necessary to maintain tritium levels in the lithium blanket at ≤ 1 ppm.[2,3] A method under development at ANL which shows promise in achieving the required low tritium level is the molten salt extraction process.[4,5] Besides being well suited for tritium control, this process has the additional advantage of simultaneously removing other nonmetallic impurities (e.g., H, D, C, N, and O) from the lithium blanket, thus minimizing the corrosive effects of lithium.

Studies previously conducted at this laboratory found that tritium (present as LiT) is preferentially extracted from liquid lithium to selected molten salts when the two liquids are contacted.[4] Based on this study, a processing scheme was proposed whereby tritium could be removed from a liquid lithium fusion reactor blanket by (1) contacting a portion of the lithium from the blanket with a molten salt, (2) reseparating the salt and metal phases, and (3) returning the purified lithium to the blanket while reprocessing the salt to recover the tritium. In development of this process, the present and most immediate task has been to experimentally verify the salt reprocessing step. To this end, bench-scale experiments are being conducted to evaluate gas sparging and electrochemical techniques as possible methods for removing deuterium and protium (used as substitutes for tritium) from molten salts.[5] In addition, an engineering scale lithium processing test loop (LPTL) has been designed which will allow experimental examination of molten salt and other blanket processing procedures on a larger scale.

Gas Sparging Studies

Sparging experiments have been performed to recover both protium and deuterium from molten salts using HCl as the reactive gas and either LiCl-KCl or LiF-LiCl-LiBr as the salt medium. In the experiments, Li and LiD (or LiH) are dissolved in a pot of molten salt. The lithium metal is introduced to simulate the anticipated condition of the salt when it returns from the lithium contacting operation in an actual processing system. A quantity of HCl equimolar to the Li plus LiD present in the salt is bubbled through the molten solution in a closed loop producing the reactions,

$$LiD + HCl \rightarrow LiCl + HD \qquad (1)$$

$$Li + HCl \rightarrow LiCl + 1/2\ H_2. \qquad (2)$$

Since hydrogen is practically insoluble in the molten salts under study, it enters the vapor phase above the salt when liberated by sparging. The rate and extent of the reactions are followed by monitoring the hydrogen isotopes in the gas stream above the salt using a mass spectrometer. Details of the experimental procedure are given elsewhere.[5,6]

Initial experiments examined recovery of deuterium from LiCl-KCl eutectic as a function of such parameters as (1) the concentration of LiD, (2) the concentration of Li, (3) the amount of HCl, and (4) the salt temperature. Results which typify this series of experiments are given in Fig. 1, where the concentration of HD above the salt (as determined mass spectroscopically) is recorded with time. As seen in Fig. 1 and as found in all experiments with LiCl-KCl, addition of LiD to the salt caused HD gas to be generated spontaneously before the sparge gas was introduced. At a later time, additional HD is generated as HCl is added to the system. Once the reactions have reached completion, the gas stream is directed through a hot titanium bed which getters out the hydrogen isotopes as shown in Fig. 1 by the return of the HD signal to its original base line. The spontaneous generation of HD is unexpected and was at first attributed to residual acidity or impurities in the system.[5] However, when excess metallic lithium, which should tie up impurities and chloride, is added to the salt, as in Fig. 1, the spontaneous generation of HD persists. In fact, no amount of Li or LiD appears to alter this spontaneous conversion. Also typical of these sparging experiments is a low HD recovery efficiency. Generally, less than 50% of the deuterium added to the salt is recovered as HD. For the experiment in Fig. 1, only 38% was recovered.

To explore both the spontaneous generation and poor recovery of HD, experiments were performed where protium was sparged from the molten salt with HCl. Results from these experiments revealed the following: (1) recovery of H_2 was significantly improved

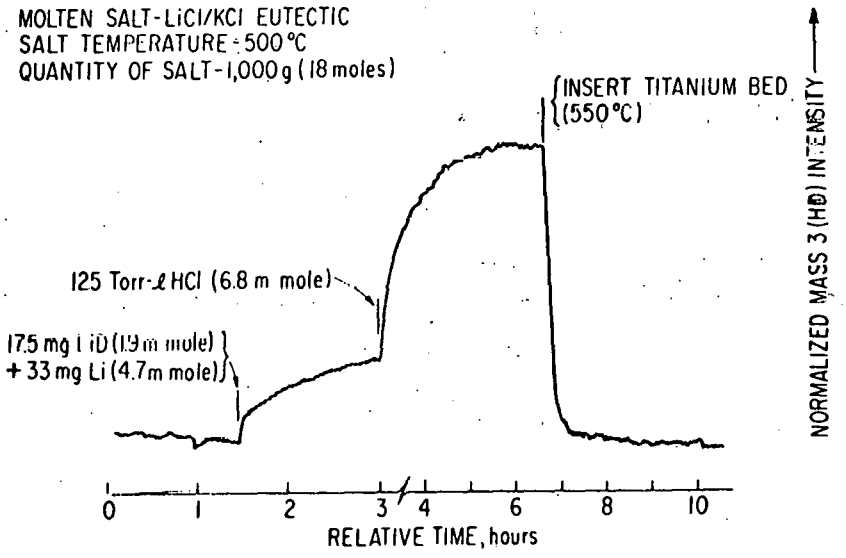

FIGURE 1. Results of a Typical Gas Sparging Experiment to Recover Deuterium from a Solution of LiD in LiCl-KCl Eutectic

(compared to the HD recoveries) being in the range of 70 to 100%; and (2) the amount of H_2 spontaneously generated represents, within experimental error, all of the protium added in the form LiH. That is, 100% of the hydride added to the molten salt spontaneously converts to H_2. This suggests that D_2 was formed in the LiD experiments and that the observed HD concentration was controlled by the amount of H_2 available for the exchange reaction

$$D_2 + H_2 \rightleftarrows 2HD. \qquad (3)$$

The reason for the spontaneous generation of D_2 and H_2 is believed to be associated with the molten salt which was selected. It has previously been recognized that metallic lithium can reduce the potassium cation in LiCl-KCl.[7,8] It also appears that lithium hydride can reduce potassium cations by the reaction

$$LiH + KCl \rightleftarrows LiCl + K + 1/2\ H_2. \qquad (4)$$

The potassium generated by the above reaction vaporizes; thus, the salt is a sink for lithium and any hydride in the salt will decompose. The implications of the above reaction do not favor the use of LiCl-KCl eutectic in any large-scale extraction process since significant amounts of potassium metal would dissolve in the liquid lithium stream returning to the reactor blanket.

Experiments were, therefore, initiated on a molten salt which contains no potassium. An all-lithium halide solid solution (9.5 w/o LiF, 22.1 w/o LiCl, and 68.4 w/o LiBr) was prepared and experiments to recover LiH

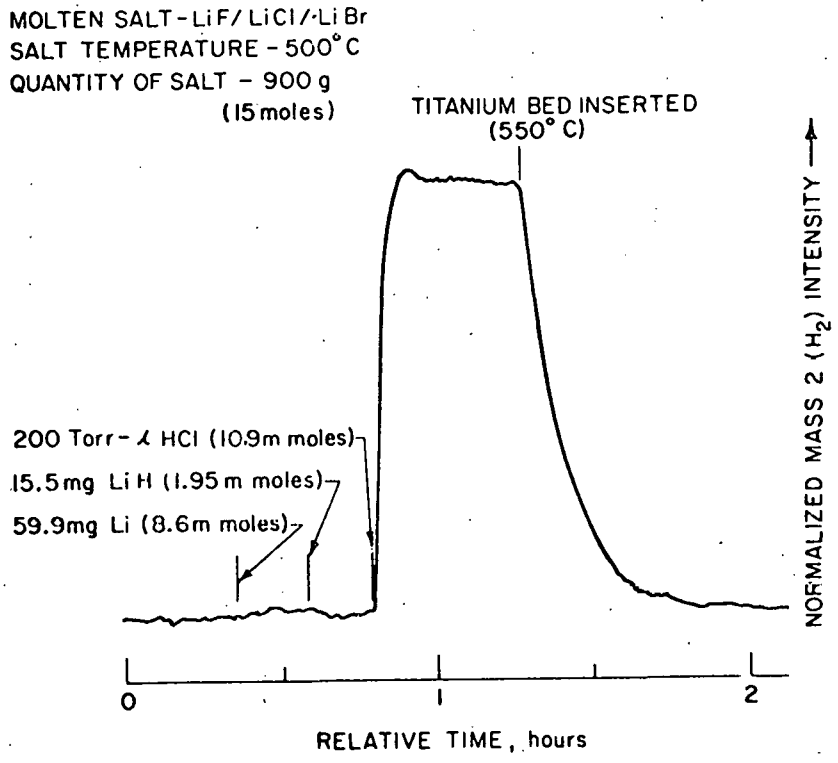

FIGURE 2. Results of a Typical Gas Sparging Experiment to Recover Protium from a Solution of LiH in LiCl-KCl Eutectic

from this salt were performed. Results for one such experiment are given in Fig. 2. Note that spontaneous generation of H_2 did not occur when LiH was added to this salt. The hydride remained in the salt until it was sparged with HCl. Recovery efficiencies for extraction of LiH from the all-lithium cation salt were typically in the range 70 to 100% for hydride concentrations of 5 to 2 wppm. For Fig. 2, the recovery was 84% of the 2 wppm hydride concentration in the salt. Also note that the protium came out of this salt an order of magnitude faster than when using LiCl-KCl. This very rapid extraction is consistent with the recovery rate expected for the sparging reactions [eqs. (1) and (2)]. In the LiCl-KCl experiment, the rate of spontaneous generation of hydrogen isotopes probably represents the rate of vaporization of potassium after its reduction.[8] The secondary rise upon addition of HCl in the LiCl-KCl experiments is controlled by the rate of isotopic exchange of the hydrogen isotopes [eq. (3)].

Using the all-lithium salt, extraction of LiD was also examined. In these experiments, the three mass peaks of interest (H_2, HD, and D_2) were continually scanned by the mass spectrometer. Results for one such experiment are given in Fig. 3. In the experiment shown, 100 Torr-ℓ of D_2 added to the cover gas was reacted with lithium added to the salt (not shown in Fig. 3). The first lithium additions did not lower the D_2 cover gas concentration presumably due to the lithium reacting with HCl or impurities in the salt. Further additions of lithium reduced the D_2 concentrations to background levels. (An experiment such as this was unsuccessful when LiCl-KCl eutectic was used as the molten salt medium.) At time, t = 15 minutes in Fig. 3, the LiD previously formed was sparged out of the salt with 400 Torr-ℓ of HCl. As is seen, H_2, HD, and D_2 are all generated from the sparging reactions. The relative heights of the three molecular isotopes confirm that they are equilibrated via eq. (3). The amount of deuterium extracted either as HD or D_2 is 96% of the original amount added to the salt. This represents, within experimental error, total recovery of the deuterium.

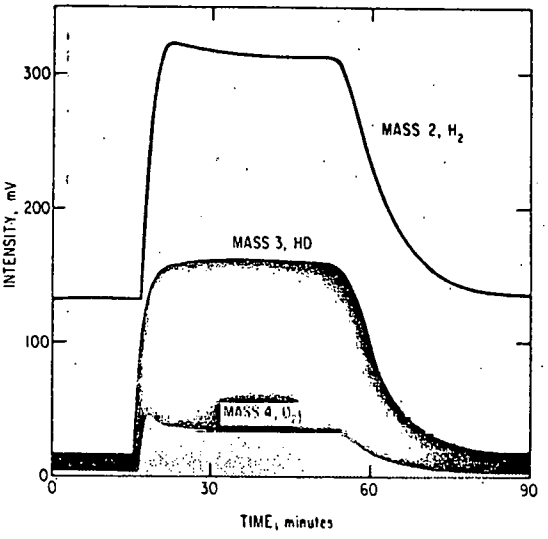

FIGURE 3. Recovery of 0.1 g LiD from 900 g LiF-LiCl-LiBr at 500°C. At time, t = 15 min, 400 Torr-ℓ of HCl was added to the sparge stream, and at t = 50 min, the gas stream was directed through a hot titanium bed.

The extraction of LiH and LiD from a molten salt (LiF-LiCl-LiBr) by sparging has been successfully demonstrated as described above. Removal appears to be complete without adding excess HCl. The complication of having the salt saturated with metallic lithium does not interfere with the recovery process beyond requiring additional amounts of HCl to react out the metal. In short, gas sparging has proven to be a viable technique for removing hydrogen isotopes from molten salts at the <5 wppm level. With further optimization and refinement of the

processing methodology, it is reasonable to expect that the steady state levels can be reduced to <1 wppm hydrogen isotopes in the corresponding lithium circuits.

Electrochemical Studies

Experiments are presently under way to develop the methodology for electrochemical extraction of hydrogen isotopes from hydride solutions in molten salts. The advantages of the electrochemical method over the sparging method are (1) reduction of interference from the metallic lithium dissolved in the molten salt and (2) elimination of the need to handle a corrosive sparge gas such as HCl. The experimental apparatus used for these studies is essentially the same as for the sparging experiments. Argon is circulated in a closed loop through the molten salt while deuterium concentrations in the argon stream are monitored with a mass spectrometer. A hollow porous electrode is used both as the gas bubbler and the anode of the cell so that the D_2 generated by electrolysis is swept out of the salt by the circulating argon before the lithium which saturates the salt can back react with the D_2. The cathode is a stainless steel rod. Experiments are performed by applying a constant voltage across the cell and then adding 5 to 10 mg of LiD to LiF-LiCl-LiBr molten salt (~900 g). Present plans are to test three different types of porous electrodes: (1) a porous graphite electrode, (2) a porous graphite electrode with a ceramic coating,[9] and (3) a porous metal electrode made of sintered 316L stainless steel. To date, both types of graphite electrode have been examined. Typical results for the uncoated and coated electrodes are given in Figs. 4 and 5, respectively.

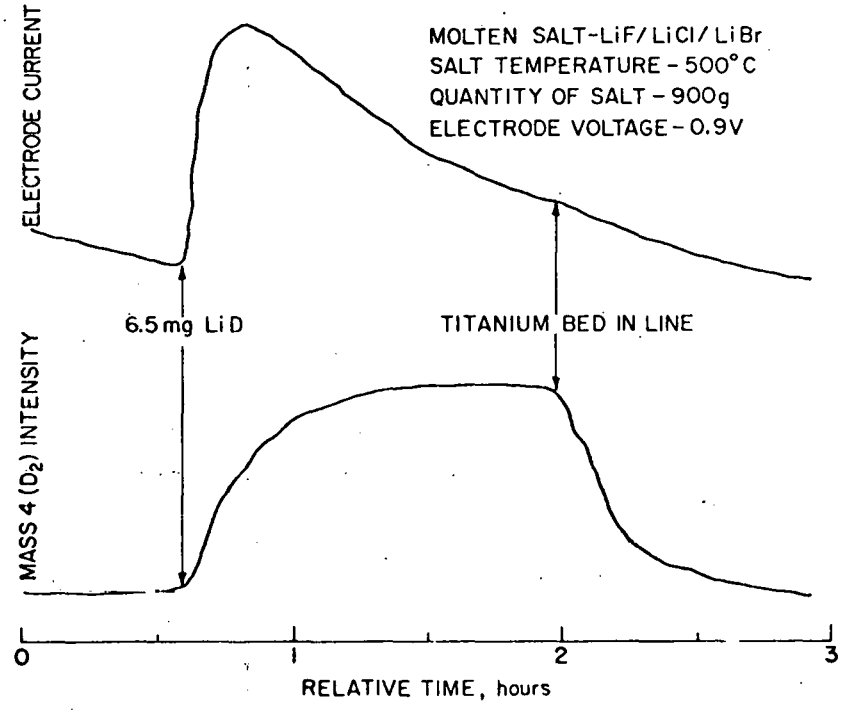

FIGURE 4. Results of a Typical Electrochemical Experiment to Evolve Deuterium using a Graphite Electrode

When the uncoated graphite electrode is used and the applied potential is at or below 0.8 volts, no significant change in either the current through the salt or the D_2 concentration in the argon stream is detected when LiD crystals are dropped into the molten salt. However, when LiD is added with 0.9 volts or more across the electrodes, both the current and D_2 concentration increase, as shown in Fig. 4. Note that the shape of both curves are consistent with what is expected for the electrochemical evolution process. The current increases sharply when the LiD is added and then decreases as the deuteride ion is depleted from the salt. The D_2 gas concentration grows in more slowly and levels off as the electrolysis progresses. Recovery efficiencies (as D_2 and HD) are typically 25 to 50% for these experiments. No buildup of LiD is occurring in the salt, which implies that the deuterium is coming out in some other molecular form. This supposition is supported by the observance of a decrease in the recovery efficiency as the electrode potential increases. Two possible mechanisms for the loss of D_2 are (1) decomposition of the salt allowing the D_2 to react to form DBr, and (2) interaction of D_2 with the graphite electrode to produce hydrocarbons (e.g., CD_4 or C_2D_2).

When using a ceramic-coated graphite electrode, D_2 is generated only above 2.5 volts, but the D_2 recovery efficiency is greatly improved. For the particular experiment shown in Fig. 5, 93% of the deuterium was recovered as D_2. This high recovery efficiency is typical of extraction experiments carried out down to 1 wppm deuterium. In comparing the experimental results for the two electrodes, an obvious feature is the different rates at which D_2 is generated. The coated electrode generates D_2 much faster

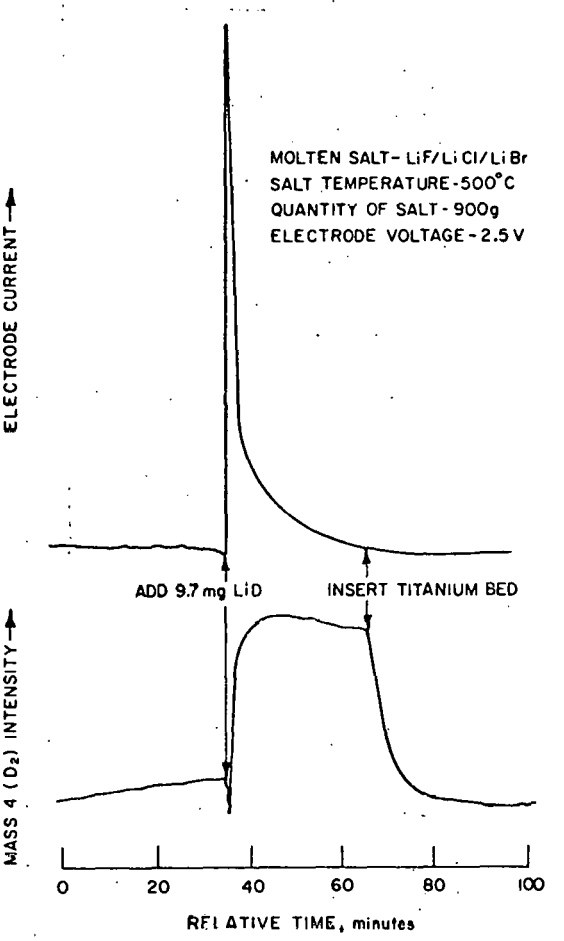

FIGURE 5. Results of a Typical Electrochemical Experiment to Evolve Deuterium using a Ceramic-Coated Graphite Electrode

than the uncoated, possibly because the ceramic layer inhibits back reaction of the D_2 with Li in the salt. However, the ceramic most likely stabilizes a polarization layer around the electrode which accounts for the much higher potential required to liberate the D_2 compared to the uncoated electrode.

It is apparent from the electrochemical experiments which have been completed to date that back reaction of D_2 with the lithium which saturates the molten salt can be successfully prevented using a sparged electrode. Recovery of hydrogen isotopes down to 1 wppm is easily achieved as has been

demonstrated. Problems which have been encountered are most likely attributable to the use of graphite as the electrode material. It is reasonable to anticipate even better performance with the stainless steel electrode now under study. If this is realized, electrochemical evolution will, in all probability, be the preferred method for recovery of hydrogen isotopes from molten salt extractants.

Lithium Processing Test Loop

With the successful demonstration of bench-scale experiments for (1) the extraction of tritium from lithium to molten salts and (2) the recovery of hydrogen isotopes from selected molten salts, plans to build a facility which integrates these experiments into an extraction processing system have begun. A multipurpose 50-gallon forced circulating lithium processing test loop (LPTL) has been designed which will (1) test the effectiveness of semi-continuous molten salt extraction using one vessel that acts as a pseudo mixer-settler; (2) evaluate the efficiency of an elevated temperature getter trap (probably containing zirconium) and a thermally regenerative cold trap (in series with the getter trap) for removing nonmetallic element impurities from lithium; and (3) develop impurity control, process, and monitoring methodology for large liquid lithium loop systems. Provisions are made in the design for attachment of additional experimental test sections, e.g., monitoring devices, other types of gettering materials, and heat-exchanger mock-ups. A simplified schematic drawing of the processing loop is shown in Fig. 6. The facility is being fabricated from 304L stainless steel and will operate at or below 550°C. Construction of the loop components is under way and operation is expected to begin in the Fall of 1977.

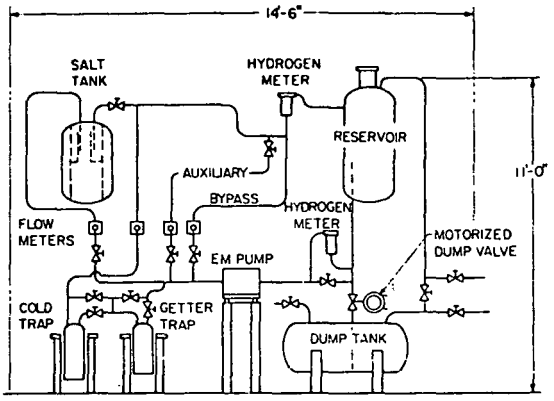

FIGURE 6. A Schematic Diagram of the Lithium Processing Test Loop (LPTL) which is being Constructed at ANL

DEVELOPMENT OF TRITIUM PERMEATION BARRIERS

An effort is currently under way at ANL to explore methods for reducing tritium permeation in near-term confinement experiments and in future fusion power reactors. The methods presently under study include (1) multiplex metal structures containing at least one layer of a material that is relatively impermeable to hydrogen isotopes and (2) ceramic and other special coatings on structural metal surfaces. The objectives, general approach and experimental procedures used in this program were described in previous publications.[10,11] A major finding of the studies carried out to date has been that aluminum bronze (10 w/o Al, 4 w/o Fe, Bal. Cu), a commercially available high-strength corrosion-resistant copper alloy, develops appreciable resistance to hydrogen permeation on standing in relatively clean environments at elevated temperature.[10] Because of the substantial technology base that exists with respect to the preparation of mechanically and metallurgically bonded copper/stainless steel composites, current efforts are focusing on the use of aluminum bronze as a permeation inhibitor in stainless steel systems.

Development of Bronze Permeation Barriers

Recent experiments have been directed towards examination of the permeation characteristics of metallurgically bonded aluminum bronze/304-SS multiplexes. Two such metallurgical multiplexes, a 304-SS/aluminum bronze sample and a 304-SS/aluminum bronze/304-SS sample, prepared by the ANL Materials Science Division, were subjected to hydrogen permeation using the all-metal high-vacuum system described in reference 11. The hydrogen permeability of both samples was found to drop from a value near that expected for a comparably thick piece of pure stainless steel to a value some 30 times lower over a period of a few weeks. Examination of the 304-SS/aluminum bronze/304-SS multiplex after permeation experiments showed that the sample had delaminated at both interfaces and that, in spite of the completely weld-enclosed nature of the interface regions (see reference 10 or 11 for sample configuration), both surfaces of the bronze inner layer were visably oxidized. A similar delamination of the 304-SS/aluminum bronze duplex is suspected to have occurred; however, at the time of writing the sample had not been dismantled for examination.

Results for the 304-SS/aluminum bronze duplex are shown in Fig. 7. In the study of this duplex, the sample was initially oriented with the bronze layer facing the downstream side of the permeation apparatus (an extremely clean environment in our system), but after nearly two months of study, the sample was re-ersed so that the bronze layer faced the upstream side. Little change in permeation rate was observed for the reversed sample when results were compared to the lowest curve in Fig. 7.

The observed reduction in hydrogen permeation rate for the aluminum bronze multiplexes over the course of the permeation

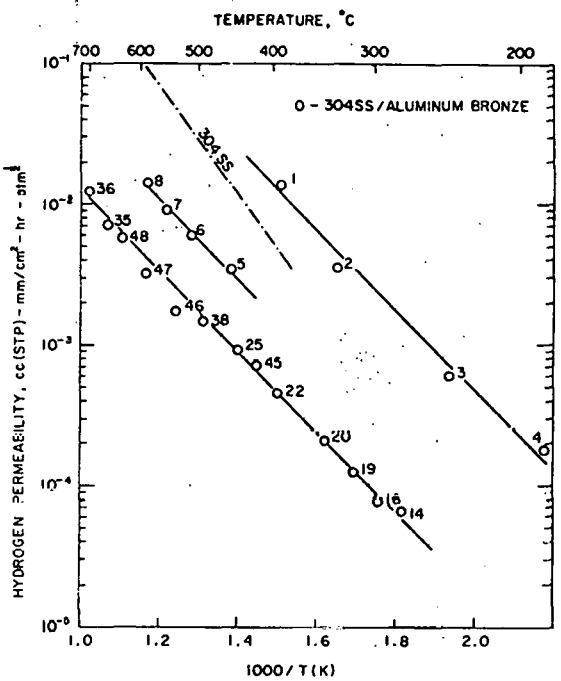

FIGURE 7. Hydrogen Permeation Data for the 304-SS/Aluminum Bronze Duplex

measurements was assumed to be associated with the delamination and subsequent surface oxidation of the bronze. The cause of the delamination was attributed to (1) inadequate surface cleaning prior to the bonding step and/or (2) reduction in metallurgical interface integrity due to the presence of aluminum. The studies do show that the low permeability of aluminum bronze is not a bulk property of the alloy but rather is due to formation of surface impurity layers -- probably aluminum oxide or a ternary oxide. Current efforts in this phase of the barrier development studies are focusing on identification and characterization of methods for applying adherent coatings of aluminum bronze or related aluminum base materials to stainless steel.

Thermal/Mechanical Properties of Multiplexes

A series of studies has been initiated

to measure the magnitude of thermal contact resistance effects in mechanical and metallurgical multiplexes. A thermal conductivity apparatus based on the guard-heater principle was assembled and studies of (1) a mechanically bonded 304-SS/Cu/304-SS multiplex tubing and (2) a piece of 304-SS tubing having the same dimensions as the multiplex were completed. The measured thermal conductivity of the 304-SS piece over the temperature range from 200 to 550°C was in reasonably good agreement with existing data. The thermal conductivity of the 304-SS/Cu/304-SS tube started out at a value roughly half that of the pure 304-SS tube but dropped asymptotically to a value approximately 20 times lower than that of the 304-SS tube over a period of about two weeks. This drop in thermal conductivity has been tentatively attributed to the buildup of oxide layers (at higher temperatures) at the two mechanical interfaces of the multiplex tube. Efforts to find solutions for potential interface heat transfer resistance problems in multiplex configurations are presently under way.

Cladding Concepts for Advanced Refractory Alloys

Because vanadium-base alloys are leading candidates as liquid lithium containment materials for lithium blanketed fusion power reactors and in light of the results in reference 11, there is sufficient incentive to search for cladding alloys (for the exterior surfaces of vanadium structures) that are air-stable at elevated temperatures (600 to 1000°C). The Haynes series of alloys offer one potentially useful class of materials for this application because their upper operating temperature limit in air is in excess of 1000°C. Assuming that the hydrogen permeability of vanadium in a Haynes alloy/vanadium/liquid lithium configuration would remain relatively high[11] over

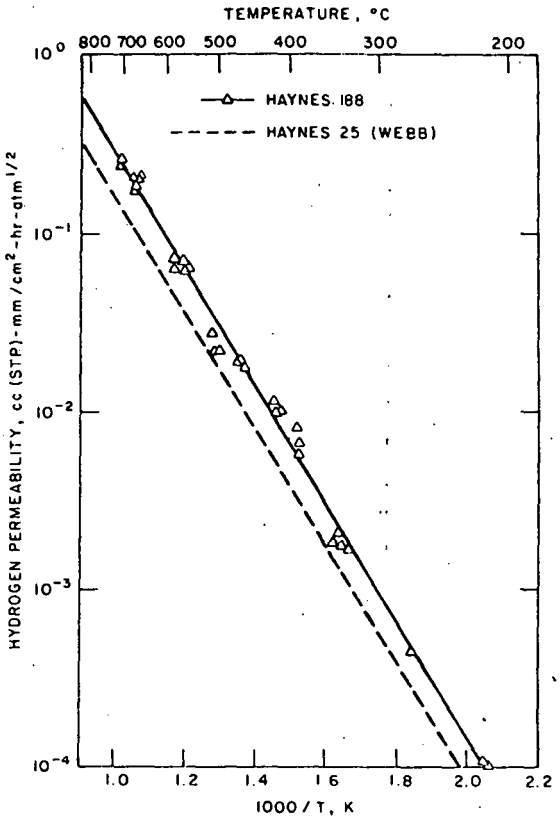

FIGURE 8. Hydrogen Permeation Data for Selected Haynes Alloys

extended operating times, the question of further tritium permeation through the cladding alloy becomes significant. Figure 8 shows that results of a hydrogen permeation study carried out in our laboratory (during the first quarter of calendar 1976) for Haynes 188 (38 w/o Co, 22 w/o Cr, 22 w/o Ni, 14.5 w/o W, 3 w/o Fe, 0.15 w/o C, 0.15 w/o La). The results were obtained for upstream hydrogen pressures in the range from 0.3 to 180 Torr and temperatures in the range from 200 to 720°C. Over this entire range of temperatures and pressures, the rate of permeation was found to be proportional to the half-power of the hydrogen driving pressure (0.5 ± 0.05) as shown in Fig. 9. The permeation curve for Haynes 25 as reported by

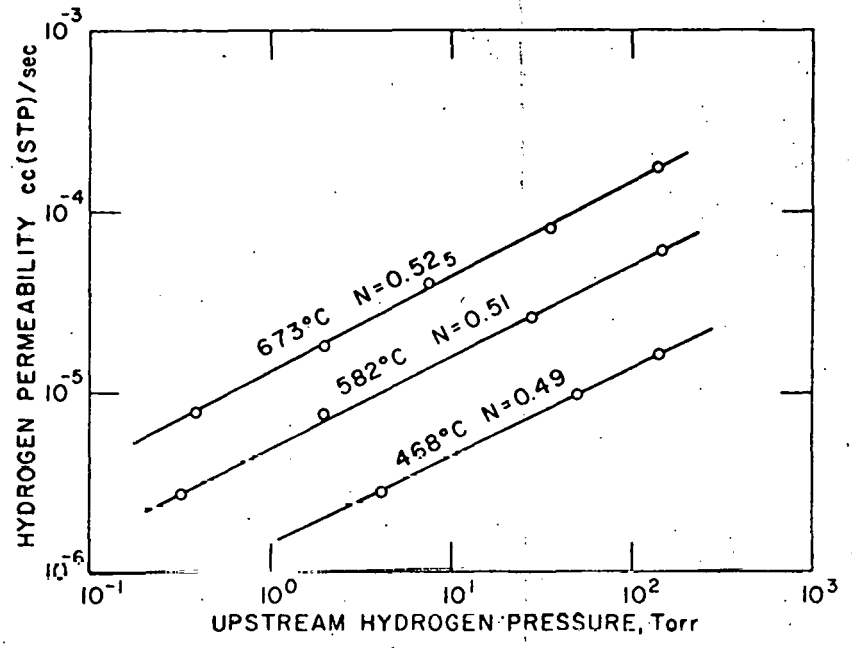

FIGURE 9. Pressure Dependence of Hydrogen Permeation Rate for Haynes-188

Webb[12] is also included in Fig. 8 for comparison purposes. The hydrogen permeabilities of these alloys are in the same range with most conventional austenitic alloys (see, for example, references 10 and 12) and can be represented by the following equations:

$$\Phi \text{ (Haynes 188)} = 545 \exp(-15{,}040/RT), \quad cc(STP)\cdot mm/cm^2\cdot hr\cdot atm^{1/2}$$

$$\Phi \text{ (Haynes 25)} = 327 \exp(-15{,}100/RT), \quad cc(STP)\cdot mm/cm^2\cdot hr\cdot atm^{1/2}$$

Depending on the actual permeability of vanadium in the clad configuration discussed above, the rate of hydrogen permeation through a Haynes 188 or 25 clad could approach that which would obtain if the vanadium were not even present. At temperatures above 500°C, the need for additional permeation barriers in Haynes clad vanadium structures appears to be essential. However, it is important to note that the effects of air oxidation on the exterior surfaces of the Haynes alloys might lead to increased permeation resistance if, for example, stable oxide layers can be made to persist.

ACKNOWLEDGMENTS

Work on the Lithium Processing Test Loop is being performed in collaboration with S. B. Skladzien and J. R. Weston. The research and development efforts described in this paper are supported by the Division of Magnetic Fusion Energy, U. S. Energy Research and Development Administration.

REFERENCES

1. E. Veleckis and V. A. Maroni, "Thermodynamic Properties of Solutions of Hydrogen Isotopes in Metals and Alloys of Interest to Fusion Reactor Technology," Proceedings of the International Conference on Radiation Effects and Tritium Technology for Fusion Reactors, October 1-3, 1975, Gatlinburg, TN, CONF-750989, U. S. Energy Research and Development Administration, Vol. III, p. 458 (1976).

2. V. A. Maroni, "An Analysis of Tritium Distribution and Leakage Characteristics of Two Fusion Reactor Reference Designs," Proceedings of the 5th Symposium on Engineering Problems of Fusion Research, November 6-9, 1973, Princeton, NJ, p. 206.

3. J. S. Watson, An Evaluation of Methods for Recovering Tritium from the Blankets

or Coolant Systems of Fusion Reactors, Oak Ridge National Laboratory Report ORNL-TM-3794 (1972).

4. V. A. Maroni, R. D. Wolson, and G. E. Staahl, "Some Preliminary Considerations of a Molten Salt Extraction Process to Remove Tritium from Liquid Lithium Fusion Reactor Blankets," Nucl. Technol. 25, 83 (1975).

5. V. A. Maroni, W. F. Calaway, E. Veleckis, and R. M. Yonco, "Solution Behavior of Hydrogen Isotopes and Other Nonmetallic Elements in Liquid Lithium," Proceedings of the International Conference on Liquid Metal Technology in Energy Production, May 3-6, 1976, Champion, PA, (in press).

6. V. A. Maroni et al., Chemical Engineering Division Fusion Reactor Research Group Annual Report: July 1975-June 1976, Argonne National Laboratory Report, in preparation.

7. P. A. Nelson et al., Development of High-Specific-Energy Batteries for Electric Vehicles Progress Report: August 1973-January 1974, Argonne National Laboratory Report ANL-8058 (June, 1974).

8. R. N. Seefurth and R. A. Shorma, "Investigation of the Reaction between Liquid Lithium and Lithium Chloride-Potassium Chloride Melts," J. Electrochem. Soc. 122, 1049 (1975).

9. D. A. J. Swinkels, "A Valve Electrode for Use in Fused Salts," Electrochem. Technol. 5, 396 (1967).

10. V. A. Maroni et al., "Experimental Studies of Tritium Barrier Concepts for Fusion Reactors," Proceedings of the International Conference on Radiation Effects and Tritium Technology for Fusion Reactors, October 1-3, 1975, Gatlinburg, TN, CONF-750989, U. S. Energy Research and Development Administration, Vol. IV, p. 329 (1976).

11. E. H. Van Deventer et al., "Effects of Surface Impurity Layers on the Hydrogen Permeability of Vanadium," J. Nucl. Mater. (in press).

12. R. W. Webb, "Permeation of Hydrogen through Metals," NAA-SR-10462, U. S. Atomic Energy Commission Report (July, 1965).

TRITIUM PROCESSING AND CONTAINMENT TECHNOLOGY FOR FUSION REACTORS: PERSPECTIVE AND STATUS*

Victor A. Maroni

ARGONNE NATIONAL LABORATORY

This paper reviews the status of selected tritium processing and containment technologies that will be required to support the development of the fusion energy program. Considered in order are the fuel conditioning and recycle systems, the containment and cleanup systems, the blanket processing systems, and two unique problems relating to tritium interactions in neutral beam injectors and first wall coolant circuits. The major technical problem areas appear to lie in the development of (1) high-capacity, rapid recycle plasma chamber evacuation systems; (2) large-capacity (≥100,000 cfm) air handling and processing systems for atmospheric detritiation; (3) tritium recovery technology for liquid lithium blanket concepts; (4) tritium compatible neutral injector systems; and (5) an overall approach to tritium handling and containment that guarantees near zero release to the environment at a bearable cost.

INTRODUCTION

The tritium handling and containment requirements of both near-term and longer-range fusion devices have been under study for nearly a decade. Although still in its infancy, the tritium technology program that is evolving in support of the development of fusion power is beginning to make substantial progress in terms of (1) defining the criteria for fusion reactor tritium facility operations and (2) identifying tractible design solutions in a number of eminent problem areas. By coupling this progress with the rather sizeable tritium technology base that already exists as a result of other tritium related programs at Savannah River Laboratory, Mound Laboratory, Lawrence Livermore Laboratory, Los Alamos Scientific Laboratory and other research and development centers, it is now possible to define in broad terms the scope of much of the work that will be required to fulfill the tritium handling and containment requirements for the first generation of DT burning fusion devices and for those that lie beyond.

The purpose of this paper is threefold: (1) to provide some perspective on the nature of the tritium processing and containment problems currently envisioned for DT burning fusion devices, (2) to identify the areas where major research and development efforts will be needed, and (3) to highlight some of the more significant advances of recent years in terms of criteria development and solution of problems. Although many of the discussions contained herein are conjectural in nature and

*Work performed under the auspices of the U.S. Energy Research and Development Administration.

representative of the author's view, a great deal of the thought and virtually all of the factual information were culled from the references accompanying this paper and from private communications to the author by knowledgeable members of the controlled thermonuclear research and tritium technology communities within the USA. The discussions following this introduction contain summaries of the technological requirements associated with (1) the mainstream fuel cycle (with emphasis on DT burning devices), (2) containment and cleanup systems, (3) blanket processing systems, and (4) several unique problem areas associated with systems that interface with the tritium handling systems. Table 1 contains an outlined summary of research and development items for each of the discussion areas. Table 2 contains a summary of the focus of work in selected ongoing research and development activities within the USA that is directly supportive of or relevant to the fusion tritium technology program.

THE MAINSTREAM FUEL CYCLE

The most important near-term tritium handling problems, and perhaps the most neglected to date, are those that involve the mainstream of the fuel cycle for DT burning fusion reactors. Because only a few percent of the fuel delivered to the plasma chamber is actually consumed during a typical burn cycle (tokamaks, mirrors, or theta-pinches), it is absolutely essential that the unburned fuel be recycled from an economic viewpoint alone. The principal functions of the mainstream fuel recycling system are (1) to provide for evacuation of the plasma chamber in a way that permits accumulation and consolidation of all the unburned fuel in an easily recycleable form; (2) to reduce particulate debris (from plasma wall interactions) and non-hydrogenous impurity element concentrations in the fuel to levels that are acceptable for refueling purposes; (3) to remove protium (^{1}H) from the D-T mixture and to adjust the D/T ratios to values required for direct refueling, energetic neutral injection, pellet fueling, etc.; and (4) to provide the means for circulation, compression, adjustment of physical and chemical state, and interim storage of the fuel. A summary discussion of each of these functions is given below; more comprehensive discussions may be found in references 1 through 8.

Plasma Chamber Evacuation Systems

Several recent studies[1-5] have provided some perspective on the evacuation requirements for experimental tokamak reactors. Clearly, there will be need to handle large gas loads (on the order of 5 Torr-liters per thermal MW) in short time periods and to do so repetitively with little or no interruption. The pumping equipment must be reliable and maintainable, must operate in a high radiation environment, must be capable of pumping all atomic and molecular species present in the plasma chamber following a burn cycle, must be sufficiently compact to be accommodated by the reactors requisite physical configuration, and must be reasonably economic in terms of capital and operating costs. Of course, the pumping systems must also be compatible with and must provide a high degree of containment for large quantities of tritium.

Three basic types of high-speed, large-capacity pumping methods have been considered for use in near-term experimental reactors[1,2,4]: (1) dynamic evacuation using diffusion or turbomolecular pumps, (2) gettering with active metals such as zirconium aluminum alloy or titanium metal, and (3) cryogenic evacuation using cryocondensation or cryosorption pumps. The dynamic methods

TABLE 1. Tritium Related Research and Development in Support of the Fusion Energy Program

I. Fuel Conditioning and Recycle
   A. Plasma Chamber Evacuation Technology
      1. Identify and develop high-capacity, rapid recycle evacuation methods.
      2. Verify compatibility with tritium and adequacy of tritium containment.
      3. Establish interface-technology with plasma chamber and with regeneration systems.
      4. Determine consequences of radiation effects and maintenance requirements.
   B. Impurity Removal and Monitoring
      1. Analyze debris transport mechanisms and determine consequences.
      2. Develop debris separation and handling technology.
      3. Develop nonmetallic element removal methodology.
      4. Develop helium removal methodology.
      5. Establish impurity monitoring methods.
   C. Hydrogen Isotope Enrichment
      1. Define separations and enrichment needs.
      2. Identify usable enrichment technology.
      3. Determine optimum processing modes (batch vs. continuous).
      4. Develop low temperature isotopomeric equilibration methods.
      5. Establish cost/benefit factors affecting alternative enrichment strategies.
      6. Proof test instrumentation and control systems for enrichment assemblies.
   D. Hardware Development
      1. Establish criteria for hardware performance.
      2. Identify hardware development needs (e.g., valves, compressors, pumps, traps).
      3. Verify compatibility with tritium and adequacy of tritium containment.
   E. Integrated Systems Tests (Fuel Cycle Simulation)
      1. Verify identification of all processing steps.
      2. Optimize processing sequence.
      3. Determine hardware and component interfacing requirements.
      4. Conduct fuel cycle simulation studies.

II. Containment and Cleanup Systems
   A. Primary Containment
      1. Establish optimum structural materials (e.g., permeation resistant, nonembrittling).
      2. Develop leak-free assembly technology for permanent and temporary connections.
      3. Develop permeation barrier methods (e.g., coatings, composites) for both ambient and elevated temperature operation.
      4. Investigate permeation rates and mechanisms at low driving pressure.
   B. Secondary Containment
      1. Identffy secondary containment requirements.
      2. Develop and test peripheral jacketing methods.
      3. Determine optimum flow patterns and geometries.
      4. Establish access and maintenance requirements.

TABLE 1 (Cont'd.)

5. Analyze features of permanent and portable enclosures (e.g., gloveboxes, fumehoods).
6. Develop purge processing technology.

C. Tertiary Containment
1. Develop and test high-velocity air circulation and processing systems.
2. Identify, characterize, and optimize oxidation catalysts, adsorber beds, thermal economizers, and regeneration procedures for air detritiation systems.
3. Determine effects of major variables (e.g., temperature, humidity, flow pattern, air mixing).
4. Develop methods to minimize residual contamination and outgassing following releases (e.g., short cleanup times, hydrophobic coatings).
5. Investigate kinetics of reactions involving tritiated species in ambient atmospheres.
6. Establish cost/benefit factors for alternative cleanup strategies.

D. Waste Disposal Technology
1. Develop strategies and methodology for maximum tritium recycle.
2. Establish technology for safe, compact, low long-term release tritiated waste disposal.

E. Integrated Systems Tests
1. Verify integrated operation of the three levels of containment (primary, secondary, and tertiary).
2. Carry out realistic deliberate-release experiments.

III. Storage, Shipping, and Safeguards

A. Storage
1. Develop and test fuel storage concepts.
2. Establish criteria for storage vault integrity.

B. Shipping
1. Establish standards for shipping and verify compliance with federal regulations.
2. Verify production capabilities.
3. Examine anticipated product and shipping costs.
4. Determine production scheduling requirements and concomitant programmatic impacts.

C. Safeguards
1. Establish safeguards implications for facility and shipping operations.
2. Determine reactor surveillance and site protection criteria.
3. Prepare safeguards planning logics for near-term and longer-range devices and facilities.

IV. Blanket Processing Technology

A. Liquid Lithium Blanket Concepts
1. Establish criteria for tritium containment, inventory, and recovery.
2. Identify and develop blanket processing methodology.
3. Verify maintainability and reliability of blanket processing systems.

B. Solid Blanket Concepts
1. Verify adequacy of tritium release rates from solid blanket materials.
2. Establish long-term performance of solid blanket materials in anticipated radiation environments.
3. Develop and test tritium

TABLE 1 (Cont'd.)

recovery methods.

C. Molten Salt Blanket Concepts
   1. Determine chemical effects of transmutation reactions that produce tritium.
   2. Develop and test tritium recovery methods.
   3. Verify maintainability and reliability of blanket processing systems.

V. Selected Additional Topics
   A. Instrumentation and Control Systems
      1. Develop fuel cycle diagnostic systems.
      2. Develop breeder blanket diagnostic systems.
      3. Establish integrated tritium facility maintenance, control, and response strategies and develop systems.
      4. Verify performance of monitoring and diagnostic methods in anticipated power reactor radiation environments.
   B. Neutral Beam Injector Interfacing
      1. Identify important tritium interactions in neutral injector systems.
      2. Establish tritium containment criteria and develop containment methods.
      3. Determine impact of tritium containment on injector maintenance.
   C. Coolant/Tritium Interactions
      1. Identify and characterize modes of tritium insertion into coolant systems.
      2. Establish tritium buildup rates for hydrogenous coolant concepts.
      3. Develop methods for removal of tritium from nonhydrogenous coolants.
      4. Examine effects of energetic tritium implantation (first wall).
      5. Examine effects of radiolysis in tritium contaminated coolants.
      6. Determine the mechanisms for, and magnitudes of, tritium releases from coolant circuitry.

---

generally require fore-pumping and/or fore-collection systems, are large in size, and may be questionable in terms of tritium compatibility and containment. The getter and cryogenic methods are committed to regenerative operation; hence, where continuous on-line pumping is necessary there would undoubtedly be need for paralleling redundant systems to permit simultaneous pumping and regeneration.

In terms of all of the above considerations, cryosorption pumping at 4 K appears to offer the best prospects for meeting plasma chamber evacuation requirements in both near-term and longer-range tokamak reactors and in related devices with similar evacuation needs. This contention is generally well supported by the recent studies of Watson and Fisher[9,10] and by the earlier work of Stern et al.[11,12]

Impurity Removal

The principal impurities identified thus far that will in all likelihood be present in the plasma exhaust of magnetic-confinement fusion devices are fine particulate solid debris and the nonmetallic elements He, O, N, and C. Considerations of the problems associated with the removal of each type of impurity are summarized below.

The harsh radiation environment anticipated for the first wall of a fusion reactor is likely to lead to a dislodging of sizeable quantities of fine particulate metal and metal compounds. Although most of this debris is expected to either settle

TABLE 2. Summary of Selected Tritium Research and Development Activities in Support of the Fusion Energy Program

Research and Development Area	Laboratory and Cognizant Personnel	Nature of Work	References
Mainstream Fuel Cycle	ORNL (J. S. Watson, P. W. Fischer, S. D. Clinton et al.)	Development of Cryopumping Technology Analysis of Fuel Cycle Strategies	4, 9, 10, 35
	LLL (R. G. Hickman, T. R. Galloway, V. P. Gede et al.)	Fuel Cycle Strategies for Minor Devices Tritium Gettering and Storage Materials and Hardware Assessments	7, 17, 18, 19, 27
	ML (L. J. Wittenberg, W. R. Wilkes et al.)	Surveys of Existing Technology Hydrogen Isotope Separations Metal Tritide Technology	3, 13, 14, 15
	ANL (V. A. Maroni, B. Misra et al.)	Analysis of Fuel Cycle Strategies Analysis of Enrichment Strategies	1, 2, 16
	LASL (J. L. Anderson, R. H. Sherman et al.)	Fuel Cycle Strategies for θ-Pinches Fuel Recycle in the INS	8, 51
Containment and Cleanup Systems	LLL (T. R. Galloway, A. E. Sherwood, M. F. Singleton et al.)	Analysis of Cleanup and Containment Strategies Tritium Oxidation, Adsorption, and Gettering Tritium Containment in Laser Fusion Tritium Containment in the RTNS	7, 27, 32, 33
	ML (W. R. Wilkes, L. J. Wittenberg, E. A. Mershad, J. Kershner et al.)	Experiments with Air Detritiation Systems Analysis of Cleanup and Containment Strategies Tritium Waste Treatment Tritium Effluent Control	3, 13, 28, 29, 31
Blanket Chemistry and Blanket Processing Technology	LASL (J. L. Anderson, D. Carstens et al.)	Studies of Liquid Metal Alloy Extraction Concepts for Processing Liquid Lithium	39
	ORNL (J. S. Watson, J. B. Talbot, J. T. Bell, F. J. Smith, G. M. Begun et al.)	Tritium Removal from Lithium Alloys Tritium Sorption from Liquid Metals Thermodynamic Studies of Hydrogen Isotope Solutions in Lithium and Lithium Alloys	35, 36, 44
	BNL (J. R. Powell, R. H. Wiswall et al.)	Analysis of Breeder Blanket Strategies Experimental Studies with Solid Blanket Materials	40
	ANL (W. F. Calaway, E. Veleckis, V. A. Maroni et al.)	Studies of Molten Salt Extraction Concepts for Tritium Removal from Liquid Lithium Thermodynamic Studies of Hydrogen Isotope Solutions in Lithium and Lithium Alloys Development of Lithium Processing Technology	37, 38
	Univ. of Wisconsin (E. M. Larsen, R. G. Clemmer, D. K. Sze et al.)	Development of Liquid and Solid Blanket Design Concepts	41, 45

TABLE 2 (Cont'd.)

Research and Development Area	Laboratory and Cognizant Personnel	Nature of Work	References
Hydrogen Isotope Permeation and Other Physicochemical Studies	LLL (P. C. Souers, J. W. Pyper, R. G. Hickman et al.)	Physicochemical Studies of Deuterium Tritide (DT) Tritium Implantation Effects	7, 49, 50
	Princeton Univ. (R. C. Axtman, E. F. Johnson, H. K. Perkins et al.)	Hydrogen Permeation at Low Pressures Tritium Holdup Due to Coatings Chemical Engineering Analyses of Tritium in Molten Salts	21, 22, 43
	ANL (E. Van Deventer, V. A. Maroni, B. Misra et al.)	Development of Permeation Barriers using Multiplex Materials Kinetics of Reactions Involving Tritiated Species	23, 38
	ORNL (J. T. Bell, S. D. Clinton, J. D. Redman, F. J. Smith et al.)	Tritium Permeation through Steam Generator Materials Oxidation of Permeating Tritium Sorption Pumping by Deep Beds	20, 35
	Sandia Livermore (W. A. Swansiger et al.)	Hydrogen Isotope Permeation through Metals	25
	N. C. State Univ. (T. S. Elleman et al.)	Tritium Diffusion in Metals and Ceramics	24

out or reattach itself to the first wall, plans must be made to accommodate the migration of some particulate material into the vacuum pumps and beyond them. Because the first wall will become highly radioactive after only a few days of operation even at modest wall loadings (0.2 to 1.0 MW/m^2), the debris will also be highly radioactive and maintenance of the vacuum pumps and the equipment immediately downstream of them will be subject to increased complexity. Large quantities of debris in the torus exhaust gases could have an adverse effect on pump lifetime and performance, but any attempt to microfilter the debris in advance of the vacuum pumps (between the plasma chamber and the pumps) would more than likely lead to unacceptably large conductance losses. During cleaning or regeneration of the vacuum system, the escaping gases will probably fluidize some of the debris that entered the pumps during the torus pumping cycle. (Hopefully, most of the debris will indeed carry through the vacuum pumps so that pump lifetimes can be extended.) Removal of this debris from the fuel recycle stream can probably be done with some combination of electrostatic precipitators or millipore filters. If possible, the debris separation system should be located immediately downstream of the cryopumps (to the extent that this location does not adversely extend regeneration times). It is difficult to make accurate predictions of the particle size, size distribution, and quantity of debris generated by a prototypal fusion device; hence, some experimentation will ultimately be required in order to test debris removal methods in flowing hydrogen streams that simulate the mainstream of reactor fuel cycles.

The perpetual presence of helium,

oxygen, carbon, nitrogen, and other nonmetallic impurities in the torus exhaust of prototypal fusion devices will, for all practical purposes, be unavoidable. In keeping with the concept of fuel recycle, and in order to reduce impurity levels in the preburn fuel mixture as far as is possible, it will be necessary to provide for continuous removal of nonmetallic elements in the plasma exhaust. This should certainly be done in advance of the isotopic enrichment step and perhaps done again in advance of fuel storage so that the capacity of the storage material is not reduced by reaction with impurities.

Impurity removal can probably be carried out in a relatively straightforward manner using appropriately selected catalytic and/or getter-type beds designed to (1) crack water, hydrocarbons, and other hydrogenous compounds and (2) actively remove the impurities by reaction to form stable, nonvolatile, nonhydrogenous compounds. If the getter bed is also employed to clear the plasma chamber evacuation system, it should be designed to sorb and release hydrogen over a relatively narrow temperature range, should be reasonably compact, and should be readily disposable. It is expected that these getter beds will have to reduce O, N, C and related nonmetallic impurities in the fuel stream to the sub-ppm range. The helium present in the cryopump exhaust either could be allowed to carry over into the enrichment system and be removed therefrom as an inert/noncondensible phase (providing this carryover does not compromise the enrichment operation) or could be separated from the hydrogen isotopes in advance of enrichment using a permeable window. In addition to the need to identify and test getter bed materials (or combinations of materials) for broad spectrum nonmetallic impurity removal, the relative merits of continuous versus various degrees of batch processing of the plasma exhaust remain to be evaluated. References 13 and 14 contain surveys and discussions of existing tritium gettering and storage experience.

Isotopic Enrichment

Isotopic enrichment of the hydrogen isotopes in the mainstream of the fuel cycle will be needed to (1) reduce protium to acceptable levels, (2) adjust the D/T ratio of the bulk fuel to values prescribed by the cold fueling criteria, and (3) separate isotopically pure D and/or T streams for energetic neutral injection where this method of plasma heating is employed. Although not necessarily a part of the mainstream fuel cycle, there may also be need of a capability to provide for enrichment of tritium from high-level wastes containing large relative amounts of protium. The methods employed for each of the above isotopic enrichment processes in DT burning reactors will depend to a large extent on the relative isotopic concentrations involved, the magnitude of separation to be achieved, the quantity of fuel to be enriched, and the total amount of tritium to be handled. Although a variety of methods have been identified which could be applied to hydrogen isotope enrichment (including cryogenic distillation, chromatography, electrolysis, laser stimulated separations, and thermal diffusion), the matching of method with application will undoubtedly depend on economy and reliability. Considering the large spent fuel flow rate for even experimental scale reactors (e.g., several kilograms per day of DT for tokamak experimental power reactors[1,4]), cryogenic distillation appears to be the most practical, reliable, and economic method for mainstream enrichment.

A number of recent studies have addressed

the question of hydrogen isotope enrichment for near-term fusion devices[1,4,15,16]. The general conclusions of these studies have been that cryogenic distillation methods would permit the required enrichments to be made for most currently conceived devices, including totally driven DT reactors where a nearly complete separation of the deuterium and tritium in the plasma exhaust must be made. These separations generally require from 3 to 6 columns with the number of theoretical stages per column ranging from 30 to 50. One or more equilibrators to re establish or alter the isotopomeric equilibria among the six isotopomeric forms of hydrogen (H_2, D_2, T_2, HD, HT, DT) is also usually needed, depending on the magnitude of H/T and/or D/T separation required. Power input levels to drive the distillation cascade (including refrigeration and compression power) are found to be only a small fraction of the total plant recirculating power (i.e., $\ll$1%).

Fuel Storage

The identification of fail-safe fuel storage methodology will be essential to the development of a minimum credible impact tritium handling facility for DT fueled fusion power plants because, in all probability, the major fraction of the tritium contained within such plants will be in the storage reservoir. Although a comprehensive design basis remains to be established for these storage systems, it is reasonable to assume that they will be disaster proof, barricaded vaults containing parallel and series arrangements of storage cells constructed in such a way that failure to operate of one or perhaps several cells does not constitute an unresolvable maintenance problem. Plausible concepts for the storage cells include (1) compressed gas cylinders, (2) thermally regenerative metal hydride beds, and (3) cryostated liquid or solid hydrogen storage tanks. Of these, metal hydride storage concepts are generally regarded as being best suited to the storage of large quantities of tritium. The storage vaults would have at least three principal access requirements: (1) reception of purified and appropriately enriched recycle fuel, (2) reception of incoming tritium from tritium production facilities, and (3) release of stored fuel to the fuel blending and delivery systems. References 1 through 7, 13, 14, and 17 discuss some strategies and methods for fuel storage that would be applicable to most fusion reactor concepts.

Materials and Hardware

The selection, qualification, and specification of materials, fabrication practices, and hardware items required to assemble fuel handling and transfer systems will be an integral part of the fuel cycle development program for coming generations of fusion devices. Included in this phase of the program would be consideration of (1) structural materials used in transfer lines, valves, pumps, compressors, vessels, secondary containment systems, and related hardware; (2) elastomers, gasket and sealing materials, lubricants, coating substances paints, and other materials employed in nonstructural applications; and (3) the general hardware methodology to be applied in tritium transfer and compression operations.

For applications at ambient temperature, the 18-8 stainless steels are regarded[18] as being qualified for use in a high level tritium environment. Welding is the preferred joining method, but junctions employing metal gasket seals could be used where removable couplings are needed to connect integrated sections of the fuel cycle. It is generally recommended that joining methods which employ polymer seals be kept to a

minimum and be restricted to low level tritium environments[3,18]. Threaded seals are not considered to be suitable for tritium service and should be avoided.

It appears advisable that hardware items such as pumps, valves, or compressors which require internally moving parts, nonetheless be designed to have fully welded structures rather than hermetric or fluid seals. Where rotating or sliding seals are unavoidable, the use of techniques employing magnetic-coupling or concentric bellows drives is recommended. All hardware items that are not fully welded will probably require a secondary containment shell with a processible atmosphere. Valves with all-welded bellows-type construction are available for use at gas pressures ranging from hard vacuum to 2500 psi and at temperatures up to 350°C. Valves of this type that are adequate in size for most fuel cycle applications are available; but large, high conductance gate-type valves suitable for use at the vacuum system/plasma chamber interface will require some development. Several types of fully welded diaphragm and bellows-type pumps and compressors have been used successfully for tritium transfer operations[19] but the throughput rates could stand considerable increase. In many cases the long-term performances of these and related hardware items needs to be examined under the conditions of radiation environment, magnetic field, and temperature that are anticipated for their use in fusion devices. References 3, 13, 18, and 19 contain discussions of criteria for materials and hardware selection, component design definition, and fabrication methodology in tritium systems.

CONTAINMENT AND CLEANUP SYSTEMS

Accepting the notion that extremely strict tritium containment guidelines will be set for future fusion power plants and, in the light of past and current experience with tritium containment in ongoing programs at laboratories in the USA and worldwide, it seems prudent to consider at least three levels of containment in fusion reactor facilities. For the purposes of this paper, these three levels will be identified as primary, secondary, and tertiary; where primary refers to the construction materials and components in direct contact with tritium, secondary refers to the various local containment enclosures surrounding major tritium handling hardware and components, and tertiary refers to the large-volume room air handling systems.

Primary Containment

As a part of the primary containment level, consideration would be given to the identification of materials, hardware, and fabrication methods that offered (1) a high degree of protection against leakage and permeation, (2) high component reliability with minimum maintenance, and (3) adequate containment without an excessive cost burden. Among the materials selection criteria would be the requirement that primary materials be resistant to embrittlement and other forms of deterioration that can occur in a tritium environment. Resistance to permeation by tritium will be important, particularly in elevated temperature (>300°C) structures. This will undoubtedly result in the need for special permeation barriers such as multiplex materials, ceramic surface coatings, and other related preparations. There have been numerous studies in recent years concerning the nature of hydrogen permeation under anticipated fusion reactor conditions. A series of reports[20-25] that provide some perspective as to the general scope and direction of currently ongoing programs is included in the references to this paper.

Secondary Containment

The secondary containment systems will consist of integral jackets and other close fitting enclosures around transfer lines, valves, and other fuel cycle hardware. Gloveboxes, fumehoods, and portable enclosures would also be utilized to house entire tritium facility systems that require hands-on operation or maintenance at regular intervals. In particular, portable enclosures would be employed during all routine and off-normal maintenance operations where a potential for tritium release exists. In all cases, the atmosphere in these secondary containment systems (be it air, nitrogen, argon, helium, etc.) would be totally separated from breathing air systems, would be monitored continuously, and would be processed to remove tritium on whatever schedule is necessary to maintain breathable air conditions in the reactor or tritium facility buildings. References 3 and 13 contain some general information on the scope of and experience with secondary containment systems.

Tertiary Containment

Tertiary containment applies to the air handling and detritiation systems servicing the reactor hall and other facility rooms where potential for either entry or egress of tritium exists. Preliminary assessments have shown that the requirements imposed by the need to provide large-scale atmospheric detritiation in even experimental scale reactor buildings are a major concern from the standpoint of (1) maintenance access during reactor down periods, (2) compactness of tritium handling equipment, (3) limitations to the spread of tritium contamination, and (4) overall tritium facility costs. During the past year, several studies[1,3,27,29] have addressed the scope of these requirements with respect to gas handling rates, exigencies of the cleanup schedule, and the dominant features of the cost/benefit algorithm. The essence of these studies is summarized below.

Consider a large reactor hall of volume, V_{TOT}, having a baseline tritium level, N°. Assume that the room air is processed at a volumetric flow rate, $\dot{V}$, and that the processor efficiency is ε. The rate of tritium removal is given by

$$\frac{dN}{dt} = \frac{\varepsilon \cdot \dot{V} \cdot N}{V_{TOT}} \qquad (1)$$

The amount of time, t, it takes to reduce a massive tritium release from the maximum value following the incident, N', back to N° is obtained by integrating Eq. (1) to produce

$$\ln \frac{N'}{N^\circ} = \varepsilon \frac{\dot{V}}{V_{TOT}} t \qquad (2)$$

Values of $\dot{V}$ for selected values of N'/N°, ε, and t are given in Table 3 for a room with $V_{TOT} = 10^7$ cu. ft. ($\sim$ EPR size)[1].

According to Engelhard Industries[26], the largest unit they have evaluated to date called for 6×10^3 cfm at a cost of $\sim 10^6$ \$ for the equipment alone. Because the tritium released to the hall will rapidly soak into the surfaces of the reactor hardware and the building itself, it is advantageous to have the capability for cleaning up spills within hours after a release. If, for example, the limit is set at ≤ 5 hours, then the $\dot{V}$ requirements would be ~ 10 times those for the two-day case in Table 3 and would be 100 times greater than the maximum size unit upon which Engelhard has made a quote.

A second approach to the massive release problem might be rapid cyclic flushing of the reactor hall by alternately compressing its contents (reducing room pressure by a factor η) and backfilling with clean air or an alternative cover gas. If the compressed

TABLE 3. Analysis of Recycle Flow Scenario

Amount Released	$\left(\frac{N'}{N°}\right)$[(a)]	$\ln\left(\frac{N'}{N°}\right)$	$\dot{V}$, cfm			
			t = 2 days		t = 14 days	
			0.5 = ε = 0.9		0.5 = ε = 0.9	
1 gm	10^4	9.2	6.4×10^4	3.5×10^4	9.1×10^3	5.0×10^3
100 gm	10^6	13.8	9.6×10^4	5.3×10^4	1.4×10^4	7.6×10^3
10,000 gm	10^8	18.4	1.3×10^5	7.1×10^4	1.8×10^4	1.0×10^4

(a) Assuming $N° = 5\ \mu Ci/m^3$ and $V_{TOT} = 10^7$ cu. ft. $= 2.8 \times 10^5\ m^3$.

TABLE 4. Analysis of Cyclic Flushing Scenario

Amount Released	$\left(\frac{N'}{N°}\right)$[(a)]	$\ln\left(\frac{N'}{N°}\right)$	$\dot{V}'$ in cfm (for pumpout time = t°/2)[(b)]			
			t = 2 days		t = 14 days	
			0.8 = η = 0.99		0.8 = η = 0.99	
1 gm	10^4	9.2	8.0×10^4	6.3×10^4	1.1×10^4	9.0×10^3
100 gm	10^6	13.8	1.2×10^5	9.7×10^4	1.7×10^4	1.4×10^4
10,000 gm	10^8	18.4	1.6×10^5	1.4×10^5	2.2×10^4	1.8×10^4

(a) Assuming $N° = 5\ \mu Ci/m^3$ and $V_{TOT} = 10^7$ cu. ft. $= 2.8 \times 10^5\ m^3$.

(b) t° = 4 hours.

gas could be stored at 14,000 psi in tanks whose total volume is 10^5 cu. ft., the tanks would then hold 10 room volumes of gas which could be cleaned up over an extended time period (several weeks) by a state-of-the art sized scrubbing system. The cleaned up gas could then be stored for subsequent flushing operations. For the case where the room is evacuated to 1/n of its normal operating pressure and backfilled every t° hours, one obtains Eq. (3).

$$\frac{dN}{dt} = \frac{n}{t°} N \qquad (3)$$

Integrating Eq. (3) for the cases that were considered in Table 3 gives

$$\ln \frac{N'}{N°} = \frac{n}{t°} t \qquad (4)$$

The results for this type of atmospheric cleanup are summarized in Table 4. (The ejector/compressor velocities, $\dot{V}'$, are based on pump-out times that are equal to t°/2.) In order to keep compressor requirements within reasonable limits, it is necessary that t_o be on the order of a few hours. A value of t_o = 4 hours was selected for the study shown in Table 4. (This is considered to be reasonable based on existing experience at several NASA space testing installations.)

Comparison of the results in Tables 3 and 4 shows that there is no practical advantage in terms of gas circulation requirements to the evacuation approach as compared to the more conventional continuous scrubbing approach. The major concern with respect to these massive tritium releases, i.e., soaking of tritium into reactor hardware and building surfaces, will have to be investigated in

considerable detail to determine what cleanup durations are acceptable. Clearly, the requirements of cleanup in two days or less imposes large gas circulation requirements and the assocated equipment can be expected to scale accordingly.

A reasonable comprehensive analysis of large-scale atmospheric detritiation for fusion power plants has been presented by Galloway et al.[27] In their study, they consider the question of large-scale cleanup from the standpoint of catalyst performance and cost. Instead of equating processing requirements with removal efficient, ε, as was done above, they use first-order kinetic, plug flow reactor design equations to represent catalytic bed performance. This approach permits the evaluation of both performance and cost simultaneously. The method described by Galloway et al.[27] was used in one EPR study[1] to determine air cleanup requirements and costs. The conclusions were that cleanup of a 100 gm tritium release to the atmosphere in a reactor hall having a volume of 10^7 cu. ft. could be made in about two days with a 10^5 cfm air handling system having a capital cost of from 20 to 30 million dollars. Overviews of atmospheric cleanup requirements and prospective strategies for fusion devices are given in references 1, 3, 6, 7, 8, 27, and 29. The status of, and recent progress in, development work on ambient and inert atmosphere cleanup systems is discussed in references 30 through 33.

BLANKET PROCESSING

The capability to recover tritium from breeder blankets at a rate equal to the breeding rate and to maintain a minimal blanket tritium inventory is essential to the concept of DT fueled fusion power plants. Lithium in some form is still regarded as the only substance capable of yielding a breeding gain greater than unity in currently conceived DT fusion reactors. The principal materials options considered to date have been liquid lithium, lithium-containing alloys (e.g., Li-Pb, Li-Al, Li-Si) and ceramics (e.g., Li-Al-O, Li-Be-O, Li-Si-O, Li_2O), and molten salts (e.g., LiF, Li-Be-F). Comparisons[34] of the different tritium breeding concepts have been made with respect to (1) required construction materials, (2) breeding ratio, (3) blanket tritium inventory, (4) prospects for adequate tritium recovery, and (5) ease of containment of tritium within the confines of the blanket structure. These comparisons generally indicate that ceramics and molten salts currently offer the best prospects for meeting anticipated blanket handling and processing requirements and that less development will, in all probability, be required for ceramics and molten salts than for liquid lithium. Fewer facts are available on solid-alloy blankets, but these materials appear to approach the ceramics in terms of inventory and recovery characteristics. Although some encouraging progress has been made in recent years, the development of practical steady-state tritium-recovery techniques for low concentrations remains a major technical uncertainty for liquid-lithium blankets. Also, the magnetohydrodynamic compatibility of liquid lithium with magnetic-confinement concepts (insofar as pumping power requirements and perturbations to plasma confinement are concerned) must still be verified. Nonetheless, in terms of breeding potential, heat transfer characteristics, lithium enrichment, and augmentation of neturon production, liquid lithium still possesses a number of advantages over the other breeder material concepts.

The remainder of this section contains a summary of the status of blanket processing technology for the breeding concepts

outlined above. This summary was abstracted from reference 34, and is representative of the opinions delivered at a recent workshop[34] on the subject of fusion reactor blanket technology.

Methods for Processing Liquid-Lithium Blankets

Methods for processing liquid-lithium blankets have received a great deal of attention. The most promising methods currently being considered are: (1) exothermic solid getters (e.g., yttrium and zirconium), (2) permeable metal windows (e.g., niobium- or vanadium-base alloys), (3) liquid-alloy getters formed from rare earth-transition metal eutectics, and (4) molten-salt extraction (e.g., with LiCl-LiF or LiF-LiCl-LiBr). Methods employing cold trapping[37] or batch distillation have, for the most part, been eliminated from further study since neither approach appears capable of achieving tritium inventories in liquid lithium that are near the range of interest (i.e., <10 wppm). Results of studies to determine the thermochemical behavior of solutions of hydrogen isotopes in liquid lithium have been summarized in several recent publications[36,37].

Exothermic getters. Thermodynamic data indicate that solid hydride formers like yttrium and zirconium should be capable of reducing tritium concentrations in liquid lithium to 1 wppm or less. Although limited bench-scale data on extraction of tritium from liquid alkali metals have not been encouraging,[35] further experiments under carefully controlled conditions are recommended. Major technical uncertainties that need near-term exploration are potential passifying effects of impurities (including principally the nonmetallic elements O, N, and C) and methods for regeneration of the getter after loading with tritium. If these studies are sufficiently encouraging, subsequent investigations would have to examine (1) the getter solubility in lithium and the potential for entrainment of degraded getter in the lithium returning to the reactor; (2) the effects on neutronics, corrosion, and mass transport; and (3) the effects of getter composition and morphological characteristics on extraction and recycle efficiency.

Permeable windows. Although the permeability of hydrogen isotopes through most metals normally occurs at a rate that is more of a nuisance than anything else, highly permeable metals (e.g., niobium or vanadium) at elevated temperatues may be used as window materials through which tritium could be extracted from liquid lithium. Calculations using existing permeation data (collected at hydrogen pressures many times higher than those anticipated in fusion reactor blankets) generally indicate that tritium concentrations in lithium in the range from 1 to 10 wppm can be maintained with large but reasonable window areas. Major technical uncertainties in need of near-term investigation relate to (1) "fogging" effects of impurities (e.g., O, N, and C) and mass-transported metals (in dissimilar metal systems only) that may be deposited on the upstream side of the window, (2) "fogging" effects on the downstream side of the window, and (3) fundamental limitations associated with surface kinetics. The possible use of downstream recovery methods employing either liquid getters or protective coatings coupled with gaseous getters should eventually come under study. Limitations imposed by temperature effects on window integrity will eventually need study as well.

Liquid alloy getters. Recent work at LASL[39] indicates that binary liquid eutectics consisting of a rare-earth metal (e.g., Ce, La, Y) and a transition metal (Co, Ni, Fe, or Mn) make highly effective

getters for removing hydrogen isotopes from liquid lithium. In principle, these liquid alloys would be capable of maintaining tritium concentrations in lithium blankets well below 1 wppm. Current uncertainties in this technique include mutual solubilities of the getter alloy and lithium and the difficulty in recovering tritium from the getter alloy. Compatibility of the getters with stainless steel needs to be investigated. Because of the potential promise of these liquid getters, near-term efforts should include examination of the above-mentioned problems. Identification of other low melting compositions (possibly ternary and higher-order mixtures) is recommended.

Molten-salt extraction. Work currently under way at ANL[37,38] indicates that molten-salt extraction may be a suitable means of recovering tritium from liquid lithium. Results to date show that adequate distribution coefficients (2 to 4 on a volumetric basis in favor of the salt) can be achieved, and potentially suitable methods for recovery of tritium from the salt are being investigated. This technique may permit the maintenance of tritium levels as low as 1 wppm in liquid lithium. Areas requiring study in the near future include (1) effects of mutual solubilities on both neutronics and salt processing, (2) compatibility of materials, (3) survey of suitable minimum-entrainment contacting and separating methods, and (4) demonstration of suitable means for recovering tritium from the salt.[38]

Tritium Recovery from Solid Breeder Blankets

Analytical[40,45] and experimental[40] work on solid blankets has been restricted mainly to performance characteristics that might influence tritium recovery, inventory, and containment. Results achieved in the BNL program[40] on ceramic breeding materials have been reasonably encouraging with respect to steady-state recovery under minimum inventory conditions (<<1 wppm). Similar results for solid Li-alloys are less understood, but efficient recovery at low inventory is indicated. Important near-term exploration of ceramic materials should include (1) determination of the effects of irradiation to high burnups on dimensional stability, tritium release rates, and chemical stability toward the sweep gas, (2) investigation of the dependence of performance characteristics on morphology (particle size, size distribution, pore structure, etc.); and (3) compatibility with containment materials and with other companion substances, including moderators (B and C) and neutron multipliers (Be and Pb). Effects of chemisorption, implantation, or chemical fixation of tritium on interior blanket structures should be examined in the context of the "hands-on" maintenance expectations for minimum-activation designs. Eventually, in-reactor testing of candidate solid breeder materials under realistic conditions (including simultaneous breeding and tritium extraction) should be made. Design optimization of sweep gas processing methods must ultimately be completed.

Tritium Recovery from Molten-Salt Blankets

Recovery of tritium from molten-salt blankets appears to be reasonably straightforward,[42-44] and inventories well below 1 wppm should be achieveable. Past analyses of sparged and unsparged desorbers have indicated that efficient removal of tritium from the salt is readily attainable in forms well suited for efficient regeneration. These analyses require experimental demonstration under conditions which take proper cognizance and control of (1) the oxidation potential of the salt system, (2) interactions between the salt and bounding walls,

and (3) the influence of magnetic fields in promoting localized electrolysis.

UNIQUE PROBLEMS

In addition to the fuel circulation and processing hardware and the various containment devices, there are a number of other special systems that may be essential to the operation of at least near-term DT reactors and whose presence could lead to significant interfacing problems with the tritium handling systems. Two such systems are neutral beam injectors and first wall cooling circuits. Some considerations related to these special interfacing problems are summarized below. As other essential reactor systems that have a direct interaction with, or that have access to, the tritium systems are identified, they too must be carefully characterized in terms of the magnitude and design impact of interfacing requirements.

Neutral Beam Injector Interfacing

Recent conceptual design studies have shown that experimental tokamak and mirror reactors may require energetic particle insertion to reach ignition. As currently conceived,[52,53] the neutral injector systems that would be used to provide these energetic particles represent a direct access to the plasma chamber, and, hence, to the tritium contained in it during a burn cycle. The beam line, the neutralizer, and the accelerator itself are all subject to tritium backflow from the plasma chamber. Thus, tritium can enter the neutral beam pumping systems and the neutralizer vapor circulation system, and pass through the electrostatic grid structure into the grid coolant. The objective of neutral beam injector interface studies should be to identify significant tritium interactions and to evolve and test designs that will permit the making of a workable injector/reactor interface. This effort should include the determination of tritium containment criteria for neutral injectors and the development of a maintenance methodology for tritium contaminated injector systems.

Tritium Migration to the First-Wall Cooling Water

The migration of tritium in and through the thermally hot structures surrounding the plasma of a DT burning reactor should be the subject of a whole paper in itself, since this migration will probably turn out to be the major contributor to tritium losses from any fusion power plant. In this section, however, the only case that will be addressed will be one in which the first wall of a near-term experimental reactor is cooled with a fluid that neither contains breeding material nor interfaces in any way with a breeder blanket; i.e., the only source of tritium entry into the coolant fluid is by permeation of fuel from the plasma chamber through the first wall structure and into the coolant channels. Although a variety of coolant fluids and structural materials could be considered in the context of this discussion, only helium and water contained in stainless steel first wall assemblies will be addressed here for purposes of illustration.

The selection of water as a coolant for the first wall blanket and shield of any fusion device raises concern regarding the consequences of tritium migration into and through the cooling circuits. The problem of tritium permeation through austenitic construction materials has long been recognized as a major area of concern for fusion power plants. Although the principal focus of attention to this problem has been on migration of blanket tritium through heat transfer circuits and eventually to the environment, the tritium in the plasma chamber

is also subject to migration; hence, the absence of a breeder blanket would not necessarily obviate concern for tritium releases resulting from the heat transfer circuitry. For purposes of analysis, permeation was assumed to occur across the entire surface of a first wall having a thickness of 5 mm and an area of 6×10^6 cm^2 (approximating presently conceived tokamak EPR's[1]). The total volume of the first wall cooling water circuit was assumed to be 10^5 liters and the tritium partial pressure in the plasma chamber was estimated at 10^{-4} Torr. Existing hydrogen permeation data for Type 316-SS (data from reference 23 were used in this case) were divided by $\sqrt{3}$ to correct for H/T isotope effects. Results of calculations made under these conditions are summarized in Fig. 1 together with related data for existing heavy water reactors. The concentrations of tritium in the first wall cooling water circuit are found to be in the range of those reached in the primary (D_2O) circuit of typical experimental heavy water reactors[46-48] after a period of about two years. It is, therefore, reasonable to assume that the inventory of tritium in the cooling water for the above case could be managed using practices employed in existing heavy water reactors. The drainage, consolidation, and disposal of the entire first wall cooling water inventory (10^5 liters) every two to three years should pose no insurmountable problems, and is probably preferable (from an economic viewpoint) to installing a tritium extraction plant[46] for the first wall coolant.

In the case of pressurized helium cooling, the assumption is usually made that any tritium entering the coolant stream would be rapidly converted to HTO through reaction with the low levels of H_2O and O_2 impurity expected to be present in helium circuits. This HTO could then be gettered or desiccated out of the helium in a relatively straightforward manner, such that tritium buildup beyond trace levels is not possible. For the cases considered in Fig. 1, but with helium cooling, the total tritium handled in the helium scrubbing system would not exceed 10 grams/year.

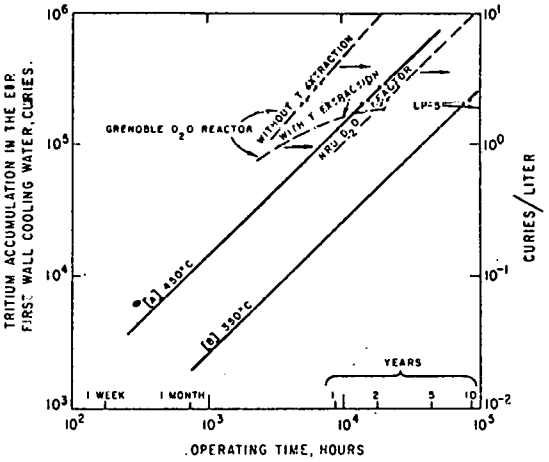

FIGURE 1. Tritium Accumulation in the First Wall Cooling Water Circuit. Material = 316-SS, Wall Area = 6×10^6 cm^2, Wall Thickness = 5 mm, Coolant Volume = 10^5 liters, Tritium (T_2) Pressure = 10^{-4} Torr.

ACKNOWLEDGMENTS

The author wishes to acknowledge helpful correspondence from E. F. Johnson (Princeton University), T. R. Galloway (Lawrence Livermore Laboratory), J. S. Watson and J. T. Bell (Oak Ridge National Laboratory), L. J. Wittenberg and W. R. Wilkes (Mound Laboratory), and E. J. Hennelly (Savannah River Laboratory). The impetus for this paper was derived from work supported by the Division of Magnetic Fusion Energy, U. S. Energy Research and Development Administration.

REFERENCES

1. W. M. Stacey, Jr., et al., "Tokamak Experimental Power Reactor Conceptual

Design Study," ANL/CTR-76-3, Argonne National Laboratory (1976).

2. W. M. Stacey, Jr., et al., "Tokamak Experimental Power Reactor Studies," ANL/CTR-75-2, Argonne National Laboratory (1975).

3. L. J. Wittenberg et al., "Evaluation Study of the Tritium-Handling Requirements of a Tokamak Experimental Power Reactor," MLM-2259, Mound Laboratory (1975).

4. J. S. Watson et al., "Scoping Studies of Tritium Handling in a Tokamak Experimental Power Reactor," ORNL-TM-5080, Oak Ridge National Laboratory (1976).

5. "General Atomic Experimental Power Reactor: Blanket/Shield, Tritium and Power Conversion Systems," GA-A13881, prepared by the Reactor Engineering Staff, General Atomic Company (March, 1976).

6. H. J. Garber, "TFTR Tritium Handling Concepts," WFPS TME-005, Westinghouse Electric Corporation (1975).

7. R. G. Hickman, "Tritium in the Fusion Engineering Research Facility," UCRL-75354, Lawrence Livermore Laboratory (1974).

8. D. T. Vier, J. L. Anderson and R. A. Krakowski, "Preliminary Design of the Tritium Handling Facilities for the Proposed Los Alamos Fusion Test Reactor," Proceedings of the Symposium on Tritium Technology Related to Fusion Reactor Systems, ERDA-50, U. S. Energy Research and Development Administration (1975) p. 133.

9. P. W. Fisher and J. S. Watson, "Cryosorption Vacuum Pumping of Deuterium, Helium, and Hydrogen at 4.2 K for Controlled Thermonuclear Reactor Applications," Symposium on Remote Systems, ANS/ENS International Conference, Washington, D. C., Nov. 14-19, 1976.

10. J. S. Watson and P. W. Fisher, "Vacuum Pumping for Controlled Thermonuclear Reactors," paper presented at the Ninth Symposium on Fusion Technology, Garmisch-Partenkirchen, Fed. Rep. of Germany, June 14-18, 1976.

11. P. J. Gareis and S. A. Stern, "Cryosorption Pumping of Helium and Hydrogen," Cryogenic Engineering News (October, 1967) p. 26.

12. G. E. Grenier and S. A. Stern, "Cryosorption Pumping of Helium at 4.2 K," J. of Vac. Sci. and Tech. 3, 334 (1966).

13. T. B. Rhinehammer and P. H. Lamberger, "Tritium Control Technology," WASH-1269, U. S. Atomic Energy Commission Report (December, 1973).

14. R. C. Bowman et al., "Metal Tritide Technology," Proceedings of the Symposium on Tritium Technology Related to Fusion Reactor Systems, ERDA-50, U. S. Energy Research and Development Administration (June, 1975).

15. W. R. Wilkes, "Hydrogen Isotope Separation System for the Tokamak Experimental Power Reactor," Proceedings of the International Conference on Radiation Effects and Tritium Technology for Fusion Reactors, CONF-750989, U. S. Energy Research and Development Administration (March, 1976).

16. B. Misra and V. A. Maroni, "Computer Modeling of Hydrogen Isotope Enrichment for Fusion Power Reactors," Proceedings of the Second ANS Topical Meeting on the Technology of Controlled Nuclear Fusion, Richland, WA, September 21-23, 1976).

17. S. A. Steward, J. F. Lakner and F. Uribe, "Storage of Hydrogen Isotopes in Intermetallic Compounds," UCRL-77455, Lawrence Livermore Laboratory (April, 1976).

18. S. L. Hanel, "Quality Assurance Guidelines for High Pressure Gas Systems," UCRL-77864, Lawrence Livermore Laboratory (1976).

19. C. L. Folkers and V. P. Gede, "Transfer Operations with Tritium--A Review," UCRL-76729, Lawrence Livermore Laboratory (1975).

20. J. T. Bell et al., "Tritium Permeation through Steam Generator Materials," Proceedings of the International Conference on Radiation Effects and Tritium Technology for Fusion Reactors, CONF-750989, U. S. Energy Research and Development Administration (March, 1976).

21. R. C. Axtmann, E. F. Johnson and C. W. Kuehler, "Permeation of Hydrogen at Low Pressures through Stainless Steel and Implications for Tritium Control in Fusion Systems," ibid.

22. H. K. Perkins et al., "Tritium Holdup Due to Coatings on the First Wall of Fusion Reactors," ibid.

23. V. A. Maroni et al., "Experimental Studies of Tritium Barrier Concepts for Fusion Reactors," ibid.

24. J. D. Fowler et al., "Tritium Diffusion in Ceramic Materials," ibid.

25. W. A. Swansiger et al., "Deuterium Permeation through 309S Stainless Steel with Thin, Characterized Oxides," J. Nucl. Mater. 53, 307 (1974).

26. E. Golankiewicz, Engelhard Industries (personal communication).

27. T. R. Galloway et al., "Mirror Reactor Blankets," UCID-17083, Lawrence Livermore Laboratory (1976).

28. J. C. Bixel and C. J. Kershner, "A Study of Catalytic Oxidation and Oxide Adsorption for the Removal of Tritium from Air," Proceedings of the Second AEC Environmental Protection Conference, April 16-19, 1974, Albuquerque, NM; WASH-1332 (1974) p. 261.

29. L. J. Wittenberg et al., "Environmental Concerns of the Tritium Inventory in a Fusion Reactor Facility," Proceedings of the Second ANS Topical Meeting on the Technology of Controlled Nuclear Fusion, Richland, WA, September 21-23, 1976.

30. W. M. Rodgers and R. Michalek, "Tritium Removal Systems," Report published by Engelhard Industries Division of Engelhard Minerals and Chemicals Corporation.

31. C. K. Kershner, "Tritium Effluent Control Project at Mound Laboratory," Proceedings of the Symposium on Tritium Technology Related to Fusion Reactor Systems, ERDA-50, U. S. Energy Research and Development Administration (June, 1975).

32. A. E. Sherwood, "Tritium Removal from Air Streams by Catalytic Oxidation and Water Adsorption," UCRL-78173, Lawrence Livermore Laboratory (June, 1976).

33. M. F. Singleton and C. L. Folkers, "Assessment of Uranium and Cerium as Getter Materials for Deuterium in Flowing Argon," UCRL-78147, Lawrence Livermore Laboratory (June, 1976).

34. J. Powell et al., "Proceedings of the Workshop on Blanket/Power Systems for Fusion Reactors," Brookhaven National Laboratory, March 29 to April 2, 1976 (in press).

35. S. D. Clinton et al., "Recent Experimental Studies Related to Controlled Thermonuclear Reactors," Proceedings of the International Conference on Radiation Effects and Tritium Technology for Fusion Reactors, CONF-750989, U. S. Energy Research and Development Administration (March, 1976).

36. F. J. Smith et al., "Chemical Equilibrium Studies of Tritium-Lithium and Tritium-Lithium Alloy Systems," ibid.

37. V. A. Maroni et al., "Solution Behavior of Hydrogen Isotopes and Other Non-Metallic Elements in Liquid Lithium," Proceedings of the International Conference on Liquid Metal Technology in Energy Production, Champion, PA, May 3-6, 1976.

38. W. F. Callaway et al., "A Review of the ANL Program on Liquid Lithium Processing and Tritium Control Technology," Proceedings of the Second ANS Topical Meeting on the Technology of Controlled Nuclear Fusion, Richland, WA, September 21-23, 1976.

39. J. L. Anderson, "An Evaluation of Low Melting Metal Eutectic Mixtures for Extracting Tritium from Lithium Blankets," ibid.

40. J. R. Powell, R. H. Wiswall, and E. Wirsing, "Tritium Recovery from Fusion Blankets using Solid Lithium Compounds," BNL-20563, Brookhaven National Laboratory (October, 1975).

41. D. K. Sze et al., "Gravity Circulated Solid Blanket Design for a Tokamak Fusion Reactor," Proceedings of the Second ANS Topical Meeting on the Technology of Controlled Nuclear Fusion, Richland, WA, September 21-23, 1976.

42. W. R. Grimes and S. Cantor, "Molten Salts as Blanket Fluids in Controlled Thermonuclear Reactors," ORNL-TM-4047, Oak Ridge National Laboratory (December, 1972).

43. G. A. Getz, "Packed-Column Removal of Tritium Fluoride from Fusion Reactor Molten Salt Breeder Loops," B.S.E. Thesis, Department of Chemical Engineering, Princeton University (May, 1976).

44. J. B. Talbot, "A Study of Tritium Removal from Fusion Reactor Blankets of Molten Salt and Lithium-Aluminum," ORNL-TM-5104, Oak Ridge National Laboratory (March, 1976).

45. R. G. Clemmer, E. M. Larsen and L. J. Wittenberg, "Tritium Handling, Breeding and Containment in Two Conceptual Fusion Reactor Designs, UWMAK II and UWMAK-III," J. Nucl. Eng. and Design (in press).

46. M. Damiani, R. Getraud and A. Senn, "Tritium and Hydrogen Extraction Plants for Atomic Power Reactors," Reprint from Sulzer Technical Review Number Nuclex 72, Sulzer Brothers, Ltd., Wintersthru, Switzerland.

47. W. R. Bush, "Assessing and Controlling the Hazard from Tritiated Water," AECL-4150, Chalk River Nuclear Laboratories (1972).

48. J. J. Hartig, Argonne National Laboratory (personal communication).

49. C. K. Briggs et al., "Estimates of Some Cryogenic DT Properties," Proceedings of the International Conference on Radiation Effects and Tritium Technology for Fusion Reactors, CONF-750989, U. S. Energy Research and Development Administration (March, 1976).

50. P. C. Souers et al., "Estimated D_2-DT-T_2 Phase Diagram in the Three Phase Region," ibid.

51. R. H. Sherman, J. R. Bartlit and R. A. Briesmeister, "Relative Volatilities for the Isotopic System Deuterium-Deuterium Tritide-Tritium," Cryogenics (in press).

52. "Tokamak Fusion Test Reactor Neutral Beam Injector Final Conceptual Design Report," ORNL-CF-75-9-15, Oak Ridge National Laboratory (October, 1975).

53. "TFTR Neutral Beam Injection System Conceptual Design," LBL-3296/UC-20, Lawrence Berkeley Laboratory/Lawrence Livermore Laboratory (October, 1975).

ISOTOPIC ENRICHMENT OF PLASMA EXHAUSTS FROM CONTROLLED THERMONUCLEAR REACTORS BY CRYOGENIC DISTILLATION*

Balabhadra Misra and Victor A. Maroni

Chemical Engineering Division
Argonne National Laboratory
Argonne, Illinois 60439

The feasibility of recycling the spent fuels from presently conceived tokamak-type power reactors via cryogenic distillation has been analyzed. As an essential step in analyzing complex mixtures consisting of the six isotopomeric forms of molecular hydrogen in widely varying ranges of concentrations, computer simulation of multicomponent distillation was carried out using an exact method of solution of the governing equations. Two distinct fuel injection schemes were analyzed using a six-column distillation cascade and a five-column distillation cascade, respectively. The two systems are: (1) 90% cold fuel injection with T/D ratio $\sim$ 1.1 and neutral beam injection of deuterons (D^0) comprising 10% of the delivered fuel, and (2) injection of equal atomic fractions of neutral tritons (T^0) and neutral deuterons (D^0). The results of the analytical studies show that the separation of the isotopomeric species of hydrogen can be carried out to any degree of purity by judicious selection of (1) the design and operating parameters and (2) the number of distillation columns, appropriately interspersed with chemical equilibrators.

INTRODUCTION

Since the mid-1960's, interest in the technological implications of energy production from controlled thermonuclear reactions has escalated rapidly. Although the scientific and engineering aspects of the handling and recovery of tritium in D-T (deuterium-tritium) fusion reactor breeder blankets have received considerable attention in recent years, little concentrated effort has been focused on the technical features of the mainstream fuel processing and recycle systems. This neglect has stemmed, at least in part, from a conviction that the purification, circulation, conditioning, storage, and delivery of the fuel could be accomplished with existing or reasonably extrapolated technology. Although the aforementioned conviction may turn out to be largely correct, there are several technical areas where much more detailed analysis remains to be performed. One of these areas -- the question of meeting hydrogen isotope enrichment requirements -- is the subject of this paper.

The estimated fuel burn-up rate during a typical burn cycle for most presently conceived magnetically confined D-T fueled fusion power reactors is on the order of a few percent of the inserted fuel; hence, based on economic considerations alone, it is essential that the unburned fuel (the

* Work supported by the U.S. Energy Research and Development Administration.

plasma exhaust) be recycled. The gross composition of the total fuel delivered to the plasma chamber, irrespective of the number and/or kind of different fuel insertion methods required, is expected to be a mixture containing equal atomic fractions of deuterium and tritium with very little (< 1 atomic %) impurity. As a result of (1) the principal thermonuclear reactions (D-T) which produce ^4He, (2) the side reactions (mostly D-D) which produce ^1H and ^3He, (3) the sputtering of first wall material, (4) transmutation reactions with the reactor structure, (5) permeation of hydrogen through the coolant containment, (6) ancillary chemical reactions, (7) out-gassing of the structure, and (8) probably some other less well defined phenomena, the gases remaining in the plasma chamber after a burn cycle are expected to contain a significant quantity of impurity species in addition to the unburned deuterium and tritium. The extent to which this spent fuel is suitable for reuse without processing after one, two, or perhaps a few burn cycles is a moot point, for sooner or later impurity removal must be undertaken, and the problem of fuel decontamination reduces to one of determining fractional processing rates. The chemical and physical state of the impurities in the plasma exhaust is also subject to speculation at this time, but it seems reasonable to assume that the normal ambient impurities (e.g., H, O, N, C) and perhaps some solid debris (dislodged from the first wall by energetic particle impacts) will accompany the unburned deuterium and tritium through the plasma amber evacuation systems.

Several scenarios have been developed for the fuel cycles of near-term conceptual fusion power reactors, and a number of these are reported in the literature.[1-5] It is not the subject of this paper to deal with the entire fuel cycle of a prototypal fusion reactor; hence, the reader should refer to the above literature for descriptions of fusion reactor fuel recycle requirements and proposed methods. For the purposes of the ensuing discussions, the assumption is made that at some point in the fuel cycle, all of the impurities except protium (^1H) and perhaps helium have been removed from the recirculating deuterium-tritium stream. It is at this point that the processing steps which satisfy hydrogen isotope separation requirements for the fuel delivery systems must be undertaken. Among the hydrogen isotope separation methods that are considered feasible for large-scale semi-continuous enrichment, cryogenic distillation appears to be best suited to the needs of the mainstream fuel recycle systems for fusion power reactors. The remainder of this paper deals with an analysis of the application of cryogenic distillation to a range of plausible isotope enrichment requirements for near-term D-T burning experimental fusion devices.

DESCRIPTION OF THE CALCULATIONAL METHOD

A variety of analytical techniques[6-8] have been used in the design of multicomponent distillation columns. While most of these methods are adequate to fulfill the needs of the chemical process industries, the exact method of solution by matrix algorithm appears to be most suitable for isotope separations. (The inaccuracies inherent in empirical schemes and trial-and-error solutions make the latter methods largely incapable of achieving the level of accuracy required in isotopic fuels analysis.) Hence, at the outset, it was decided to proceed with analyses based on an

exact method of solution of the governing equations to ensure that the accuracy of the analytical results would be limited only by the accuracy of the thermodynamic and phase equilibrium data.

A complex distillation column may contain many feeds, side streams, and other special features. The feed compositions may vary widely and may be introduced at any stage (or plate). Development of the computer simulation for a single distillation column was based on the general features shown in Figure 1. Once the basic computer program that contained the essential characteristics of a single column was developed, other special features were added by appropriately modifying the mathematical model. Several simplifying assumptions, of necessity, were made before the development of the mathematical model was carried out. The ideal equilibrium stage concept in conjunction with the laws of conservation of mass and energy were utilized to describe the functional relations among the various components. These assumptions may be stated briefly as follows: (1) The pressure drop across the column is negligible so that the column may be assumed to operate at a constant pressure. (2) Heat losses are small so that the column may be assumed to be operating adiabatically. (3) The molar heat of vaporization of all components is the same so that constant molar vapor flow may be assumed. (This is not a very restrictive assumption because the differences among the molar heats of vaporization of the six isotopic species of hydrogen are small.) (4) The vapors and liquids of the isotopes form ideal mixtures. The last assumption is not unrealistic for isotopes of the same element, especially at low pressures. Also, this assumption assures the validity of the laws of Raoult and Dalton; thus, the equilibrium relationship between the vapor mole fraction and liquid mole fraction may be represented by:

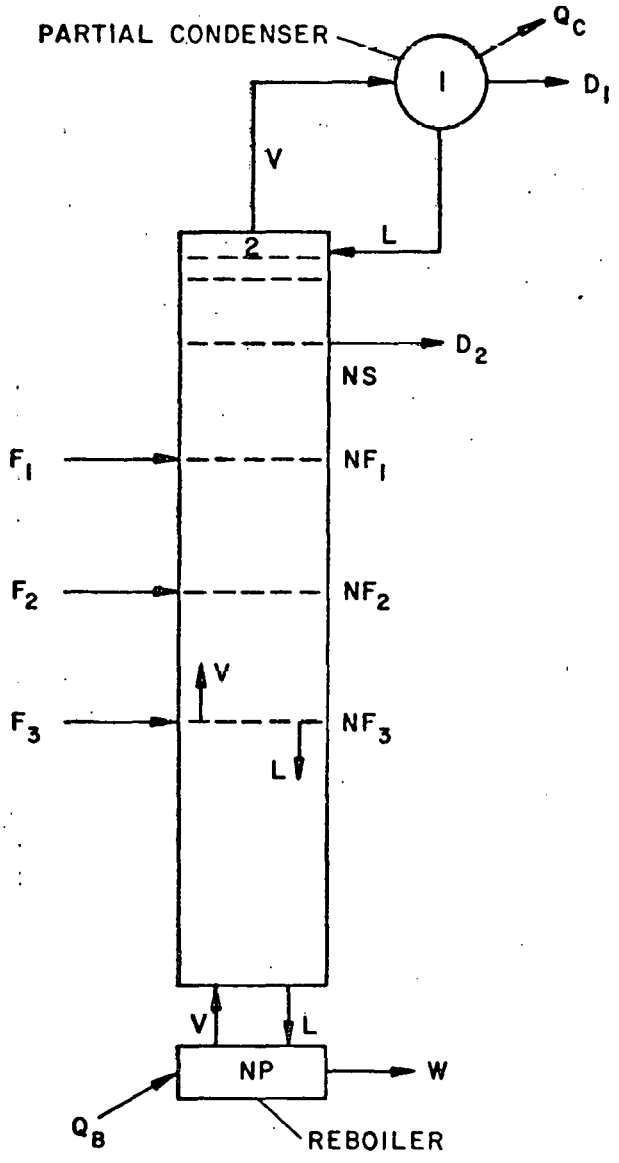

FIGURE 1. Schematic Drawing of a Complex Distillation Column. (See Nomenclature for definition of symbols.)

$$y_i = k_i x_i \qquad (1)$$

$$k_i = \frac{p_i}{P} \qquad (2)$$

where

y_i = mole fraction of component i in vapor phase

x_i = mole fraction of component i in liquid phase

= equilibrium constant for component i between the two phases

p_i = partial pressure of component i

P = total pressure of the system

The composition of the feeds and the rates of the feeds, the distillates, and the side streams are assumed to be known. For a given number of equilibrium plates (NP), assumed feedplate (NF_1, NF_2, etc.) and side stream (NS) locations, and reflux ratio (L/D), the functional relationship between the various components across the distillation column can be expressed mathematically as follows. For component i, of a total of NC components, the law of conservation of mass and phase equilibrium leads to NP (NP = number of theoretical stages) equations, each containing NP terms. By denoting the plate number as j and component number as i, the following set of NP equations may be written:

$$-a_{1,1}\,x_{1,i} + a_{1,2}\,x_{2,i} + 0 + 0 + \ldots = b_{1,1} \qquad (3\text{-}1)$$

$$a_{2,1}\,x_{1,i} - a_{2,2}\,x_{2,i} + a_{2,3}\,x_{3,i} + 0 + \ldots = b_{2,1} \qquad (3\text{-}2)$$

$$0 + a_{3,2}\,x_{2,i} - a_{3,3}\,x_{3,i} + a_{3,4}\,x_{4,i} + 0 + \ldots = b_{3,1} \qquad (3\text{-}3)$$

$$\vdots$$

$$0 + 0 + \ldots + a_{NP,NP-1}\,x_{NP-1,i} - a_{NP,NP}\,x_{NP,i} = b_{NP,1} \qquad (3\text{-}NP)$$

where

$a_{j,i}$ are coefficients of $x_{j,i}$, which are functions of the distribution constants and all internal and external flow rates of vapor and liquid, and

$b_{j,1}$ are the constants of the linear equations, which are functions of rate of feed and feed composition.

The above set of NP equations may be expressed in matrix algebra as follows:

$$AX = B \qquad (4)$$

where

A = NP x NP coefficient matrix

X = NP x 1 solution vector

B = NP x 1 column vector

The nature of the physical problem is such that it leads directly to the tridiagonal matrix represented by equations (3-1), (3-2) ... (3-NP). It should be noted that there are NC sets of independent equations (one for each component) of the type represented by matrix equation (4). For a physical problem, since the determinant of the NP x NP square matrix is non-singular, the solution of equation (4) is given by

$$X = A^{-1}B \qquad (5)$$

where A^{-1} is the inverse of matrix A. Hence, the solution of equation (4) results in NP values of component i, one value corresponding to each equilibrium stage. Similarly, the solution of the remaining sets of equations of type (4) gives the mole fractions of the other components in the liquid mixture. Thus, the mole fractions of all components at each equilibrium stage are determined simultaneously.

The correct solution is obtained when the following criterion is satisfied (with an acceptable degree of tolerance) simultaneously at each stage.

$$\sum_{1}^{NC} y_i = 1 = \sum_{1}^{NC} k_i x_i \qquad (6)$$

From this brief discussion, it is apparent that successful solution of the above set of equations depends on development of reliable convergence criteria. For ideal mixtures, the equilibrium constant, k, may be represented as a function of pressure and temperature. Since the column is assumed to operate at a constant pressure, the equilibrium constant is dependent on temperature only. Existing vapor pressure data[9] for the six isotopomeric molecular forms of hydrogen (H_2, HD, D_2, DT, HT, T_2) were used to calculate the equilibrium constants. For a typical spent gas mixture, the vapor pressure data for the range from 20 to 30 K were found to be adequate to cover the entire range of interest. For component i, k_i may be represented by an n^{th} degree polynomial:

$$k_i = C_{1,i} + C_{2,i}T_j + C_{3,i}T_j^2 + \cdots + C_{n,i}T_j^n \qquad (7)$$

where $C_{1,i}$, $C_{2,i}$, etc., are constants, and T_j is the temperature of the liquid mixture at plate j. Since the operating temperature range for the column at pressures in the range from 500 to 2000 Torr is quite limited, a fourth degree polynomial was found to adequately represent the data. A subroutine was written to obtain the polynomial fitting coefficients for each component by least squares methods. A typical set of fitting coefficients used in this study is given in Table 1 (for P = 1000 Torr).

Before proceeding with the calculations, initial values for the end temperatures of the column were assumed, guided by the saturation temperature corresponding to the composition of the feed mixture. Additionally, the temperature drop across the column was assumed to be a linear function of the number of theoretical stages so that a set of starting values for the equilibrium constants could be estimated. To accelerate the convergence, Newton-Raphson interpolation techniques were applied to estimate a set of new temperatures for each plate during the successive iterative steps.

The solution of a set of linear equations for a typical component involves very large numbers. For example, the determinant of a 30 x 30 square matrix for most of the hydrogen isotopes represented by equation (4) is of the order of 10^{33}. To reduce the round-off errors, the main program, as well as all of the subroutines, were written in double precision. Thus, the propagation of round-off errors that are

TABLE 1. Fitting Coefficients for Distribution Constants at P = 1000 Torr

Species	Value of i	Fitting Coefficients				
		$C_{1,i}$	$C_{2,i}$	$C_{3,i}$	$C_{4,i}$	$C_{5,i}$
H_2	1	7.659677D-01[a]	-6.033137D-02	-4.640048D-04	-5.739917D-05	1.101835D-05
HD	2	-3.348612D 00	5.975073D-01	-3.747318D-02	7.909861D-04	2.763535D-06
HT	3	-8.368202D-01	1.927116D-01	-1.259054D-02	1.058304D-04	9.132107D-06
D_2	4	6.550951D-01	-7.090902D-02	5.194761D-03	-4.188036D-04	1.410413D-05
DT	5	-2.210739D 00	3.766744D-01	-2.012363D-02	2.002574D-04	8.059631D-06
T_2	6	-6.398138D 00	1.030710D 00	-5.778316D-02	1.156992D-03	-1.492615D-06

[a] D-01 corresponds to $X10^{-1}$.

ierent in conventional iterative solutions is minimized. In order to ascertain the validity of the matrix inversion method adopted in solving equation (4), the solution vectors were back substituted to see whether the original constant vectors would be obtained. For all the cases considered, no error in the computational techniques could be found.

A detailed description of the main computer code, including FORTRAN listings, the supporting subroutines, and data input/output options is given in Reference 10. The versatility of the computer code may be demonstrated by analysis of a number of cases, as summarized below.

RESULTS OF SINGLE COLUMN SENSITIVITY STUDIES

To study how enrichment of the spent fuel proceeds across a distillation column, a number of simplified cases with only a single feed and no side stream draw-off were analyzed. The composition of the feed (spent fuel) was assumed to be representative of presently conceived tokamak-type reactors such as the ANL Experimental Power Reactor (ANL/EPR).[1,2] Several cases were analyzed by varying the number of theoretical stages, reflux ratio, feed plate location, and operating pressure in order to (1) study the behavior of distillation columns handling isotopes of hydrogen, and (2) detect any anomalous behavior of the computer code such as failure to converge. Some of these results are summarized in Table 2.

Effect of Number of Theoretical Stages

As the number of theoretical stages is increased, separation of the lighter fractions from the heavier fractions is enhanced (see rows 3, 9, 10 and 11 in Table 2). r example, if the number of theoretical stages is increased from 15 to 30, the deuterium atom concentration in the distillate is increased from 75 to 83%. However, the atom percentage of protium remains unchanged. This is due to the fact that essentially all of the protium appears in the distillate even when the column has only 15 theoretical stages.

Effect of Reflux Ratio

The degree of separation of the lighter constituents from the heavier constituents increases as the reflux ratio is increased (see rows 1 through 5 in Table 2). However, the increase in the degree of separation becomes asymptotic as higher and higher reflux ratios are employed.

Feed Plate Location

The effect of the feed plate on degree of separation depends on the feed composition. For the few cases analyzed by varying the feed plate location for a feed of fixed composition, the effect of the feed plate location was found to be minor (see rows 6 through 8 in Table 2).

Operating Pressure

As discussed in the previous sections, for a fixed feed composition, the separation of the more volatile fractions depends on the number of theoretical stages, reflux ratio, and the design characteristics of the distillation column. As the number of theoretical stages and reflux ratio are increased, the degree of separation of the more volatile fraction from the less volatile fraction increases. In many situations, however, the effects of these two variables do not significantly change the degree of separation. Also, increase in the number of equilibrium stages, as well as increase in the reflux ratio, results in increased liquid holdup and operating cost. As shown below, similar results can be achieved by varying the

TABLE 2. Summary of Operating Parameters and Analytical Results for a Single Cryogenic Column

Parameter	Column Pressure	No. of Plates	Feed Plate Location	Reflux Ratio	Atom % Top Product			Atom % Bottom Product		
					H	D	T	H	D	T
Effect of Reflux Ratio	1000 Torr	30	15	5	6.8	72.4	20.8	0.08	38.9	61.0
				10	7.0	80.0	13.0	0.02	35.6	64.3
				15	7.0	83.2	9.8	~0	34.4	65.6
				20	7.0	84.7	8.3	~0	33.8	66.2
				25	7.0	85.5	7.5	~0	33.4	66.6
Effect of Feed Plate			10	15	7.0	81.7	11.3	~0	35.0	65.0
			15		7.0	83.2	9.8	~0	34.7	65.3
			20		7.0	83.0	10.0	0.02	34.4	65.5
Effect of No. of Plates		25	12		7.0	81.1	11.9	0.01	35.2	64.8
		20	10		6.9	78.7	14.4	0.02	36.2	63.8
		15	8		6.9	75.4	17.7	0.06	37.6	62.3
Effect of Pressure	500 Torr	30	15	15	7.0	86.2	6.8	~0	32.6	67.4
	1000 Torr				7.0	83.2	9.8	~0	34.4	65.6
	1500 Torr				7.0	81.0	12.0	~0.01	35.3	64.7
	2000 Torr				7.0	79.4	13.6	~0.02	36.0	64.0
	2500 Torr				6.9	78.1	15.0	~0.03	36.5	63.4

[a]

[a]Input Composition = 2.10 at. % H, 48.95 at. % D, 48.95 at. % T.

operating pressure, which is conceptually much simpler.

To study the effect of pressure, a single distillation column was used for simplicity. The results for a typical feed mixture at pressures of 500, 1000, 1500, 2000, and 2500 Torr are summarized, respectively, in rows 12 through 16 of Table 2. The most significant effect of pressure seems to be on the atom fraction of tritium in the distillate. The tritium fraction increases from 7% to 15% when the pressure is increased from 500 Torr to 2500 Torr. The pressure has lesser effect on the other two hydrogen isotopes. As the atom percent of hydrogen in the bottom fraction is essentially zero for all cases, the operating pressure should have no effect on protium fraction. The atom fraction of deuterium in the distillate decreases from 86% to 78% as the pressure is increased from 500 Torr to 2500 Torr.

CRYOGENIC ENRICHMENT SCENARIO FOR A PROTOTYPAL FUSION POWER REACTOR

Before an enrichment scheme for typical near-term power reactors can be developed, the composition of the spent fuels and the purity requirements for the reinjectable fuels must be established. The following composition of the spent gases may be considered as representative of a typical experimental power reactor such as the ANL/EPR[1,2]: protium 2.1 at. %, deuterium 48.95 at. %, and tritium 48.95 at. %. For the presently conceived ANL/EPR fuelinjection scheme, the following are some of the requirements for the light and the heavy fractions: (1) The lightest fraction should contain all of the protium atoms with as little tritium as possible so that it can

(if necessary) be sent to waste consolidation and burial without further processing. (2) One of the heavy fractions must contain > 98 atom % deuterium so that it may serve as the fuel for the neutral beam injector. (3) The composition of the other heavy fractions should be such that the ratio of tritium to deuterium atoms is approximately 1.1 so that the fuel composition resulting from cold fuel and neutral injection has T/D $\simeq$ 1.0. An examination of the feed composition and reinjection requirements as listed above indicated that several distillation columns operating in cascade would be required. Figure 2 shows the six-column cascade developed for the ANL/EPR. It should be noted that a large number of cascade arrangements are possible to meet the above requirements and the Figure 2 represents an adequate, but not necessarily an optimum, separation scheme.

A second computer algorithm was developed and added to the computer code described above as a subroutine to analyze multicolumn cascades. With flow schematics as shown in Figure 2, convergence was observed to be very slow and tedious. To

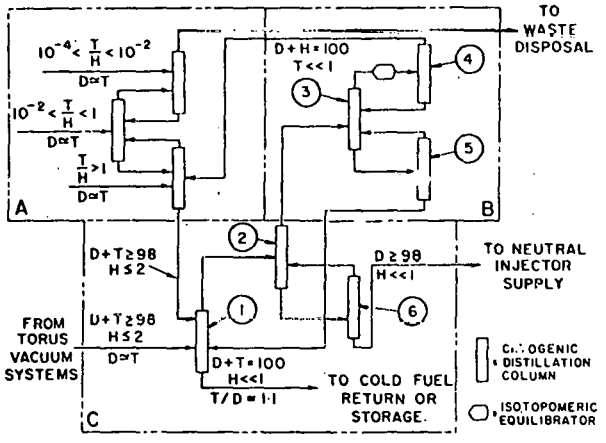

FIGURE 2. Cryogenic Enrichment Scenario for the ANL/EPR.

avoid this difficulty, feed No. 3 (bottom product from column No. 5) to column No. 1 was fixed after establishing its approximate composition during initial iterative calculations. This speeded up the convergence, although it was not possible to exactly match the composition of these two liquid mixtures. The analytical results are summarized in Table 3.

Figure 2 shows that columns No. 1, 4 and 6 are the product columns, with columns No. 2, 3 and 5 serving as intermediaries. Since the deuterium content in the feed to column No. 6 is 97%, the effect of the operating parameters on column No. 6 was minimal. Parametric investigations of the effects of the operating variables carried out for column No. 1 (see Table 2) show that these variables generally have little significant effect on the overall performance of the cascade.

An examination of the bottom products from columns No. 1 and No. 6 (see Table 3) shows that the compositions of these two streams essentially satisfy requirements (2) and (3) above. However, the distillate from column No. 4 could not be directly discharged into waste consolidation and burial without further reprocessing because of its high tritium content. An attempt was made to reduce the tritium content in the distillate from column No. 4 by varying the number of theoretical stages, reflux ratio and operating pressure. The tritium content could not be reduced to acceptable levels because of (1) the presence of some tritium at HT and (2) carryover of a portion of the DT into the distillate (because DT is more volatile than T_2). Hence, all of the protium atoms cannot be removed easily by distillation alone without carryover of some tritium atoms. An examination of the

TABLE 3. Summary of Operating Parameters for the TEPR Cryogenic Distillation Cascade[a]

Column Number[b]	Feed Plate	Total Feed (moles)	Feed Composition (at %) H	D	T	Top Product Total Moles	Top Product Atomic Percentages H	D	T	Bottom Product Total Moles	Bottom Product Atomic Percentages H	D	T
1	10 15 20	100	4.12	49.57	46.31	18	21.9	63.0	15.1	82	0.2	46.6	53.2
2	15 20	23	17.35	70.57	12.08	13	30.3	50.0	19.7	10	0.5	97.3	2.2
3	10 15 20	23	38.51	34.86	26.63	8	50.9	31.1	18.0	15	31.9	36.9	31.2
4	15	8	50.9	31.1	18.0	3	53.0	45.9	1.1	5	49.7	22.3	28.0
5	15	15	31.9	36.9	31.2	5	48.7	4.6	46.7	10	23.5	53.0	23.5
6	15	15	0.5	97.3	21.7	5	1.0	97.9	1.1	5	0	96.7	3.3
4[c]	15	8	50.8	29.2	20.0	3	96.1	4.5	0	5	22.2	44.8	32.7

[a] 30 Theoretical stages per column; column pressure 1000 Torr, except for column No. 1 operating at 500 Torr.

[b] See Fig. 2 for location in cascade.

[c] After chemical equilibration at 300 K.

equilibrium relationship among the six species of hydrogen isotopes shows that it is feasible to separate the protium atoms without carryover of tritium atoms by means of a chemical equilibration followed by cryogenic distillation as described below.

The isotopomeric composition of the equilibrium feed mixture that distills from the top of column No. 3 can be altered by shifting the equilibria among the various molecular hydrogen species. In the liquid state, the chemical equilibria among the six species are essentially frozen. By warming up the mixture to room temperature in a chemical equilibrator, especially in the presence of a catalyst (e.g., palladium on asbestos), new equilibria among the six species can be established, as described by the following equations.

$$H_2 + D_2 \rightleftarrows 2HD \quad (8)$$

$$H_2 + T_2 \rightleftarrows 2HT \quad (9)$$

$$D_2 + T_2 \rightleftarrows 2DT \quad (10)$$

$$H_2 + DT \rightleftarrows HT + HD \quad (11)$$

$$D_2 + HT \rightleftarrows DT + HD \quad (12)$$

$$T_2 + HD \rightleftarrows HT + DT \quad (13)$$

Equation (10) shows that DT can be split into T_2 and D_2, and equation (12) shows that by adding D_2 to HT, a more volatile component, HD, is produced which can be separated from less volatile DT. Thus, chemical equilibration followed by cryogenic distillation can lead to removal of essentially all protium atoms without significant loss of tritium atoms.

Although there are six chemical equations as shown above, there are only three independent equations that need to be solved to estimate a new composition of the feed mixture. However, the combined equations are nonlinear and, hence, are cumbersome to solve. A subroutine was written to solve these equations to establish the new composition of the feed mixture. The analytical results after chemical equilibration are shown in the bottom row of Table 3.

CRYOGENIC ENRICHMENT SCENARIO FOR MORE STRINGENT ENRICHMENT REQUIREMENTS

Based on the studies presented in this paper, it is apparent that the fuel enrichment requirements of a fusion device are largely determined by the fuel supply stream(s) composition requirements. It is also a reasonable assumption that most D-T burning experimental reactors (tokamaks or otherwise) will produce an exhaust system composition that is not significantly different from the one used above for the ANL/EPR. In order to extend the cryogenic distillation analyses to a machine with more stringent mainstream enrichment requirements than the EPR, the case of a fully injected tokamak reactor was considered. The previously described Tokamak Engineering Technology Facility[11] (TETF) was used as a point of departure for this analysis, because the TETF has the requirement that all deuterium and tritium atoms are delivered to the plasma chamber in the form of isotopically separated energetic neutral particle beams. The exhaust stream composition was taken to be 0.2 at. % H_2, 0.8 at. % HD, 0.8 at. % HT, 27.7 at. % D_2, 42.8 at. % DT, and 27.7 at. % T_2.

Since the D_2 and T_2 fractions represent less than 56% of the exhaust stream, complete recycling of the spent fuel cannot be accomplished by cryogenic distillation alone. The other requirement, as in the ANL/EPR, is to remove most of the protium atoms without carryover of significant quantities of tritium atoms. To fulfill the above reinjection requirements (i.e., separate streams of > 95% D_2 and > 95% T_2), one can qualitatively visualize the following steps: (1) Separate the heaviest component (T_2) as the bottom product containing a T_2 fraction $\geq$ 0.95 with no protium atoms present. (Based on the multi-component distillation program, as discussed above, this can be accomplished with one or more distillation steps.) (2) Remove a lighter product containing most of the D_2 molecules and the protium atoms. (3) Distill this product further to separate D_2 from protium- and tritium-bearing compounds. (4) Subject the protium-bearing compounds to a chemical equilibration followed by additional cryogenic distillation to remove most of the protium fraction with very little carryover of tritium atoms.

Carrying out the above steps will automatically lead to liquid fractions that are rich in DT, with lesser amounts of T_2 and D_2; hence, a second type of equilibration is now required to break up the DT fraction as follows:

$$2DT \rightleftarrows D_2 + T_2$$

The data on the equilibrium constant for the above reaction show that when a mixture containing equal atomic fractions of D and T is heated up (in the presence of an appropriate catalyst to speed up the reaction), the equilibrium mixture has the following approximate composition (above 50 K, the equilibration temperature has only a minor effect on the composition of the equilibrium mixture):

D_2 = 25%
T_2 = 25%
DT = 50%

It may be observed that the composition of the above mixture is very similar to that of the original feed and, hence, may be returned to the first distillation column.

Figure 3 represents a schematic of the separation scheme derived for the TETF type device. A fairly comprehensive

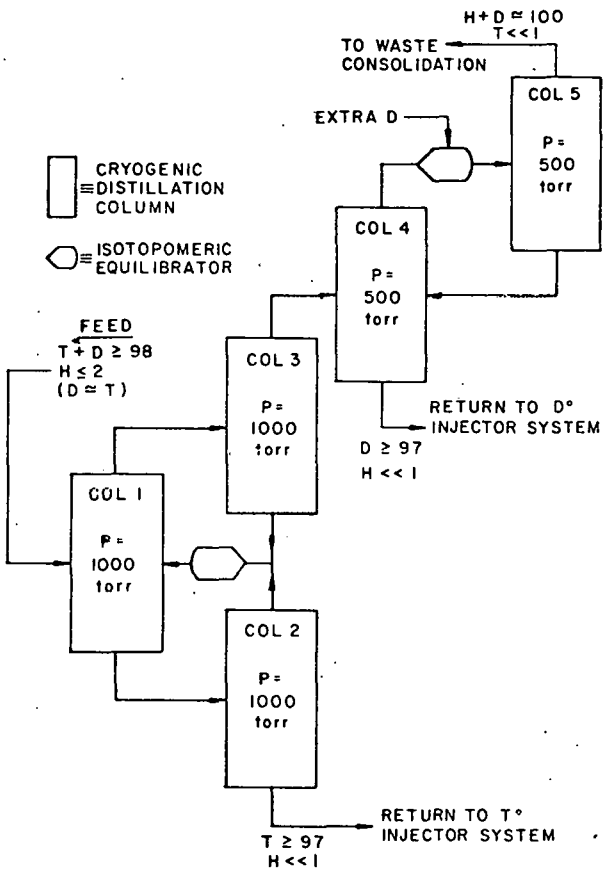

FIGURE 3. Cryogenic Enrichment Scenario for ANL/TETF

parametric investigation to study the effect of the operating variables was carried out for the enrichment scheme represented in Figure 3. The analytical results for the five-column cascade shown in Figure 3 are summarized in Table 4. An examination of the composition of the bottom product from column No. 4 will show that tritium-rich and deuterium-rich fractions containing little or no protium atoms can be obtained to meet the fuel recycle requirements. Compparison of the top products from column No. 5, with and without a chemical equilibrator, shows that a chemical equilibrator reduces the tritium fraction in the top product from 8.4% to 0.6%.

ESTIMATES OF REFRIGERATION POWER REQUIREMENTS

A preliminary assessment of power input demands for the types of distillation cascades represented in Figures 2 and 3 showed that the cyclic heating and refrigeration associated with the operation of equilibrators constituted the major electrical driving power load if the equilibrators handled a sizeable fraction of the total mass flow through the cascade. An estimate of the refrigeration power drawn by the equilibrator feeding into column No. 1 in Figure 3 was made based on the assumption that this equilibrator is operating between 300 K and 20 K and handles a total flow of 22 moles/hour of an equimolar mixture of deuterium and tritium. The heat capacity and latent heat of vaporization of the DT mixture were taken to be 29.1 joules/mole·K and 1385 joules/mole, respectively. For the case of an ideal, thermodynamically reversible liquefication process, the refrigeration power demand was found to be $\sim$ 7 watt·hour/mole or $\sim$ 1.55 kilowatt for the 22 mole/hour flow rate. (The use of a factor of 10 for the actual/ideal work ratio is in line with the values of 4.7 and 13 reported by Scott[13] for the liquefaction of air and helium, respectively. The overall power input to the cryogenic enrichment equipment for a fusion power plant is unlikely to exceed 10 kilowatts and, hence, will be a very small fraction of the plant's total recirculating power based on current estimates.[2]

CONCLUSIONS

Mathematical simulation of multicomponent distillation and computer solution of the resultant equations were carried out.

TABLE 4. Summary of Operating Parameters for the TETF Cryogenic Distillation Cascade[a]

Column Number[b]	Feed Plate	Total Feed (moles)	Feed Composition (at %)			Top Product				Bottom Product			
						Total Moles	Atomic Percentages			Total Moles	Atomic Percentages		
			H	D	T		H	D	T		H	D	T
1	15 20	100	0.49	49.64	49.87	50	1.0	74.9	24.1	50	0	24.4	75.
2	15	50	0	24.4	75.6	27	0	42.5	57.5	23	0	3.2	96.
3	15	50	1.0	74.9	24.1	25	2.0	93.9	4.1	25	0	55.9	44.
4	15 20	28	1.77	94.51	3.72	5	9.4	87.1	3.5	23	0.1	96.1	3.
5	15	5	9.4	87.0	3.6	2	23.1	68.5	8.4	3	0.2	99.4	0.
5[c]	15	5.5	8.6	88.2	3.2	2.5	18.8	80.6	0.6	3	0	94.6	5.

[a]30 Theoretical stages per column; pressure for columns 1, 2, 3 equal to 1000 Torr, pressure for columns 4 and 5 equal to 500 Torr.

[b]See Fig. 3 for location in cascade.

[c]After chemical equilibration at 300 K.

Since the computational steps are based on an exact solution method, the accuracy of the analytical results is expected to be limited only by the accuracy of the thermodynamic and phase equilibrium data. Although the computer code was developed specifically for enrichment of the spent fuels from presently conceived tokamak-type fusion reactors, the scope of this program is much broader, in that it can be used in the design and analysis of multicomponent distillation for any liquid mixture, provided, of course, that the necessary thermodynamic and phase equilibrium data are available. The program is very efficient so that a number of parametric investigations to study the effects of design and operating variables can be carried out even with limited resources. The program does, however, require a fairly large computer storage (approximately 250 K bytes).

Using this general purpose computer code as a basis, a distillation cascade consisting of six cryogenic columns was developed and analyzed for the ANL/EPR. The analytical results show that enrichment of the spent fuel, sufficient to meet the fuel injection requirements of the ANL/EPR, can be carried out in a straightforward manner.

Similar analytical studies of spent fuel enrichment for the ANL/TETF show that complete recycling of the fuel for a totally beam-driven device is possible with an enrichment system consisting of only five distillation columns and two chemical equilibrators.

The most important conclusion that may be drawn from the study of the two systems is that, in addition to meeting fuel injection requirements, separation of the isotopomeric species of hydrogen can be carried out to any degree of purity by judicious selection of (1) the design and operating parameters (e.g., number of theoretical stages, reflux ratio, operating pressure, etc.) and (2) the number of distillation columns, appropriately interspersed with chemical equilibrators. Generally speaking, most of these conclusions are in accord with an earlier study by Wilkes.[12]

ACKNOWLEDGEMENTS

The authors are grateful to Robert Sherman and W. R. Wilkes for several helpful discussions. The guidance and

encouragement of F. A. Cafasso and W. M. Stacey, Jr., is also gratefully acknowledged. Support for this work was obtained through the Argonne National Laboratory Experimental Power Reactor Studies Program funded by ERDA's Division of Magnetic Fusion Energy.

REFERENCES

1. W. M. Stacey, Jr., et al., "Tokamak Experimental Power Reactor Studies," ANL/CTR-75-2, Argonne National Laboratory (1975).
2. W. M. Stacey, Jr., et al., "Tokamak Experimental Power Reactor Conceptual Design Study," ANL/CTR-76-3, Argonne National Laboratory (1976).
3. J. S. Watson, et al., "Scoping Studies of Tritium Handling in a Tokamak Experimental Power Reactor," ORNL-TM-5080, Oak Ridge National Laboratory (1975).
4. Reactor Engineering Staff, "General Atomic Experimental Power Reactor: Blanket/Shield, Tritium, and Power Conversion Systems," GA-A13881, General Atomic Company (1976).
5. L. J. Wittenberg, et al., "Evaluation of the Tritium Handling Requirements of a Tokamak Experimental Power Reactor," MLM-2259, Mound Laboratory (1975).
6. R. H. Perry and C. H. Chilton, Chemical Engineers' Handbook, McGraw-Hill Book Co., New York (1973).
7. N. R. Amundson, Mathematical Methods in Chemical Engineering, Matrices and Their Applications, Prentice Hall, Inc., Englewood Cliffs, New Jersey (1966).
8. B. D. Smith, Design of Equilibrium Stage Processes, McGraw-Hill Book Co., New York (1963).
9. H. M. Mittelhauser and G. Thodos, "Vapor Pressure Relationship up to Critical Point of Hydrogen, Deuterium and Tritium, and Their Atomic Combinations," Cryogenics 4, 368 (1964).
10. B. Misra and V. A. Maroni, "Multicomponent Isotopic Separation and Recirculation Analysis," ANL-76-92, Argonne National Laboratory (August, 1976).
11. W. M. Stacey, Jr., et al., "Tokamak Engineering Technology Facility Scoping Study," ANL/CTR-76-1, Argonne National Laboratory (March, 1976).
12. W. R. Wilkes, "Hydrogen Isotope Separation System for the Tokamak Experimental Power Reactor," Proceedings of the Conference on Radiation Effects and Tritium Technology for Fusion Reactors, Gatlinburg, Tennesses, October 1-3, 1975; USERDA Report CONF-750989 (March, 1976), p. IV-266.
13. R. B. Scott, Cryogenic Engineering, D. Van Nostrand Co., Inc., Princeton, New Jersey (1959).

NOMENCLATURE

$a_{j,i}$	Coefficients of linear equation
$b_{j,1}$	Constants of the linear equation
A	NP x NP coefficient matrix
$a_{i,j}$	Members of matrix A
B	NP x 1 column matrix
$c_{1,i}, c_{2,i} \cdots c_{n,i}$	Polynomial fit coefficients
D_1, D_2	Distillate and side stream flow rates
F_1, F_2, F_3	Feed rates
i, I	Component designation
j, J	Equilibrium stage or plage number
k_i	Equilibrium constant for component i between the liquid and vapor phases
L	Liquid flow rate
L/D	Reflux ratio
n	Degree of polynomial
NP	Number of theoretical stages, or plates
NF_1, NF_2, NF_3	Feed plate numbers
NC	Number of components in the feed mixture
NS	Side stream plate number
P_i	Vapor pressure of component i
P	Total pressure of system
Q_C, Q_B	Heat flow rates for the total condenser and reboiler, respectively
T_j	Temperature of liquid mixture on plate j
V	Vapor flow rate
W	Bottom product removal rate
X	NP x 1 solution matrix
$x_{j,i}$	Mole fraction of component i in liquid phase on plate j
$y_{j,i}$	Mole fraction of component i in vapor phase on plate j

MULTIDIMENSIONAL NEUTRONICS ANALYSIS OF MAJOR PENETRATIONS IN TOKAMAKS*

M. A. Abdou, L. J. Milton, J. C. Jung, and E. M. Gelbard
ARGONNE NATIONAL LABORATORY, ARGONNE, ILLINOIS 60439

The blanket/shield system in tokamaks must provide for large size penetrations that can cause substantial streaming of nuclear radiation. Multidimenional neutronics calculations are used to examine the gross effects of major penetrations and their special shielding requirements. The study shows that it is feasible to shield against the effects of penetrations. However, the special shields for evacuation, neutral beam, and radio-frequency ducts occupy a substantial fraction of the reactor interior and their cost represents a significant cost item.

I. INTRODUCTION

The blanket/shield system in a Tokamak Experimental Power Reactor[1-4] (EPR), and in future tokamak fusion reactors as well, is required to accommodate a variety of penetrations including those for vacuum pumping, neutral beam and/or radio frequency (rf) heating, and experimental and maintenance access. These penetrations occupy typically ~5-10% of the blanket/shield volume. Penetrations such as those for vacuum pumping and neutral beam heating represent large void regions (~0.5-1 m^2 in cross-sectional area) which extend from the first wall (directly visible to the plasma neutrons), radially through the blanket/shield, and on out between the toroidal-field (TF) coils. The functional requirements of the neutral beam ducts exclude any possibility of introducing any significant bends in the duct. Sharp bends in the evacuation ducts greatly reduce the efficiency of vacuum pumping and they force the designer to increase the size of the ducts.

The need to guard against the potential problems that can be created by radiation streaming assisted by the presence of these penetrations, is obvious. The blanket/shield system provides, in general, about six orders of magnitude attenuation of nuclear radiation in order to protect the TF coils and auxiliary systems located on the exterior of these coils from excessive radiation damage, nuclear heating, and induced activation. The volume fraction of the major penetrations indicate that these penetrations would cause more than 1% of the neutrons to escape into the exterior of the primary (bulk) shield. Thus the additional special penetration shield will have to provide roughly four orders of magnitude of attenuation for neutrons streaming in the presence of penetrations. Therefore, the special shields for penetrations represent a very significant part of the shielding system in EPR and are expected to remain equally important in future tokamak reactors. The design of a penetration shield is more difficult, however, than the design of the primary bulk shield in two respects: (1) treatment of penetrations requires three-dimensional neutronics analysis; and (2) the geometry of the reactor imposes severe restrictions on the availability of space for penetration

*Work supported by the U. S. Energy Research and Development Administration.

shields, above and beyond the space restrictions on the bulk shield. Moreover, as will be shown later in this paper, the neutral beam ducts can be shielded on the sides only. Thus, there is always a straight-through path for the neutrons, a path leading to the beam injector and onto the exterior of the reactor.

The penetrations in a tokamak reactor can be classified, in general, into two types: (1) major penetrations; and (2) normal penetrations. The major penetrations are those penetrations that are large in size and their functional requirements do not permit substantial modifications in their shape. These major penetrations include, for example, the evacuation, neutral beam, and rf ducts. On the other hand, the normal penetrations are small and are ameanable to substantial shaping of their path inside the blanket/shield. Among the penetrations in this category are, for example, the coolant channels, clearances between shield blocks, and some of the small penetrations for diagnostics. This classification is of great importance with respect to the development of a strategic procedure for the design of a reactor. The effects of normal penetrations can be regarded as moderate perturbations on the performance of the system. Thus, although the impact of these normal penetrations should be anticipated qualitatively in the early stages of the design, their detailed design and analysis can be deferred until later stages of the overall reactor design process without much penalty. On the other hand, the effects of the major penetrations and their special shields on many of the reactor components is so great that these effects must be factored into the design as early as possible. By treating the major penetrations and their special shields as an integral part of the reactor system, many of the tradeoffs and conflicts can be resolved at early stages of the design. This paper presents some results of a neutronics study on the effects of major penetrations in tokamaks and analysis of their special shield requirements. More detailed information is given in Refs. 3 and 4.

II. CALCULATIONAL MODEL

Any penetration analysis depends to a great extent on many specific details of the reactor geometry and characteristics. The preliminary reference design for EPR documented in Refs. 1 and 2 was used for the initial parts of the penetration scoping study. This reference design has a major radius, R, of 625 cm and a circular plasma cross section with a minor radius, a, of 210 cm. There are 16 TF coils; each has a D-shaped vertical cross section with a horizontal bore of 7.7 m and a vertical bore of 11 m. A horizontal cross section of a TF coil is 0.60 m thick and 0.90 m wide. The blanket and primary shield consist of alternating zones of stainless steel (SS) and boron carbide (B_4C). A small segment of the blanket/shield at the inner side of the torus is 1.0 m thick while the rest of the blanket/shield is 1.31 m thick. In the reference design, as in any tokamak reactor, the inner segment of the blanket/shield cannot be utilized for placement of any major penetrations. These are generally accommodated on the top, bottom, and outer side of the torus. Therefore, the specific details of the inner segment of the blanket/shield will be ignored for the purpose of this work, and the blanket/shield is assumed to surround the plasma with a uniform thickness of 1.31 m. The inner radius of the first wall is 2.40 m. There are 32 vacuum ducts in the design, and each is cylindrical with an 0.85 m diameter. Two vacuum ducts are located at the top and bottom of the torus, equally spaced between each pair of the TF magnets. A cylindrical neutral beam duct with an 0.85 m diameter is located between each pair of TF magnets,

centered around the midplane, and its axis is nearly tangential to the toroidal magnetic axis.

The neutronics analyses were carried out using a three-dimensional geometric model with the continuous energy Monte Carlo Code VIM[5] and nuclear data from ENDF/B-IV.[6] Three-dimensional geometries are best treated at present with the Monte Carlo method. These calculations are inherently machine- and man-time consuming, making a thorough three-dimensional analysis of the full reactor geometry very costly. Therefore, a somewhat simplified three-dimensional geometric model, which is less costly but incorporates the basic features of the reactor geometry and accounts for all first-order effects of penetrations, was developed as described in detail in Ref. 3.

Figure 1 shows a schematic of the geometric representation for analysis of the vacuum ducts and their shields. If the toroidal magnetic axis is assumed to be a straight line, then Fig. 1 represents a cross section in the x-z plane where the z-axis is taken along the toroidal magnetic axis and the x-axis is parallel to the poloidal axis and passes through the plasma centerline. The system is symmetric around the midplane. A cross-section view in the x-y plane would show the blanket and the bulk shield as a set of concentric circles surrounding the circular plasma and scrape-off regions with one cylindrical vacuum duct at the top and another at the bottom. Figure 2 shows a schematic of the geometric representation for the analysis of the neutral beam ducts and their shields. A set of orthogonal coordinate systems (x,y,z) is also used here. The z-axis, as in Fig. 1, represents the toroidal magnetic axis, but the x-axis in the midplane and the y-axis is parallel to the poloidal axis. The axis of the beam duct is in the midplane (x-z plane) and makes an angle θ_b with the x-axis. Note that in both Figs. 1

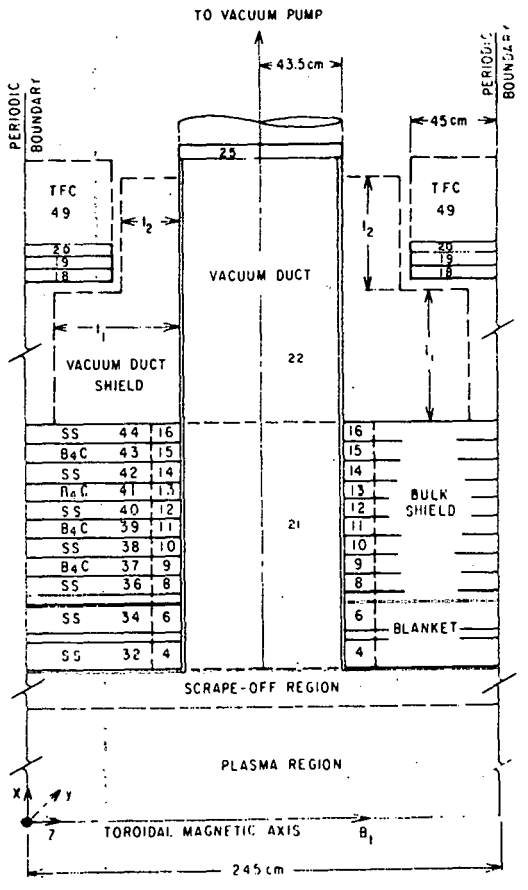

FIGURE 1. Schematic of Geometrical Representation for Analysis of Vacuum Ducts and Their Shields

and 2 the minor radius, r, for a point, is simply $r = \sqrt{x^2 + y^2}$.

In Figs. 1 and 2 some spatial zones are indentified by numbers that will be useful in later discussions. Zone 1 represents the plasma region and Zone 2 the scrape-off region. Zones 3-16 and 31-44 constitute the blanket-bulk shield. The wall of the penetration duct is represented as 1 cm thick tube of stainless steel that extends from the first wall to the exterior of the TF coils. The portion of the penetration duct inside the blanket and bulk shield is defined as Zone 21 and the corresponding portion of the duct wall is Zone 23. The

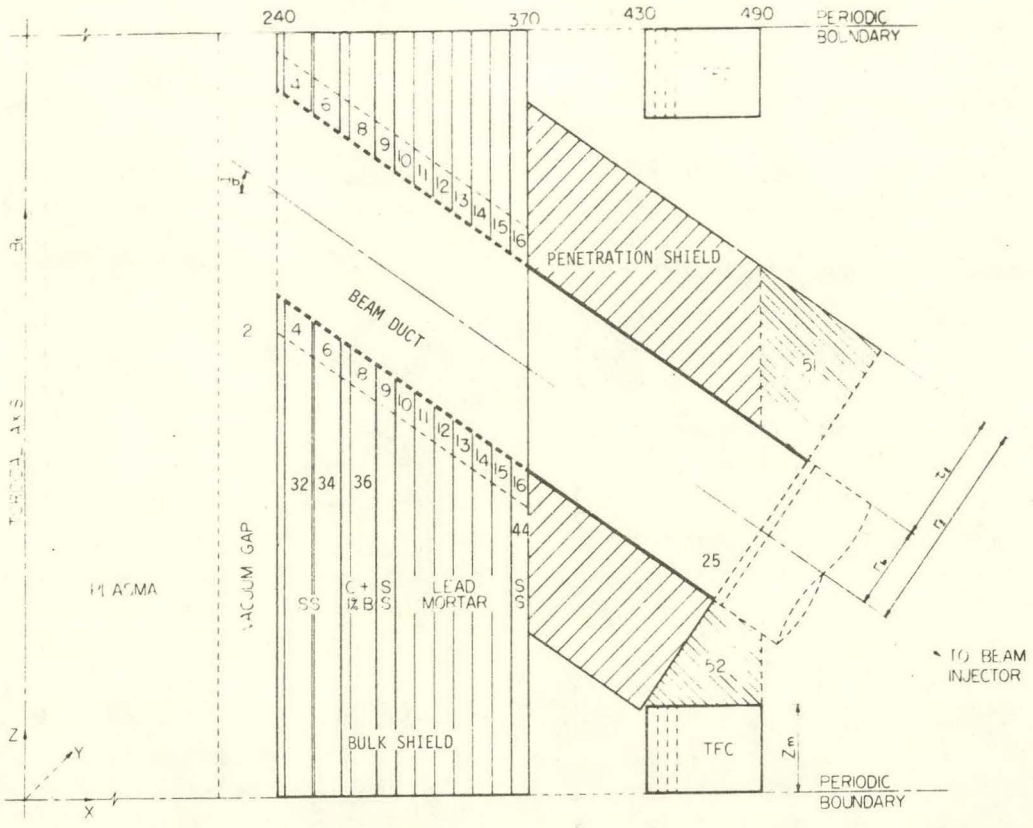

FIGURE 2. Schematic of Geometry Representation for Analysis of Neutral Beam Penetrations and Their Shields

part of the penetration duct outside the blanket-bulk shield is Zone 22 and the corresponding portion of the duct wall is Zone 24. The neutral beam and evacuation duct extend far beyond the TF coils in a detailed design. A neutral beam duct generally extends ~2.5 m beyond the TF coils and leads to the large size chamber of the beam injector. Many components are located inside the beam injector, such as the neutralizer, bending magnets, cryosorption panels, ion source, and accelerator. An evacuation duct leads to a vacuum pump. An evacuation duct can be bent before it is connected to a vacuum pump, but at the expense of a reduction in the pumping efficiency. If the vertical bore of the magnet is large enough, the vacuum duct can be bent external to the bulk shield and before it reaches the TF coils. In order to quantify the level of radiation streaming into the beam injectors and vacuum pumps, a 5 cm thick stainless steel disc was placed as an "end cap" on the penetration duct and is shown as Zone 25 in Figs. 1 and 2. The TF coils composition is homogenized as 50% SS + 50% Cu. These coils are divided into poloidal concentric rings, each 5 cm thick (depth). Each ring is divided into two zones. One zone is bound between two planes located at y = -100 and y = +100 and the other zone constitutes the rest of the ring. The first 5 cm ring consists of Zones 18 and 28 and the second 5 cm ring consists of Zones 19 and 29 with Zones 18 and 19 as the regions closer to the penetration duct.

III. ANALYSIS OF UNSHIELDED PENETRATIONS

Calculations for seven design sets, A-G

were made. Each set examines one or more aspects of the penetrations and their shield. This section is devoted to an analysis of the unshielded penetrations. Although it is clear that special shielding has to be provided to counteract the penetration effects, this analysis of unshielded penetrations is useful in providing insight into the requirements of such special shielding. Various schemes for shielding the penetrations are examined in the next section.

Design Set A includes three cases (1, 2, and 3), all of which have no penetrations, i.e. the blanket-bulk shield is solid and continuous everywhere. The variable parameter here is the blanket-bulk shield thickness, which is 131, 111, and 91 cm for cases 1, 2, and 3, respectively. The blanket and bulk shield composition for case 1 is that shown in Fig. 1. Cases 2 and 3 are obtained by eliminating outer parts of the shield with the appropriate thickness. The innermost radius of the TF coils in all cases is 430 cm. Table 1 shows the total neutron fluxes (normalized to 1 MW/m^2 neutral wall loading) at several key locations and the neutron leakage per DT neutron. In Table 1 and other tables in this paper, the percentage values in parentheses after each flux or leakage value represent the statistical error (i.e. the standard deviation) as estimated by VIM. These results show that increasing the thickness of the bulk shield by 20 cm reduces the level of nuclear radiation at the TF coils by a factor of >15. The tolerable level of nuclear radiation at the TF coils is generally determined from a tradeoff study of the conflicting requirements of the various reactor components and an optimization procedure to minimize the overall cost of the reactor per unit power output.[2,7] One constraint that cannot be violated, however, is that the radiation level at the TF coils must not exceed a level that permits the components of the superconducting magnet to function properly without excessive radiation damage and nuclear energy deposition. The magnet protection criteria depend on the design of the magnet and the specific superconducting and stabilizing materials. The radiation levels of cases 1 and 3 cover the range of acceptable levels for tokamak reactor designs that are of practical interest at present.[2,7]

Design Set B consists of cases 4, 5, and 6 which are similar to designs 1, 2, and 3, respectively, except for incorporating a cylindrical penetration duct that is 0.85 m

TABLE 1. Neutron Fluxes Normalized to a Neutron Wall Loading of 1 MW/m^2 for Design Set A

Case No.:	1	2	3
Thickness of Bulk Shield, cm	131	111	91
Diameter of Penetration Duct	none	none	none
No. of Histories	20,000	16,000	16,000
ϕ_{18}	9.93(6) (±18%)	1.85(8) (±14%)	3.19(9) (±13%)
ϕ_{19}	7.28(6) (±18%)	1.23(8) (±15%)	2.20(9) (±14%)
ϕ_{28}	9.93(6) (±18%)	1.85(8) (±14%)	3.19(9) (±13%)
ϕ_{29}	7.28(6) (±18%)	1.23(8) (±15%)	2.20(9) (±14%)
ϕ_{25}	9.90(6) (±18%)	1.85(8) (±14%)	3.20(9) (±13%)
Neutron Leakage per DT Neutron	1.16(-7)(±14%)	1.91(-6)(±13%)	2.93(-5)(±11%)

in diameter, as shown in Fig. 1. Results for cases 4, 5, and 6 are shown in Table 2. Comparison of results in this table with results shown in Table 1 for Design Set A shows that:

(1) The presence of penetrations causes a strong spatial variation of the TF coil neutron fluxes in the poloidal direction (i.e. along the circumference of the D-shape). The ratio of the neutron flux in region 18, ϕ_{18}, to that in region 28, ϕ_{28}, is $\sim$12. The penetrations also cause large variations in the toroidal direction across the TF coils.

(2) The penetrations increase the neutron flux in the TF coils by several orders of magnitude.

(3) Increasing the bulk thickness of the blanket-bulk shield from 0.91 to 1.31 m reduces the neutron flux at the magnet by a factor of $\sim$300 in the absence of penetrations but by only a factor of $\sim$3 when penetrations are present.

(4) The large-size penetrations assist a greater number of neutrons at high energy to reach the TF coils. This causes the increase in the transmutation, atomic displacement, and nuclear heating rates at the TF coil due to the presence of penetrations to be generally higher than the increase in the total neutron flux.

(5) The neutron leakage per DT neutron in the presence of penetrations is $\sim$2-3%, while in the absence of penetrations it varies from 1.2×10^{-7} for the 1.31 m bulk shield to 3×10^{-5} for the 0.91 m bulk shield.

(6) The neutron flux at the end cap, Zone 25, is $\sim 1.2 \times 10^{13}$ n/cm^2 sec. (For comparison, the neutron flux at the first wall is 7.6×10^{14}.) This means that auxiliary systems located at the end of the penetration duct receive a significantly high dose of radiation.

The large-size penetrations enable a large number of neutrons and photons to reach magnets in two ways: (1) by creating possible direct line-of-sight from the plasma region to the magnets; and (2) increasing the population of the neutrons and photons in the blanket/shield regions in the vicinity of the void penetration where they can travel into the magnets through short paths in the blanket/shield. This second effect, generally called penetration-assisted radiation streaming, becomes more dominant as the size of the void penetration is decreased and the line-of-sight streaming is reduced. Both direct and assisted streaming are sensitive to the size of penetration for a given reactor configuration, as shown next.

Table 3 shows the neutron fluxes and leakage for cases 7 and 8 compared with case 4 discussed above. The diameter of the cylindrical penetration is varied from 0.85 m in case 4 to 0.42 m in case 7, and to 0.20 m in case 8. The results in Table 3 show that the neutron fluxes at the TF coils are reduced by more than an order of magnitude when the cross section area of the void penetration is reduced by a factor of 4. From the very limited number of cases in Table 3, it can be tentatively concluded that the total neutron flux at the TF coils is roughly proportional to the square of the cross section area of the void penetration. Thus the neutron flux at the TF coils is approximately proportional to d^4, where d is the characteristic dimension of the penetration cross section (e.g. d is the diameter of a circular cross section or the side length of a square cross section). These correlations are brought up here only to demonstrate qualitatively the great dependence of radiation streaming on the size of penetrations. The geometry of the system and the shape of the penetration are also important. For example, a penetration with a rectangular cross section with one side much larger than the other side is likely to result in less radiation streaming than another penetration with the same cross

TABLE 2. Total Neutron Fluxes Normalized to a Neutron Wall Loading of 1 MW/m^2 for Design Set B

Case No.:	4	5	6
Thickness of Bulk Shield, cm	131	111	91
Diameter of Penetration Duct, cm	85	85	85
Orientation of Penetration	perpendicular[a]	perpendicular	perpendicular
Penetration Shield Composition	none	none	none
No. of Histories	20,000	10,000	10,000
ϕ_{18}	4.08(12) (±9%)	6.19(12) (±17%)	1.03(13) (±9%)
ϕ_{19}	2.67(12) (±11%)	4.13(12) (±19%)	7.77(12) (±8%)
ϕ_{28}	3.42(11) (±7%)	7.11(11) (±8%)	1.14(12) (±14%)
ϕ_{29}	1.90(11) (±11%)	4.00(11) (±13%)	6.84(11) (±16%)
ϕ_{21}	1.59(14) (±3%)	4.59(14) (±4%)	1.50(14) (±6%)
ϕ_{22}	2.22(13) (±6%)	2.16(13) (±11%)	2.37(13) (±8%)
ϕ_{23}	1.48(14) (±3%)	1.50(14) (±4%)	1.27(14) (±5%)
ϕ_{24}	1.63(13) (±8%)	1.47(13) (±10%)	1.83(13) (±9%)
ϕ_{25}	1.19(13) (±10%)	1.14(13) (±17%)	1.83(13) (±12%)
Neutron Leakage per DT Neutron	1.97(-2) (±6%)	2.54(-2) (±8%)	3.18(-2) (±8%)

(a) Axis of duct is perpendicular to the toroidal axis as shown in Fig. 1.

TABLE 3. Total Neutron Fluxes Normalized to a Neutron Wall Loading of 1 MW/m^2 for Design Set C.

Case No.:	4	7	8
Thickness of Bulk Shield, cm	131	131	131
Diameter of Penetration Duct, cm	85	42	20
Penetration Shield Composition	none	none	none
No. of Histories	20,000	20,000	50,000
ϕ_{18}	4.08(12) (±9%)	3.51(11) (±18%)	1.10(10) (±56%)
ϕ_{19}	2.67(12) (±11%)	1.85(11) (±25%)	8.04(9) (±70%)
ϕ_{28}	3.42(11) (±7%)	2.56(10) (±34%)	2.50(9) (±65%)
ϕ_{29}	1.90(11) (±11%)	1.86(10) (±32%)	2.03(9) (±79%)
ϕ_{21}	1.59(14) (±3%)	1.24(14) (±6%)	8.65(13) (±7%)
ϕ_{22}	2.22(13) (±6%)	6.18(12) (±24%)	7.62(11) (±65%)
ϕ_{23}	1.48(14) (±3%)	1.14(14) (±7%)	8.65(13) (±7%)
ϕ_{24}	1.63(13) (±8%)	3.61(12) (±27%)	5.16(11) (±64%)
ϕ_{25}	1.19(13) (±10%)	4.30(12) (±43%)	5.35(11) (±100%)
Neutron Leakage per DT Neutron	1.97(-2) (±6%)	1.181(-3) (±20%)	8.26(-5) (±45%)

section area but with a square or circular cross section. Both direct and assisted streaming are strongly dependent on the size and shape of the penetration.

Comparing ϕ_{23} as well as ϕ_{24} for the three cases in Table 3 shows that the neutron fluxes along the walls of the penetration vary also with the penetration size. The neutron fluxes in the portion of the duct walls inside the blanket-bulk shield increase by ~30% when the diameter of the duct is doubled. The variation in the neutron fluxes in the portion of the duct walls outside the blanket-bulk shield with the size of the duct is much more pronounced. These results indicate that the spatial variation in response rates such as gas production and nuclear heating along the duct walls depends on the size of penetration and is generally stronger for smaller-size penetrations.

IV. SHIELDING OF MAJOR PENETRATIONS

The effect of major void penetrations can be classified into two categories. The first category includes the effects on reactor components external to the bulk shield due to a dramatic enhancement of radiation streaming. The effects on the penetration walls and blanket-bulk shield in the vicinity of the penetrations are included in the second category. Effects in the first category can be guarded against by incorporating efficient penetration shields, as examined in this section.

There are several shielding schemes which might be used to protect reactor components external to the bulk shield from enhanced radiation streaming caused by large-size penetrations. These are:

(1) Movable Shield Plug -- If the functional requirements of a penetration permit that the penetration be closed during the plasma burn, then a shield plug can be moved at the beginning of each pulse to close completely the penetration region embedded in the bulk shield.

(2) Local Component Shield -- Reactor components affected by radiation can be surrounded by a shield capable of reducing the radiation level in the component to a tolerable level.

(3) Bulk Shield Extension -- The bulk shield can be extended into and in between the TF coils, and onto the outside as necessary.

(4) Local (Exterior) Penetration Shield -- Each penetration is surrounded as it emerges from the bulk shield by an appropriate local shield. This shield must suffice to reduce the radiation level at the TF coils and at all other auxiliary systems located in the reactor building to a permissible level.

Each of these shielding approaches has its own merits and disadvantages. The movable shield plug is the easiest to define in terms of nuclear requirements, since it needs to have the same dimensions as the penetration itself and it can be of a composition similar to that of the blanket-bulk shield. The most important advantage of the movable shield plug is that, in contrast to all other approaches, it completely eliminates the penetration effects and restores the effectiveness of the bulk shield. It also requires the smallest inventory of shielding materials of the four options. Whether a movable shield plug is less costly and is more favorable than the other shielding schemes has yet to be determined from detailed studies including engineering and reliability considerations. A movable shield plug weighs several thousands of kilograms for the size of penetration discussed in this work. It also requires incorporating mechanical and electrical components as well as automatic control system, all of which must have high quality performance. Moreover, failure of these components has to be anticipated and the consequences must be assessed and factored into the design.

There is a finite probability that the movable shield plug will fail to close the penetration before initiation of the plasma burn. In such situations, a significant number of neutrons and photons would stream through the penetration. Repair of a major failure in the shield plug would have to be made remotely and would involve a down-time period for the reactor. However, in view of many disadvantages associated with other shielding schemes, a movable shield plug has to be considered as a serious candidate for penetration shielding. A movable shield plug should be considered only, of course, for penetrations whose functional requirements permit that they can always be closed during the entire duration of the plasma burn. This immediately eliminates, for example, a movable shield plug as a viable approach for neutral beam ducts in beam-driven devices and for divertors.

This study does not find the movable shield plug to be a viable approach for the neutral beam ducts for several reasons. One specific reason for near-term devices up to and including the tokamak EPR is that these machines may have to be operated in a beam-driven mode, either to offset subignition confinement or to prolong burn pulses. In this case, the beam duct cannot be closed during the time of plasma burn. For future tokamaks beyond EPRs, the movable shield plug does not appear attractive for the neutral beam ducts for reasons that include the following:

(1) During the plasma heating phase, the neutral beam is injected for a finite period of time and the fusion power increases steadily. The total energy of the neutrons emitted during the beam injection phase depends on the characteristics of the design but it is generally significant. Thus, radiation streaming during the plasma heating phase when the shield plug cannot be used is very likely to be intolerable. The same problem arises when the beam is used to extend the burn pulse.

(2) The neutral beam ducts have to provide a straight-through path from the neutralizer to the plasma chamber. Thus, the mechanical movements of the shield plug to close the neutral beam duct will involve rotational as well as displacement movements. This will involve time delay in closing the beam duct with the plasma already in the ignition phase. Moreover, complicated patterns of movements for placing the shield plug inside the beam duct will magnify the risk of failure that will always be associated with periodic mechanical movements of massive weights on a short time scale.

The second approach for penetration shielding is local shielding of components that are affected by radiation. This approach can be easily rejected as the primary approach on the ground of the large volumes of reactor components that have to be shielded; it is, however, a useful supplemental shielding method for some small-size equipment that is overly sensitive to nuclear radiation. Simple extension of the bulk shield is not an efficient technique for reducing radiation levels.

The local penetration shield approach takes full advantage of the specific shapes of penetrations, and of the fact that the penetrations may be located relatively long distances apart. In this approach, each penetration is surrounded as it emerges from the bulk shield by local shielding. The shapes and compositions of the local shields can be carefully adjusted so as to conserve space and minimize cost. With this local penetration shield approach, the dimensions of the bulk shield, for a given material composition, should be no greater than the minimum required for the protection of the TF coils in regions far away from the penetrations (i.e. in the complete absence of any penetration effects). The local

penetration shield approach requires extensive nuclear analysis to determine the appropriate material composition and the optimum geometrical shape for each particular type of penetration. In this study, a modest attempt is made to examine the gross features of a local penetration shield.

Because of constraints on available space for local penetration shields it is important to find an effective shield material which is not unduly expensive. Such a composition was found in Refs. 2 and 7 for typical fusion reactor spectra to be a mixture of stainless steel and boron carbide. Design Set D in Table 4 allows for a penetration shield whose composition is 50% SS + 50% B_4C in case 9, all stainless steel in case 10, and all B_4C in case 11. The geometry of the system is as shown in Fig. 1, with the inner radius of the TF coils as 4.30 m. The penetration shield is 0.30 m thick and extends from the bulk shield to the end cap. The results in Table 4 show that the 50% SS + 50% B_4C penetration shield in case 9 gives much better overall attenuation than we find in cases 10 and 11. Comparing cases 9 and 11 shows that the 50% SS + 50% B_4C penetration shield lowers the radiation level at the TF coils and other components on the side of the shield by about a factor of 7 compared with the all-B_4C penetration shield. However, the radiation level in both cases is essentially the same at the open ends. The problem is just that — open ends. Some neutrons, travelling in the void duct, strike the penetration shield adjacent to the side of the duct, but others do not; many neutrons scatter from the side penetration shield into the duct where they can travel for a long path before they can make another collision on the side shield. Thus, the attenuation of neutron fluxes outward in the void duct will tend to be weak. This effect, as will be seen shortly, persists regardless of the thickness of the penetration shield.

Comparing case 9 in Table 4 with case 4 in Table 2 shows that the use of an 0.30 m thick penetration shield results in a factor of 40 reduction in the neutron fluxes at the TF coils. However, in reference to case 1 in Table 1, the penetration shield needs substantial improvement to provide an additional four orders of magnitude in attenuation in order to completely eliminate the penetration effects at the TF coils. Design Set E in Table 5 examines the effects of the penetration shield thickness and length. In cases 12, 13, and 14, only the first 15 cm of the magnet depth are included in the calculation in order to eliminate the computer time consumed in tracking particles traveling inside the TF coils (i.e. in region 49 in Fig. 1). Case 9 of Table 4 is also shown in Table 5 for comparison purposes. All penetration shields in cases 12, 13, 14, and 9 have a 50% SS + 50% B_4C composition. The penetration shield in case 12 is 0.30 m thick and covers only 0.55 m of the duct length external to the bulk shield. The penetration shield in case 13 has the same length as that of case 12 but is 0.75 m thick. The penetration shield in case 14 is 0.75 m thick in the region between the bulk shield and inner surface of the magnet then narrows down to fully occupy the 0.34 m thick region between the TF coils.

Results for cases 12 and 9 in Table 5 show that removing the portion of the penetration shield between the TF coils increase the neutron fluxes at the TF coil by a factor >2. Increasing the thickness of the penetration shield to 0.75 m without shielding the penetration segment which lies between the TF coils is an inefficient approach, as can be seen on comparing the TF coil fluxes for cases 13 and 9. The results in Table 5 show that increasing the thickness of the penetration shield from 0.30 m in case 9 to 0.75 m in case 14 (with the penetration covered from the outer surface of the bulk

TABLE 4. Total Neutron Fluxes Normalized to a Neutron Wall Loading of 1 MW/m^2 for Design Set D

Case No.:	9	10	11
Thickness of Bulk Shield, cm	131	131	131
Diameter of Penetration Duct, cm	85	85	85
Penetration Shield Composition	50% SS + 50% B_4C	SS	B_4C
Dimensions of Penetration Shield	$t_2 = t_1 = 30$ cm $\ell_1 + \ell_2 = 119$ cm	$t_2 = t_1 = 30$ cm $\ell_1 + \ell_2 = 119$ cm	$t_2 = t_1 = 30$ cm $\ell_1 + \ell_2 = 119$ cm
No. of Histories	30,000	10,000	10,000
ϕ_{18}	9.69(10) (±20%)	1.93(12) (±13%)	7.08(11) (±19%)
ϕ_{19}	6.04(10) (±23%)	1.27(12) (±23%)	3.30(11) (±20%)
ϕ_{28}	9.97(9) (±18%)	1.78(11) (±13%)	1.67(10) (±25%)
ϕ_{29}	7.37(9) (±22%)	1.14(11) (±21%)	1.67(10) (±27%)
ϕ_{21}	1.68(14) (±3%)	1.72(14) (±4%)	1.55(14) (±4%)
ϕ_{22}	3.37(13) (±5%)	4.53(13) (±8%)	2.32(13) (±8%)
ϕ_{23}	1.53(14) (±3%)	1.56(14) (±6%)	1.39(14) (±4%)
ϕ_{24}	2.88(13) (±5%)	-	-
ϕ_{25}	1.67(13) (±7%)	2.25(13) (±11%)	1.17(13) (±17%)
Neutron Leakage per DT Neutron	4.04(-3) (±7%)	1.10(-2) (±8%)	4.44(-3) (±12%)

TABLE 5. Total Neutron Fluxes Normalized to a Neutron Wall Loading of 1 MW/m^2 for Design Set E

Case No.:	12	13	14	9
Thickness of Bulk Shield, cm	131	131	131	131
Diameter of Penetration Duct	85	85	85	85
Penetration Shield Composition	50% SS + 50% B_4C	50% SS + 50% B_4C	50% SS + 50% B_4C	50% SS + 50% B_4C
Dimensions of Penetration Shield	$t_1 = 30$ cm $\ell_1 = 55$ cm $t_2 = \ell_2 = 0$	$t_1 = 75$ cm $\ell_1 = 55$ cm $t_2 = \ell_2 = 0$	$t_1 = 75$ cm $\ell_1 = 59$ cm $t_2 = 34$ cm $\ell_2 = 15$ cm	$t_1 = t_2 = 30$ cm $\ell_1 + \ell_2 = 119$ cm
No. of Histories	20,000	30,000	30,000	30,000
ϕ_{18}	2.17(11) (±21%)	1.31(11) (±12%)	1.32(9) (±79%)	9.69(10) (±20%)
ϕ_{19}	2.13(11) (±23%)	1.80(11) (±16%)	1.08(9) (±86%)	6.04(10) (±23%)
ϕ_{28}	2.11(10) (±26%)	4.84(8) (±41%)	2.44(8) (±100%)	9.37(9) (±18%)
ϕ_{29}	1.06(10) (±34%)	3.14(8) (±42%)	NS[a]	7.37(9) (±22%)
ϕ_{21}	1.58(14) (±4%)	1.52(14) (±3%)	1.58(14) (±2%)	1.68(14) (±3%)
ϕ_{22}	2.46(13) (±5%)	2.48(13) (±5%)	2.91(13) (±3%)	3.37(13) (±5%)
ϕ_{23}	1.44(14) (±4%)	1.38(14) (±3%)	1.41(14) (±3%)	1.53(14) (±3%)
ϕ_{24}	2.02(13) (±6%)	2.09(13) (±5%)	2.36(13) (±5%)	2.88(13) (±5%)
ϕ_{25}	1.23(13) (±10%)	1.14(13) (±8%)	1.28(13) (±7%)	1.67(13) (±7%)
Neutron Leakage per DT Neutron	9.60(-3) (±6%)	9.18(-3) (±6%)	8.80(-3) (±5%)	4.04(-3) (±7%)

(a) NS = no score = no neutrons reached this region in the histories run.

shield to in between the TF coils) reduces the neutron fluxes at the magnets by a factor of ~70. There is an important difference between the penetration shields in cases 9 and 14 besides the different thickness. In case 9 the penetration shield covers the penetration fully, i.e. it extends to the end cap. In case 14, however, the penetration shield covers only those portions of the penetration which lie between the bulk shield and the TF coils, and extends in between the TF coils for only 0.15 m. Thus, the portion of the TF coils (0.15 m depth) included in the calculation is protected from direct line-of-sight exposure of any region inside the penetration duct in both cases. However, in case 14 the portion of the duct beyond the TF coils is left bare. This causes the neutron leakage in case 14 to be about twice that in case 9. A comparison of the neutron fluxes in zone 25, ϕ_{25}, and the neutron leakage for cases 9 and 14 reaffirms an important conclusion obtained earlier in this section. Regardless of how thick the penetration shield is made to be, extending the penetration shield to surround the portions of the void duct beyond the TF coils is necessary in order to protect auxiliary systems and equipment located external to the TF coils.

On comparing the results for cases 14 and 1, one sees that the attenuation obtainable with thick penetration shield in case 14 (0.75 m thick and tapered off to 0.34 m in between the TF coils) needs to be improved by an additional two orders of magnitudes in order to completely eliminate the penetration effects at the TF coils. Comparing the results of case 14 in Table 5 with Case 3 in Table 1 shows that if the magnet protection criteria are satisfied by the attenuation provided by the 0.91 m thick blanket-bulk shield in the absence of penetrations, then the penetration shield specified in case 14 is adequate to eliminate the penetration effects at the TF coils. Thus, the size of the penetration shield, as expected, depends strongly on the tolerable radiation level at the TF coils.

In cases 1 to 14 the width of the repeating segment, W_s, which is the distance along the z-axis between the two symmetry planes shown in Fig. 1 was taken as 2.45 m. The inner radius of the magnet, r_m, was taken in these cases to be 4.30 m. If the outer minor radius of the bulk shield is r_0, then the radial clearance, Δ_{sm}, between the bulk shield and the toroidal field coils is given as $\Delta_{sm} = r_m - r_0$. Obviously, the penetration effects and the design of the penetration shield should depend on W_s and Δ_{sm} in addition to the dependence on other parameters discussed earlier in this section and the previous section. The value of W_s depends on the major radius, the spacing between each pair of TF coils, and the coil width in the vicinity of penetration. For a given r_0, the value of Δ_{sm} depends on the actual shape of the toroidal-field coils, and on the location of the penetration. For a D-shaped TF coil, Δ_{sm} is larger on the top and bottom of the torus than on the outside at midplane. Conversely, W_s is smaller on the top and bottom of the torus than on the outside at midplane. This introduces a basic difference between the geometric representation of the evacuation ducts and that of the neutral beam ducts, in addition to the difference in orientation of the ducts. It will be recalled that the axis of the evacuation duct is perpendicular to the magnetic axis, while the neutral duct axis is almost tangential to the magnetic axis. In the following, the differences in the neutronics effects of the two types of penetrations are examined.

In the EPR design given in Ref. 1, and used for guidance in geometric representation of this penetration scoping study, each TF coil has a D-shaped vertical cross section with a horizontal bore of 7.7 m and a vertical

bore of 11 m. Thus, for the evacuation ducts located at the top and bottom of the torus, W_s = 2.45 m and Δ_{sm} = 1.79 m. Design Set F in Table 6 includes three cases: 15, 16, and 17 for the evacuation ducts. Case 15 is for unshielded evacuation duct. It should be noted that case 15 is similar to case 4 in Table 2 except that Δ_{sm} is 0.59 m in case 4 and 1.79 m in case 15. Comparing the results for these two cases shows that extending the vertical bore of the TF coils actually increases the neutron fluxes at the coils while the neutron leakage remains approximately the same. Case 16 in Table 6 incorporates a penetration shield that is 0.75 m thick and extends 0.60 m beyond the outer surface of the bulk shield. Thus case 16 is essentially the same as case 13 except that Δ_{sm} is 1.79 m in case 16 and 0.59 in case 13. Again, a larger number of neutrons can reach the TF coils when the magnet vertical bore is increased if the penetration shield is not extended to reach in between the coils. Case 17 in Table 6 is the same as case 16, except that the penetration shield length is increased from 0.60 m in case 16 to 1.0 m in case 17. This increase of 0.40 m in the penetration shield length reduces the neutron fluxes at the TF coils by only a factor of ~2. Although the volume of the penetration shield in case 17 is more than 60% larger than that in case 14, the radiation level at the TF coils in case 17 is about a factor of 670 greater than that in case 14. This again is due to the fact that a portion of the evacuation duct near and in between the TF coils is left "bare" in case 17. A significant conclusion to be drawn, therefore, is that, for all practical purposes, increasing the bore of the TF coils cannot eliminate the need for effective shielding surrounding the evacuation duct in the regions where it passes between the TF coils. This is unfortunate since to make room for such a shield, it is necessary that the clearance space between a pair of TF coils be $\geq d + 2t_{ps}$, where d is the duct diameter and t_{ps} is the thickness of the penetration shield. To satisfy this requirement for a given major radius, d, t_{ps}, and TF coil width, the number of TF coils has to be reduced. The resulting increase in the magnetic field ripple then leads to enhancement of particle diffusion from the plasma. To avoid this situation, it seems that the vertical bore of the TF coils has to be increased, and the increase should be utilized in a different approach. If the increase in the magnet vertical bore is such that Δ_{sm} is significantly larger than $d + t_{ps}$ then the evacuation duct can be bent as it emerges from the bulk shield. Thus, the vacuum pumps can be moved so that they will no longer be visible to neutrons in the primary portion of the evacuation ducts, and at the same time both branches of the duct can be completely surrounded on all sides with penetration shield in order to protect the TF coils.

Cases 18 through 21 in Table 7 examine some of the neutronics aspects of the neutral beam ducts with the geometric representation shown in Fig. 2. The width of the repeating segment, W_s, in all these cases is 3.90 m, which leaves 3.0 m clearance between each pair of TF coils. The inner radius of the magnet, r_m, is 4.30 m in all cases. Cases 18 and 19 incorporate no penetration shield. In cases 19, 20, and 21 the axis of the beam duct makes a 55-deg angle with the toroidal magnetic axis, i.e., θ_b = 35° (see Fig. 2). For comparison, the axis of the beam duct in case 18 has a θ_b = 0°, i.e. this duct is perpendicular to the toroidal magnetic axis. Thus, case 18 is similar to case 4 except that W_s is 3.90 m in case 18 and 2.45 m in case 4. When the neutron fluxes in both cases are normalized to the same neutron wall loading, the results for the two cases provide a useful comparison

Table 6. Total Neutron Fluxes Normalized to a Neutron Wall Loading of 1 MW/m^2 for Design Set F

Case No.:	15	16	17
Thickness of Bulk Shield,[a,b] cm	131	131	131
Diameter of Penetration Duct, cm	85	85	85
Penetration Shield Composition	none	50% SS + 50% B_4C	50% SS + 50% B_4C
Dimensions of Penetration Shield	--	ℓ_1 = 60 cm	ℓ_1 = 100 cm
	--	t_1 = 75 cm	t_1 = 75 cm
	--	$\ell_2 = t_2 = 0$	$\ell_2 = t_2 = 0$
No. of Histories	20,000	20,000	20,000
ϕ_{18}	4.87(12) (±10%)	1.79(12) (±11%)	8.93(11) (±9%)
ϕ_{19}	3.61(12) (±10%)	1.31(12) (±15%)	5.61(11) (±12%)
ϕ_{28}	9.44(11) (±7%)	2.60(11) (±9%)	1.13(11) (±10%)
ϕ_{29}	6.12(11) (±6%)	1.44(11) (±9%)	6.86(10) (±11%)
ϕ_{21}	1.55(14) (±3%)	1.60(14) (±4%)	1.51(14) (±4%)
ϕ_{22}	1.58(13) (±7%)	1.62(13) (±7%)	1.90(13) (±7%)
ϕ_{23}	1.34(14) (±3%)	1.43(14) (±4%)	1.32(14) (±4%)
ϕ_{24}	1.12(13) (±6%)	1.23(13) (±7%)	1.48(13) (±7%)
ϕ_{25}	6.69(12) (±14%)	5.47(12) (±12%)	6.02(12) (±13%)
Neutron Leakage per DT Neutron	1.99(-2) (±5%)	8.94(-3) (±7%)	7.05(-3) (±8%)

(a) Blanket/shield composition is that shown in Fig. 1

(b) Basic geometry is as shown in Fig. 1.

(c) Basic geometry is as shown in Fig. 2.

TABLE 7. Total Neutron Fluxes Normalized to a Neutron Wall Loading of 1 MW/^{2} for Design Set G.

Case No.:	18	19	20	21
Thickness of Bulk Shield,[a,b] cm	131	131	131	131
Diameter of Penetration Duct, cm	85	85	85	85
Orientation of Penetration	$\theta_b = 0$	$\theta_b = 35°$	$\theta_b = 35°$	$\theta_b = 35°$
Penetration Shield Composition	none	none	50% SS + 50% B_4C	50% SS + 50% B_4C
Thickness of Penetration Shield	--	--	50 cm	70 cm
No. of Histories	20,000	20,000	40,000	40,000
ϕ_{18}	7.54(11) (±11%)	9.62(11) (±12%)	1.69(9) (±62%)	1.35(8) (±68%)
ϕ_{19}	5.97(11) (±13%)	5.83(11) (±16%)	2.06(9) (±67%)	3.41(8) (±65%)
ϕ_{28}	1.18(11) (±13%)	1.13(11) (±17%)	2.20(9) (±59%)	6.11(7) (±64%)
ϕ_{29}	7.30(10) (±17%)	7.78(10) (±18%)	9.20(7) (±75%)	3.43(7) (±79%)
ϕ_{25}	1.45(13) (±12%)	8.21(12) (±20%)	9.19(12)(±11%)	1.92(12) (±9%)
Neutron Leakage per DT Neutron	1.45(-2) (±6%)	9.45(-3) (±6%)	3.92(-3) (±6%)	4.00(-3) (±6%)

(a) Blanket/shield composition is that shown in Fig. 1.

(b) Basic geometry is as shown in Fig. 1.

(c) Basic geometry is as shown in Fig. 2.

between the effects of a penetration located at the top (or the bottom) of the torus and another that is located on the outside centered around the midplane. The neutron flux at the end cap, ϕ_{25}, is approximately the same in both cases (the difference is within the statistical uncertainty in the Monte Carlo calculations). Since the penetration size is the same in the two cases but W_s is substantially different, it can be concluded that the neutron flux inside the void penetration is fairly independent of the ratio of the void penetration volume to that of the blanket-bulk shield. The dependence on the penetration size was shown earlier in Section III to be very strong. Comparing ϕ_{18}, ϕ_{19}, ϕ_{28}, and ϕ_{29} for cases 4 and 18, one finds that the radiation level at the TF coils in case 18 is about a factor of 5 smaller than that in case 4. This means simply that increasing the clearance between the TF coils reduces the number of neutrons streaming into the TF coils. Thus, increasing the clearance between the TF coils should lead to an increase in the neutron leakage. When the neutron leakage per DT neutron is renormalized so that the DT neutron current at the first wall is the same in cases 4 and 18, the neutron leakage in case 18 is found to be indeed 30% higher than that in case 4.

With $\theta_b = 0°$ in case 18 and $\theta_b = 35°$ in case 19, the results for the two cases should provide an indication of the sensitivity of the neutronics effects of the beam duct to the orientation of the beam duct axis with respect to the magnetic axis. The differences in the neutron fluxes for the two cases as shown in Table 7 are found to be near the limits of the statistical uncertainty. Additional computation to reduce the statistical error was found unwarranted as these results already indicate that the neutronics effects of the beam ducts are not overly sensitive to the orientation of the beam axis with respect to the magnetic axis. There are many compensating and counteracting effects that tend to reduce the dependence on θ_b.

A penetration shield of 50% SS + 50% B_4C surrounds the beam duct in both cases 20 and 21 and extends from the outer bulk-shield boundary to the end cap. The beam duct shield is 0.50 m thick in case 20 and 0.70 m thick in case 21. The 0.50 m thick beam duct shield provides a factor of ~570 reduction in the maximum neutron flux, ϕ_{18}, at the TF coils. The 0.70 m thick beam duct shield reduces ϕ_{18} by a factor of 12 relative to that with the 0.50 m thick shield. Comparing the results for case 21 with those for case 1 shows that the 0.70 m thick beam duct shield needs to be improved further in attenuation effectiveness by about a factor of 13 in order to reduce the maximum neutron flux at the TF coil to that in the absence of the beam duct. On the other hand, if the radiation level at the TF coils obtainable in case 2 is acceptable, then the 0.70 m thick beam duct shield is sufficient to protect the superconducting coils against radiation streaming caused by the neutral beam ducts. Note, however, that the neutron fluxes at the end cap and the neutron leakage obtainable with the 0.70 m thick beam duct shield are still very high. Thus, in order to protect other auxiliary systems located outside the TF coils, this beam duct shield should be extended (and tapered in proportion with the reduction in the radiation level) to the chambers of the beam injectors. Inside these chambers, the nuclear heating in the crysorption panel is ~0.02 W/cm^3 for 1 MW/m^2 neutron wall loading and the absorbed dose in the bending magnet insulator is $\sim 10^{11}$ rad/(MW-yr/m^2).

The effects of radiation streaming on the nuclear performance of the walls of the neutral beam ducts and the blanket and shield regions in the vicinity of the ducts are found to be large. The neutron heating in

the water coolant at the inner edge (at the first wall) of the beam duct wall is ~10 W/cm^3 and drops by less than a factor of 10 along the entire length of the beam wall inside the blanket-bulk shield. For comparison, the neutron heating drops along the same distance but in regions far removed from the ducts by a factor of 5×10^4. This strong redistribution of neutrons and secondary gammas requires that ~20 cm thick region in the bulk shield surrounding the beam duct be provided with an efficient heat removal system similar to that employed in the blanket. In as much as the walls of the beam ducts must meet the same requirements as are imposed on the first wall, these duct walls pose potentially serious problems similar in magnitude and complexity to those imposed on the first wall.

While this study shows that it is feasible to shield against the effects of penetrations, the results also show that the special shields for the evacuation, neutral beam, and radio frequency ducts occupy a substantial fraction of the reactor interior and their cost represents a significant cost item.

REFERENCES

1. W. M. Stacey, Jr., et al., "Tokamak Experimental Power Reactor Studies," ANL/CTR-75-2, Argonne National Laboratory (1975).
2. M. A. Abdou"Nuclear Design of the Blanket/Shield System for a Tokamak Experimental Power Reactor," *Nucl. Technol.*, 29, 7 (1976).
3. W. M. Stacey, Jr., et al., "Tokamak Experimental Power Reactor Conceptual Design," ANL/CTR-76-3, Argonne National Laboratory (1976).
4. M. A. Abdou and J. Jung, "Nuclear Analysis of a Tokamak Experimental Power Reactor Conceptual Design," *Nucl. Technol.*, to be published.
5. E. M. Gelbard and R. E. Prael, "Monte Carlo Work at Argonne National Laboratory," in *Proc. NEACRP Meeting of a Monte Carlo Study Group*, ANL-75-2, Argonne National Laboratory (1974); also R. E. Prael and L. Milton, "A User's Manual for the Monte Carlo Code VIM," FRA-TM-84, Argonne National Laboratory (1976).
6. D. Garber, C. Dunford, and S. Pearlstein, "Data Formats and Procedures for the Evaluated Nuclear Data File, ENDF," BNL-NCS-50496 (ENDF-102), Brookhaven National Laboratory (1975); also TID-4500 (1975).
7. M. A. Abdou and C. W. Maynard, "Nuclear Design of the Magnet Shield for Fusion Reactors," in *Proc. 1st Topical Meeting on the Technology of Controlled Nuclear Fusion*, CONF-740402-P1 (1974), p. 685.

To appear in the Proceedings of the 2nd Topical Meeting on the Technology of Controlled Nuclear Fusion, Richland, Washington, September 21-23, 1976. (INVITED PAPER)

ION, PHOTON-SURFACE INTERACTIONS IN FUSION REACTORS†

M. Kaminsky

Argonne National Laboratory
Argonne, Illinois 60439

ABSTRACT

The surfaces of major components of thermonuclear fusion reactors such as the first wall, beam limiters, or divertor walls will be exposed to particle and photon bombardment from primary plasma radiations and from secondary radiations. The impact of energetic particles (e.g. ions, atoms) on surfaces can cause such phenomena as physical and chemical sputtering, vaporization, radiation blistering, particle impact induced desorption, backscattering of impinging particles, and nuclear reactions. The impact of energetic photons on surfaces can cause photo-desorption, photo-decomposition of surface compounds, photo-catalysis, photo-electron emission, and surface heating due to photo-adsorption in near-surface regions. Such affects in turn can (a) seriously damage and erode the bombarded surface and (b) release major quantities of impurities which can contaminate the plasma.

A summary of some of the major surface effects leading to plasma contamination and surface erosion will be given.

INTRODUCTION

For the development of fusion power four major plasma confinement concepts are being pursued in the USA at this time.[1] Three concepts use magnetic fields to confine a plasma for either pulsed or steady state operation: the tokamak, mirror, and theta-pinch reactors. The fourth concept uses inertially-confined fusion plasmas which are produced by compressing, for example, small size pellets of frozen deuterium-tritium to very high density and temperature using intense beams of photons[2,3] (e.g. lasers), electrons[4], or ions.[5]

It has been recognized[6-8] that during the operation of present-day plasma machines and of future fusion reactors the interaction of plasma radiations such as ions (atoms) and photons with exposed surfaces of components can cause a variety of surface effects. In turn, such surface effects can cause (a) the release of plasma contaminants, and (b) the damage and erosion of the irradiated surfaces, and thereby limit the operation of plasma machines and fusion reactors.

To determine the amount of plasma contaminants released from surfaces as well as the thickness ℓ of material removed in time t it will be necessary to know both the yields $S_{\mu\nu}(E, \alpha)$ and rates $R_{\mu\nu}(E, \alpha)$ of the various contaminant release and erosion processes, respectively, for the projectile species μ as a function of projectile energy E and angle of incidence α for the release or erosion process ν. In addition, it will be necessary to know the flux $\phi_\mu(E, \alpha)$ for the projectile species μ interacting with the surfaces of exposed components. At this time our knowledge of the yield values and erosion rates for the various types of projectiles and their parameters is very limited for the materials suggested for use in fusion reactor applications. To what extent such yield values and erosion rates will be affected by synergistic effects due to the simultaneous bombardment of surfaces by high fluxes of energetic particles of various types and photons is almost completely unknown. In addition, our present knowledge of the important plasma parameters

governing the escape of energetic particles and photons and their contributions to the fluxes ϕ_μ (E, α) is also very fragmentary for the various types of fusion reactors envisioned.

In the following a review of the types of particle and photon radiations expected in certain large size plasma devices and fusion reactors will be given.

PLASMA RADIATIONS

For an estimate of the amount of plasma contaminants and of the amount of material removed in time t from irradiated surfaces it is necessary to know the flux ϕ_μ of a particular projectile species μ (e.g. in D-T fuel operated fusion reactors: D, T, He, neutron, electron, photon) for a given energy E (or energy spectrum) and angle of incidence α (or angular distribution). It is important to recognize that the ϕ_μ (E, α) - values for ions (atoms) and photons, for example, depend not only on the particular type of plasma device or fusion reactor (e.g. tokamak reactor, mirror reactor, theta-pinch reactor, inertially-confined reactor), but also on its design parameters (e.g. for tokamaks: major radius, plasma radius, current and temperature, first wall radius, toroidal and poloidal magnetic fields), and on its operating conditions (e.g. pulsed, quasi-steady state, steady state). The estimated flux value and mean energy $\bar{E}$ of a particular species μ can vary by many orders of magnitude for a confinement system of the same type (e.g. tokamak systems) but of different design and operating conditions. Table I illustrates the significant differences in the estimated fluxes and mean energies of certain types of particles and photons striking the first wall of the following tokamak devices listed in the order in which they may become operational: ISX (ORNL)[9], TFTR (Princeton)[10], TEPR-I (ANL design)[11], and UWMAK-I (Univ. of Wisconsin-Madison design-I)[12]. In general, one notices how the fluxes of neutrons and helium projectiles increase with increasing power level of a reactor.

TABLE I: ESTIMATED PROJECTILE FLUXES AND MEAN ENERGIES FOR TOKAMAK DEVICES AND REACTORS

PROJECTILE TYPE	ESTIMATED FLUXES, ϕ, $\left(\frac{\text{PROJECTILES}}{\text{cm}^2\ \text{sec}}\right)$ / ESTIMATED MEAN ENERGIES, $\bar{E}$ (keV)	ISX (ORNL)[9] HYDROGEN PLASMA, PLASMA DENSITY 4×10^{13} cm^{-3}, 22 DISCHARGES / ~100 PULSES/YEAR	TFTR (PRINCETON)[10] D-T PULSES, PLASMA DENSITY $4\text{-}8\times10^{13}$ cm^{-3}, 0.5-1.0 sec PULSE LENGTH ~100 PULSES/YEAR	TEPR-I (ANL DESIGN)[11] 150 MWth, PLASMA DENSITY 1×10^{14} cm^{-3} PULSE LENGTH (FLAT TOP) 30-60 sec	UWMAK-I DESIGN[12] 5000 MWth, PLASMA DENSITY 0.4-0.8$\times10^{14}$ cm^{-3}, PULSE LENGTH UNSTABLE 14.2 sec PULSE LENGTH STABLE 61 sec BURN TIME 90 MINUTES
H	ϕ	1.2×10^{16}	-	-	-
	$\bar{E}$	0.46	-	-	-
D	ϕ	NOT SPECIFIED	$2.6\text{-}5.2\times10^{16}$	5×10^{14}	6.4×10^{13}
	$\bar{E}$		4.0-6.0	1.0	23.0
T	ϕ	NOT SPECIFIED	$2.6\text{-}5.2\times10^{16}$	5×10^{14}	6.4×10^{13}
	$\bar{E}$		4.0-6.0	1.0	23.0
He	ϕ	-	$3.6\text{-}7.2\times10^{12}$	7×10^{11} 3×10^{13}	1.7×10^{11} 4.7×10^{12}
	$\bar{E}$	-	~ 3500	3500 ~ 1.0	~ 100.0 23.0
n	ϕ	-	$3.6\text{-}7.2\times10^{12}$	8×10^{12} 3×10^{13}	9.4×10^{13} 3.4×10^{14}
	$\bar{E}$	-	14,100	14,100 ~14,100	14,100 100-14,100
e^-	ϕ	NOT SPECIFIED	} NOT SPECIFIED	} NOT SPECIFIED	} NOT SPECIFIED
	$\bar{E}$	0.50			
ELECTROMAGNETIC RADIATION	SYNCHROTRON RADIATION, POWER DEPOSITION, W cm^{-2} / ENERGIES	} NOT SPECIFIED	} NOT SPECIFIED	0.8	} NOT SPECIFIED
				$2\times10^{-3} < E < 4\times10^{-2}$ eV	
	BREMSSTRAHLUNG, POWER DEPOSITION, W cm^{-2} / ENERGIES	6.34		1.0	
		NOT SPECIFIED	NOT SPECIFIED	1.0 keV (Boltzmann Distrib.)	} NOT SPECIFIED

Table I does not include the fluxes and mean energies of particles and photons impinging on the surfaces of other important tokamak reactor components such as divertor-collector surfaces (for divertor designs see references 13, 14), the beam dump areas for the neutral (or negative ion) beam injectors (in two component tokamak systems), and beam limiters.

For surface erosion phenomena not the flux levels but the fluence levels are of dominant importance. From Table I it becomes readily apparent that while the flux level of the hydrogen isotopes in TFTR is larger than in EPR-I, the annual fluence level is approximately three orders of magnitude smaller than in EPR-I; as will be discussed later this leads one to expect that surface erosion of the first wall will not be as serious in TFTR as in EPR-I.

Significant differences in the estimated fluxes and mean energies of projectiles however, exist not only between different tokamak devices and reactors but also between the reactors of different confinement concepts. Table II lists some such values for the first wall bombardment of the following proposed machines: a D-T mirror reactor (200 MW_e)[15], a D-T theta-pinch reactor (RTPR: 1440 MW_e)[16], and a laser fusion test facility (LFTF: 100 MJ yield per microexplosion, thermonuclear burn time $\sim$ 10 ps)[17]. A comparison of the values for the estimated mean energies of D, T and He projectiles for UWMAK-I (Table I) and the D-T mirror reactor (Table II) shows differences of more than one order of magnitude. Since both plasma contaminant release processes and surface erosion effects depend strongly on the type of projectile and its energy, significant differences on the influences of such process and effects on the operation of a UWMAK-I type tokamak reactor and a D-T mirror reactor will have to be expected.

TABLE II: ESTIMATED FLUXES AND ENERGIES OF PROJECTILES INCIDENT ON FIRST WALL OF D-T MIRROR REACTOR[15], D-T THETA PINCH REACTOR[16], AND LASER FUSION TEST FACILITY[17].

PROJECTILE TYPES	ESTIMATED FLUXES, ϕ, ($\frac{\text{PROJECTILES}}{\text{cm}^2\ \text{sec}}$) / ESTIMATED ENERGIES, $\bar{E}$, keV	D-T MIRROR REACTOR 200 MW_e	D-T THETA-PINCH REACTOR RTPR, 1440 MW_e	LASER FUSION TEST FACILITY 100 MJ YIELD MICROEXPLOSION, FIRST WALL RADIUS, l = THERMONUCLEAR BURN TIME = 10^{-11} sec
D	ϕ	5.4×10^{14}	NOT SPECIFIED	NOT SPECIFIED
	$\bar{E}$	550		
T	ϕ	3.2×10^{14}	NOT SPECIFIED	NOT SPECIFIED
	$\bar{E}$	580		
He	ϕ	3.5×10^{13}	NOT SPECIFIED	NOT SPECIFIED
	$\bar{E}$	1200		
n	ϕ	8×10^{13}	1.7×10^{14} | 6×10^{14}	1.8×10^{14}
	$\bar{E}$	14,100	14,100 | 100<E<14,100	14,100
e^-	ϕ	9.3×10^{14}	NOT SPECIFIED	NOT SPECIFIED
	$\bar{E}$	58		
ELECTROMAGNETIC RADIATION	SYNCHROTRON RADIATION: POWER DEPOSITION, W cm^{-2} / ENERGY	2.6 / X-RAY RANGE	NOT SPECIFIED	NOT SPECIFIED
	BREMSSTRAHLUNG: POWER DEPOSITION, W cm^{-2} / ENERGY	225 / FAR INFRARED RANGE	71 JOULE cm^{-2} $PULSE^{-1}$ / NOT SPECIFIED	$\sim$ 8 JOULE cm^{-2} $PULSE^{-1}$ / BROAD MAXIMUM IN 1-10 keV RANGE

Tables I and II reveal also the significant differences in the operating conditions of the reactors and facilities listed, especially the differences in the thermonuclear burn times. It should be realized that in contrast to the quasi-steady state operation of EPR-I or UWMAK-I (Table I), the laser induced pellet microexplosions ($\sim 10^{-11}$ sec) in a laser fusion test facility will result in thermal gradients from

non-uniform heating of surface regions due to the sudden deposition of energy of thermonuclear burn products; this in turn will cause stresses. At this time our knowledge of the type of surface phenomena occurring during such a short time is too limited to allow an assessment of their effect on surface erosion and plasma contaminant release.

In estimating the projectile fluxes in Tables I and II the assumption has been made that the projectile radiations are spatially isotropic and result in a uniform irradiation of the exposed surfaces (e.g. first wall). This assumption, however, is not generally justified. For example, it has been pointed out[18,19] that the wall loading profile in a tokamak is complicated by the banana-like orbits of the alpha particles, resulting in a highly peaked wall loading as a function of the poloidal angle. For a low-β, axisymmetric tokamak operating in the collisionless regime, the 3.5-MeV alpha particle losses to the first walls of such tokamak devices as TFTR, EPR-I and UWMAK-I occur either to the upper or lower half plane of the particular device, depending on the direction of the toroidal magnetic field.[18,19] The occurrence of peaked projectile impacts in localized surface areas ("hot spots") has been observed in operating tokamak devices[20], and has been ascribed to localized plasma radiation release due to plasma instabilities and/or to run-away electrons. Furthermore, in detailed radiation transport calculations it has been shown[21] that first wall surfaces can be irradiated preferentially in certain areas by bremsstrahlung if, for example, a finite stream of impurities ("wedge incursion"-e.g. a leaking vacuum vessel port as gas source) is allowed to penetrate the plasma from one side and to reach the center of it (see Figure 1).

The existing information on electromagnetic irradiations of first wall surfaces for the various plasma devices listed in

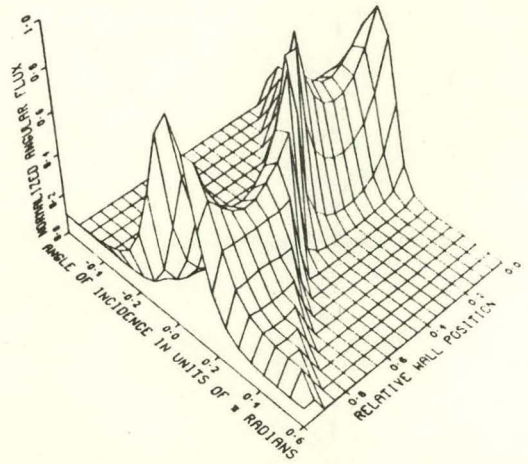

FIGURE 1. The Effect of a Localized Impurity Stream ("Impurity Wedge") Extending From the Wall to the Plasma Center on the Bremsstrahlung's Flux on the First Wall Surface as a Function of Poloidal Angle ϕ (e.g. relative wall position of 0.5 corresponds to ϕ=180°) and Angle of Incidence. (Reference 21)

Table I and II is rather fragmentary. Recently, the spectrum of synchrotron and bremsstrahlung radiations for a tokamak reactor system that is somewhat smaller in size than UWMAK-II[22] has been calculated[23]. The following machine parameters were used: plasma radius: 2.5m, first wall radius: 2.75m, aspect ratio: 3, toroidal magnetic field on axis: 40 KG, an average electron temperature and density of 10-keV and 10^{14} particles cm^{-3}, respectively. The toroidal field is assumed to vary with major radius R as 1/R across the cylinder. The spectrum of the radiation deposited at a point on the equatorial plane of the torus is shown in Fig. 2. The authors point out that the spectra shown will vary with poloidal angle but the results given here can be taken as characteristic of a tokamak fusion reactor. One notices that the synchrotron spectrum shown in Fig. 2 is peaked at about $7\omega_c^e$ (ω_c^e is the electron cyclotron frequency) which is typically in the 8×10^{11} Hz range ($\lambda \sim 0.3$mm). The bremsstrahlung spectrum is much broader, being nearly uniform up to energies near the maximum

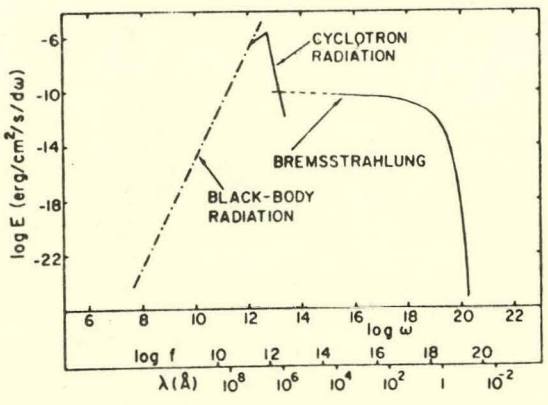

FIGURE 2. The Spectrum of Cyclotron and Bremsstrahlung Emitted by a Thermonuclear Tokamak D-T Plasma for Electron Temperatures of 10-keV and a Toroidal Magnetic Field of 40 KG. (Reference 23)

electron temperature of 10-keV; at this temperature the frequency is $\sim 10^{18}$ Hz ($\lambda \sim 1.0$ Å).

Finally, it should be pointed out that Tables I and II list only certain types of primary radiations impinging on first wall surfaces. However, in actual fusion reactor operations the surfaces will also be exposed to secondary radiations from (n,γ), (n, p), (n, α), and other nuclear reactions and from secondary particles (e.g. secondary ions and electrons) and photons (e.g. energetic ion and electron induced x-ray emission) in the presence of the external magnetic confinement field.[6,8]

GENERAL CONSIDERATIONS REGARDING PLASMA CONTAMINATION AND SURFACE EROSION

The contamination of plasmas from surface released impurities will affect detrimentally the plasma characteristics in several ways. Firstly, the addition of high-Z impurity atoms (or ions) to a D-T plasma will increase the effective charge Z_{eff} of the plasma, where Z_{eff} is given by[24]

$$Z_{eff} = \frac{1+\sum_i (n_i/n_{D,T})Z_i^2}{1+\sum_i (n_i/n_{D,T})Z_i} = \frac{1+\sum_i f_i Z_i^2}{1+\sum_i f_i Z_i} \quad . \qquad (1)$$

Here n_i is the impurity atom (ion) density, $n_{D,T}$ is the D-T plasma density (assuming $n_D = n_T$), Z_i is the charge of species i, and f_i is the impurity fraction of species i. An increase in the value of Z_{eff} due to an increase in the value of n_i and/or Z_i results not only in enhanced plasma resisivity, but also in distortions of plasma density and temperature profiles.[24,25] Under certain plasma conditions heavy impurities tend to diffuse toward the plasma center and collect on the axis of the discharges thereby seriously affecting the steady-state operation of a reactor.[26,27] Secondly, increases in Z_{eff} cause increasing radiation losses which make the attainment of ignition conditions more difficult. For example, a value of $Z_{eff}=9$ would prevent ignition of a tokamak reactor of a certain design unless additional power were injected.[24] If the impurities were purely iron (Z=26), an iron impurity density of 1.8% of the D-T plasma density ($f_i=0.018$) would be sufficient to yield $Z_{eff}=9$. The plasma power loss due to the presence of impurities occurs mainly via bremsstrahlung, line, and recombination radiation. If these losses are too high during start-up, they prevent the ignition of the plasma as mentioned above. If these losses increase above critical values during the plasma operation, they can cool the plasma temperature below fusion reaction temperatures. For example, for a hydrogen isotope plasma (Z=1), the ratio R of the power losses due to bremsstrahlung from the plasma with and without a contaminant of atomic number Z_i is given by[6,8]

$$R = 1 + f_i (Z_i + Z_i^2) + f_i^2 Z_i^3, \qquad (2)$$

where the symbols have the same meaning as in equation (1). If one assumes that for efficient and economic operation of a hydrogen isotope-fueled reactor the increase in bremsstrahlung losses due to the presence

of an impurity should not exceed 20% (R=1.2), Equation (2) can be solved for an upper limit of $f_{i,m}$. For fully ionized iron $f_{i,m} = 2.8 \times 10^{-4}$. For impurity ions (atoms) which are not fully stripped, the value of $f_{i,m}$ should be kept even smaller than the one listed above. It is one goal of surface studies to identify those surface phenomena which yield impurity fractions which are too high for the proposed operating conditions of plasma devices and reactors.

For an estimate of the number n of impurity atoms released from an irradiated surface area A in time t, it is necessary not only to know the flux ϕ_μ (E, α), but also the particle release S_μ (E, α) for a particular release process ν. To obtain the total number n it is necessary to sum the yield values for the individual release processes ν (e.g. physical and chemical sputtering, blistering, vaporization) that can be caused by each particular projectile species μ. The number of atoms (ions) released is given by[6]

$$n = \sum_i n_i = \sum_{\nu} \sum_{\mu} [\phi_\mu(E, \alpha)\ S_{\mu\nu}(E, \alpha)]\ A \cdot t. \quad (3)$$

In order to obtain realistic estimates of n it becomes clear from equation (3) that realistic values of ϕ_μ (E, α) and $S_{\mu\nu}$ (E, α) need to be obtained. At present there exists a lack of such ϕ_μ (E, α)- and $S_{\mu\nu}$ (E, α)-values for fusion reactor operating conditions.

For an estimate of the volume V of material removed in time t from an irradiated surface area A it will be necessary to know the flux ϕ_μ (E, α) of each projectile species μ and the surface erosion yield $R_{\mu\nu}$ (E, α) for the release processes ν caused by projectile species μ. The volume V is given by

$$V = \sum_{\nu} \sum_{\mu} [\phi_\mu\ (E, \alpha)\ R_{\mu\nu}\ (E, \alpha)]\ A \cdot t \cdot \frac{\lambda}{N} \quad (4)$$

where N is the number of atoms in a monolayer and λ is the thickness of a monolayer of the material under bombardment. One should note that in some instances a $S_{\mu\nu}$-value (see equation 3) may be identical with a $R_{\mu\nu}$-value (see equation 4) for a particular projectile μ and process ν (e.g. physical sputtering by He).

At the present a lack of realistic ϕ_μ (E, α)-values does not allow realistic estimates of V-values. Some tolerable upper limits on V for the useful operation of various components exposed to plasma radiations will have to be found. For example, for a unit area of irradiation of $A_1 = 1cm^2$, the thickness loss of a plasma container wall should probably not exceed 20% of its original thickness if it is to maintain its structural integrity. If one assumes a wall thickness of about 3mm and a desirable wall lifetime of $\sim$ 6 years, the maximum permissible annual thickness loss is 0.1mm, or the maximum permissible annual loss of volume V_y for an area of $A_1 = 1cm^2$ is $0.01cm^3$.

Equations (3) and (4) do not take into account that under the simultaneous impact of ions (atoms) and photons synergistic effects may occur that lead to nonlinear particle release and surface erosion processes.

PLASMA CONTAMINANT RELEASE FROM SURFACES UNDER ION AND PHOTON IMPACT

During the start-up period of a fusion reactor the impact of energetic ions (atoms) on surfaces will cause plasma contaminant release predominantly by such processes as desorption, physical and chemical sputtering, and vaporization (e.g. from "hot spots"). The impact of energetic photons during this period will cause impurity release by photodesorption, photoelectron induced desorption, vaporization ("hot spots") and possibly by photo-catalysis. During the more extended thermonuclear burn-period of a reactor, additional release processes such as blister rupture, gas re-emission of implanted gas from non-

blistered areas, and neutron sputtering will contribute to the contaminant release, with desorption playing a less important role.

Desorption

It is now firmly established that the desorption of adsorbed gases from surfaces can occur under the impact of photons and electrons (e.g. primary electrons from plasma region or secondary electrons caused by ion, electron or photon impact, and returned to the surface by a magnetic confining field), and by thermal phenomena.[6, 8,28-31] It is also widely agreed that ion impact can cause desorption[6,8,28-31], although quantitative studies of this phenomenon have not been conducted yet to the best knowledge of this author. This lack of information is probably due to the fact that physical and chemical sputtering of adsorbed gas species can mask the ion induced desorption, although differences in the energy distribution of the released species (the mean energies of sputtered species are expected to be higher than those of desorbed species) may allow a distinction of the relative contribution of these two processes to the observed particle release.

For low energy photons in the 2-7 eV range (visible and ultraviolet radiation) the release of gases from surfaces of such solids as ZnO, Fe, Ni, Zr, W, stainless steel, CdS, TiO_2 and SnO_2 have been reported (for an extensive review see ref. 28). For example, Lichtman et.al.[32] irradiated stainless steel with photons in the 2-7 eV energy range under ultrahigh vacuum conditions and found that the dominant desorbing species was CO_2 with smaller concentrations of desorbing CO, CH_4, H_2O and H_2 being detectable. The quantum yield for CO_2 release was observed to increase with increasing photon energy (see Fig. 3), and it had, for example, a value of 5.5×10^{-3} molecules per photon at a photon energy of 6.7-eV. More recently, photodesorption studies on stainless steel surfaces (non-discharge cleaned) in the x-ray range (mean photon energies varied from 18-24 keV) under ultrahigh vacuum conditions were conducted.[33] It was observed that CO_2 and O_2 were the dominant species, with additional species such as CO, CH_4, O, H_2 and H_2O being present in smaller concentrations. The quantum yield for CO_2 release was observed to decrease with increasing mean photon energy (in contrast to the energy dependence observed at low energies, ref. 32), and had values ranging from $2\text{-}4 \times 10^{-4}$ molecules per photon for two different degreased stainless steel targets at a mean photon energy of 24-keV (see Fig. 3).

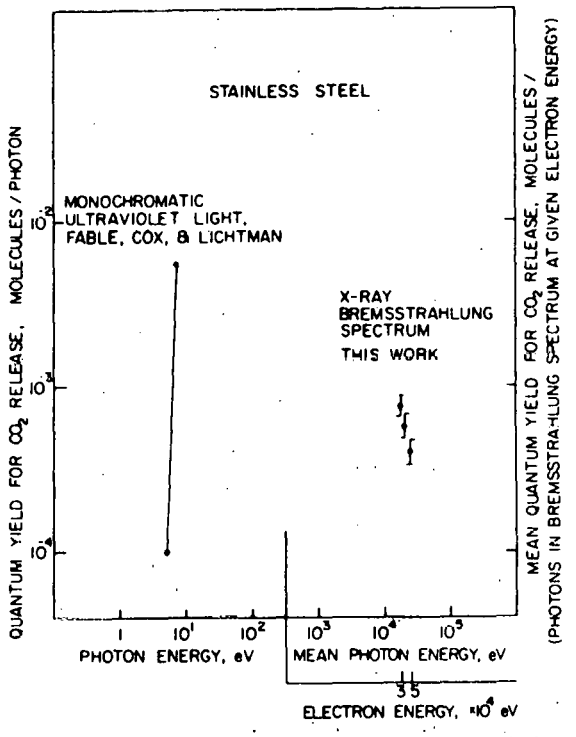

FIGURE 3. Dependence of Quantum Yield (Mean Quantum Yield) on Photon Energy (Mean Photon Energy) in the UV (Ref. 32) and X-Ray Regions (Ref. 33) for Release of CO_2 from Degreased stainless steel.

The authors pointed out that the energy dependence of the photon adsorption coefficient correlates well with the observed increase in the quantum yield for CO_2 release in the

5-7 eV photon energy range, and with the observed decrease for the mean photon energy from 18 to 24-keV. The authors more recently performed similar studies[34] on discharge cleaned stainless steel surfaces and observed a decrease in the CO_2 release quantum yield from $2x10^{-4}$ atoms per photon for the non-discharge cleaned surfaces to $6x10^{-5}$ atoms per photon for the discharge cleaned one. If one chooses the mean quantum yield value for CO_2 from non-discharge cleaned stainless steel for a mean photon energy of 18 keV ($7.5x10^{-4}$ molecules per photon) and the relevant parameters of UWMAK-I design[12] (bremsstrahlung power loading of 28.2W cm^{-2}) a relatively high CO_2 gas release rate of about $\sim 1x10^{13}$ molecules cm^{-2} sec^{-1} from stainless steel surfaces will result. In this estimate it was assumed that the bremsstrahlung spectrum is typical for a tungsten bremsstrahlung at 30 keV electron energy, while in actuality the spectrum may be shifted to lower energies and lead even to an increase in the above mentioned gas release yields.

The desorption of both ions and neutrals from surfaces under electron impact has been widely studied (for reviews see ref. 30,31). In the context of this paper it should be realized that the impact of energetic ions and photons on surfaces will cause the emission of secondary electrons, which in turn can strike the surface in the presence of an external magnetic confining field. In general, the cross sections for the electron interaction with adsorbed gas species are of the same order of magnitude as the values for a similar interaction in the gas phase (e.g. for 100 eV electrons impinging on a CO-covered Mo surface gave a cross section for CO-desorption of $\sim 10^{-16}$ cm^2).[30] Furthermore, the electron impact on adsorbed molecules can cause the release of fragment species. The electron bombardment of adsorbed CO can result in the release of O^+ and CO^+ ions, and this observation appears to be rather insensitive to the substrate materials used (W, Nb, Re). In contrast to the typical species observed for photodesorption from degreased stainless steel surfaces (e.g. CO_2, CO), electron induced desorption for electron energies varying from 0-4000 eV the most dominant ion species released were H^+, O^+, F^+, and CO^+, with H^+ and F^+ giving the largest signals.[30] In the opinion of this author desorption phenomena will play an important role in contaminant release during the start-up period of reactors.

Physical Sputtering

If energetic ions (atoms) impinge on surfaces they initiate collision cascades within the solid and cause in turn the emission of atom and/or ions from the surface regions. This process releases not only impurities into the plasma region but also causes surface erosion. Since detailed reviews of physical sputtering have appeared elsewhere[35-40], only a few points relevant to fusion reactor applications will be made. The physical sputtering yields (i.e., the mean number of particles released from the surface per incident projectile) are proportional to the energy deposited into nuclear motion (proportional to nuclear stopping power) near the surface and inversely proportional to surface binding energy.[41-44] The yield depends on a number of parameters such as the energy and angle of incidence of the projectiles, the atomic mass of both projectiles and target atoms, the temperature and the surface condition. Unfortunately, the agreement between sputtering theory and experimental data is not satisfactory for the type of light projectiles (D, T, He) expected in fusion reactor operations. In contrast to heavy-ion sputtering (e.g. Xe^+) the sputtering with light ions is always influenced by (1) large angle scattering, (2) a surface

correction, and (3) electronic stopping. Figure 4 illustrates the energy-dependence of the sputtering yields from niobium bombarded with helium and hydrogen isotope ions. The theoretical values are based on Sigmund's theory[41] with the appropriate corrections.[42-44] This procedure represents the dependence of yield on the projectile energy quite well, but gives yield values which are consistently higher than those observed experimentally. A reduction of the calculated yields for D^+ incident on Nb by approximately a factor of ten leads to a better agreement over the energy range from 10^2 to 5×10^4 eV. A broad maximum occurs between 4-5 keV for helium and between about 2-4 keV for the hydrogen isotopes. For light target metals such as beryllium, the corresponding maxima are predicted[45] in the range from ∿ 0-1 keV, although experimental data are scarce for this energy range.

In fusion reactor operations the surfaces of components will be irradiated with light ions having a broad energy distribution. Average sputtering yields $\bar{S}$ (E) have been calculated[45] by using a lethargy function for a Maxwellian distribution of deuterons impinging on Be and Fe. The $\bar{S}$ (E)-curves appear flattened in comparison to the S (E)-curves for monoenergetic ions, and the maximum yield is slightly lower.

Sigmund's theory suggests that for not too oblique angles of incidence α the yields change approximately as $(\cos\alpha)^f$, where f is a constant which depends on the mass ratio M_2/M_1 of target to incident projectile. For $M_2/M_1 < 1$, f ∿ 1.7; for $M_2/M_1 > 1$, f slowly decreases until it reaches a value somewhat less than 1. While for A^+ ions on Cu the agreement between calculated and experimental values of S (α) is reasonably good[39], this is not the case for lighter ions (e.g. 1.05 keV Ne^+ on Cu[46]).

The transit time for impurities leaving the surface and reaching the outer plasma edge is determined by the energy distribution of the sputtered species and the distance between surface and plasma edge. For detailed reviews of the energy distribution of sputtered species the reader is referred to references 36-39. Random cascade theory predicts that under appropriate conditions the energy spectrum of sputtered atoms varies like E_s^{-2} (E_s is the energy of sputtered particle) at high energies. The effect of the surface binding energy V_0 modifies the distribution at low energies; the distribution passes through a maximum in the region of ∿ V_0 and then falls linearly to zero at E_s=0. For systems such as A^+ on Au the agreement between theory and

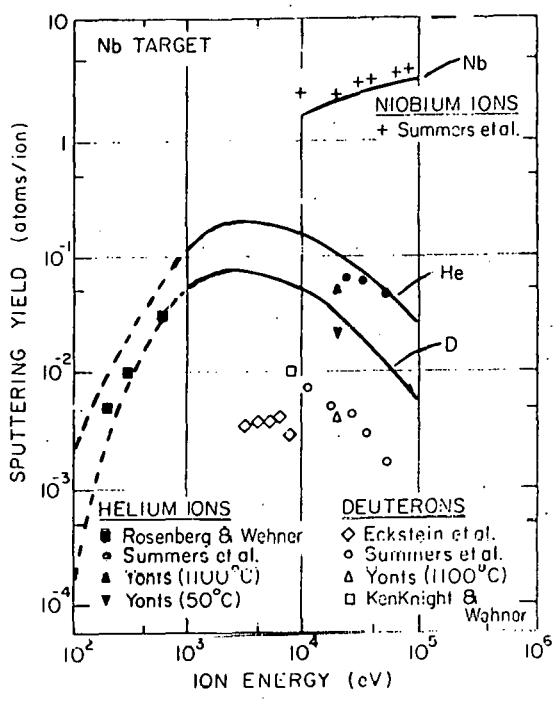

FIGURE 4. Sputtering yield for Niobium as a Function of Incident Ion Energy. The Incident Ions are D^+, He^+, and Nb^+. The solid curves have been calculated according to Sigmund's theory[41], using the appropriate corrections for backscattering, electronic stopping, and the surface reflection.[42-44] The dotted lines have been interpolated between calculated sputtering threshold values and values calculated according to Sigmund.

experiment is quite good. (For 20 keV A^+ on Au a broad maximum exists between 3-5 eV.) For light ions on heavy metals data are badly needed. The effect of neutron sputtering on plasma contamination will be discussed in a different paper at this conference.

Chemical Sputtering

Whenever incident projectiles react chemically with atoms in the surface regions (e.g. formation of volatile compounds, changes in chemical composition of surface layers) chemical sputtering can occur, contributing to the release of surface contaminants. For a more detailed review of chemical interactions of projectiles with surfaces the reader is referred to references 47, 48. In a fusion reactor, the reactive ions will be mainly H^+, D^+, and T^+. An example of a potentially serious reaction occurs when hydrogen interacts with the carbon atoms of a graphite liner ("carbon cloth concept"[49]) to form hydrocarbons such as methane, ethane, propane and acetylene.[50-52] The rate of reaction varies markedly with temperature and also with the type of carbon (e.g. pyrolytic, glassy, reactor grade graphite). For hydrogen isotope ion bombardment of carbon a maximum in the chemical sputtering yield curve has been observed for a carbon temperature of $\sim$ 600°C at a H_3^+-ion energy of $\sim$ 2.0 keV. The observed yield value[52] ($S \sim 0.08$ atom/ion) is more than one order of magnitude higher than physical sputtering theory would predict.

Evaporation

The release of plasma contaminants by evaporation during fusion reactor operations can become important when the energy of plasma radiations is deposited on exposed surfaces nonuniformily either in time (flash evaporation-e.g. in fast-pulsed reactors) or in space (local "hot spots"). Some typical vapor pressure curves for some metals of potential interest for fusion reactor components (e.g. V, Mo, Nb) have been given previously.[6] However, the formation of volatile compounds under certain reactor operating conditions may lead to substantially higher rates of evaporation than would be predicted for the elemental metals at the same temperature. For example, the vapor pressure of the molybdenum oxide MoO_3 10^{-4} Torr at 565°C and 10^{-2} Torr at 636°C (for Mo the values would be $< 10^{-14}$ Torr for both temperatures). Such high vapor pressures would lead to intolerably high plasma contamination.

Blistering - Gas Re-emission

If energetic particles penetrate a lattice they may displace lattice atoms from their sites and create vacancies and interstitials. When the incident particles have slowed down sufficiently they may be trapped in the lattice either interstitially or substitutionally. When the implanted particles have a low solubility in the lattice, they can combine with the vacancies created by the lattice displacements and nucleate gas bubbles. With increasing dose and/or temperature such bubbles can coalesce and form larger bubbles, the size of which depends on particle energy and dose, and the target temperature and microstructure. If such bubbles form in near surface regions and the gas pressure is high enough, bubbles may plastically deform the surface layers above them (form blisters), and when the deformation is extreme, the surface layers may exfoliate (blister rupture and flaking) [for a detailed review of radiation blistering see reference 53].

The release of gas bursts by blister rupture had been observed first mass spectrometrically during the irradiation of monocrystalline copper with 125-keV D^+ ions.[54] Extensive measurements of helium gas reemission from Nb, V, Mo, stainless steel and Pd during helium irradiation have been made

more recently (see reference 55 and the references contained therein). Figure 5 shows an example of helium re-emission from vanadium as a function of helium fluence for three different irradiation temperatures.[55] For 400°C irradiation it can be seen that abrupt changes in re-emission occurs after a certain doses are attained. The sudden onset of re-emission, with a peak value well in excess of 100% of the incoming flux has been observed to occur at nearly the same dose as that at which blister rupture is observed optically.

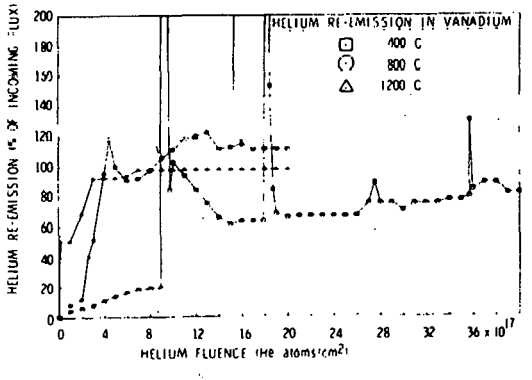

FIGURE 5. Helium Re-Emission From Vanadium During 300-keV He^+ Implantation as a Function of Dose at Three Different Implantation Temperatures. (Reference 55)

Such release of gases with temperatures approximately equal to the wall temperature can contribute to plasma cooling.

SURFACE DAMAGE AND EROSION CAUSED BY ION AND PHOTON IMPACT

Energetic ions and photons striking the surfaces of structural components of fusion reactors can cause serious surface damage, changes in the chemical composition of the surface and in the surface topography, and lead to serious surface erosion, thereby limiting the lifetime of the irradiated components. With the exception of desorption processes all of the other processes mentioned above as contributors to plasma contaminant release can also cause surface damage and erosion. In addition, processes such as photo-decomposition, surface embrittlement, and radiation induced precipitates and fatigue cracks in surface regions need to be considered. At this time our knowledge of the surface erosion yields $R_{\mu\nu}(E, \alpha)$ for the more dominant surface erosion processes is very limited for materials and operating conditions envisioned in fusion reactors. In fact, only recently has the importance of radiation blistering as a potentially serious surface erosion process in fusion reactor operations been fully recognized.[6,8] A brief review of recent studies of some erosion processes with special emphasis on radiation blistering follows.

Surface Erosion by Radiation Blistering

It has been pointed out earlier[6,8] that radiation blistering could seriously damage and erode surfaces of components exposed to certain types of plasma radiations in fusion reactors. For example, the blistering erosion yield for 304 stainless steel at 450°C for 100-keV helium bombardment to a dose of 0.5 C/cm^2 was $\sim$ 3 atoms/ion, a value which is nearly two orders of magnitude larger than the estimated combined physical sputtering yields for 25-keV D^+, T^+ and 100-keV He^+.[62] From the above quoted erosion yield an annual thickness loss of about l_y=0.05mm per year can be estimated for a helium-flux of 5×10^{12} helium ions cm^{-2} sec^{-1}, a yield value which would contribute to about half the maximum allowable annual thickness loss for a 3mm thick stainless steel first wall with a desired lifetime of $\sim$ 6 years.

Only a brief summary of the major parameters affecting the blistering process will be given here, since a major detailed review will appear elsewhere.[53]

Projectile-Target System

The solubility and diffusivity of the implanted gas in solids are two of the important parameters affecting the blistering process. In general, hydrogen isotopes have

higher solubility and diffusivity in metals than inert gases such as helium. Therefore, it has been observed[63] that for metals such as Nb, helium irradiation caused more of a blistering effect than deuterium under irradiation conditions in which the samples received actually a higher deuteron dose, which should have favored deuterium blistering. In non-metals, for example, in certain ceramic coatings, the deuterium permeability (determined by solubility and diffusitivity) can be considerably smaller than for helium. Recent irradiations of ceramic coatings with deuterons and helium ions under identical irradiation conditions show a more pronounced blistering effect by the impact of deuterons than for helium ions for samples held at room temperature.[64]

Projectile Energy

The depth profile of ions implanted in a solid as well as the energy deposited into damage are functions of the projectile energy and affect the formation of gas bubbles and subsequent blisters significantly. An increase in the projectile energy tends to increase the blister diameter, blister skin thickness, and the critical dose for blister appearance, but appears to decrease the number of blisters formed per unit area of irradiated surface ("blister density"). Figure 6 illustrates the increase in blister diameter and skin thickness for niobium irradiated at room temperature with increasing energy of helium ions in the energy range from 30 to 80 keV.[68] This general trend has been observed to exist for the energy range from 10-1500 keV.[65-66]

For an estimate of the volume of surface materials lost by blister exfoliation the knowledge of the skin thickness and the area from which it has been lost is necessary. For the helium ion energy range from 30 to 1500 keV a good correlation between the calculated projected ranges (using Lindhard, Scharff, Schiotts[75] and Brice's formalism[76]) has been observed for niobium, as illustrated in Figure 7. It appears that for niobium the skin does not separate from

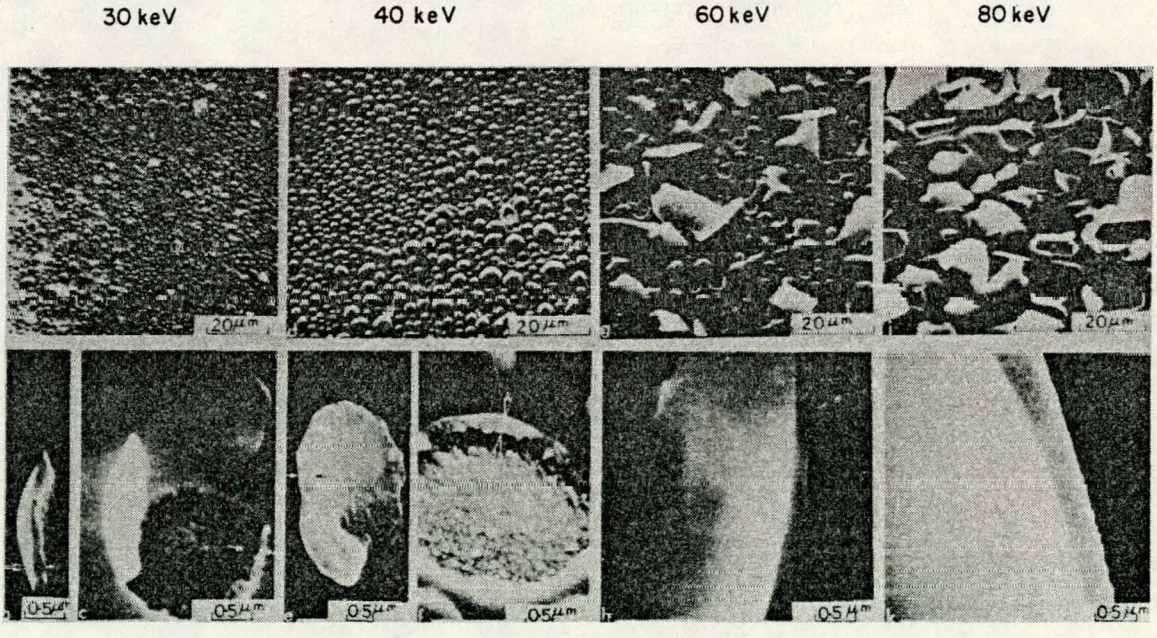

FIGURE 6. Scanning electron micrographs of annealed polycrystalline niobium irradiated at room temperature to a dose of 0.5 C/cm^2 with $^4He^+$ ions at energies of (a)-(c) 30-keV, (d)-(f) 40-keV, (g)-(h) 60-keV, and (i)-(k) 80-keV. Blister skin thickness and crater depth are shown in (b)-(c) (30-keV), (e)-(f) (40-keV), (h) (60-keV) and (k) (80-keV). (Reference 65)

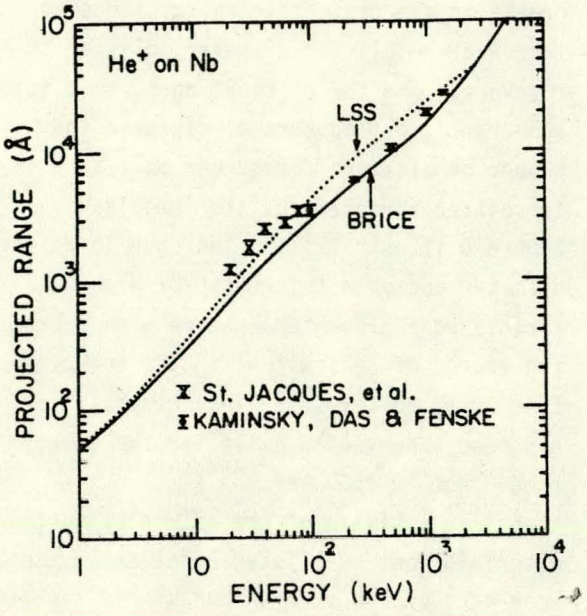

FIGURE 7. Calculated projected ranges of $^4He^+$ ions in niobium as a function of projectile energy. The dotted curve was calculated according to Lindhard et.al. (Mat. Fys. Medd. Dan. Vid. Selsk. 33, (1963) no. 14, and the solid curve according to Brice (Phys. Rev. A6, (1972) 1791). Measured skin thickness values are indicated by I (Reference 66), and X (Reference 65).

the bulk material in the region of maximum lattice damage but near the region where the implanted gas has a maximum and high stresses in the material exist.

It has been pointed out[67,68] that at low ion energies (e.g. 1-5-keV He^+ ions) physical sputtering will become the dominant surface erosion process and will reduce or eliminate surface blistering.

Flux and Dose

A distinction is often made between the critical dose C_b needed to form gas bubbles in the bulk of the material during irradiation, and the critical dose C_{bl} for the appearance of blisters on the surface.[53] For example, for vanadium irradiated at 500°C with 240-keV He^+ ions, a critical dose $C_b = 1 \times 10^{17}$ ion cm^{-2} has been observed, resulting in bubbles with diameters $\geq$ 40 Å. For higher irradiation temperature of 600°C this value decreases significantly to 7×10^{14} ions cm^{-2}. For room temperature irradiation of niobium with 500-keV He^+ ions the critical dose for blister appearance was $C_{bl} \sim 2 \times 10^{18}$ ions cm^{-2}, and at 900°C it decreased to $\leq 6.3 \times 10^{16}$ ions cm^{-2}. This trend can be understood if one considers the dependence of the critical pressure for blister appearance on the yield strength, σ_y, and the values of blister radius and thickness, r and t, respectively [$P_{cr} = (4\ \sigma_y\ t^2)/3\ r^2$]. Since the yield strength σ_y of most metals decreases with an increase in temperature, for constant values of r and t, the value for P_{cr} will decrease correspondingly.

Once the C_{bl}-values have been exceeded, the dose values will affect the blister diameter, blister density and the exfoliation of the blister skin.[53] It should be mentioned that some authors (e.g. ref. 68) observed that room temperature irradiation of Nb with 15-keV He^+ ions to a dose of 1.5×10^{18} ions cm^2 produced blisters, but that an increase in dose to 6×10^{19} ions/cm^{-2} produced roughened surfaces on which blisters could not be identified. Biersack[69] irradiated Nb with 6 keV He^+ ions to very high doses (1.2×10^{20} ions cm^{-2} - 5×10^{21} ions cm^{-2}) and observed the extremely roughened surfaces shown in Figure 8. To what extent differential sputtering (due to some potential carbon contamination on the surface) and blistering contributed to the observed erosion is not clear according to the author.[69]

The blister density and the critical dose for blister appearance has been observed to be affected by the flux in some cases,[53] where the balance between gas trapping and gas release is critical.

Target Temperature

The target temperature affects the average blister diameter, blister density and the exfoliation of blister skin (which determines the erosion yield) significantly.

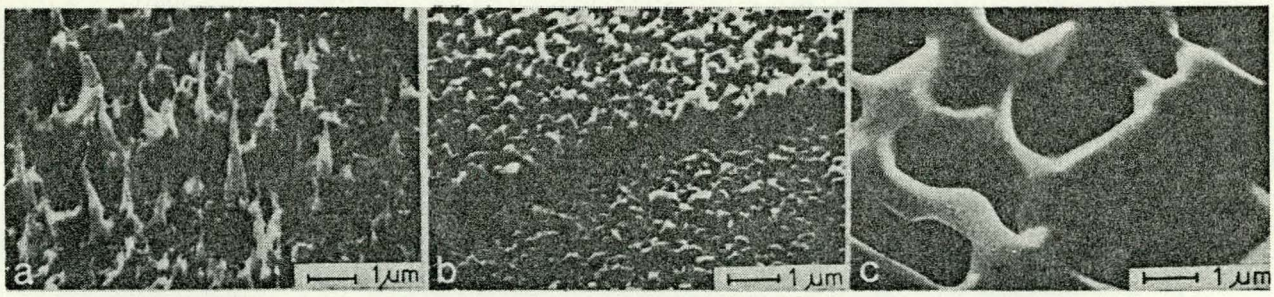

FIGURE 8. Scanning electron micrographs of polycrystalline niobium surfaces irradiated with 6 keV He^+: (a) dose of $5x10^{20}$ He^+/cm^2 at 800°C, (b) dose of $1.25x10^{20}$ He^+/cm^2 at 800°C, and (c) dose of $1.25x10^{20}$ He^+/cm^2 at 1200°C. (Reference 67)

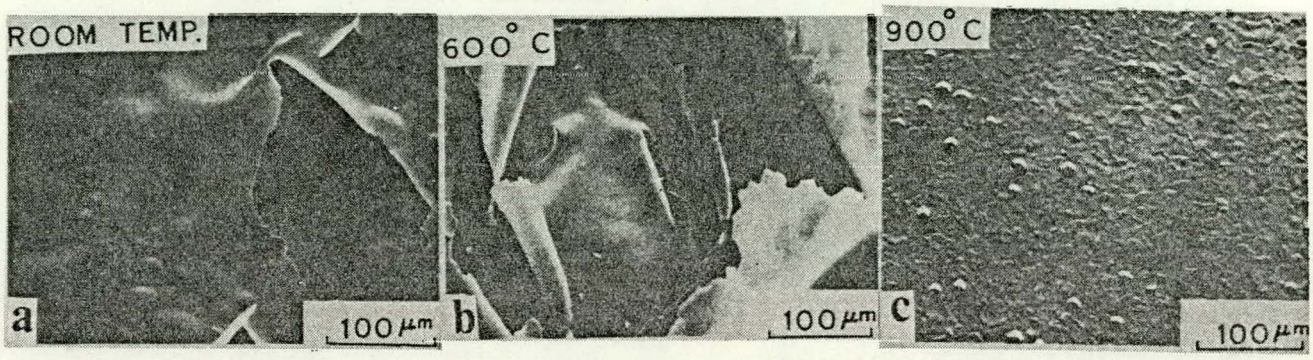

FIGURE 9. Scanning electron micrographs of annealed polycrystalline vanadium surfaces after irradiation with 0.5-MeV $^4He^+$ ions to a total dose of 1.0 C/cm^2: (a) at room temperature, (b) at 600 ± 20°C, and (c) at 900 ± 20°C. (Reference 70)

Figure 9 illustrates[70] this for the irradiation of annealed polycrystalline vanadium with 0.5-MeV $^4He^+$ ions to a total dose of $6.3x10^{18}$ ions cm^{-2}, at room temperature, 600°C and 900°C. One notices that the exfoliation at 600°C is much larger than at room temperature or 900°C. The erosion yields have been estimated for a number of metals and alloys irradiated with helium ions as a function of temperature, and Figure 10 shows a plot of some of the available data.[53] The observed change of erosion yield with temperature has been related to the temperature dependence of the yield strength of the irradiated material, the changes in the gas kinetic pressure in the bubble with temperature, and the helium release through the surface at high temperatures. The maximum in the erosion yield occurs where the temperature is high enough for the surface to be deformed easily, but low enough so that the helium release from

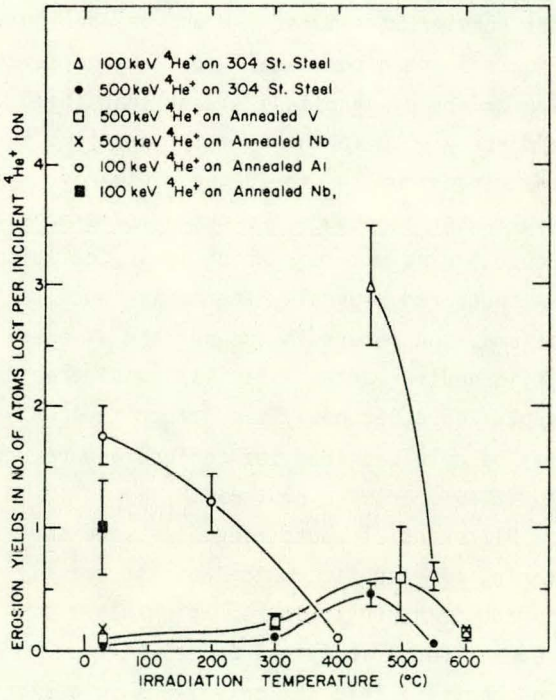

FIGURE 10. Erosion rates for different metals and alloys as a function of irradiation temperature for different projectile energies and total doses. (Reference 53)

the surface region is still very small (for a more detailed discussion see ref. 53).

Physical and Chemical Sputtering

Both physical and chemical sputtering will contribute not only to the release of plasma contaminants but also to surface damage and erosion. At this time considerably more information is already available on physical sputtering yields than for chemical sputtering yields for ion (atom) impact on surfaces. In this context the physical sputtering yield S_μ can be equated with the surface erosion yield R_μ for physical sputtering by the projectile type μ. Figure 4 showed the sputtering yield S as a function of particle energy for D^+, He^+ and Nb^+ ions incident on niobium under normal incidence. For D^+ and He^+-ion energies in the range from 10^2-10^3 eV, and for > 50 keV the yield values are low enough, so that surface erosion would not be a significant problem unless the ion fluxes ϕ were very high (see equation 4). The situation is different for heavier mass ions. As one can see in Figure 4 the niobium self sputtering yields are orders of magnitude higher than the D^+ and He^+ yields for niobium for energies in the range from 10^4 to 10^5 eV. Clearly one would want to reduce the number of energetic neutral niobium atoms which leave the wall as sputtered neutrals, thermalize with the plasma, and return to the surface as energetic neutral atoms. Similar considerations apply for other heavy mass impurities which may be released from the surface and return to it as energetic neutrals.

Differential sputtering, i.e. the sputtering of a surface which consists of different components each of which has a different sputtering yield causes surface roughening. This not only leads to a significant enlargement of the surface area but affects also photo-and particle reflection processes.

The information on chemical sputtering erosion rates for relevant fusion reactor materials and operating conditions is extremely scarce and for discussions of the topic the reader is referred to references 47, 48.

Evaporation, Surface Embrittlement, Fatigue-life

Thermal evaporation is a potential source of surface erosion due to local heating of surfaces ("hot spots") by plasma radiations or due to pulse evaporation if the plasma is dumped into the first wall at the end of a burn cycle. Furthermore, the skins of blisters, which are in poor thermal contact with the rest of the bulk due to the trapped gas, can be heated by radiation from the plasma to temperatures which substantially increase thermal evaporation. Intense x-ray irradiation of insulator surfaces has been shown to cause cracking, flaking, and evaporation, due to the steep temperature gradients which can build up in near surface regions.[71]

Reactive gases such as hydrogen and deuterium implanted in certain metals can cause an embrittlement of the surface regions. It is also expected that fatigue cracks may develop at the surface of stressed components under plasma radiations. Data are badly needed to explore if such embrittlement and fatigue processes will contribute significantly to surface damage and erosion under fusion reactor operating conditions.

POTENTIAL SOLUTIONS TO REDUCE PLASMA CONTAMINATION AND SURFACE EROSION

Reductions in the release of plasma contaminants may be achieved by selection of materials with low vapor pressure and low physical and chemical sputtering and blistering yields. Some studies center around the development and use of materials (including coatings) that have a low atomic number Z. For example, it has been suggested[49] that a curtain of woven graphite cloth placed between the plasma and the metal vacuum wall can help to prevent particles released from

the wall (e.g. by neutron sputtering) from re-entering the plasma. In addition, such a curtain can help prevent erosion of the wall by processes such as blistering and physical sputtering by intercepting most of the ions and neutral atoms leaking from the plasma. Although surface damage to graphite fibers has been observed[57] when irradiated with 100-keV He^+ ions at room temperature, such damage is greatly reduced at elevated temperatures (e.g. 800°C) which might be attained in fusion reactor operations. The chemical interaction of hydrogen with graphite fibers has been observed to lead to serious surface erosion[72], however, for temperatures ranging from ∿ 850°C-1000°C the chemical erosion process of graphite is greatly reduced (see discussion in section on chemical sputtering).

It was also recently discovered[58-60] that blister rupture (and the concomitant release of gas bursts) could be drastically reduced in materials with a small grain size and a dispersed second phase, such as sintered beryllium powder and sintered aluminum powder (SAP 895). The erosion yield for SAP 895 (sintered aluminum powder with a nominal 10.5% dispersed Al_2O_3) is estimated to be 3 orders of magnitude less than in annealed aluminum for 100-keV helium ion irradiation to a total dose of 1.0 C cm^{-2} at room temperature.[58] A reduction in surface erosion has been observed in sintered beryllium powder compared to vacuum cast beryllium irradiated with 100-keV helium ions at room temperature (to a dose of 1 C cm^{-2}) and at 600°C (to a dose of 0.5 C cm^{-2}), see Figure 11 (taken from reference 72). There appear to be two main reasons for the observed reduction in surface exfoliation due to blistering in sintered metals: (1) the trapping of small gas bubbles at grain boundaries and oxide particles; and a yield strength which is greater than for non-sintered metals, especially at elevated temperatures. It appears feasible to deposit beryllium (as a low-Z material) with a favorable microstructure on stainless steel by plasma spraying for potential fusion reactor applications.[72]

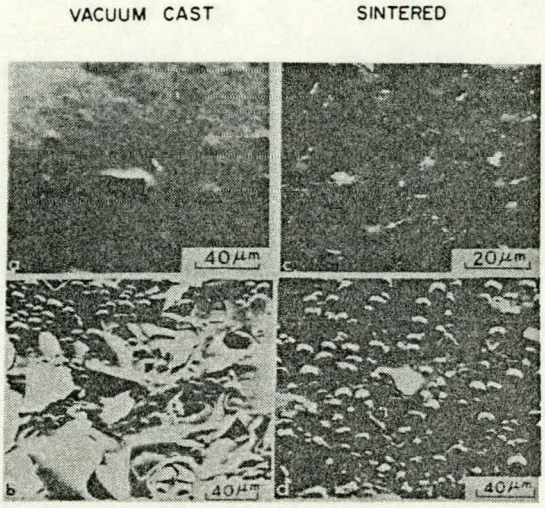

FIGURE 11. Scanning electron micrographs of beryllium irradiated at room temperature and at 600°C with 100-keV He^+ ions: (a) Vacuum-cast beryllium at room temperature (1 C/cm^2); (b) Vacuum-cast beryllium at 600°C (0.5 C/cm^2); (c) Sintered beryllium at room temperature (1 C/cm^2) and (d) Sintered beryllium at 600°C (0.5 C/cm^2). (References 60, 72)

A substantial reduction in surface erosion due to radiation blistering has been observed in metals such as Al, stainless steel, V, and Nb at temperatures above 0.4-0.5 T_m, where T_m is the melting point in K. Irradiation at this temperature leads to a porous surface containing micron-size holes. This type of surface tends to inhibit blistering even under high-dose conditions which normally cause rupture or flaking. In fusion reactor operations, however, the maintenance of structural components (which are exposed to plasma radiations) at temperatures > 0.4 T_m may be a problem. Therefore, other solutions have been searched for. Cold working of a metal has been observed to reduce erosion by blistering in certain cases.[74] The increased dislocation density and the large number of subgrains in a cold-worked material can give rise to a dispersion of the trapped gas (e.g. helium) and prevent

the coalescence of this gas into larger bubbles. Furthermore, the yield strength in a cold-worked material is higher than in the same material annealed. This leads to reduction in blister rupture.

For theta-pinch reactors the use of high resistivity first walls has been suggested to prevent electrical breakdown between the plasma and blanket segments during the short implosion-heating stage. Some protective, glassy ceramic coatings on thin metal substrates have been developed for use in fusion reactors (D. Keefer, Atomics International). During the irradiation of such coatings (e.g. 52.3% SiO_2, 40.5% BaO, 7.2% Al_2O_3 on a Nb-1% Zr substrate) with 100 and 250-keV He^+ and D^+ ions at room temperature some blister formation could be observed (see Figure 12), however, no helium or deuterium blisters were observed at 300°C under otherwise identical irradiation conditions.[61,64] The absence of blisters at high temperatures is thought to be due to the sharp increase in permeation rate with temperature observed for both helium and deuterium in most glasses.[53]

Other studies are based on design improvements of components (e.g. better cooling of system components such as beam limiters, beam dumps of injectors) which receive high plasma power depositions, in order to reduce excessive contaminant release (e.g. via sputtering and vaporization).

Still other studies deal with improved methods for removing most of the released plasma contaminants before they can reach the plasma region (e.g. divertor methods, ionization sheaths in near wall regions, and gas purge methods in pulsed plasma operations). Divertors may also help to reduce the probability for the occurence of hot spots due to charged-particle impact in localized areas, and also to reduce the impact of heavy impurity ions on the surface from which they were initially released.

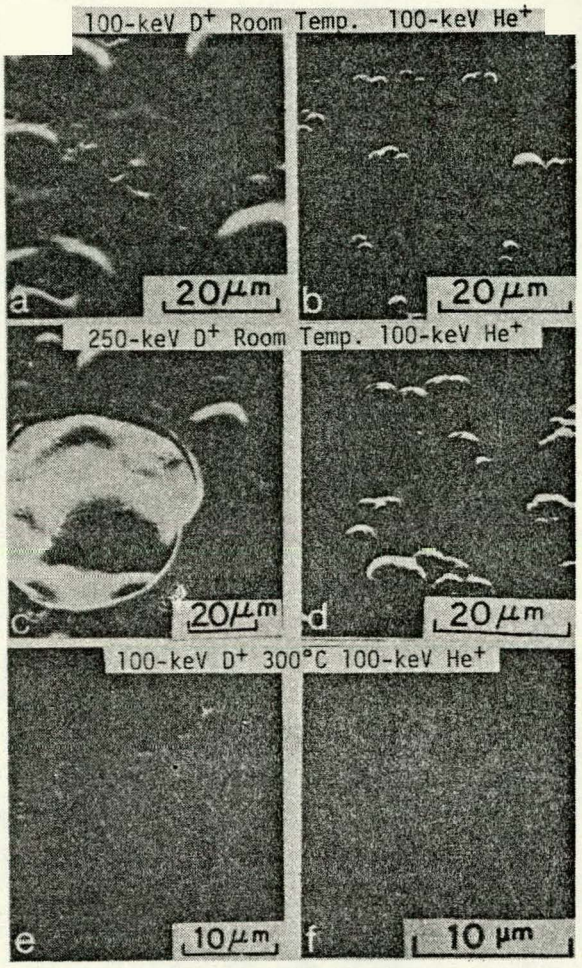

FIGURE 12. Scanning electron micrographs of ceramic coatings on Nb-1% Zr alloy after irradiation to a total dose of 0.6 C/cm^2 with: (a) 100-keV D^+ ions at R.T.; (b) 100-keV He^+ ions at R.T.; (c) 250-keV D^+ ions at R.T.; (d) 250-keV He^+ ions at R.T.; (e) 100-keV D^+ ions at 300°C; (f) 100-keV He^+ ions at 300°C. (References 61, 72)

CONCLUSIONS

The need for obtaining reliable yield values for the various particle emission and surface erosion processes for the relevant plasma parameters and materials considered for fusion applications has become clear. At this time most of the relevant information on yield values is scarce and has been obtained with single radiation sources using mainly monoenergetic beams. In fusion reactor operations, however, the surfaces will be bombarded simultaneously with various types of ions and photons having broad energy and angular distributions. This may give

rise to the occurrence of synergistic effects. Therefore, studies of simultaneous, multiple particle and photon irradiations of surfaces are needed. Only with the proper identification and understanding of the most deleterious effects will it become meaningful to develop methods to reduce, and possibly eliminate, serious plasma contamination and wall erosion.

ACKNOWLEDGEMENTS

I am grateful to Dr. S. K. Das, Dr. T. Rossing, Mr. G. Fenske, Mr. P. Dusza and Mr. D. Kurth for preparing some of the figures, performing some of the calculations and for proof reading the manuscript. Proper references to the particular issues of the journals from which some of the figures were taken have been made in the manuscript.

REFERENCES

1. R. L. Hirsch, Current status and the outlook for fusion power, in Conf. on Energy Alternatives-Technologies, Economics and Priorities, Atomic Industrial Forum, Inc., Washington, D.C., 1975.
2. J. S. Clarke, et.al., Phys. Rev. Lett. 30, 89 (1972).
3. K. A. Brueckner, IEEE Trans. Plasma Sci. 1, 13 (1973).
4. F. Winterberg, Phys. Rev. 174, 212 (1968).
5. J. W. Shearer, Nucl. Fusion, 15, 952 (1975).
6. M. Kaminsky, IEEE Trans. Nucl. Sci. 18, 208 (1971) see also in Proc. Intn'l. Working Session on Fusion Reactor Tech., CONF-719624, p. 86.
7. R. Behrisch, Nucl. Fusion 12, 695 (1972).
8. M. Kaminsky, Plasma Physics and Controlled Nuclear Fusion Research, Vol. 2, IAEA, Vienna, 1975) p. 284; see also CRC Critical Review in Solid State Sciences, 6, 433 (1976).
9. R. Colchin, private communication, Oak Ridge National Laboratory (1976).
10. Two Component Torus-Joint Conceptual Design Study, Princeton Plasma Physics Laboratory and Westinghouse Electric Corporation (1974).
11. W. M. Stacey, Jr., et.al., Argonne Natn'l. Lab., Report ANL/CTR-75-2 (1975).
12. G. Kulcinski, et.al., J. Nucl. Mat. 53, 31 (1974).
13. D. Meade, PDX Preliminary Proposal, PPPL, Special Report 73/2, 1973.
14. F. Tenney, J. Nucl. Mat. 53, 43 (1974).
15. J. Lee, J. Nucl. Mat. 53, 76 (1974).
16. R. Krakowski, et.al., J. Nucl. Mat. 53, 54 (1974).
17. (a) J. A. Maniscalco, et.al., Trans. Amer. Nucl. Soc. 22, 66 (1975); see also (b) J. Hoving, in Proc. of Faculty Inst. on Fusion Materials and Curriculum Development, Argonne Natn'l Lab., Argonne, IL, 8/9-13/76 (in preparation).
18. L. Hively and G. Miley, to be presented at the Amer. Nucl. Soc. Winter Meeting, Washington, D. C., Nov. 1976.
19. L. Hively, Progress Report-CTR Plasma Engineering Studies, No. COO-2218-41 (Univ. of IL, Urbana, April 15, 1976).
20. P. H. Rebut, et.al., J. Nucl. Mat. 53, 16, (1974).
21. S. Grammel, et.al., Proc. of 6th Symp. on Engg. Problems of Fusion Research (IEEE, New York, 1975) p. 1204.
22. UWMAK-I, a conceptual Tokamak Power Reactor Design, (Univ. of WI, Madison, WI, 1975).
23. R. W. Conn, et.al., to appear in Proc. of 2nd Intn'l Conf. on Surface Effects in Controlled Fusion Devices, San Francisco, CA, Feb. 1976 (J. Nucl. Mat.).
24. J. Hogan, et.al., J. Nucl. Mat. 53, 1 (1974).
25. L. Artsimovich, Nucl. Fusion, 12, 215 (1972).
26. D. Duchs, et.al., J. Nucl. Mat. 53, 102 (1974).
27. J. Taylor, Phys. Fluids, 4, 1142 (1961).
28. D. Lichtman, et.al., Photodesorption: A Critical Review, (Univ. of WI, Milwaukee, WI, 1976).
29. S. Brumbach, et.al., Proc. of the"Symp. on Rad. Effects on Solid Surfaces", 170th Natn'l. Meeting of Amer. Chem. Soc., Aug. 1975 (to appear in Adv. in Chem. Series).
30. M. J. Drinkwine, et.al., Electron Stimulated Desorption: A Critical Review (Univ. of WI, Milwaukee, WI, 1976).
31. D. Lichtman, to appear in Ref. 17 (b).
32. G. Fabel, et.al., Surface Science 40, 571 (1973).
33. S. Brumbach, et.al., J. Appl. Phys. 47, 2844 (1976).
34. S. Brumbach, et.al., to appear in Ref. 23.
35. R. Behrisch, Ergebn, der Exakten Naturwissen schaften, 35, 295 (1964).

36. M. Kaminsky, Atomic and Ionic Impact Phenomena on Metal Surfaces (Academic Press, New York, 1965).

37. G. Carter and J. Colligon, Ion Bombardment of Solids (Amer. Elsevier Pub. Co., New York, 1968).

38. G. M. McCracken, Rep. Prog. Phys. 38, 241 (1975).

39. H. Winters, to appear in Ref. 29.

40. H. H. Anderson, in Physics of Ionized Gases 1974, ed. V. Vujnovic (The Inst. of Physics, Zagveb, 1975), p. 361.

41. P. Sigmund, Phys. Rev. 184, 383 (1969).

42. R. Weissman, et.al., Rad. Effects 19, 7 (1973).

43. R. Weissman, et.al., Rad. Effects 19, 69 (1973).

44. H. H. Anderson, et.al., J. Appl. Phys. 46, 2416 (1975).

45. S. Danyluk and P. Bratt, to appear in Ref. 23; see also, ANL/CTR/TM-60, Argonne Natn'l. Lab.,1976).

46. H. Oechsner, Z. Physik 261, 37 (1973).

47. D. M. Gruen, in Chemistry of Fusion Technology (Plenum Press, 1975).

48. D. M. Gruen, et.al., J. Chem. Phys. 60, 89 (1974).

49. G. Kulcinski, et.al., Nucl. Fusion 15, 327 (1975).

50. G. J. Thomas, et.al., to appear in Ref. 29.

51. N. P. Busharov, et.al., to appear in Ref. 23.

52. J. Roth, et.al., in Ref. 51.

53. S. K. Das, et.al., to appear in Ref. 29.

54. M. Kaminsky, Adv. in Mass Spectrometry 3, 69 (1964).

55. W. Bauer, et.al., J. Nucl. Mat. 53, 127 (1974).

56. M. Kaminsky, Proc. of Intn'l. Conf. on Rad. Test Facilities for the CTR Surface and Materials Program, ANL/CTR-75-4 (Argonne Natn'l.Lab., Argonne, IL, 1975) p. 16.

57. R. Ekern, et.al., Proc. of 6th Symp. on Engg. Problems of Fusion Research (IEEE, New York, 1976) p. 1146.

58. S. K. Das, et.al., Appl. Phys. Lett. 27, 197 (1975).

59. S. K. Das, et.al., in Ref. 57, p. 1151.

60. S. K. Das, et.al., to appear in Ref. 23.

61. M. Kaminsky, et.al., Nucl. Tech. 29, 303 (1976).

62. S. K. Das, et.al., J. Nucl. Mat., 53 115 (1974).

63. M. Kaminsky, et.al., Rad. Effects 18, 245 (1973).

64. T. D. Rossing, et.al., to appear in Ref. 23.

65. R. G. St-Jacques, et.al., to appear in Ref. 23.

66. M. Kaminsky, et.al., Appl. Phys. Lett. 27, 521 (1975).

67. J. Biersack, Rad. Effects 19, 249 (1973).

68. J. G. Martel, et.al., J. Nucl. Mat. 53, 142 (1974).

69. J. Biersack, to appear in Ref. 23.

70. M. Kaminsky, et.al., Nucl. Tech. 22, 373 (1974).

71. J. Phillips, Los Alamos Scientific Lab. (private communication).

72. T. D. Rossing, et.al., submitted to J. Vac. Science and Technology.

73. S. K. Das, et.al., Nucl. Met. 18, 240 (1973).

74. S. Veprek and M. R. Hague, Appl. Phys. 8, 303 (1975).

75. J. Lindhard, et.al., Mat. Fys. Medd. Dan. Vid. Selsk. 33, no. 14 (1963).

76. D. K. Brice, Ion Implantation Range and Energy Deposition Distribution, Vol. 1 (Plenum Data Comp., New York, NY, 1975).

†Work performed under the auspices of the U.S. Energy Research and Development Administration.

RADIATION-ENHANCED PRECIPITATION IN A V-10 wt % Ti ALLOY*

S. C. Agarwal and A. Taylor
Materials Science Division
Argonne National Laboratory
Argonne, Illinois 60439

A V-10 wt % Ti alloy was irradiated with 2.7 MeV $^{51}V^{+}$ at 650°C to doses of 2-60 dpa. No void swelling was observed at any dose. The irradiation resulted in an enhancement of a precipitation process similar to that observed in unirradiated materials. The precipitates in irradiated specimens were found to have the NaCl-type cubic crystal structure with a lattice parameter of TiO. The orientation relationship between the matrix and the precipitates was the same as that observed under thermal equilibrium conditions in unirradiated materials.

INTRODUCTION

Vanadium-base alloys containing Ti and Cr are potential candidate materials for the CTR first wall. Addition of Ti or Cr to vanadium not only improves its strength but also suppresses void formation and the attendant swelling, a major problem associated with CTR first-wall operation. Santhanam et al.[1] studied V-1 wt % Ti irradiated with 3-MeV $^{51}V^{+}$ ions at 700°C to doses between 2.5 and 55 displacements per atom (dpa). At low doses (<22 dpa), the microstructure consisted of a high density of coherent precipitates with no voids. At higher doses, however, voids were observed near grain boundaries and in areas denuded of precipitates. The precipitates were reported to be platelets with {100} habit. It is likely that the reduced void swelling observed in V-Ti alloys may be due to the precipitates which form during irradiation. Similar behavior has also been observed in studies of void swelling in unalloyed vanadium.[2,3] The most likely origin of the observed irradiation-induced phases in V-base alloys is the interstitial impurity content of the material. This has recently been confirmed for unalloyed vanadium.[4]

The Ti content in V-base alloys that are of interest for CTR applications is likely to be of the order of several percent. Since both V and Ti have strong affinities for interstitial impurities and tend to form interstitial compounds, it is difficult to obtain these alloys in the form of homogeneous solid solutions, which is necessary if irradiation-induced precipitation effects are to be characterized. Although the V-Ti phase diagram indicates a body-centered-cubic (bcc) solid solution ~80 wt % Ti at ~700°C, an increase in Ti content with an increase in the solubility of oxygen in V-Ti alloys can lead to the formation of oxides. The purposes of the present study were to establish the identity of irradiation-induced phases in V-Ti systems and to examine the suppression of void swelling at various dose levels.

EXPERIMENTAL

Vanadium and titanium were obtained in the form of 6-mm-dia rod from MRC. The

*Work supported by the U.S. Energy Research and Development Administration.

supplier's analysis showed that the interstitial impurity content of vanadium was O, 15 ppm; C, 120 ppm; and N, 16 ppm (all compositions are in ppm by weight). A V-10 wt % Ti alloy ingot was prepared by a combination of inert-gas arc melting and levitation melting techniques. The ingot thus obtained was then cold rolled into 0.02-cm-thick sheet. A ribbon of the cold-rolled V-10 Ti (20 by 0.4 by 0.02 cm^3) was then homogenized at 1300°C for 4 h in a dynamic vacuum of $\sim 10^{-8}$ torr followed by quenching with He gas cooled with liquid N_2. It can be clearly seen from Fig. 1 that the above combination of preparation techniques has been advantageous in obtaining the V-10 Ti in the form of homogeneous solid solution. Figure 1(a) is an optical micrograph of the cold-rolled sheet showing dendritic structure with some solute segregation. Figure 1(b) shows the precipitation that occurs when the alloy is homogenized at 1200°C for 15 h in an evacuated quartz capsule backfilled with 0.5 atm of ultrahigh-purity argon and then quenched in water at the ambient tem t Figure 1(c) shows the improvement achieve in obtaining a homogeneous solid solution when the homogenization was carried out b direct resistance heating at 1300°C for 4 in a dynamic vacuum of $\sim 10^{-8}$ torr followe by quenching with He gas at the liquid-N_2 temperature.

Examination of unirradiated specimens the above V-10 Ti alloy by TEM confirmed the absence of precipitates. Specimens (3-mm-dia disks) of the homogenized alloy were prepared for irradiation by standard methods described in detail elsewhere.[5] Sixteen specimens in a 4 by 4 array were then irradiated with 2.7-MeV $^{51}V^+$ ions to dose levels of 2-60 dpa at 650°C in the A 4-MeV dual-beam irradiation facility usin standardized procedures previously

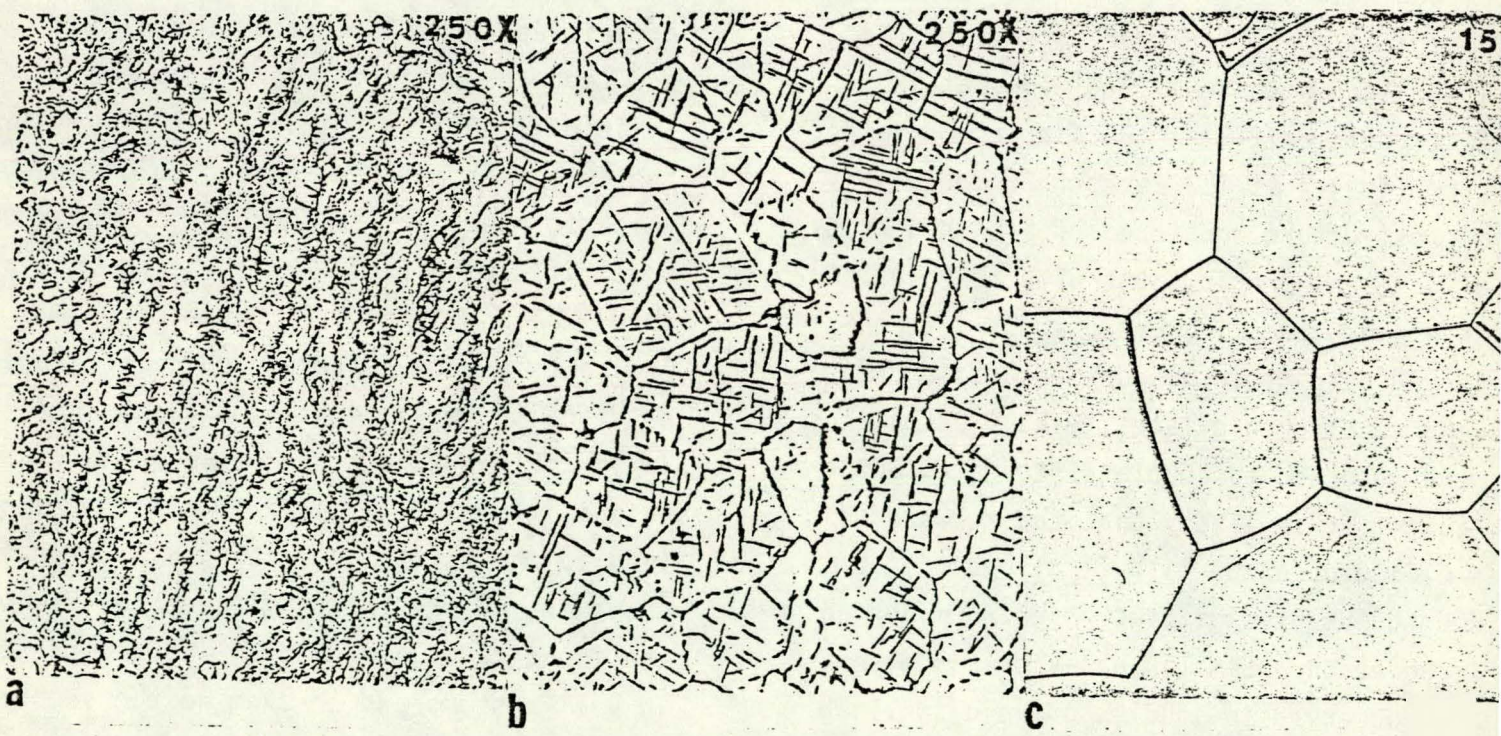

FIGURE 1. Microstructures of V-10 wt % Ti Alloy. (a) As cold rolled. (b) Annealed for 15 h at 1200°C in an evacuated quartz capsule backfilled with 0.5 atm of ultrahigh-purity argon and water quenched. (c) Annealed for 4 h at 1300°C in a high-vacuum furnace in a dynamic vacuum of $\sim 10^{-8}$ torr followed by quenching with He gas cooled with liquid N_2

described.[5] During the 7-h irradiation, the total gas pressure decreased from $\sim 10^{-8}$ to 5×10^{-8} torr. Residual-gas analysis showed approximate partial pressures of $\sim 3 \times 10^{-9}$ torr for water and $\sim 4 \times 10^{-8}$ torr for carbon monoxide, dioxide, and nitrogen.

Following irradiation, specimens for TEM examination were prepared by sectioning the specimens to a depth of ~7000 Å below the irradiated surface and then thinning from the back side to perforation. The section depths were determined with an interference microscope to within ±300 Å. Deposited energy densities as a function of depth, calculated from Brice Codes RASE3 and DAMG2,[6] were converted to displacements per atom using a threshold energy of 40 eV. For 2.7-MeV V^+ irradiation, the depth of maximum damage was 8300 Å, with a corresponding damage density per ion of 63.8 eV/A.

RESULTS AND DISCUSSION

The characteristic microstructural feature of the irradiation zone was a fine precipitation. No voids were detected in the irradiated V-10 Ti specimens for the entire range of doses studied (2-60 dpa nominal). Beyond the irradiated zone of a high-dose specimen, the microstructure contained only a very fine unresolved feature with poor contrast in the bright-field. No additional spots or streaks, in the selected area diffraction (SAD) patterns were observed. However, a high density of dislocations and platelet precipitates was observed in all irradiated specimens. Figure 2(a) shows precipitates and dislocations for 5-dpa specimens. The corresponding SAD pattern, given in Fig. 2(b), confirms that the foil is in exact [111] orientation of cubic crystals. Perhaps the unresolved structure observed in the control specimen is an early stage of precipitation under thermal equilibrium conditions and profuse precipitation in the irradiated specimen is due to enhancement of precipitation by ion irradiation. Under equilibrium conditions, in the temperature range 600-700°C, fully developed TiO with the NaCl-type structure is known to form in V-base Ti alloys after aging for several days.[7]

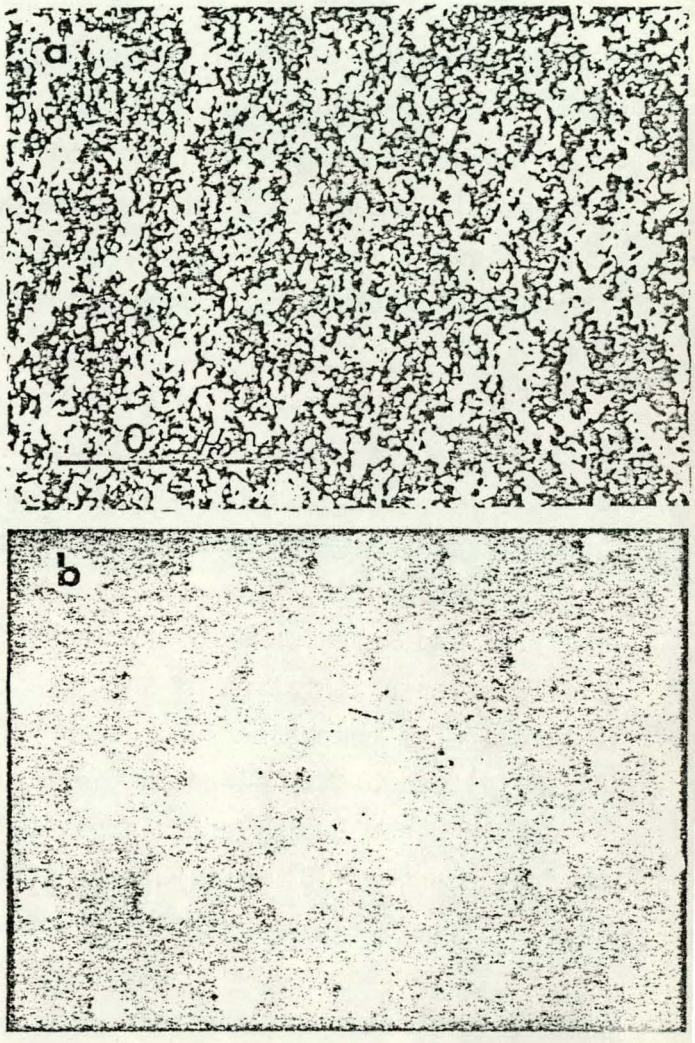

FIGURE 2. (a) Bright-field Micrograph Showing Dislocations and Precipitates in V-10 Ti Irradiated to ~5 dpa at 650°C. (b) SAD of Fig. 2(a) in exact [111] orientation. Mag. 58,000X .

The morphology of the precipitates observed in the irradiated specimens was examined in some detail. In Fig. 2(b), the precipitates observed in the irradiated specimens do not show any diffraction

features on SAD patterns in exact {111} foil orientation. However, in exact {100} foil orientation, streaking is observed in [100] directions. The streaking becomes profuse for the high-dose specimens, as shown in Fig. 3. The intensity of the streaks increases as the dose level increases [Figs. 3(a)-3(d)]. Figure 3(e), which is a dark-field image obtained from the streak marked "A" in Fig. 3(d), clearly confirms the platelet nature of the precipitates. Thus, the precipitate in V-10 Ti appears to form coherently with bcc V-rich solid solution and has a {100} habit. The increase in intensity of the streaks with dose, Figs. 3(a)-3(d), suggests a dependence of volume fraction of the precipitate on dose.

Figure 4(a) shows SAD in an orientation tilted ∿5° from the exact {111} bcc orientation [Fig. 2(b)]. Now additional precipitate spots can be seen near the matrix (bcc) spots. These spots were analyzed and were found to originate from a {110}-type orientation of NaCl cubic lattice. The composite SAD pattern in Fig. 4(a) can be explained on the basis of a pattern generated by superimposing (111) bcc pattern on (110) NaCl pattern with $[110]_{bcc} \parallel [001]_{NaCl}$. The diffraction pattern thus generated is shown in Fig. 4(b) and closely resembles the pattern in Fig. 4(a). The composite diffraction patterns in Figs. 4(a) and 4(b) represent only one of the three possible orientations of the precipitates. The lattice parameter computed from the d-spacings in Fig. 4(a) gave a value of ∿4.20 Å, which is in good agreement with the 4.19 ± 0.06 Å value for TiO reported in literature.[7] Thus, the precipitates observed in the irradiated specimens appear to be TiO with NaCl-type cubic crystal lattice. The orientation relationship between the bcc matrix and t TiO platelets was found to be

$$(001)_{bcc}V \parallel (001)_{NaCl}TiO$$

$$[110]_{bcc}V \parallel [010]_{NaCl}TiO.$$

To examine the dose dependence of prec pitation, the TEM specimens were brought the orientation given in Fig. 4(a) and th the precipitate spot marked "A" in Fig. 4 was used for imaging the precipitates in dark-field. Because of the high dislocat density, precipitates could be clearly se only in the dark-field image. Figures 5(5(d) show the precipitate structures for nominal dose levels of 5, 15, 30, and 55 dpa, respectively. As the dose increa the precipitate density increases system- atically and is quite high for the 55-dpa specimen [Fig. 5(d)]. However, no appre- ciable change occurred in the precipitate size with dose. The volume fraction of t precipitate has not been measured. Thus, it appears that 650°C V^+ irradiation of V-10 Ti results in precipitation of TiO. The precipitation process is enhanced by irradiation, which is reflected in the dose dependence of the precipitate densit Work to determine the interstitial compos tion of the irradiated layer is in progre

It should be noted that no voids are formed in this alloy in contrast to a pea swelling of ∿0.4% at 14 dpa found for unalloyed vanadium at the same temperatur The mechanisms responsible for the void- swelling suppression remain to be elucida

CONCLUSIONS

1. Interstitial impurity pick u alloy preparation of V-Ti alloys can be significantly reduced by carefully choosi the preparation methods and environments.

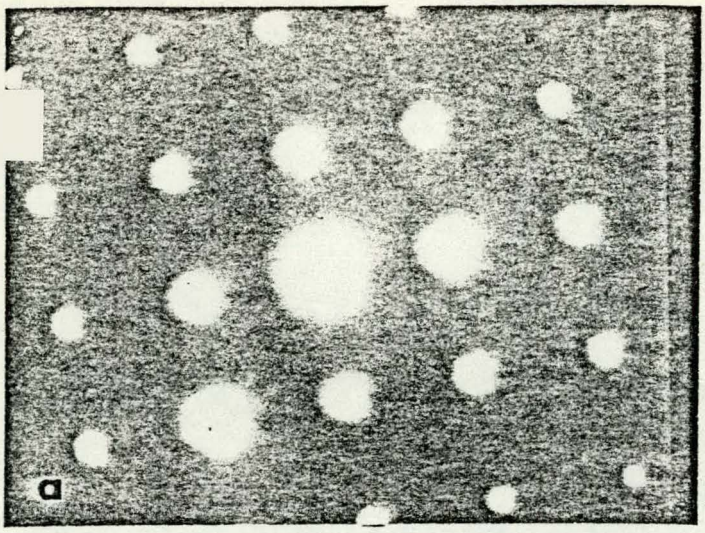

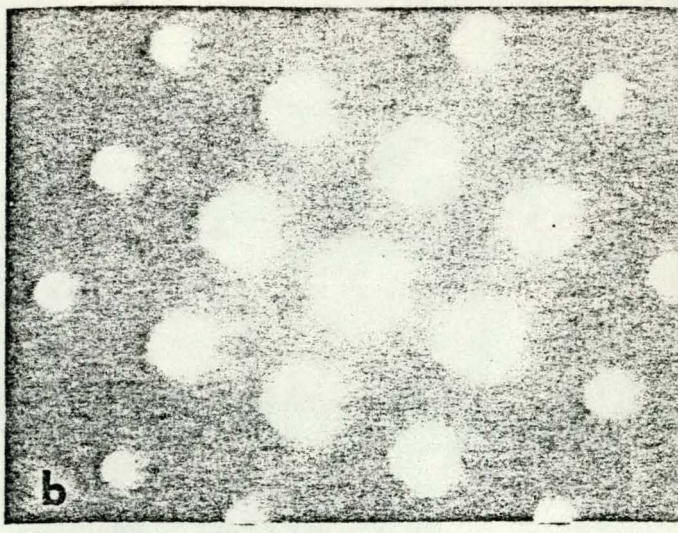

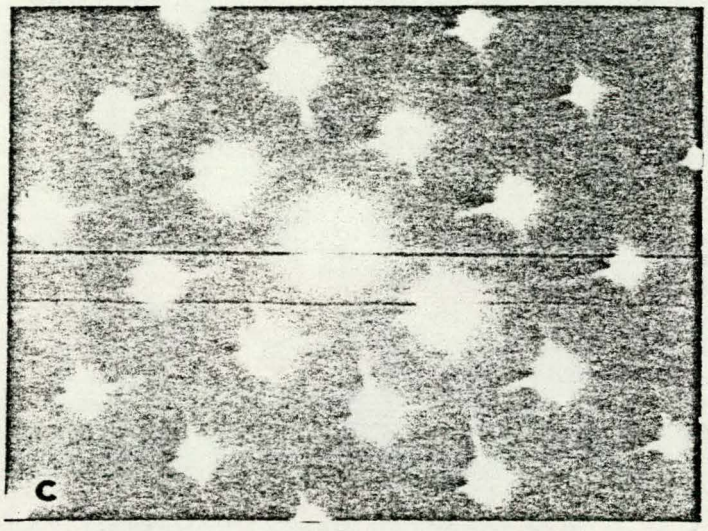

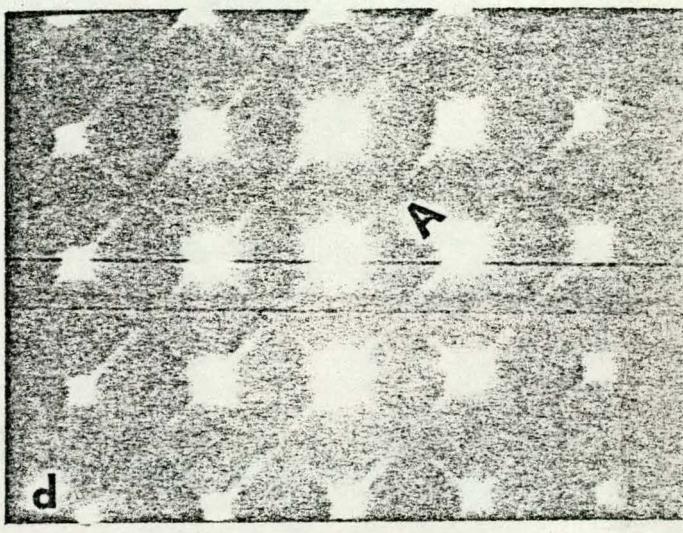

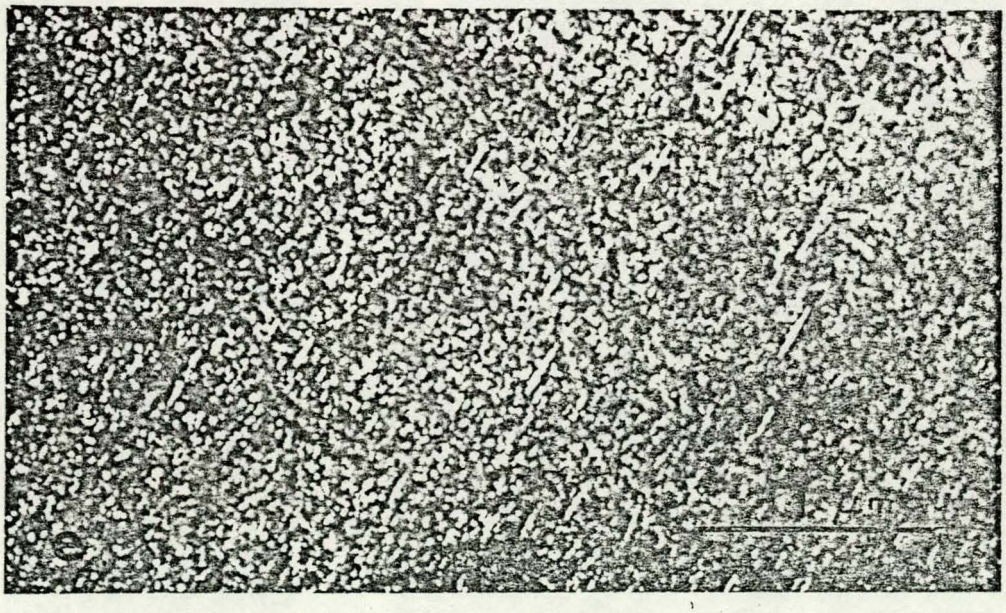

FIGURE 3. Exact [100] Zone SAD Patterns for V-10 Ti Showing [100] Streaking. (a) ∿5 dpa. (b) ∿15 dpa. (c) ∿30 dpa. (d) ∿55 dpa. (e) Dark-field image from <100> streak marked "A" in (d). Mag. 29,000X

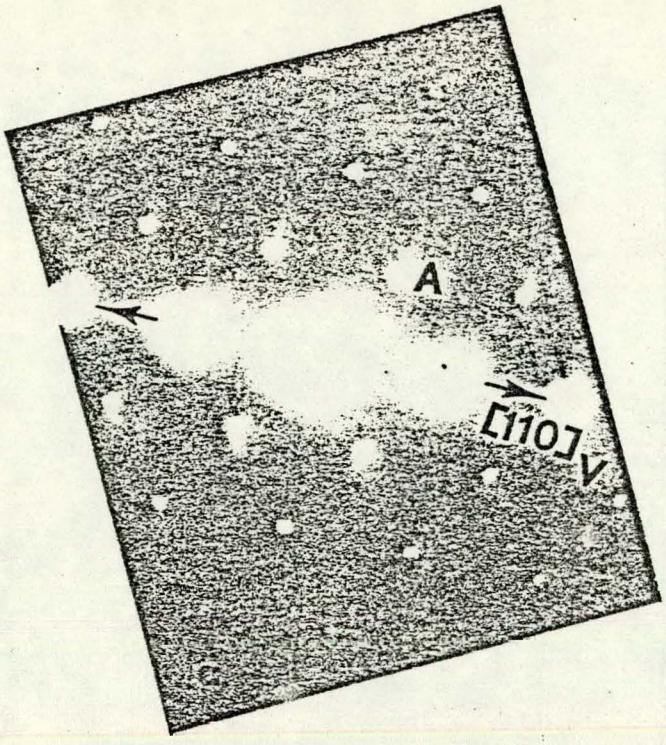

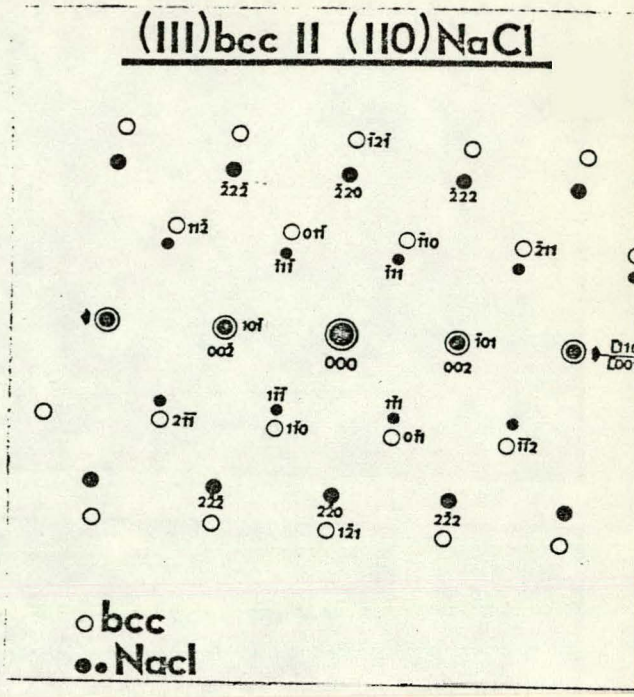

FIGURE 4. SAD Patterns for V-10 Ti in a Near [111] Zone. (a) SAD pattern from ∿5-dpa specimen. (b) SAD pattern generated by superimposing (111) standard pattern for the bcc crystal on the (110) pattern for the NaCl-type lattice with (111)bcc || (110)NaCl and [110]bcc || [001]NaCl

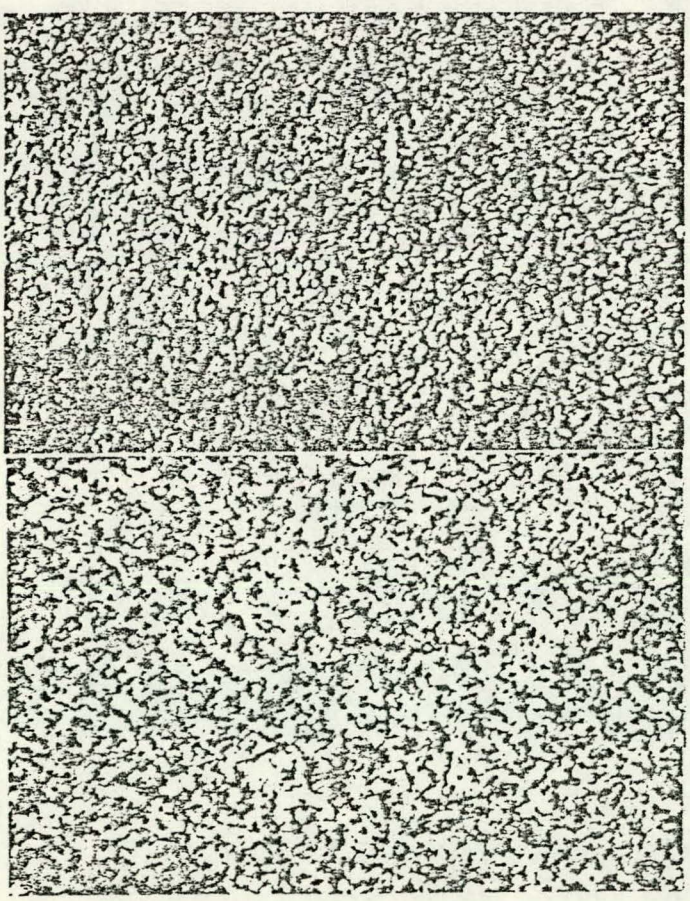

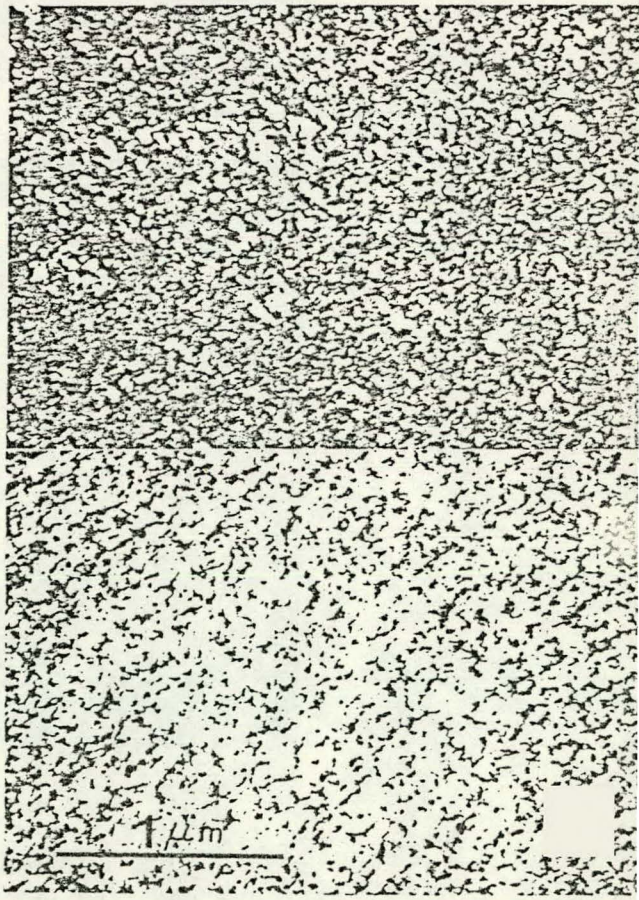

FIGURE 5. Dose Dependence of Precipitation in Irradiated V-10 Ti. Dark-field images from spot "A" in Fig. 4(a) in a near [111] zone. (a) ∿5 dpa. (b) ∿15 dpa. (c) ∿30 dpa. (d) ∿55 dpa. Mag. 29,000X

2. Irradiation enhances the precipitation of TiO in V-10 Ti.

3. The crystal structure and orientation relationships of the TiO precipitates in the irradiated V-10 Ti are the same as those observed in unirradiated material in which TiO has been precipitated thermally.

4. Addition of 10 wt % Ti to vanadium completely suppresses void swelling.

REFERENCES

1. A. T. Santhanam, A. Taylor, B. J. Kestel, and C. Steves, J. Vac. Sci. Tech. 12(1), 528 (1975).
2. S. C. Agarwal and A. Taylor, Proc. Intl. Conf. on Radiation Effects and Tritium Technology for Fusion Reactors, CONF-750989, Vol. I, 1975, p. 150.
3. W. J. Weber, G. L. Kulcinski, R. G. Lott, P. Wilkes, and H. V. Smith, Jr., Proc. Intl. Conf. on Radiation Effects and Tritium Technology for Fusion Reactors, CONF-750989, Vol. I, 1975, p. 130.
4. S. C. Agarwal, D. I. Potter, and A. Taylor, Proc. Eighth Intl. ASTM Symp. on the Effects of Radiation on Structural Materials, St. Louis, MO, 1976.
5. A. Taylor, J. R. Wallace, D. I. Potter, D. G. Ryding, and B. O. Hall, Proc. Intl. Conf. on Radiation Effects and Tritium Technology for Fusion Reactors, CONF-750989, Vol. I, 1975, p. 158.
6. D. K. Brice, Sandia Laboratories, SLA-73-0416, 1973.
7. K. H. Kramer, J. Less-Common Metals 21, 365 (1970).

ELEVATED-TEMPERATURE TENSILE PROPERTIES OF V-15Cr-5Ti CONTAINING HELIUM INTRODUCED BY ION BOMBARDMENT AND TRITIUM DECAY*

R. F. Mattas, H. Wiedersich,
Materials Science Division
Argonne National Laboratory
Argonne, Illinois 60439

D. G. Atteridge, A. B. Johnson, and J. F. Remark
Battelle, Pacific Northwest Laboratory
Richland, Washington 99352

The tensile properties of V-15 wt % Cr-5 wt % Ti containing 25-35 appm He have been investigated from 600 to 800°C. Helium charging was accomplished by the "tritium trick" and both thin-sheet and cylindrical specimens were tested. Specimens containing helium showed decreases in elongation at temperatures of 700°C and above, but the cylindrical specimens with or without helium exhibited considerably greater elongations than the sheet specimens under corresponding conditions. A comparison of the tensile properties of the sheet specimens charged by the "tritium trick" with the properties of Cyclotron-injected sheet specimens from a previous study indicates that the Cyclotron-injected specimens exhibited greater ductility than the specimens charged by the "tritium trick." The onset of gross embrittlement occurred between 700 and 750°C in both cases.

INTRODUCTION

Alloys of the transition metals vanadium, niobium, and molybdenum are candidates for fusion reactor first-wall structural materials.[1] An impediment to their use is, however, the lack of knowledge of the long-term mechanical-property changes that occur in reactor environments. Little is known about the effect of internal helium on the mechanical properties of transition metals at elevated temperature. These materials, when exposed to fusion radiation, are expected to accumulate from 25 to 75 atomic parts of helium per million matrix atoms (appm) per year through (n,α) reactions. The helium which is essentially insoluble in metals, is removed from the lattice by the formation of bubbles in the material and/or by diffusion out of the material. The bubbles that form at grain boundaries can accelerate grain-boundary sliding, which begins to operate as a deformation mechanism near one half the melting point ($1/2T_m$). In addition, tensile stresses at elevated temperatures can produce bubble growth and coalescence along grain boundaries. The result is premature intergranular cracking and failure at elevated temperature.

The simulation of fusion reactor conditions is vital to predict the effects of helium embrittlement on mechanical properties. The mechanical-property data from

*Work supported by the U.S. Energy Research and Development Administration.

joint ANL/PNL investigation of nonreactor helium-implantation methods will be discussed in the present report. Both of the s ation techniques developed to date, n y helium ion injection and helium production by tritium decay, were included in the present study. The former method consists of injection of high-energy helium ions into relatively thin samples. The latter method consists of diffusion of tritium into the sample, the decay of tritium to ^3He, and removal of the remaining tritium by hot vacuum extraction.[2-4] A detailed description of this helium-charging technique, known as the "tritium trick", is given elsewhere.[4]

Each simulation method has advantages and disadvantages. Both techniques are capable of introducing large quantities of helium into metals in a short period of time, but neither technique matches the displacement damage to helium production ratio expected in fusion reactors. The atom displacement damage during ion bombardment is orders of magnitude less than expected in fusion reactors for an equivalent production of helium,[4] whereas the tritium decay reaction yields essentially no atom displacement damage. The greatest disadvantage of the ion-bombardment technique is the inherent specimen thickness limitation (~10 mils) due to the limited penetrating power of the helium. Essentially no size limitation is imposed by the tritium-trick method, since diffusion processes are used to distribute the tritium in the metal. The major disadvantage of the tritium-trick method is the difficulty encountered in ch ng materials with low tritium solubilities. High-pressure charging (up to 100 atm) must be used for low solubility materials, such as stainless-steels, in order to obtain significant helium production rates.

The environments encountered in the two simulation procedures and in fast reactors are likely to result in different helium bubble distributions. Helium bubbles were found to nucleate nonhomogeneously on internal structural defects and on grain boundaries in commercial-purity niobium charged with helium by the tritium trick.[5] The resultant bubble distributions in ion bombarded material are a strong function of the specimen bombardment temperature, with low specimen temperatures yielding homogeneous bubble distributions and high specimen temperatures yielding nonhomogeneous bubble distributions more typical of helium bubble distributions produced in nuclear reactors.[6]

The present ANL/PNL program was initiated to compare the results of the two helium charging techniques on the same material. The material studied, V-15Cr-5Ti, is a high-strength, creep-resistant alloy, the mechanical properties of which have been previously investigated with specimens helium charged by ion bombardment.[7,8] Vanadium alloys exhibit high tritium solubilities and thus are amenable to helium charging by the tritium trick.

EXPERIMENTAL PROCEDURE

The V-15Cr-5Ti alloy used in this study is from the same stock as that used in the previous helium ion-bombardment study.[8] Both thin sheet and cylindrical specimens were fabricated from this material. The sheet specimens, with a 0.01 x 0.2 x 1.0 in. test section, were duplicates of those used in the earlier investigation, which allowed a direct comparison of the two charging techniques. The cylindrical specimens, 0.11 in. dia. x 0.75 in. test section, allowed a comparison between the thin sheet

and "bulk" geometries. The specimen configurations are compared in Fig. 1. All material was annealed for 1 h at 1250°C. This anneal treatment was used in the original ion-bombardment experiment.

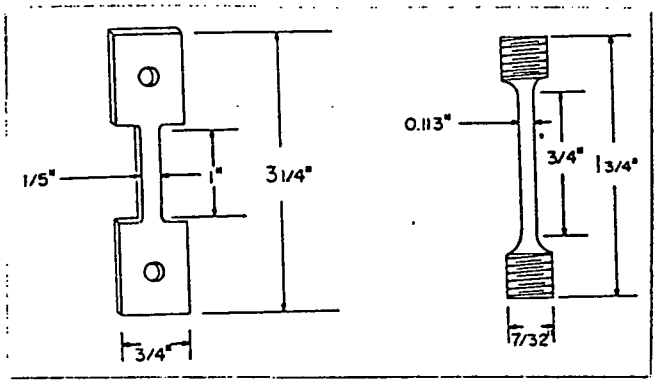

FIGURE 1. Sheet and Cylindrical Specimen Geometries

All helium charging for this program was performed at PNL by the tritium-trick technique. The charging cycle was essentially the same as reported earlier for vanadium.(4) The basic charging method is outlined as follows:

(1) absorption of tritium gas by the vanadium alloy specimens at 400°C;

(2) decay at room temperature of a portion of the tritium to ^3He; and

(3) removal of the excess tritium from the helium-implanted specimen by hot vacuum extraction at 750°C.

Five sheet specimens and three cylindrical specimens were helium implanted during this program.

Both the sheet and cylindrical specimens were tested following the same procedures used in the original ion-bombardment investigation.(8) All specimens were tested at temperatures and helium concentrations comparable to those of the original study.

All tensile tests were carried out in an Instron tensile test machine in vacuum at a strain rate of 0.02/min. After the samples were placed in the tensile grips and the vacuum chamber was evacuated, the furnace was heated quickly to the test temperature. The samples were allowed to equilibrat 10-15 min for the foil specimens and 3_ ...n for the cylindrical specimens before the test was started. The total time between furnace startup and shutdown varied from 30 to 45 min for the sheet specimens and from 45 to 60 min for the cylindrical specimens. The sample temperature, monitored by thermocouples in contact with the gauge length, varied between 2 and 4°C after equilibrium was attained. The sheet specimens were tested in a vacuum of 2-3 x 10^{-5} torr with a thin sheet of zirconium around the sample to act as a getter [This foil was not used in the original study.(8)] The cylindrical specimens were tested at a pressure of <1 x 10^{-5} torr without a foil getter. The sample appearance after testing was unchanged from that before the test.

TEST RESULTS AND DISCUSSION

Ten sheet and four cylindrical samples were tested in the present tritium trick study. Five of the ten sheet samples and three of the four cylindrical samples contained ~35 appm helium. Twelve sheet samples were tested in the ion-bombardment study, with five of the twelve containing ~25 appm helium. The tensile test results for the three specimen batches are presented in Table 1 as a function of test temperature for the different helium implantation techniques and specimen geometries. The results presented in Table 1 will be discussed in the following sections. The first section consists comparison of the mechanical properties of sheet specimens charged by ion bombardment and the tritium trick; the second section consists of a comparison between the two

TABLE 1. Elevated-temperature Test Results for V-15 wt% Cr-5 wt% Ti with and without Helium

Test emperature (° C)	Calculated Helium Content	Strength (ksi) 0.2% Yield	Strength (ksi) Ultimate	Elongation Uniform	Elongation Total	Reduction In Area (%)
	Foil specimens helium implanted by ion bombardment[a]					
650	0.0	51.2	83.7	11.2	11.4	75.0
700	0.0	49.0	85.6	13.3	13.5	69.0
	25.0	49.9	86.6	12.7	13.2	58.0
750	0.0	49.6	84.0	13.9	15.5	64.2
	25.0	49.0	79.9	7.4	7.6	25.4
800	0.0	45.7	77.2	11.9	15.7	53.1
	25.0	47.5	68.6	4.4	4.5	15.7
850	0.0	42.5	65.1	9.6	18.2	54.0
	25.0	47.4	59.5	2.9	3.2	15.9
900	0.0	37.7	56.2	7.8	16.4	49.7
	0.0	38.7		7.2	24.6	
	25.0	40.8	51.5	2.3	2.3	17.1
	Sheet specimens helium implanted by tritium decay					
600	0.0	53.0	89.0	14.1	14.1	68.0
	27.5	55.0	87.0	10.8	10.8	64.0
650	0.0	52.0	86.0	15.5	15.9	68.0
	27.0	54.0	87.0	10.3	10.3	62.0
700	0.0	50.0	88.0	15.5	15.9	58.0
	29.0	54.0	69.0	3.8	3.8	37.0
750	0.0	51.0	82.0	13.5	15.7	48.0
	38.0	51.0	65.0	3.2	3.2	30.0
800	0.0	43.0	72.0	13.2	20.1	28.0
	39.0	43.0	54.0	1.3	1.3	7.5
	Cylindrical specimens helium implanted by tritium decay					
700	38.0	53.2	88.0	10.6	12.4	
750	0.0	55.3	98.2	15.0	26.2	
	29.0	50.7	75.0	7.7	10.0	13.1
800	30.0	42.7	64.0	6.1	6.6	11.2

(a) From Ref. 8.

specimen configurations containing tritium-charged helium; and the third section contains a comparison of all sheet specimen data with the cylindrical specimen data.

SHEET SPECIMENS

Tensile tests of the control, ion-bombarded, and tritium-trick charged specimens were performed in the temperature range from 600 to 900°C. The mechanical properties for both sets of control specimens are compared in Fig. 2. The properties of both sets of specimens are in close agreement as a function of temperature.

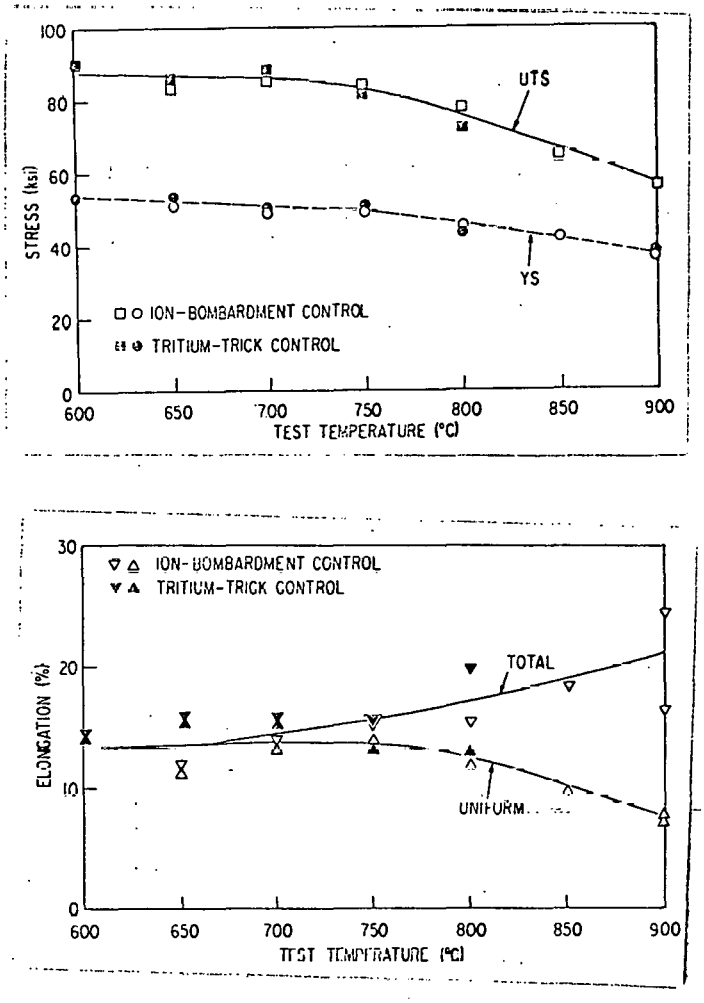

FIGURE 2. Elevated-temperature Test Results for V-15Cr-5Ti Sheet Control Specimens

All controls were as-annealed sheets except for the 750°C tritium-trick control, which was deuterium charged in a simulated tritium charging time-temperature cycle. Although the 750°C control exhibits

increased yield strength and decreased elongation, the authors believe these values are within the data scatter obs between the two sets of controls t temperatures and therefore do not i any significant effect on the mechanic properties by the charging and extract of deuterium and the accompanying therm cycling.

The mechanical properties correspon to the two helium charging techniques presented as a function of test tempera in Fig. 3. The average mechanical pro ties of the control specimens are also plotted in the figure for comparison. is evident that both helium-charging methods result in substantial decrease elongation at test temperatures of 750

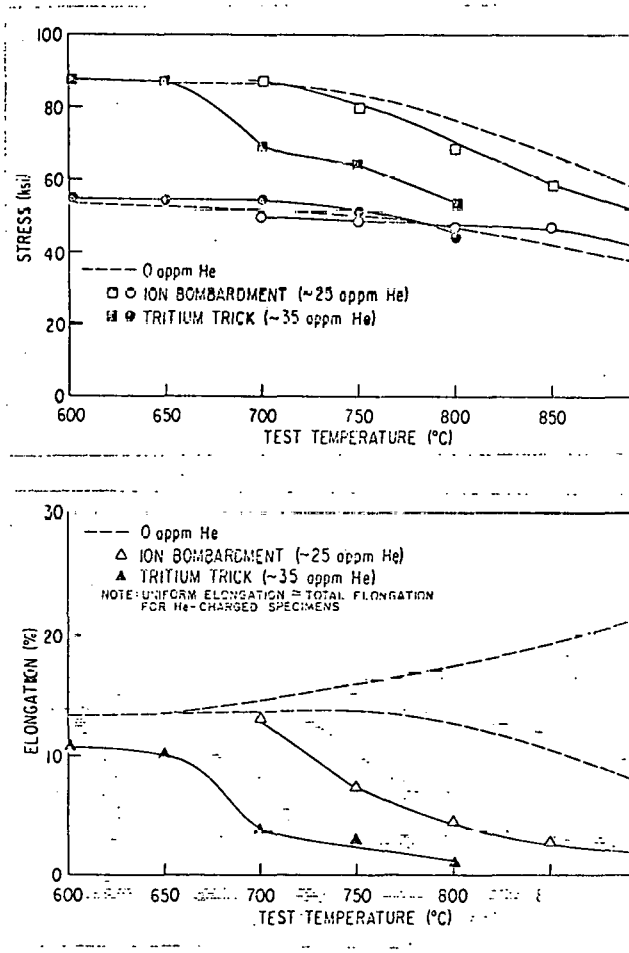

FIGURE 3. Elevated-temperature Tensile Test Results for V-15Cr-5Ti Sheet Speci Containing Helium

id above, with the individual helium-
harged specimens exhibiting essentially no
ifference between uniform and total elonga-
i alues. The tritiated specimens con-
i...tly exhibited lower elongation values
han the ion-bombarded specimens, whereas
he ion-bombarded specimens exhibited con-
iderably higher ultimate strengths than the
ritiated specimens. The yield strength
rom the two helium-charging methods are
omparable within the experimental scatter
and evident for the control specimens
Fig. 2).

The engineering stress-strain curves for
he 750°C control and helium-charged speci-
ens are compared in Fig. 4. At low strains
ll the curves match quite closely, whereas
t high strains, the ion-injected sample
xhibits a somewhat higher work-hardening
ate and the tritium-trick charged sample
xhibits a somewhat lower work-hardening
ate than the control sample. The average
ork-hardening rate of all ion-bombarded
specimens, as determined from Table 1 by
he difference between the yield and ulti-
nate strengths divided by the uniform elong-
ation, is considerably greater than that of
he respective tritium-trick charged and
control samples. All samples tested at or
elow 750°C exhibited a yield point, whereas
hose tested at or above 800°C did not.
Fracture of the tritium-trick charged
specimens generally occurred in a more
irregular manner than fracture of either the
ion-injected or control samples, as shown by
the load drop at fracture initiation shown
in Fig. 4.

preliminary SEM study of the specimen
fracture surfaces indicates that a consis-
tent fracture morphology pattern occurs,
which is a function of specimen elongation
values and independent of test temperature.

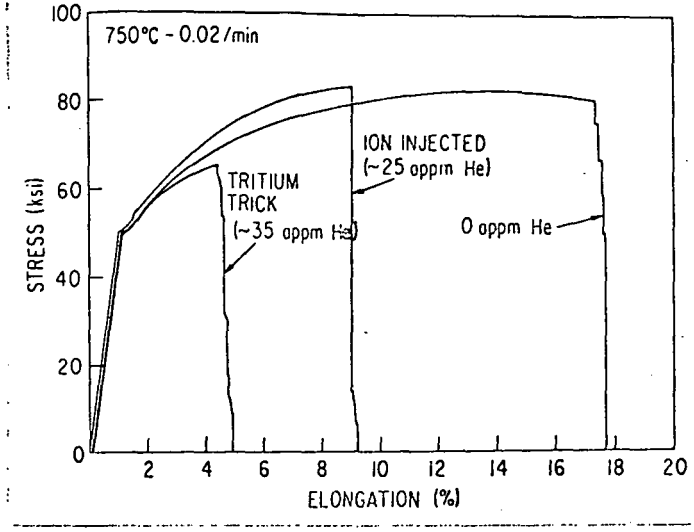

FIGURE 4. Engineering Stress-strain Curves for Helium-charged and Control Sheet Specimens Tested at 750°C

No intergranular fracturing was present in any of the control specimens nor in any of the helium-containing specimens that exhibited uniform elongations of 10% or greater; this includes the 700°C ion-bombarded specimen and the 600 and 650°C tritium-tricked specimens. Intergranular fracture was found in the 750°C ion-bombarded specimen and the 700°C tritium-trick specimen (7.4 and 3.8% uniform elongation, respectively). Some ductile rupture fracture area was still present in the 800°C ion-bombarded specimen (4.4% uniform elongation) and the 750°C tritium-trick specimen (3.2% uniform elongation), whereas the 900°C ion-bombarded specimen and the 800°C tritium-trick specimen exhibited almost complete intergranular failure (2.3 and 1.3% uniform elongation, respectively). A comparison of the fracture surfaces of the control and tritium-trick charged specimens tested at 800°C is shown in Fig. 5.

The differences between the specimen elongations associated with the two chargin methods may be due to one of several factors. The greater degree of embrittlement

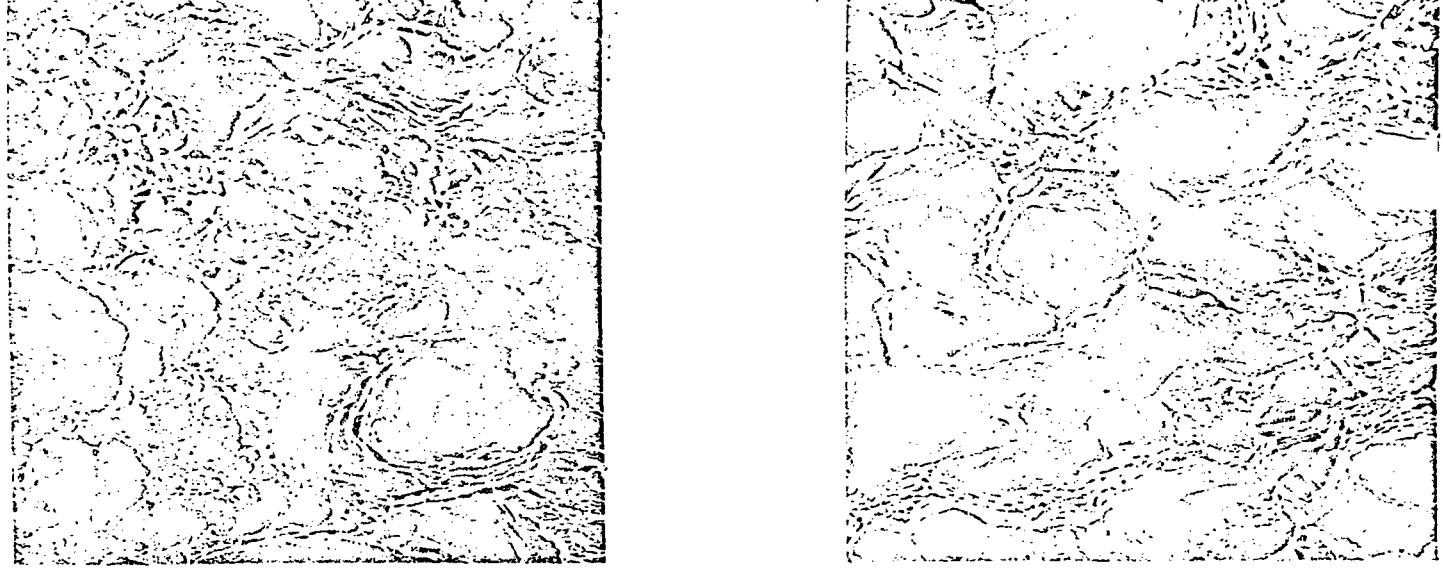

FIGURE 5. Fracture Surfaces of Sheet Specimens Containing 0 and 39 appm He Tested at 800°C

observed in the specimens charged by the tritium trick may be due to the lack of atom displacement damage during helium charging, since radiation damage is present in the ion-bombarded specimens. Another reason for the differences in elongation between the two charging methods may be the somewhat higher helium concentration in the specimens charged by the tritium trick. However, this appears unlikely in view of the large difference in elongation at 700°C with a rather small difference in helium concentration. Another factor may be the pretest thermal cycle seen by the tritiated specimens. This thermal cycle may produce different pretest bubble distributions in the tritiated specimens when compared with the ion-bombarded specimens, which may account for the resultant difference in elongations. A final reason for the elongation differences may be different impurity levels in the specimens. Refractory metals quickly absorb interstitial impurities (O, C, N) at elevated temperatures, and differences in the environments of the two charging techniques and in the vacuum conditions during tensile testing could res in significant impurity differences. In stitial impurities have a marked effect strength and ductility of refractory met and hence, impurity differences may infl ence the test results. It should be not that SEM analysis revealed that the cont specimens for the original ion-bombardme study did not exhibit surface grain-boun separation, whereas those in the present study exhibit considerable surface grain- boundary decohesion.

SHEET AND CYLINDRICAL SPECIMENS CHARGED B TRITIUM TRICK

The tensile test data plotted in Fig. compare the high-temperature mechanical properties of sheet and cylindrical spec mens charged to ~35 appm helium by the tritium trick. It is evident that both specimen configurations give the same yi strengths, and yield strength is ess al unaffected by 35 appm helium. Cons ab differences occur in other properties, wi the cylindrical specimens exhibiting con- siderably greater elongation and ultimate strength values then the sheet specimens.

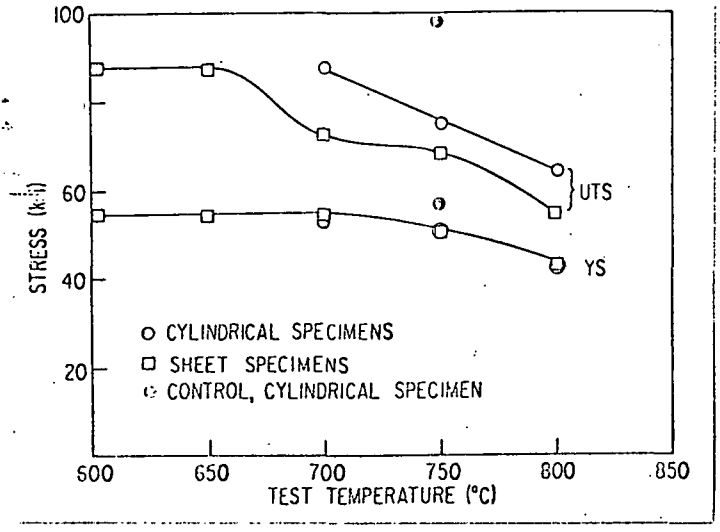

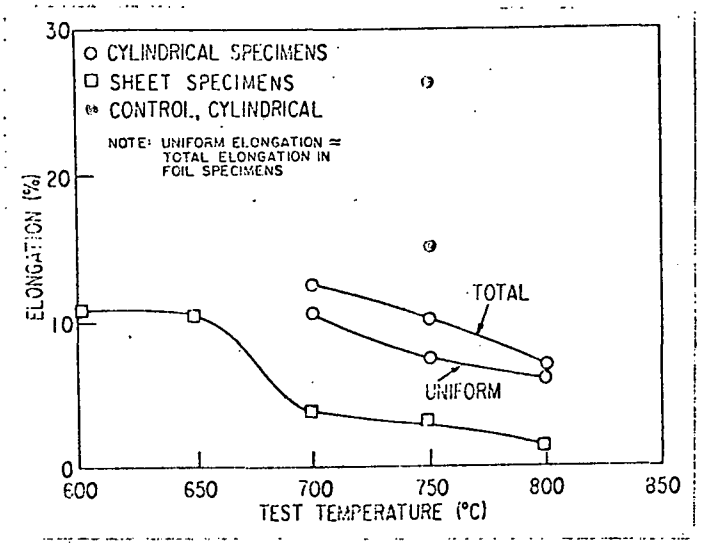

FIGURE 6. Elevated-temperature Tensile Test Results for Sheet and Cylindrical V-15Cr-5Ti Specimens Helium Charged by Tritium Decay

However, the general trends of all mechanical properties agree, i.e., the yield strength is essentially unaffected by the presence of helium, and the ultimate strengths and elongations are decreased by the presence of helium.

The effects of specimen geometry are shown in Fig. 7, which compares the engineering stress-strain curves of the control and helium-charged specimens tested at 750°C. The cylindrical specimens exhibit considerable differences between the

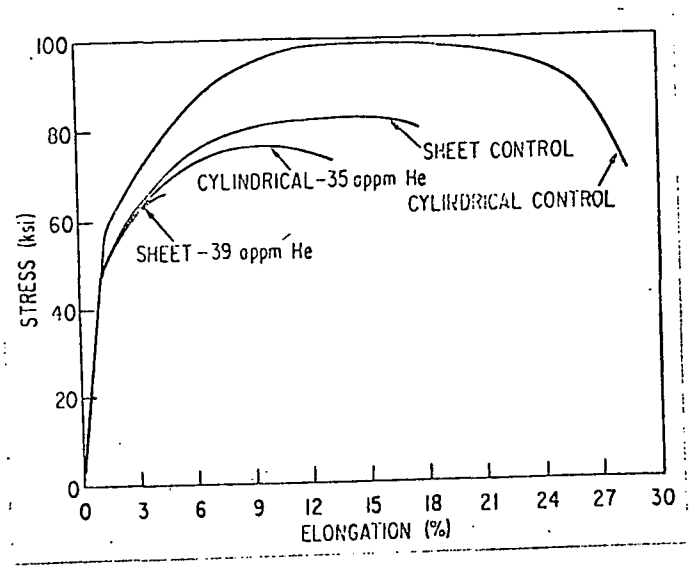

FIGURE 7. Engineering Stress-strain Curves of Sheet and Cylindrical Samples Tested at 750°C

uniform and total elongation, whereas the sheet specimens show almost no differences between total and uniform elongation. Also at larger strain (≥4%), the sheet specimens show a decrease in the strain hardening-rate compared with the equivalent cylindrical specimens, which results in plastic instabilities at reduced plastic strains. The helium-charged cylindrical specimen at 750°C also exhibits a decrease in the strain-hardening rate with respect to the control specimen. The increased ductility of the cylindrical specimens over the thin sheet specimens is consistent with similar tests in "pure" Type 316 stainless steel.[9] Also, the yield strength of the stainless steel samples was shown to be independent of specimen geometry.

COMPARISON OF CYLINDRICAL SPECIMEN DATA WITH ALL SHEET SPECIMEN DATA

It is evident, from Table 1 and Figs. 3 and 6, that both helium-charging techniques for sheet samples, as well as both specimen geometries for samples charged by the tritium trick, result in decreased elongations, when compared with the control samples.

These data, however, indicate that the use of sheet specimens consistently results in a marked decrease in the elongation values compared with the cylindrical specimens, as the sheet specimens exhibit little or no elongation beyond uniform elongation. Limited data indicate that the total elongation of the helium-charged cylindrical samples decreases at a slower rate as the temperature increases when compared with the sheet specimens. Only in the case of the ion-bombardment experiment do the helium-charged samples show an increased strain-hardening rate greater than the control samples.

The authors believe, however, that the consistency between helium-charging methods and specimen configurations in predicting the susceptibility of V-15Cr-5Ti to helium-induced mechanical-property degradation is the important result of the present study. The fact that difference exist between the sheet and cylindrical specimens is not surprising in view of the previously reported results.[9] The absolute mechanical-property values for a given material will have to be developed using standard ASTM specimens, but correct yield strengths and conservative elongation trends can certainly be obtained using sheet specimens. Relatively comparable trend lines can also be developed using either the tritium trick or the ion-bombardment helium charging method.

CONCLUSIONS

1. V-15Cr-5Ti exhibits a reduction in uniform and total elongation at low helium contents (25-35 appm) when tested at elevated temperatures regardless of implantation method or specimen configuration.

2. Yield strength in V-15Cr-5Ti is unaffected by the helium concentrations up to 35 appm, the specimen configuration, or the helium implantation method.

3. In sheet samples, specimens charged by the tritium trick exhibit lower ductility than those charged by ion injection. The onset of gross embrittlement dur tensile testing occurs between 700 a 750°C.

4. Cylindrical specimens, with or with out helium, exhibit larger elongations th sheet specimens under corresponding conditions.

REFERENCES

1. W. M. Stacey, Jr., et al., "Tokamak Experimental Power Reactor Studies," Argonne National Laboratory, ANL/CTR-75-2 (1975).

2. R. G. Hickman, "Helium Doping of Niob with Tritium," Proc. First Topical Mtg on Technology of Controlled Nuclear Fusion, CONF-740402-P2, Vol. II, 1974, p. 535.

3. D. G. Atteridge, L. A. Charlot, A. B. Johnson, Jr., J. F. Remark, and R. E. Westerman, "Effects of Helium Implanted by Tritium Decay on the High Temperature Mechanical Properties of Niobium," Proc. Intl. Conf. on Radiat Effects and Tritium Technology for Fusion Reactors, CONF-750989, Vol. II, 1975, p. 307.

4. J. F. Remark, A. B. Johnson, Jr., H. Farrar, IV, and D. G. Atteridge, Nucl. Tech. 29(3), 369 (1976).

5. L. A. Charlot, J. L. Brimhall, and D. G. Atteridge, "Transmission Microscopy on Helium Implanted Niobium Tensile Specimens," Battelle Pacific Northwest Laboratory, BNWL-SA-5795, May 1976.

6. M. Heerschap, E. Schuller, B. Langerin and A. Trapini, J. Nucl. Mater. 46, 207 (1973).

7. W. C. Kramer, W. R. Burt, Jr., F. J. Karasek, J. E. Flinn, and R. M. Mayfield, "Vanadium Alloy Screening Studies and Fabrication of V-15w/oTi-7.5w/oCr Tubing for Nuclear Fuel Cladding," Argonne National Laboratory, ANL-7206 (1966).

8. A. T. Santhanam, A. Taylor, and S. D. Harkness, Nucl. Met. 18, 302 (1973).

9. A. J. Auer, and A. A. Sagüés, "Foil Specimens for the Investigation of Mechanical Properties in Ion Simulation Experiments," Proc. Intl. Conf. on Radiation Effects and Tritium Technology for Fusion Reactors, CONF-750989, Vol. II, 1975, p. 64.

GRASS-CODE CALCULATION FOR THE BEHAVIOR OF HELIUM IN AUSTENITIC STAINLESS STEELS*

Che-Yu Li

CORNELL UNIVERSITY

Jeffrey Rest, Steven Danyluk, and Roger B. Poeppel

ARGONNE NATIONAL LABORATORY

The GRASS code developed to calculate fission-gas behavior in ceramic fuels has been adapted for CTR applications and can be used to calculate the helium behavior in metals. The results show that the code, after modification to account for the experimentally observed bulk pores in austenitic stainless steels, models the grain-boundary bubbles in a reasonable manner. The bulk pores are likely to be voids at large sizes.

INTRODUCTION

Austenitic stainless steels are among the most promising candidate materials for the first wall of the near-term Tokamak reactor. The nuclear fission programs have generated extensive data for these steels under irradiation conditions. In the CTR, high helium concentrations are expected to develop in these steels as a result of transmutation reactions that occur when 14-MeV neutrons interact with the first wall. The significant difference in the microstructures produced under fast-neutron irradiation with and without high helium generation is the presence or absence of pores on the grain boundaries.[1] Grain-boundary pores are known to cause intergranular fracture and severely reduce the ductility of a material. Therefore, it is essential that the number density and size distribution of grain-boundary pores produced in simulation experiments be similar to those produced in the CTR so that a proper assessment of the mechanical properties of first-wall materials can be made. Current models for void nucleation and growth do not take into account the existence of pores on grain boundaries. The purpose of the present work is to demonstrate how the GRASS code can be used to examine the behavior of helium in austenitic stainless steels, emphasizing the evolution of grain-boundary pores.

The GRASS code was developed at Argonne National Laboratory to model the formation and migration of fission-gas bubbles in ceramic fuels.[2,3] It treats four classes of gas bubbles, i.e., (a) free in the bulk, (b) trapped on dislocations, (c) trapped on grain boundaries, and (d) residing along the grain edges (triple points). In the fission-gas calculation, we assume the bubbles contain sufficient gas atoms such

*Work supported by the U.S. Energy Research and Development Administration.

that the surface tension is balanced by the gas pressure. The growth of bulk bubbles is the result of bubble coalescence caused by random and biased bubble motion. Biased motion, for example, can be produced by the existence of a temperature gradient that causes a bubble to move up the gradient. A bubble is assumed to be trapped when it contacts the grain boundary. The grain-boundary bubbles will grow by coalescing with other bubbles on the grain boundary and with incoming bubbles from the bulk. In the present work, the GRASS code has been modified to model a metallic first wall. Biased bubble motion due to the temperature gradient, re-solution of gas bubbles, and other features related to the behavior of ceramic fuels are suppressed. When helium behavior in austenitic stainless steels is modeled, the helium-generation rate, the estimated helium bubble diffusivity, the dependence of the diffusivity on the bubble size,[2,4] and the grain size of the material are included in the model. The output of the code calculations includes the number density and size distribution of helium in the bulk and on the grain boundaries.

We shall first review briefly the methods of calculation used in the GRASS code. The required modifications and input for modeling helium behavior in austenitic stainless steels at elevated temperatures will be introduced. A pore is considered a bubble if the helium pressure is balanced by the surface tension and is considered a void if the helium pressure is insufficient to balance the surface tension. We shall show that the GRASS code adequately models the helium bubbles on the grain boundaries. The GRASS code calculations suggest that when bulk pores are large they are voids, even when the helium-production rate is high. The application of the present model to the evaluation of radiation-damage simulation experiments in CTR research will be discussed.

GRASS CODE

The detailed description of the GRASS code has been presented elsewhere.[2,3] Coalescence by random walk in the grain matrix will be described to illustrate the type of computation involved. The basic equations for lattice bubble coalescence in GRASS are the same as those employed by Gruber,[5] but the calculational procedure is more approximate. In general, the determination of the bubble-size distribution requires the simultaneous solution of an extremely large set of coupled nonlinear integro-differential equations for bubbles from a few angstroms (single gas atom) to many microns in radii. For calculational procedures (i.e., reasonable code running times), the bubbles are classified by an average size, where size is defined in terms of the number of gas atoms per bubble. The bubble classes are ordered so that the first class refers to bubbles that contain only one gas atom. If S_i denotes the average number of atoms per bubble for bubbles in the ith class (called i-bubbles henceforth), then the bubble-size classes are defined by

$$S_i = mS_{i-1}, \qquad (1)$$

where $m \geq 2$, $i \geq 2$, and $S_1 = 1$. In the lattice, the probability per unit time P^R_{ij} of an i-bubble coalescing with a j-bubble, where the bubbles move by random migration, is given by

$$P^R_{ij} = 4\pi(R_i + R_j)(D^\ell_i + D^\ell_j), \qquad (2)$$

where R_i is the average i-bubble radius (cm), and D^ℓ_i is the average lattice i-bubble diffusion coefficient (cm^2/s). The

rate of coalescence C_{ij} of i-bubbles with j-bubbles is given by

$$C_{ij} = P^R_{ij} F_i F_j, \quad (3)$$

where F_i is the number density of i-bubbles. For $i = j$, C_{ij} becomes

$$C_{ii} = 1/2\ P^R_{ij} F_i^2, \quad (4)$$

so that each pairwise coalescence is counted only once. When an i-bubble and a j-bubble coalesce ($i \geq j$), the resultant bubble can either be in the ith class or in the $i + 1$ class, according to Eq. (1). We define T_{ijk} to be the probability that a coalescence between an i and a j-bubble results in a k-bubble, where $i = k$. If, on the average, the total number of gas atoms remains constant, it follows that

$$T_{ijk} S_k + (1 - T_{ijk}) S_{k+1} = S_i + S_j, \quad (5)$$

or

$$T_{ijk} = \frac{S_{k+1} - S_i - S_j}{S_{k+1} - S_k}, \quad (6)$$

and the probability that the coalescence results in a $k + 1$ bubble is given by

$$T_{ijk} = \frac{S_i + S_j - S_k}{S_{k+1} - S_k}. \quad (7)$$

The array T_{ijk} is the probability that an i-bubble becomes a k-bubble as a result of its coalescence with a j-bubble. The rate N_{ik} at which i-bubbles become k-bubbles is given by

$$N_{ik} = \sum_{j \leq i} C_{ij} T_{ijk}. \quad (8)$$

The j-bubble is assumed to disappear; gas atoms are absorbed into the i-bubble. The rate χ_j of disappearance is given by

$$\chi_j = \sum_{i \geq j} C_{ij} T_{ijk}. \quad (9)$$

The migration of the fission gas from the grain matrix to the grain boundary is treated in the GRASS code as diffusion of single atoms only.[3] Once on the grain boundary, the fission gas can migrate and coalesce.

The choice of a functional relationship between the diffusivity of gas bubbles and their radii depends on the model for bubble motion, i.e., diffusion or reaction-rate limited. In GRASS code, the bubble diffusivities are assumed to have a size dependence

$$D_n = D_A (R_A / R_n)^x, \quad (10)$$

where D_n is the diffusivity of a bubble with radius R_n, D_A is the atomic diffusivity of helium in stainless steel, R_A corresponds to the radius of a bubble containing a single gas atom, and x is chosen to fit experimentally determined values of bubble diffusivities.

The rate of change of the bubble number density $\dot{F}_i$ can be written as a sum of terms such as N_{ij}'s and χ_j's and the rate of helium atom production.[2,3] The equations of the $\dot{F}_i$'s thus form the set of differential equations from which the evolution of the bubble-size distribution can be computed.

HELIUM IN AUSTENITIC STAINLESS STEEL

The computations, using the GRASS code in the present work to model the helium in austenitic steels, are for the isothermal case with a temperature of 500°C. The helium-production rate is a constant 500 ppm/yr. The grain size of the material is 30 μm. The helium pressure within the bubble is assumed to be balanced by the surface tension, which is taken to be 2000 ergs/cm^2. The gas law used is a modified form of the van der Waals equation.[2,3]

The diffusivity of helium bubbles in austenitic stainless steel is estimated, based on the data reported by Walker.[4]

The experimental data for bubble sizes smaller than 65 Å are used. The dependence of the bubble diffusivity on the bubble radius is calculated according to Eq. (10) with the exponent x estimated as 2.9. The activation energy for bubble diffusivity is estimated to be 2 eV, however, the activation energy is assumed to be 1 eV for bubbles diffusing along grain boundaries. The diffusivity of a bubble in the grain matrix containing 100 helium atoms is 1.4×10^{-17} cm^2/s at 500°C. The bubble diffusivity is assumed to be higher on the grain boundary. The difference is calculated by assuming that the value of D_o (preexponential constant) differs by a factor of 10^6 at room temperature.

In the GRASS code, the probability of coalescence between two single atoms calculated according to Eq. (2) is modified by a factor fN, which has a value of 1.0 or smaller to account for the probability that two single atoms drift apart after collision.

The computation is performed for ranges of values of the factor fN discussed above and the bulk and grain-boundary diffusivities D_b and D_{gb}. This is to ensure that the results of the code computation do not represent the consequences of a set of arbitrarily chosen values.

Typical results of the code computation are shown in Fig. 1. These results are obtained with fN = 1.0, and with the values of D_b and D_{gb} calculated as described in this section. This set of parameters will be designated henceforth as the fN(Ref), D_b(Ref), and D_{gb}(Ref), respectively.

The calculated results shown in Fig. 1 are for an irradiation time of 6.8×10^3 h. It is seen that the bulk bubbles are, for the most part, extremely small and show a peak at 25 Å with a corresponding number density of 3.8×10^{15}/cm^3. Few bulk bubbles larger than the peak size are shown to exist (Fig. 1). The grain-boundary bubbles are much larger. Their size distribution is qualitatively similar to that of the bulk bubbles and peaks at 350 Å with a corresponding number density of 2.8×10^{11}/cm^3.

Table 1 is a summary of the results of

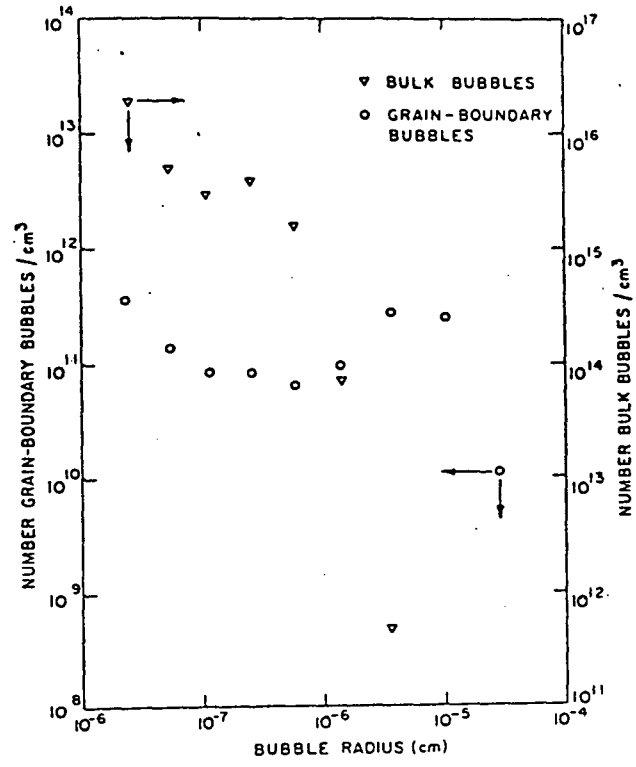

Figure 1. Typical GRASS code output for the Number Density of Grain-boundary and Bulk Bubbles vs Bubble Radius. For this calculation, the helium-generation rate was 500 ppm/yr, and the diffusivity of a bulk bubble containing 100 helium atoms was 1.4×10^{-17} cm^2/s. The calculated data are for an exposure time of 6.8×10^3 h. The bulk and grain-boundary bubble-size distributions peak at 25 and 350 Å, respectively. For comparison, the corresponding HFIR data give an average bulk bubble radius of ~250 Å and an average grain-boundary bubble radius of ~600 Å, with a number density of ~10^{12}/cm^3 for the latter.

TABLE 1. GRASS-code Output of Bulk and Grain-boundary Bubble Distribution after $\sim 6.8 \times 10^3$ h of Irradiation at 500 ppm/yr He Production Rate

fN	D_b	D_{gb}	Bulk Bubbles		Grain-boundary Bubbles	
			Peak Radius (Å)	Peak No. Density (cm^{-3})	Peak Radius (Å)	Peak No. Density (cm^{-3})
1.0	Ref	Ref	25	3.8×10^{15}	350	2.8×10^{11}
0.1	Ref	Ref	25	2.9×10^{15}	990	3.7×10^{11}
0.01	Ref	Ref	25	2.0×10^{15}	990	4.8×10^{11}
0.001	Ref	Ref	25	1.2×10^{15}	990	5.7×10^{11}
0.001	10 × Ref	Ref	57	2.5×10^{14}	990	8.2×10^{11}
0.001	1000 × Ref	Ref	57	3.6×10^{12}	990	9.8×10^{11}
0.001	Ref	100 × Ref	25	1.2×10^{15}	2800	5.9×10^{10}
0.001	Ref	0.01 × Ref	25	1.2×10^{15}	350	5.0×10^{12}

other calculations with different input values of fN, D_b, and D_{gb}. The results show qualitatively the same size distributions as those in Fig. 1. In Table 1, the peak radius and the peak number density after 6.8×10^7 h of irradiation are given.

It is seen from Fig. 1 and Table 1 that the results of the calculation are not strongly influenced by the values of the input parameters. However, specimens irradiated in HIFR show a significantly different size distribution for the bulk bubbles. For an irradiation of ~1 hr in HIFR that produces a total helium content of 1790 ppm with a varying helium-generation rate, the average bulk and grain-boundary bubble radii are ~250 and ~600 Å, and the corresponding number densities are $\sim 10^{14}$ and $\sim 10^{12}/cm^3$, respectively.

With the range of input parameters used in the present work, we expect to model the helium bubble behavior on grain boundaries. However, with a reasonable assumption for the value of bulk bubble diffusivity, we do not expect that the calculated bulk bubble size will be large enough to agree with the experimental data of CTR interest. Physically, this is because the large bubbles have low diffusivities. For example, after an extended postirradiation anneal, at temperatures significantly higher than one half of the absolute melting temperature, the average diameter of bulk helium bubbles in aluminum is <100 Å.[6] This experimental result qualitatively supports the results of the present calculations.

The calculated number density and size distribution of grain-boundary cavities are in agreement with those observed in HFIR experiments. These results indicate that the GRASS code can be used to calculate the evolution of grain-boundary cavities in a metal with a high helium-generation rate. The present results also suggest that the grain-boundary cavities observed in HFIR experiments are likely to contain sufficient gas atoms so that the surface tension is balanced by gas pressure.

The previous discussion suggests, however, that coalescence due to bubble motion alone is not sufficient to account for the size of the bulk cavities and they are probably voids rather than helium bubbles. Therefore, the calculation of the growth rate of cavities in the bulk under conditions that correspond to the HFIR irradiations will require additional mechanisms.

DISCUSSION

The two topics to be discussed are: (1) the significance of the present work on the design of various radiation-damage simulation experiments for CTR research, and (2) the required modifications to the GRASS code to model the bubble and void growth simultaneously.

Simulation Experiments

It is seen from the present work that the bubble diffusivities both in the bulk and on the grain boundary play an important role in controlling the number density and the size of grain-boundary bubbles as well as the number density of the bulk pores even though the latter may become voids at large sizes. Typically, in simulation experiments that are accelerated tests, the neutron flux and the helium-injection rate are proportional and greater than expected in a CTR. Caution should be exercised in these experiments because even though the experiments may be carried out at higher temperatures compared to those of expected CTR conditions, the temperature dependence of bubble diffusivity ($\sim$2 eV) will not allow the diffusivity to increase proportionally with the neutron flux. The latter usually increases by a factor of $\sim$1000. One would expect that codes such as GRASS will have to be used in data extrapolation when the experimental conditions are not completely satisfactory.

The helium-bubble diffusivity can be influenced by the segregation of impurities at the bubble surface.[2,3] This type of segregation has been investigated, for example, by Okamoto and his co-workers.[7] Quantitative information is required on the effects of flux level on the extent of segregation, and therefore the bubble diffusivity, to fully understand the significance of the data from simulation experiments.

Other factors such as the time dependence of the helium-generation rate and the ratio of grain size to specimen thickness should also be considered in detail in the design of simulation experiments.

Modifications to GRASS Code

Bulk pores grow by two mechanisms: (1) the coalescence of cavities and (2) the absorption of vacancies. The growth rate of small pores is controlled by coalescence of pores while the growth rate of large pores is controlled by absorption of vacancies. The small pores are essentially gas bubbles while the large pores are voids. As the small pores grow by coalescence they attain a critical size beyond which vacancy absorption dominates the growth rate. They then grow as voids rather than as bubbles.

The growth by vacancy absorption results from the vacancy supersaturation produced by displacement damage. One can estimate the growth rate by using various void-growth models for fast-neutron irradiation.[8,9] The rate of growth by coalescence with other helium bubbles can be estimated by the sum of the terms as given in Eq. (3). The critical size beyond which the pore becomes a void can be determined by comparing the two rates described above. It is expected that the

critical size will vary slowly with time because the vacancy supersaturation will change with the microstructural evolution (size and number density of point defect sinks).

The growth of voids can result from the coalescence with helium bubbles (including helium atoms) and from vacancy absorption. For convenience of computation, it is desirable to define a new pore size classification based on volume because when two voids or a void and a bubble coalesce their volume is conserved. The new void classes are defined by the volumes V_i where the V_i are calculated from a gas law and the S_i defined by Eq. (1).

One may define a new T'_{ijk} equivalent to the T_{ijk} in Eq. (5). The new T'_{ijk} can be calculated by assuming that, on the average, the total volume is conserved. We can write

$$T'_{ijk}V_k + (1 - T'_{ijk})V_{k+1} = V_i + V_j. \quad (11)$$

Equations (6)-(8) will still be applicable, with the substitution of T_{ijk}'s by T'_{ijk}'s and S_i's by V_i's.

The rate N'_{ik} at which i-voids become (i + 1) voids can be calculated from the modified Eqs. (7) and (8) and the rate of vacancy absorption

$$N'_{ik} = \sum_{j \geq i} C_{ij} T'_{ijk} + \frac{F_i c_i V_i^{2/3}}{V_k - V_i} \quad (12)$$

where k = i + 1, and the second term is the rate of vacancy absorption with c_i the rate constant that also contains the atomic volume[8] and a geometrical factor.

One can use the N'_{ik}'s and χ_j's to construct a set of differential equations from which the evolution of the void-size distribution can be calculated. For the bulk cavities smaller than the critical size and the grain-boundary bubbles, the existing GRASS-code formulation will still be applicable. The grain-boundary bubbles have been found to be pinned to grain-boundary precipitates. This possibility can be easily modeled in the GRASS-code calculation.

SUMMARY

The GRASS code has been adapted to model the helium behavior in metals under anticipated CTR conditions. The code has been used to estimate the size and number density of grain-boundary bubbles in austenitic stainless steels. The code must be modified to model the evolution of bulk pores that become voids. The significance of the results of the present work pertining to the design of radiation-damage simulation experiments for CTR research has been discussed.

REFERENCES

1. F. W. Wiffin and E. E. Bloom, Nucl. Tech. 25, 113 (1975).
2. R. B. Poeppel, in Proc. Conf. on Fast Reactor Fuel Element Technology, Am. Nucl. Soc., p. 311 (1971).
3. J. Rest, M. G. Seitz, S. M. Gehl, and L. R. Kelman, "Development and Experimental Verification of SST-GRASS: A Steady State and Transient Fuel Response and Fission-product Release Code," to be published in the Proc. of OECD-CSNI Meeting on "The Behavior of Water Reactor Fuel Elements Under Accident Conditions," Norway, September (1976).
4. C. K. Walker, J. Nucl. Mater. 37, 171 (1970).
5. E. E. Gruber, J. Appl. Phys. 38, 243 (1967).
6. K. Y. Chen and J. R. Cost, J. Nucl. Mater 52, 59 (1974).
7. P. R. Okamoto and H. Wiedersich, J. Nucl. Mater. 53, 336 (1974).
8. L. K. Mansur, P. R. Okamoto, A. Taylor, and Che-Yu Li, ASTM Special Technical Pub. 570 (1976), p. 272.
9. S. D. Harkness and Che-Yu Li, Met. Trans. 2, 1457 (1971).

INTERNAL DISTRIBUTION

1. M. Abdou
2. F. Adams
3. S. C. Agarwal
4. M. Benson
5. P. Bertoncini
6. T. H. Blewitt
7. C. Boley
8. C. C. Bolta
9. J. N. Brooks
10. R. J. Burke
11. F. A. Cafasso
12. W. F. Calaway
13. I. Charak
14. S. Danyluk
15. J. B. Darby, Jr.
16. S. G. Das
17. J. E. Draley
18. D. Ehst
19. K. Evans, Jr.
20. J. A. Fasolo
21. E. Gelbard
22. S. Grammel
23. H. L. Griffin
24. D. M. Gruen
25. S. D. Harkness
26. A. J. Hatch
27. R. R. Heinrich
28. C. E. Johnson
29. J. C. Jung
30. M. S. Kaminsky
31. S. H. Kim
32. Y. K. Kim
33. A. Krauss
34. R. L. Kustom
35. B. A. Loomis
36. V. A. Maroni
37. R. Mattas
38. F. E. Mills
39. L. J. Milton
40. B. Misra
41. J. Moenich
42. A. Moretti
43. F. Nolfi
44. J. Norem
45. J. S. Patten
46. D. Patterson
47. P. J. Persiani
48. E. N. Pettitt
49. E. G. Pewitt
50. R. B. Poeppel
51. D. Potter
52. W. Praeg
53. J. Rest
54. J. L. Robinson
55. D. Rose
56. B. Siskind
57. P. Smelser
58. A. B. Smith
59. D. L. Smith
60. D. L. Smith
61. D. Y. Smith
62. R. Smith
63. W. M. Stacey, Jr.
64. H. Stevens
65. A. Taylor
66. F. Thalgott
67. L. Turner
68. E. H. VanDeventer
69. S. T. Wang
70. C. J. Wierdak
71. H. Wiedersich
72. C. Youngdahl

EXTERNAL DISTRIBUTION

73. R. G. Alsmiller, Jr., ORNL
74. N. Amherd, EPRI
75. D. G. Atteridge, PNL
76. R. Axtmann, Princeton University
77. C. C. Baker, GA
78. J. Baublitz, DMFE
79. J. W. Beal, DMFE
80. R. Blanken, DMFE
81. S. Locke Bogart, DMFE
82. R. Boom, R. Conn, G. Kulcinski and C. Maynard, Univ. of Wisconsin
83. G. Bosler, Los Alamos
84. W. Briggs, McDonnell-Douglas

EXTERNAL DISTRIBUTION (Cont'd)

85. J. D. Callen, ORNL
86. G. A. Carlson, R. W. Werner and L. Wood, Lawrence Livermore Laboratory
87. F. F. Chen, Univ. of California
88. J. F. Clarke, ORNL
89. F. Coffman, DMFE
90. B. Coppi, MIT
91. N. Anne Davies, DMFE
92. J. Davis, McDonnell-Douglas
93. S. O. Dean, DMFE
94. J. F. Decker, DMFE
95. D. DeMichele, Texas A & M
96. D. Dinge, PNL
97. W. E. Drummond, University of Texas at Austin
98. W. L. Ellis, DMFE
99. S. Fernbach, Lawrence Livermore Laboratory
100. C. Finfgeld, DMFE
101. H. K. Forsen, Exxon Nuclear Company
102. T. K. Fowler, Lawrence Livermore Laboratory
103. H. P. Furth, Princeton University
104. M. B. Gottlieb, Princeton University
105. W. C. Gough, EPRI
106. J. N. Grace, DMFE
107. S. A. Gralnick, Princeton University
108. C. Henning, DMFE
109. G. Hopkins, GA
110. R. J. Impara, DMFE
111. G. R. Ingram, DMFE
112. D. L. Jassby, Princeton University
113. A. B. Johnson, PNL
114. T. Kammash, University of Michigan
115. E. E. Kintner, DMFE
116. D. Klein, Westinghouse
117. H. Kouts, BNL
118. S. C. Kuo, United Technologies Research Center
119. C. Y. Li, Cornell University
120. L. Lidsky, MIT
121. T. S. Lykoudis, Purdue University
122. B. Ma, University of Iowa
123. J. McGoff, DMFE
124. G. H. Miley, F. H. Southworth and R. Turnbull, University of Illinois
125. R. G. Mills, Princeton University
126. K. Moses, DMFE
127. M. Murphy, DMFE
128. J. Neff, DMFE
129. T. Ohkawa, GA
130. J. J. Osher, Lawrence Livermore Laboratory
131. J. Powell, BNL
132. L. K. Price, DMFE
133. R. E. Price, DMFE
134. J. F. Remark, PNL
135. T. C. Reuther, Jr., DMFE

136. F. Ribe, Los Alamos
137. M. Roberts, ORNL
138. D. J. Rose, MIT
139. J. L. Scott, ORNL
140. D. M. C. Stauber, Grumman Aerospace Corp.
141. D. Steiner, ORNL
142. C. Taylor, Livermore
143. F. H. Tenney, Princeton University
144. K. Thomassen, Los Alamos
145. B. Twining, DMFE
146. J. Williams, DMFE
147. W. R. Wilkes and L. J. Wittenberg, Monsanto Research Corp.
148. G. L. Woodruff, University of Washington
149. K. Zwilsky, DMFE